Hochschule für Angewandte Wissenschaften Hamburg
Hamburg University of Applied Sciences

Masterarbeit

Michael Clasen

High-Speed Messverfahren für die instationäre Umströmung und die Strukturoszillationen eines beweglich aufgehängten Tragflügels im Windkanal

Fakultät Technik und Informatik
Department Maschinenbau und Produktion

Faculty of Engineering and Computer Science
Department of Mechanical Engineering and Production Management

Michael Clasen

High-Speed Messverfahren für die instationäre Umströmung und die Strukturoszillationen eines beweglich aufgehängten Tragflügels im Windkanal

Masterarbeit eingereicht im Rahmen der Masterprüfung

im Studiengang Berechnung und Simulation im Maschinenbau
am Department Maschinenbau und Produktion
der Fakultät Technik und Informatik
der Hochschule für Angewandte Wissenschaften Hamburg

in Zusammenarbeit mit:
Helmut-Schmidt-Universität/
Universität der Bundeswehr Hamburg
Professur für Strömungsmechanik
Holstenhofweg 85
22043 Hamburg

Erstprüfer: Prof. Dr.-Ing. Ulf Teschke
Zweitprüfer: Univ.-Prof. Dr.-Ing. habil. Michael Breuer

Abgabedatum: 9. November 2020

Zusammenfassung

Michael Clasen

Thema der Masterthesis

High-Speed Messverfahren für die instationäre Umströmung und die Strukturoszillationen eines beweglich aufgehängten Tragflügels im Windkanal

Stichworte

High-Speed Particle-Image Velocimetry (HS-PIV, 2D), Digital-Image Correlation (DIC, 3D), (Un)synchronisierte Messungen, Tragflügel vom Typ NACA-0012, Windkanal vom Typ Göttingen Subsonic, Seifenblasen-Generator, DEHS-Generator

Kurzzusammenfassung

Diese Arbeit umfasst experimentelle Untersuchungen des strömungsmechanischen und strukturdynamischen Verhaltens eines im Windkanal positionierten Tragflügels, welcher über Dreh- und Blattfedern elastisch gelagert ist. Durch den Windkanal wird eine freie Luftströmung generiert, welche im Reynoldszahl Bereich des laminar-turbulenten Übergangs eingestellt wird. Mithilfe von non-invasiven, bildgebenden Messverfahren werden die Bewegungen des Flügels, die ebenen Strömungsfelder des umgebenden Fluidmediums und deren Wechselwirkung miteinander untersucht. Die Strömungsfelder werden durch die High-Speed Particle-Image Velocimetry (HS-PIV) vermessen. Für das Schwingverhalten des Flügels wird die Messtechnik Digital-Image Correlation (DIC) verwendet. Darüber hinaus wird eine Machbarkeitsstudie erstellt, die eine zeitliche Synchronisation beider Messmethoden erörtert, Umsetzungsideen generiert und erste Messergebnisse bewertet.

Michael Clasen

Title of the thesis

High-speed measuring methods for the unsteady circulation and the structural oscillations of an elastically mounted wing in a wind tunnel

Keywords

High-speed particle-image velocimetry (HS-PIV, 2D), digital-image correlation (DIC, 3D), (un)synchronized measurements, wing of NACA-0012 type, wind tunnel of Göttingen subsonic type, soap-bubble generator, DEHS generator

Abstract

This report includes the experimental investigations of the fluid mechanical and the structural dynamic behavior of a wing which is positioned in a wind tunnel and elastically mounted by torsional and leaf springs. An air free-stream is generated by a wind tunnel which is adjusted in the transitional laminar-turbulent Reynolds number regime. With non-invasive image measuring methods, the motions of the wing, the velocity fields of the surrounded fluid medium and their interaction are investigated. The velocity fields are measured by the high-speed particle-image velocimetry (HS-PIV). For the vibrational behavior of the wing, the measuring technique digital-image correlation (DIC) is used. Furthermore, a feasibility study is presented, which discusses the temporal synchronization of both measuring methods, generating practical applications and evaluating first measurement results.

HAW HAMBURG

Aufgabenstellung

für die Masterthesis

von Herrn **Michael Clasen**
Matrikelnr.: **2209489,**

in Zusammenarbeit mit der Helmut Schmidt Universität, Hamburg, Professur für Strömungsmechanik.

PfS **Professur für Strömungsmechanik (PfS)**
Institut für Mechanik

Univ.–Prof. Dr.–Ing. habil. Michael Breuer

HELMUT SCHMIDT UNIVERSITÄT

High-Speed Messverfahren für die instationäre Umströmung und die Strukturoszillationen eines beweglich aufgehängten Tragflügels im Windkanal

Fluid-Struktur-Interaktionen (FSI) spielen in vielen Bereichen der Technik eine zentrale Rolle, insbesondere auch in der Aerodynamik von Windkraftanlagen und in der Luftfahrt. Zur detaillierten Untersuchung des Phänomens an Tragflügeln ist im Labor der Professur für Strömungsmechanik im Windkanal ein Flatter-Prüfstand für einen Tragflügel mit einem translatorischen und einem rotatorischen Freiheitsgrad aufgebaut und bereits umfangreich erprobt worden [1].

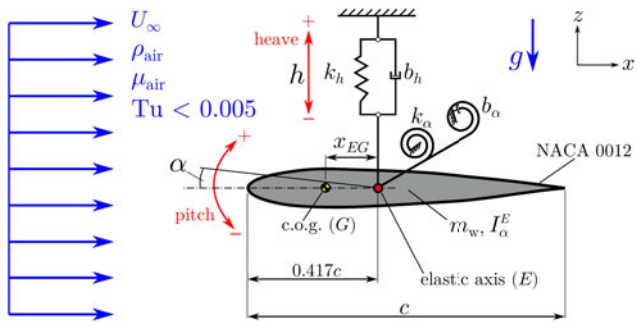

(a) Schematischer Tragflügel mit zwei Freiheitsgraden.

(b) Windkanal der PfS.

Ziel dieser Arbeit ist die Durchführung von zeitlich hochaufgelösten Strömungs- und Strukturmessungen, um das dynamische Verhalten des Tragflügels zu charakterisieren. Diese Messungen sollen mittels der zur Verfügung stehenden Hochgeschwindigkeits-Messtechnik (High-Speed PIV/DIC) erfasst und mit den bereits gesammelten Daten verglichen werden.

Für diese Arbeit ist folgender Arbeitsablauf geplant:

1) **Vorbereitung des Prüfstandes und der Messtechnik**
   - Integration des Rahmens des Flatterprüfstands in die Spiegelaufnahme des PIV-Systems
   - Einführung in die Messtechnik inkl. Applikation im Windkanal
2) **Nicht-synchrone Strömungs- und Strukturmessungen**
   - Strömungsmessungen (2D HS-PIV) am unbewegten und bewegten Tragflügel mit dem Schwerpunkt auf instationären Phänomenen
   - Strukturmessungen (3D HS-DIC) am bewegten Tragflügel
   - Vergleich mit vorhandenen Messdaten [1]
3) **Machbarkeitsstudie für synchronisierte PIV-DIC Messungen**
   - Erprobung der Nutzbarkeit des PIV-Lasers als Lichtquelle für DIC-Messungen
   - Evaluation der Möglichkeiten zur synchronen Erfassung des FSI-Problems (u.a. Triggern der Messung, Zusammenführung der Messdaten beider Systeme, etc.)
4) **Schriftliche Dokumentation der Ergebnisse**

Das Thema liefert einen detaillierten Einblick in die experimentelle Laborarbeit mit moderner Hochgeschwindigkeits-Messtechnik. Die hierbei erlangten Erfahrungen sind sowohl für weiterführende wissenschaftliche Arbeiten als auch für industrielle Tätigkeiten relevant.

Betreuer an der HSU:	Dr.-Ing. J. N. Wood
Kontakt:	H 11 Raum 107, Tel. 040/6541-3768
	woodj@hsu-hh.de

Literatur:

[1] J. N. Wood, M. Breuer, G. De Nayer, (2020). *Experimental investigations on the dynamic behavior of a 2-DOF airfoil in transitional Re number regime based on digital-image-correlation measurements*. Journal of Fluids and Structures, July, 2020, https://www.sciencedirect.com/science/article/pii/S0889974619307674

Hamburg, den 31. Mai 2020

U. Teschke

Acknowledgements

During this master thesis, individual people have contributed to the success of this work. Hereby, I would like to appreciate and thank for their help.

First of all, Mr. Univ.-Prof. Dr.-Ing. habil. Michael Breuer has enabled this thesis by providing a working possibility at the chair PfS and the laboratory of the Helmut-Schmidt University Hamburg. I have received helpful advice and and several ideas for improvement related to this documentation. Mr. Prof. Dr.-Ing. Ulf Teschke has supervised this thesis as well and moreover, during my time of studying at the University of Applied Sciences Hamburg, I could always ask for his advice, he has been a mentor for me.
At the laboratory at PfS, Mr. Dipl.-Ing. Wolfgang Warnecke and Mr. Martin Kitzmann (Technician) have supported me with their technical know-how and their work experience by introducing the properties and the handling of the wind tunnel and the test stand. Especially, I would like to point out Mr. Dr.-Ing. Jens Nikolas Wood, or shortly "Nick", who has been the supervising tutor of this thesis. His creativity in the performance of experiments, his talent of teaching the PIV and DIC technique and his motivating skills have influenced me positively.
Finally, I would like to thank my parents, Bozenna and Jens Clasen, for their empathy, patience and encouragement.

In gratitude,

Michael Clasen
Hamburg, November 2020

Contents

List of Figures

List of Tables

Nomenclature

The abreviations or notations used in this report are explained below with their unit. If a notation does not appear in this section, it is explained in the context of the report.

Abbreviation

AoA	Angle of Attack
ARF	Advanced Recording File
ASCII	American Standard Code for Information Interchange
AVI	Audio video interleave (file)
BMP	Bitmap (image file)
BNC	Bayonet Neill Concelman
CAD	Computer-aided design
CCD	Charge-coupled device semiconductor
CMOS	Complementary metal-oxide
c.o.g	center of gravity
COS	Coordinate system
CPU	Central Processing Unit
CTA	Constant-temperature anemometer
DAQ	Data acquisition board
DEHS	Di-Ethyl-Hexyl-Sebacat
DFT	Discrete Fourier Transform
DIC	Digital-image correlation

Abbreviation (continuance)

1D	One-dimensional
2D	Two-dimensional
3D	Three-dimensional
disp z	displacements in z-direction
DOF	Degrees of freedom
E	Elastic axis (of the airfoil)
e.g.	exempli gratia
FFT	Fast Fourier Transform
Fig.	figure
fps	Frames per second (unit)
FSI	Fluid-Structure Interaction
G	center of gravity
GB	Giga byte (unit)
HS-DIC	High-Speed digital-image correlation
HS-PIV	High-Speed particle-image velocimetry
Hz	Hertz (unit)
i.e.	id est
IW	Interrogation window
LAO	Large amplitude oscillations
LCO	Limit-cycle oscillations
LDA	Laser Doppler anemometry
LED	Light-emitting diodes
LES	Large-eddy-simulations
LSO	Light sheet optics
MP	Monitoring point
MPx	Mega pixels (unit)
MPPS	Most penetration particle size
NACA	National Advisory Committee for Aeronautics
NASA	National Aeronautics and Space Administration

Abbreviation (continuance)

Nd:YLF	Neodym: Yttrium-Lithium-Fluorid
PfS	Professur für Strömungsmechanik
PIV	Particle-image velocimetry
PLA	Polylactic acid
pps	Pulses per second
PSD	Power-Spectral-Density
Px	Pixels (unit)
RANS	Reynolds-Averaged Navier-Stokes equations
rpm	Rounds per minute (unit)
SAO	Small amplitude oscillations
SDCI	Single-drop digital communication interface (for small sensors and actuators)
Tab.	Table
TIF	Tagged Image File
TURNS2D	Transonic Unsteady Rotor Navier-Stokes 2D solver
USB	Universal Serial Bus
Vel.	Velocity
Vel. Mag.	Velocity magnitude

Notation

$\overline{A}$	Arithmetic mean value of A
$E(s^2)$	Expectation value of the squared standard deviation
$\underline{\underline{H}}$	Hessian matrix containing the second-order derivatives of the correlation function
$\underline{\underline{I}}$	Identity matrix
∇	Nabla-operator (vector) for partial derivation containing the elements $(\partial/\partial x, \partial/\partial y, \partial/\partial z)^T$
$\underline{P}^*$	Provisional solution (*) vector used for further optimization

Notation (continuance)

$\mathrm{rms}(\Delta z)$	Root mean square value of Δz
$\underline{\underline{R}}$	Matrix
$\underline{\underline{R}}^T$	Transpose of $\underline{\underline{R}}$
$\underline{\underline{R}}^{-1}$	Inverse of $\underline{\underline{R}}$
$\underline{t}$	Vector
$\overline{XO_l}$, $\overline{XO_r}$, $\overline{O_lO_r}$	Connection lines between the object point X and (between) the focal points O_l, O_r
$\Delta\tilde{z}$	Variation of Δz
$\overline{\Delta\tilde{z}}$	Mean variation of z

List of symbols

Greek symbols

α	Pitch angle	[°]
$\alpha(y_w)$	Euler angle "pitch" for the rotation of the world coordinate axis y_w	[rad]
η	Energy efficiency ratio	[−]
κ	Horizontal stretching parameter for the schematic deformation of a grid cell (DIC processing)	[px]
κ_1, κ_2	Intrinsic parameters related to the radial distortion within the image plane (calibration of DIC)	$[10^6/\mathrm{m}^2]$
λ	Wave length of laser beam	$[10^{-9}\,\mathrm{m}]$
μ	Dynamic viscosity	$[\mathrm{N\,s/m}^2]$
μ_f	Dynamic viscosity of the fluid	$[\mathrm{N\,s/m}^2]$
μ_p	Dynamic viscosity of the tracer particles	$[\mathrm{N\,s/m}^2]$
μ	Estimated expectation value related to the z-displacements (statistical quantity used for DIC)	[m]
ω_d	Eigen angular frequency	[1/s]
$\overline{\omega}$	Heave-to-pitch frequency ratio	[−]
ψ	Vertical stretching parameter for the schematic deformation of a grid cell (DIC processing)	[px]

Greek symbols (continuance)

$\psi(z_w)$	Euler angle "tilt" for the rotation of the world coordinate axis z_w	[rad]
ρ	Density	[kg/m^3]
ρ_f	Density of the fluid	[kg/m^3]
ρ_p	Density of the tracer particles	[kg/m^3]
σ	Standard deviation related to the z-displacements (statistical quantity used for DIC)	[m]
τ_f	Characteristic time scale of the fluid	[s]
τ_p	Tracer particle response time	[s]
$\tau(s)$	Local shear stress depending on the position s	[N/m^2]
$\theta(x_w)$	Euler angle "yaw" for the rotation of the world coordinate axis x_w	[rad]
φ	Phase shift angle of sinusoidal oscillations	[°]
$\Lambda_{h,\alpha}$	Logarithmic decrement for heave, pitch	[−]
Φ	Intersection angle of projection lines (DIC)	[°]

Latin symbols

$A^{\mathrm{DIC}}_{\mathrm{Laser}}$	Usable speckle pattern area illuminated by the PIV-laser (DIC)	[m^2]
$A^{\mathrm{DIC}}_{\mathrm{ref}}$	Usable speckle pattern area illuminated by standard light (DIC)	[m^2]
b_α	Viscous rotational damping coefficients according to pitch	[N m s]
b_h	Viscous transitional damping coefficients according to heave	[N s/m]
c	Chord line length of the airfoil	[m]
c_p	Pressure coefficient	[−]
c_f	Skin friction coefficient	[−]
C_D	Aerodynamic drag coefficient	[−]
C_L	Aerodynamic lift coefficient	[−]
C_{spat}	2D spatial calibration factor	[10^3 px/m]

Latin symbols (continuance)

d_p	Mean soap bubble diameter	$[10^{-6}\,\mathrm{m}]$
D	Diameter	[m]
D_α	Damping ratio of pitch	[−]
D_h	Damping ratio of heave	[−]
f	Frequency	[Hz]
f	Focal length	[m]
f_α	Frequency of pitch	[Hz]
f_{cam}	Sample rate (camera)	[fps ≡ 1/s]
f_h	Frequency of heave	[Hz]
f_u	Main frequency within the FFT generated from the time history of velocity u (PIV-Monitoring point in the wake)	[Hz]
f_w	Main frequency within the FFT generated from the time history of velocity w (PIV-Monitoring point in the wake)	[Hz]
$f_{CTA,CV}$	Frequency of the convection of vortices in the wake measured by CTA	[Hz]
$f_{CTA,LCO}$	Frequency of the wake flow measured by CTA as a result of the limit-cycle oscillations of the airfoil	[Hz]
$f_{DIC,LCO}$	Frequency of the limit-cycle oscillations of the airfoil measured by DIC	[Hz]
f_{LCO}	Frequency of the limit-cycle oscillations	[Hz]
f_{PR}	Laser pulse repetition rate	[pps ≡ 1/s]
F'_D	Aerodynamic drag force	[N]
F'_L	Aerodynamic lift force	[N]
g	Gravitational constant	$[\mathrm{m/s^2}]$
H	Height	[m]
$H_{1,2}(x_0, y_0)$	Principle point of the image plane 1, 2 with the image coordinates x_0, y_0	[−]
I^E_α	Mass moment of inertia related to the elastic axis	$[\mathrm{kg\,m^2}]$
k	Scaling factor for optimization (DIC calibration)	[−]
k_α	Torsional spring stiffness	[Nm/rad]
k_h	Heave spring stiffness	[N/m]

Latin symbols (continuance)

l	Span of the wing	[m]
l_h	Effective spring length	[m]
L	Length	[m]
L	Maximum profile thickness of the airfoil	[m]
m_w	Total mass of the elastically mounted wing system	[kg]
$m_{w,e}$	Summed weight of the extra masses for case I, III	[kg]
$m_{w,m}$	Mass of the elastic mounting	[kg]
$m_{w,0}$	Mass of the wing	[kg]
M_T	Torque, torsional moment	[Nm]
n	Number of crossing points on the calibration target	[−]
n_{air}	Rotation speed of the air blower in the wind tunnel	[rpm $\equiv (60\,\mathrm{s})^{-1}$]
O_l	Focal point of the left DIC-camera	[−]
O_r	Focal point of the right DIC-camera	[−]
p_∞	Far-field pressure	[N/m^2]
$p(s)$	Local pressure depending on the natural coordinate s	[N/m^2]
$p(x, y, z)$	Local pressure depending on the position vector (x, y, z)	[N/m^2]
$P(x_c, y_c, z_c)$	Object point in camera coordinates	[−]
P_{max}	Maximum performance of the air blower in the wind tunnel	[N m/s]
$P_{w,I}$	Monitoring point for case I (DIC)	[−]
$P_{w,III}$	Monitoring point for case III (DIC)	[−]
r	Radius within the image plane with $r^2 = x_i'^2 + y_i'^2$	[m]
$\underline{r}_c$	Position vector of the camera COS with the Cartesian components x_c, y_c, z_c	[m, m, m]
$\underline{r}_w$	Position vector of the "world" COS (calibration target) with the Cartesian components x_w, y_w, $z_w = 0$	[m, m, m]
R_a	Mean surface roughness	[10^{-6} m]
R'	Aerodynamic resultant force	[N]
R^2	Accuracy of the linear regression curve	[−]
$\underline{\underline{R}}(\underline{r}_w)$	Rotation matrix (3×3) related to $\underline{r}_w$	[rad]

Latin symbols (continuance)

Re_c	Reynolds number related to the chord line length of the airfoil	[−]
s	Horizontal scale factor (DIC)	[−]
s	Natural coordinate along the airfoil profile	[m]
$\vec{s}$	Displacement vector of the PIV-processing with the horizontal and vertical components m and n	[px, px]
Sk	Stokes number	[−]
Sr	Strouhal number	[−]
t	Thickness of the airfoil	[m]
t	Time	[s]
$\underline{t}$	Translation vector (3×1) with the Cartesian elements t_x, t_y, t_z	[m, m, m]
t_0	Beginning time of the single-period oscillation of the airfoil (synchronized PIV-DIC)	[s]
T	Time period of oscillation	[s]
T_d	Time period in between two amplitudes of a decaying, sinusoidal oscillation	[s]
Tu	Intensity of turbulence	[−]
u	Horizontal displacement in the image plane (radial distortion)	[px, px]
u	Fluid velocity component in x-direction	[m/s]
u_{ref}	Generated free-stream velocity by the air blower	[m/s]
u_τ	Friction velocity	[m/s]
u_{ts}	Settling velocity of the tracer particles	[m/s]
$\overline{u}$	Time-averaged mean value of the fluid velocity component u (part of Reynolds separation)	[m/s]
u'	Fluctuation of the fluid velocity component u (part of Reynolds separation)	[m/s]
U_{cv}	Vortex convection velocity	[m/s]
U_∞	Free-stream velocity in x-direction provided by the wind tunnel	[m/s]

Latin symbols (continuance)

U_{max}	Maximum free-stream velocity in the wind tunnel	[m/s]
v	Fluid velocity component in y-direction	[m/s]
v	Vertical displacement in the image plane (radial distortion)	[px, px]
w	Fluid velocity component in z-direction	[m/s]
$\overline{w}$	Time-averaged mean value of the fluid velocity component w	[m/s]
w'	Fluctuation of the fluid velocity component w (part of Reynolds separation)	[m/s]
W	Width	[m]
x	Cartesian coordinate in horizontal direction	[m]
x_{EG}	Horizontal distance between the elastic axis E and the center of gravity G	[m]
$x_v(t)$	Vortex convection position as a time-dependent function	[−]
$(x_d; y_d)$	"Distorted" image coordinates measured in the image plane	[px, px]
$(x_i; y_i)$	Position vector within the image plane	[px, px]
$(x'_i; y'_i)$	Position vector within the image plane with the offset of (x_0, y_0)	[px, px]
(x_0, y_0)	Position vector of the principle point H within the image plane	[px, px]
$(x'_p; y'_p)$	"Predicted" position vector within the image plane with the offset of (x_0, y_0)	[px, px]
y	Cartesian coordinate in spatial direction	[m]
z	Cartesian coordinate in vertical direction	[m]

Greek and Latin symbols

Δf^{2-DOF}	Beat frequency	[Hz]
$\overline{\Delta s}$	Mean distance in between the shed vortices in the wake	[m]
Δs_{tot}	Total distance between the furthest vortex in the wake and the trailing edge	[m]

Greek and Latin symbols (continuance)

Δt_{cam}	Image acquisition time (camera)	[s]
Δt_{FS}	Inter-frame straddling time (camera)	[s]
Δt_{LD}	Laser delay time	[s]
Δt_{PIV}	Laser pulse straddling-time	[s]
Δt_{PR}	Pulse repetition time	[s]
Δz_h	Amplitude of the heave-displacements in z-direction	[m]

Chapter 1

Introduction

1.1 Motivation

Fluid-structure interactions (FSI) are an omnipresent phenomenon in nature and technics. They describe the cooperation of fluid flows and structural movements. FSI will play a central role in several disciplines in the future, such as the effective energy production out of environmental resources. Besides already existing offshore wind and water turbines, modern energy harvesting systems are developed nowadays. As an example, Cardona et al. [6] investigated the energy harvesting of an oscillating hydrofoil system mounted on the lower side of a pontoon boat. Fig. 1.1 shall give an impression of the design. The two hydrofoils can move vertically up and down, which is called heave, as well as they can rotate around their mounting axis, which is called pitch. By a surrounding fluid flow the hydrofoils are self-started and operating with 90° phase shift to each other, whereat a connected generator converts the heave and pitch motions into electric energy. To present some practical data, an amount of 1.2 MW could be gained at a driving speed of about 2 m/s in the Taunton River (USA, Massachusetts). The energy efficiency ratio *water-to-wire* (kinetic to electric energy) was measured by $\eta = 22\%$.
At the Professur für Strömungsmechanik (PfS) of the Helmut-Schmidt-University, FSI phenomena of light-weight structures under turbulent fluid loads are investigated. Elaborate numerical simulations are carried out, which are validated by experimental studies. Until now, typical FSI-benchmarks have been developed considering dynamically highly flexible structures with large non-linear deformations. As an example, the work of De Nayer and Breuer [7] may be mentioned here: The behavior of a fixed cylinder with a flexible thin rubber plate and a rear mass passed by a turbulent fluid flow in a water tunnel at $\mathrm{Re_D} = 30,470$ related to the diameter D of the cylinder is numerically simulated. The description of the test case can be seen in Fig. 1.2a. An overview of some results

is depicted in Fig. 1.2b referring to complementary experimental investigations that were carried out by Kalmbach and Breuer [13] previously. The structural measurements were done with a laser triangulation sensor showing the normalized oscillation curve in lateral y-direction. The fluid flow measurements were done with particle-image-velocimetry (PIV) showing the field of the normalized fluid velocity component u/U_∞ in mainstream direction and v/U_∞ in lateral direction.

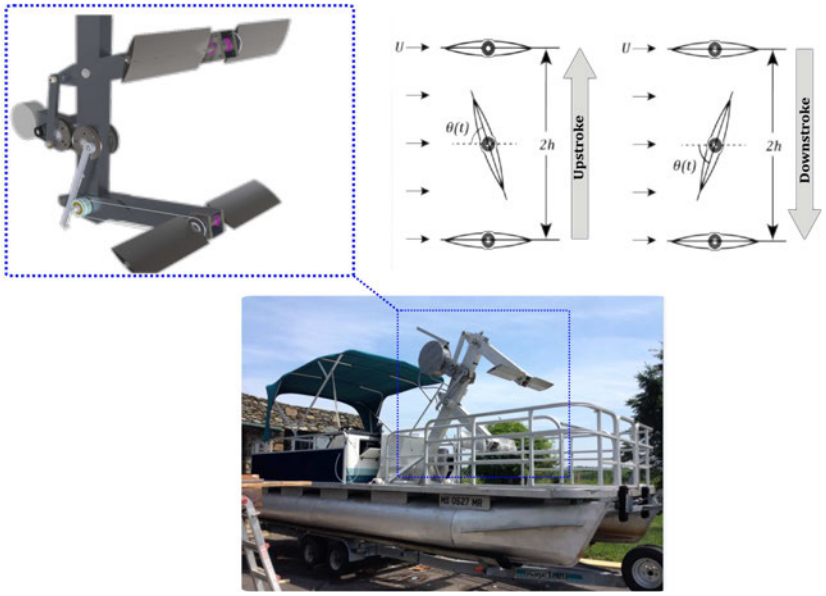

Figure 1.1: Energy harvesting oscillating hydrofoil system [6]. (Top-left) the CAD-model. (Top-right) the motion mechanism. (Bottom) the real design mounted on top of a pontoon boat for transit reasons.

In the laboratory of the PfS, modern setups and measurement techniques are used: Presently, a subsonic wind tunnel of Göttingen-type (closed loop design) is mainly used delivering free-streams with low turbulence intensities and a velocity magnitude up to 28 m/s. With the current setup, measurements of structural movements and fluid flows are conducted by high-speed imaging methods like the digital-image correlation (DIC) and particle-image velocimetry (PIV). The DIC-method is able to measure three-dimensional (3D) structure deformations using at least two cameras, which focus from different perspectives onto the object. As briefly mentioned before, the PIV-method is used to measure two-dimensional (2D) velocity fields of a fluid flow in a defined area. Both image-based methods have the advantage that they are non-invasive, which means that they do not disturb actively the observed physical process by any sensor. Furthermore, the results can show a visible spectrum of structural deformations or fluid velocity distributions within a control volume, whereas other conventional point-wise techniques are restricted to the measurement of the temporal behavior of a characteristic parameter and often influence the physical process by their sensors.

At PfS, it is of great interest that experiments deliver simultaneous results of FSI phenomena, i.e., for the fluid flow and the structure movement, similar to modern numerical simulations. However, this was not possible until now due to the lower temporal resolution of the previous PIV-system. A synchronization with the existing High-Speed DIC system (HS-DIC) was difficult for the experimenter to realize so far. Recently, PfS has acquired a High-Speed PIV system (HS-PIV). Thus, both image-based methods are now comparable concerning their performance level which allows to operate both synchronously in time. The feasibility of the synchronized HS-PIV and HS-DIC-measurements shall be demonstrated in this thesis based on the example of a flutter test stand consisting of an elastically mounted wing with an airfoil of the type NACA 0012. It is a relatively simple system, since the airfoil is rigid and the elastic mounting allows solely two degrees of freedom (DOF). By confirming previously published experimental results [23] that have already been obtained for the flutter test case using the HS-DIC system mentioned above, the success of the synchronized measurement method can be appropriately evaluated. In the following an overview of the present literature connected to existing synchronized PIV-DIC-methods as well as investigations on elastically mounted NACA 0012 airfoils is provided.

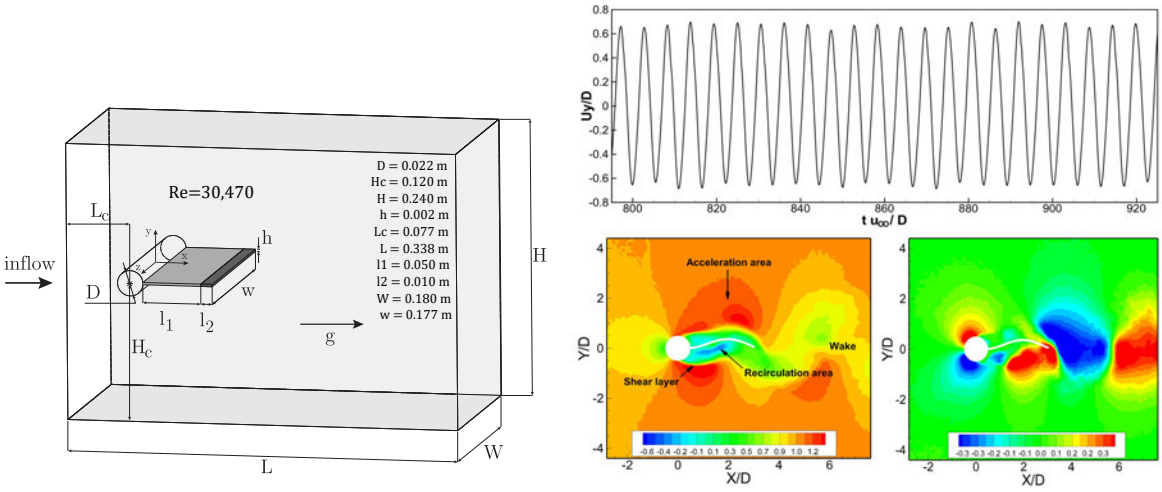

(a) Test case

(b) Extraction of experimental results of the structure (top) and the fluid flow velocity in mainstream direction (u/U_∞, bottom left) and vertical direction (v/U_∞, bottom right).

Figure 1.2: Investigation of the PfS on the test case FSI-PfS-2a [7, 13].

1.2 Literature overview

Beginning with the synchronized PIV-DIC-measurement method, the work of Zhang et al. [30] presents experimental FSI studies for the purpose of finding material solutions for high-performance marine vessels that are resilient against water shock waves. Spatially- and temporally-resolved measurements of the plate deflection and fluid velocity shall give insight into the impulsive hydrodynamic loading of air-backed structures. The experimental setup as well as the hardware connection and data transfer are depicted in Fig. 1.3.

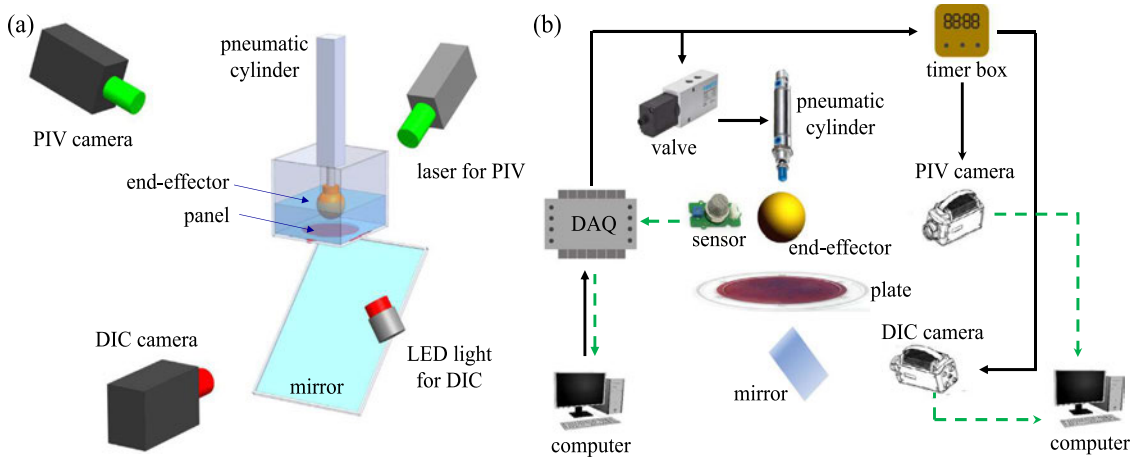

Figure 1.3: Schematic of the setup of [30]. (a) The main experimental components: Water tank with panel on the bottom, spherical end-effector, pneumatic cylinder, PIV- and DIC-system. (b) The hardware (black solid lines) and data transfer (green dashed lines): Two computers for hardware control and data storage, DAQ board, proportional directional control valve, timer box for simultaneous triggering and data acquisition.

The main experimental object is a transparent water tank ($L \times W \times H = 0.22\,\mathrm{m} \times 0.195\,\mathrm{m} \times 0.18\,\mathrm{m}$) with a flexible panel clamped at its bottom side with a thickness of $h = 0.005\,\mathrm{m}$. By a spherical end-effector, which is attached to a pneumatic cylinder, the water surface is penetrated. For this purpose, air pressure supply is controlled by a proportional directional control valve. The excitation mechanism and the measurement are initiated by a data acquisition board (DAQ), which is controlled by a computer. The simultaneous DIC- and PIV-measurements are triggered by a timer box and the captured image data are sent to a second computer for processing. The DIC- and PIV-camera have a resolution of 1632×1200 pixels, measuring with the acquisition frame-rate of 1000 Hz. Summarizing some results, Fig. 1.4 depicts the field distributions for the pressure (right) and velocity (left) measured by PIV from the side-perspective in the y-z-plane around the effector and deformed plate at the second time point of recording. The pressure field distribution was computed by inserting the velocity field data into the incompressible

Navier-Stokes-equations and by numerical integration of the pressure gradients. The numerical integration was induced by the initial condition of a reference pressure, which had been measured by an additional pressure sensor mounted at the bottom of the endeffector. The results of the hydrodynamic pressure loads can be considered in the dimensioning of covering panels, i.e., in submarines.

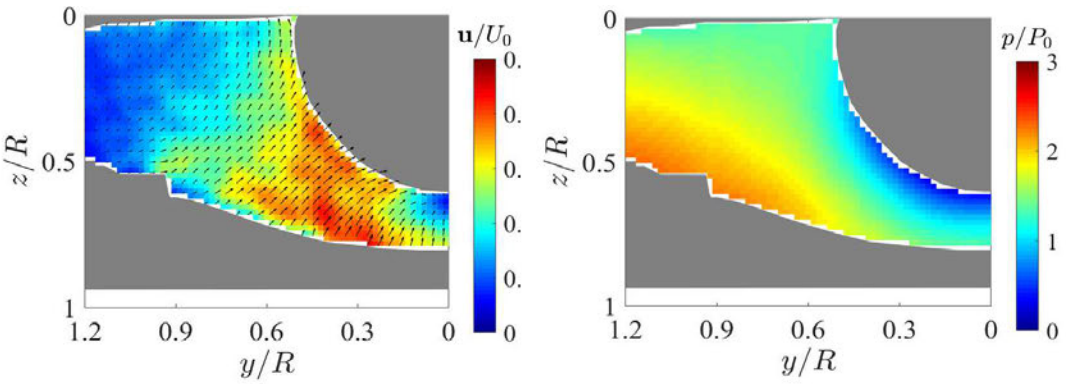

Figure 1.4: Exemplary PIV result of [30] for one instant in time in the excitation cycle: Normalized velocity distribution u/U_0 (left). Normalized pressure distribution p/p_0 (right).

A further experimental work considering synchronized PIV-DIC-measurements was carried out by Zhang and Porfiri [32] investigating the unsteady FSI phenomena by a water-backed impact of a compliant plate, fixed on a water surface. Practically, the findings of this study can be used for optimizing composite structures in the naval and aerospace design. Typically appearing scenarios can be a tool falling on a panel of a boat hull or an aircraft landing on an aircraft carrier or a floating airport. However, focussing on the experimental setup depicted in Fig. 1.5, there is a similarity to the one in Fig. 1.3: Common elements are the controlling devices like the DAQ-board, the timer box and the sensor. A microcontroller is additionally interconnected here, which controls the position of the impactor by an electromagnet. The impactor is a free fall object exciting the flexible plate with a thickness of $h = 0.01\,\mathrm{m}$ clamped at the top side of the water tank touching the water surface. The transparent open water tank has the dimensions ($L \times W \times H = 0.8\,\mathrm{m} \times 0.32\,\mathrm{m} \times 0.35\,\mathrm{m}$). The orientation and location of the DIC- and PIV-system is slightly altered compared to the setup in [30] while the resolution and acquisition frame-rate of the DIC- and PIV-cameras remained constant.
In Fig. 1.6 the behavior of the water environment underneath the flexible plate is depicted. Due to the symmetric setup, only half of the area around the plate is investigated, delivering the field distributions for the pressure (right) and velocity (left) measured by PIV in the x-z-plane regarding the long edge of the plate. The hydrodynamic pressure field was calculated from the velocity field based on a Poisson equation.

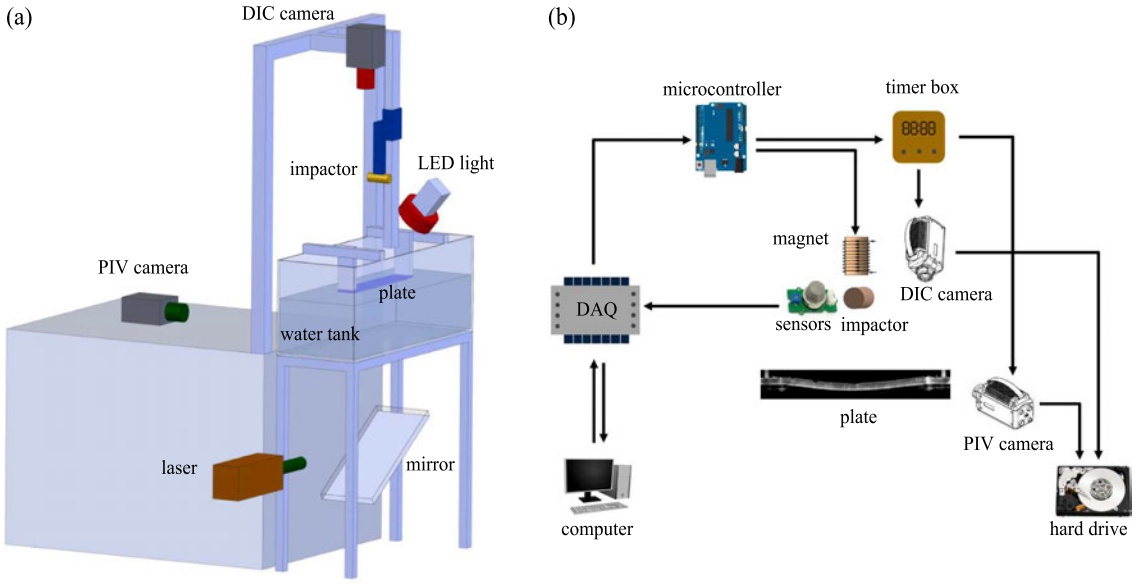

Figure 1.5: Schematic of the setup of [32]. (a) The main experimental components: Water tank with plate on the surface, impactor, pneumatic cylinder, PIV- and DIC-system. (b) The hardware transfer (black solid lines): Hardware control and data storage by computer, DAQ board, microcontroller, magnet, impactor, timer box for simultaneous triggering and data acquisition.

It was found, that the water medium has a higher damping effect on the structural response of the plate than the air medium, which is due to the different mass and inertia properties.

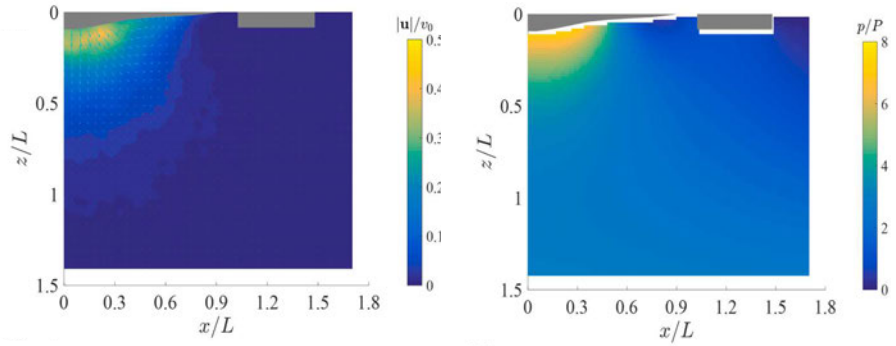

Figure 1.6: Exemplary PIV result of [32] for one instant in time in the excitation cycle: Normalized velocity distribution $|u|/v_0$ (left). Normalized pressure distribution p/P (right).

Another work of Zhang et al. [31] investigated the estimation of hydrodynamic loading and structural response of a flexible cantilever plate immersed in a steady unidirectional flow of a water tunnel system. Pressure fields are reconstructed from the velocity fields obtained by PIV, while structural displacement fields are measured by DIC.

This study is relevant for FSI-phenomena like aeroelasticity of airfoils and hydrodynamic impact on marine structures. The schematic of the experimental setup is depicted in Fig. 1.7. The water flow is conducted in a water tunnel with the dimensions 0.15 m × 0.15 m × 2.4 m (L × H × W), while the flexible cantilever plate with a thickness of 2.5 mm is clamped with one edge at a support construction so that its plane is perpendicularly directed towards the main flow. The water flow is adjusted in several levels within the Reynolds number regime $935 \leq \mathrm{Re} \leq 3846$ and the flexible plate oscillates always below the flutter border. The PIV-system uses the illumination of a laser and one camera while the laser sheet is redirected by two mirrors illuminating both fluid areas at the front and back plane of the flexible plate. The PIV-camera focuses on a control section of 43 mm × 58 mm (vertical × horizontal). The DIC-system uses the illumination by white light and a camera captures the two-dimensional deformations of the side edge of the plate.

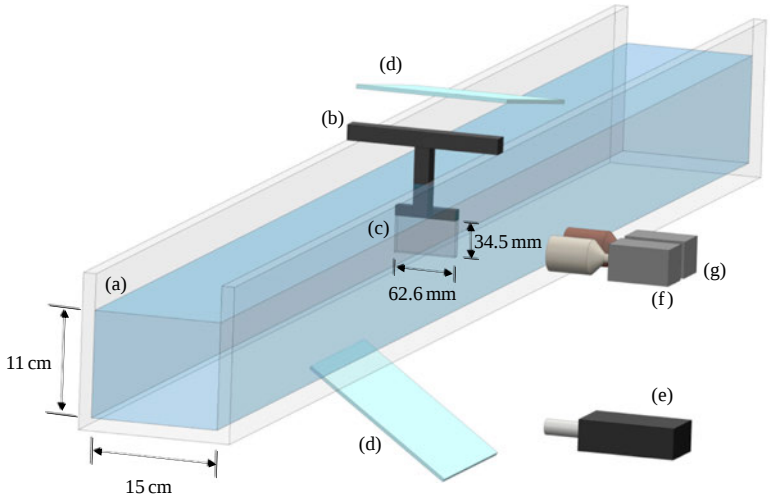

Figure 1.7: Schematic of the experimental setup of [31] for hydrodynamic load estimation with a synchronized PIV-DIC system on the example of a flexible cantilever plate passed by a water flow. The following components are included: (a) water tunnel, (b) support, (c) flexible plate, (d) mirrors, (e) laser, (f) camera for PIV, (g) camera for DIC.

For the determination of the hydrodynamic loading, the fluid velocity data of PIV and the structural data of DIC are separately utilized: By inserting the deflection data of DIC into a finite element programm, the pressure on both sides of the plate is computed by the a-priori method, assuming that the pressure distribution follows, i.e., a polynomial character. By inserting the velocity field data of PIV into the steady incompressible 2D-Navier-Stokes-equations for Newtonian fluids, the pressure distribution can be computed by integrating the pressure gradients. Here, the integration is initiated by a known reference value of zero pressure at the boundary corner of the control section.

The effective load results in the difference between the pressure magnitudes at the front and back side of the plate. Additionally, a drag coefficient is calculated to evaluate the hydrodynamic force on the plate surface. The determination of the hydrodynamic loading, which is separately executed by the DIC- and PIV-data processing, achieves approximately equal results for both methods.
Giovannetti et al. [9] investigated the measurement accuracy of a synchronized 3D-PIV-DIC setup on the example of a flexible wing with NACA 0015 airfoil mounted in a wind tunnel. The experimental setup can be seen in Fig. 1.8 from two perspectives. As the plan view in Fig. 1.8a reveals, the DIC- and PIV-systems were configured stereoscopicly with two cameras each directed with a certain intersection angle. While the DIC-cameras capture the deformations of the underside of the airfoil illuminated by LED lights, the PIV-cameras focus on a laser sheet illuminating a vertical plane in the wake flow. To distinguish LED and laser light, the PIV-cameras were arranged with a low-pass filter and the LED lights were covered with magenta gel filters.

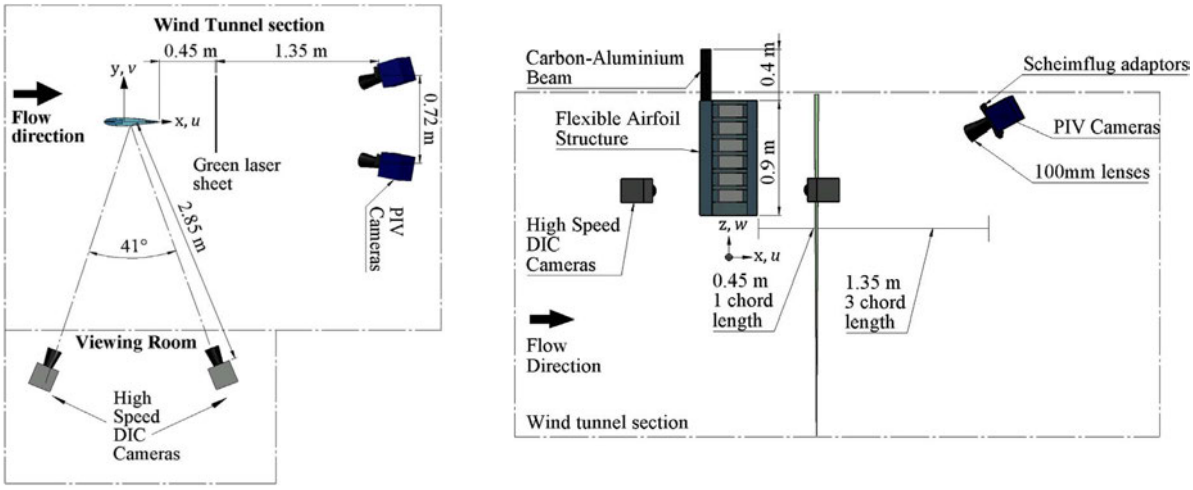

(a) Plan view

(b) Side view

Figure 1.8: Experimental setup of the synchronized PIV-DIC method in a wind tunnel with the main measurement devices and a flexible airfoil structure as test object [9].

The side view in Fig. 1.8b shows the flexible airfoil, which is elastically mounted onto a load-carrying Carbon-Aluminium beam fixed to the upper side of the wind tunnel. In this study, the wind speed was varied from 10 to 25 m/s at a turbulence level less than 0.2 % in a test section of 3.5 m × 2.4 m ($L \times H$). As a result it was found that the synchronization of DIC and PIV leads to a measurement uncertainty of less than 5 % for DIC and 3.5 % for PIV, varying in between the fluid flow velocity range, which is rather acceptable. The DIC uncertainties were measured according to translation and rotation for static and dynamic motions. The measurement uncertainties of PIV were determined a-posteriori

from a statistic correlation algorithm software using the converged field distributions of the velocity components. Thus, by superposing two sequentially captured images in the way that every segment of the second image is shifted back by the displacement field data, a correlation function is pixel-wisely computed to evaluate the accuracy of the vector field distribution. To evaluate the synchronized PIV-DIC measurement methods from [9, 30–32], it can be seen as a disadvantage that the DIC-system requires a separate LED light source, instead of using the PIV-laser as an illumination source effectively for both methods.

Moving further from synchronized PIV-DIC measurements to existing experimental investigations on elastically mounted NACA 0012 airfoils, the work of Metivier et al. [14] may be mentioned here. Self-sustained pitch oscillations (1-DOF) were analyzed in the transitional Reynolds number regime $5 \times 10^4 \leq \mathrm{Re}_c \leq 1.2 \times 10^5$ where the Reynolds number is based on the chord length c of the airfoil. The experimental setup is depicted in Fig. 1.9. Especially for $\mathrm{Re}_c = 9.4 \times 10^4$, there are limit-cycle oscillations (LCO) measured with a main frequency of $f_{LCO} = 3\,\mathrm{Hz}$ and continuous pitch amplitudes of $\theta = \pm 4°$. LCO are sinusoidal vibrations with continuous amplitudes, which are caused by the separation of a laminar boundary layer at the trailing edge of the airfoil. The definition can be further distinguished into small amplitude oscillations (SAO) and large amplitude oscillations (LAO).

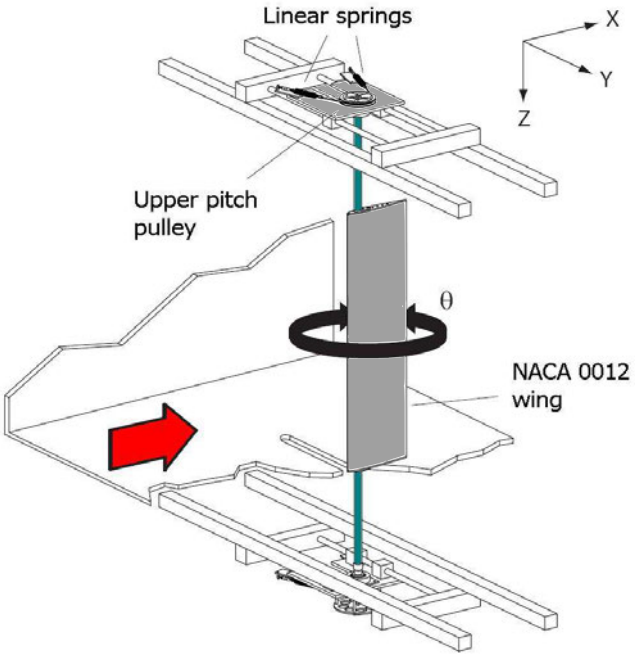

Figure 1.9: Experimental setup of the NACA 0012 [14] allowing 1-DOF-pitch oscillations by a pitch pulley combined with two linear springs.

As the name says, SAO are restricted to smaller amplitudes appearing at a certain Reynolds number of the surrounding fluid flow. The LAO are restricted to larger amplitudes, which appear at an increasing Reynolds number. Going on with the experimental study, the behavior of the airfoil was investigated for varying effects of inertia and boundary layer tripping: It was found that if the moment of inertia is increased, the amplitudes of the oscillating airfoil increase as well, whereas its natural frequency decreases. Additionally, a trip wire was fixed on one surface side of the airfoil, which causes transition and thus a turbulent flow instead of the former laminar separation of the boundary layer on that side. The benefit was that the LCO reduced to half of the former amplitudes, while the corresponding frequency slightly increased. Additionally, Poirel and Mendes [18] have continued their experimental studies by investigating the airfoil being able to do heave and pitch motions at once (2-DOF). The results have shown two types of LCO, one with small amplitudes and another with large amplitudes. The small amplitude oscillations are nearly identical to the former 1-DOF pitch investigations of LCO with laminar boundary layer separation. The heave motion does not influence the oscillation process, whereas it might increase the energy transfer between the fluid and the structure. The large amplitude oscillations (LAO) were noticed as a steady precursor of flutter instability. At $\mathrm{Re}_c = 7.5 \times 10^4$ the heave and pitch amplitudes were separately measured as $h = \pm 0.065\,\mathrm{m}$ and $\theta = \pm 65°$ with a heave-to-pitch frequency ratio of $\overline{\omega} = 1.63$ at a heave spring stiffness of $k_h = 1484\,\mathrm{N/m}$. By varying the heave spring stiffness, it was concluded that for heave-to-pitch frequency ratios above unity, flutter is possible for higher Reynolds numbers and for $\overline{\omega} < 1$ it is rather hindered.

At PfS, investigations on the 2-DOF-characteristics of the airfoil NACA 0012 in the transitional Reynolds number regime $9.66 \times 10^3 \leq \mathrm{Re}_c \leq 8.77 \times 10^4$ were carried out as well. In the experimental setup, there were three different cases considered. By adding extra masses at defined positions along the chord length of the airfoil, it was possible to vary the center of gravity resulting in three different configurations. Based upon this test case, experimental and numerical investigations of the dynamic behavior of the airfoil at various Re numbers were conducted: The numerical paper of De Nayer et al. [15] offers simultaneous results of the fluid flow and the structural behavior for two of the three cases. This is done by a FSI-solver, which couples large-eddy-simulations (LES) of the airflow based on the 3D-Navier-Stokes equations with the structural equations based on Newton's second law for the translational and rotational dynamics of the rigid airfoil. The experimental paper of Wood et al. [23] contains structural measurements based on the DIC technique for all three cases. Additionally, hot-film measurements of the fluid flow were done with a constant-temperature anemometer (CTA) measuring the spectra of

the flow fluctuations at a defined point in the wake. In both papers, the eigenfrequencies and modes of the heave and pitch motion of the airfoil were investigated as well as the development of oscillations at increasing Re numbers. The damping effect, induced by the dynamic load of certain fluid flows, was shown. Furthermore, the phenomena of LCO (SAO, LAO) as well as flutter were detected in the higher Reynolds number regime. The papers on the numerical and the experimental investigations are the background, which this thesis is developed from. Existing experimental results [23] shall be confirmed due to structural data measured by DIC and numerical results [15] shall be validated due to fluid flow data determined by HS-PIV for two configurations.

1.3 Objectives and structure of the thesis

The primary aim of the thesis is the installation and evaluation of synchronized DIC and PIV measurements. The feasibility of synchronized measurements is investigated and furthermore measurement results are discussed. At first, unsynchronized DIC measurements are done, delivering separate reliable results for comparison purpose. Then, the technical setup is modified. The laser, which is the illumination source of the PIV measurements so far, shall also be used as the light source in case of the DIC setup. The synchronous usage of the PIV and DIC cameras shall be utilized by applying the output trigger signal of the PIV camera as a trigger input signal for the DIC system. Besides linking the hardware, internal parameters like the sampling rate shall be equal for both systems in order to perform synchronized PIV-DIC measurements. The secondary aim, after testing the synchronous PIV-DIC measurement method on the example of a simple test model, is the analysis of the NACA 0012 airfoil concerning the appearing physical phenomena. The structure of the thesis is as follows:

- Chapter 2 contains the presentation of the experimental setup. First, the nomenclature and the aerodynamic properties of the airfoil NACA 0012 are explained. Second, the current test-stand with the elastically mounted wing system as well as the wind tunnel system are introduced.

- Chapter 3 describes the main measurement techniques, i.e., particle-image velocimetry (PIV) for the fluid flow and the digital-image correlation (DIC) for the structural displacements. Furthermore, the technical implementation of the synchronization of both methods is presented. In addition, the statistical measuring quantities by PIV and DIC are demonstrated.

- Chapter 4 presents the measurement planning with the eigenfrequency analysis and the sequence of Re numbers that are adjusted in the wind tunnel system. For the unsynchronized methods, internal parameters, each separated for the PIV and DIC setup, are mentioned, e.g., how the laser is pulsing or how fast and extensive the cameras are working. Then, the internal parameters are adjusted simultaneously for the synchronized PIV-DIC method.

- Chapter 5 contains the measurement results and evaluation. First, the unsynchronized DIC measurement results are presented and compared to already existing results at PfS. Second, the synchronized PIV and DIC measurement results are shown with the description of the fluid flow field and the comparison between the unsynchronized and synchronized method related to the PIV and DIC results. The current experimental results are compared with the DIC- and CTA-results of Wood et al. [23] and with the results of the numerical FSI-simulations by De Nayer et al. [15].

- Chapter 6 concludes the master thesis and provides an outlook for further investigations based on the synchronized measurement system.

In the following chapter, the laboratory setup of PfS is introduced with the wind tunnel system and the test stand of the NACA 0012. The characteristics of the design and mounting of the airfoil are explained as well as the several cases of the study.

Chapter 2

Experimental setup

In the following, the experimental setup of the current investigations is introduced. The test stand is the elastically mounted wing system with 2-DOF, interacting with the fluid flow in the transitional Reynolds number regime, which is provided by the wind tunnel. Thus, the NACA 0012 airfoil, the construction of the wing system and the properties of the wind tunnel of GÖTTINGEN SUBSONIC TYPE are discussed.

2.1 Test-stand: Elastically mounted airfoil NACA 0012

The test-stand of the current measurements consists of the wing system with the airfoil of type NACA 0012, which is elastically mounted in the translational and rotational direction and thus provides a dynamic system with 2-DOF, the heave and pitch motion. In the following, the properties of the airfoil system are explained by means of the nomenclature of the shape, the aerodynamic properties and the current setup design.

2.1.1 Airfoil nomenclature

Beginning with the nomenclature of the shape of the airfoil, the abbreviation NACA 0012 originates from National Advisory Committee for Aeronautics, which was a federal U.S. Agency as a forerunner of the NASA. In 1933, several airfoil designs were published with these initials and sequences of numbers[1]. The basic design idea of the shape is considered in Fig. 2.1 depicting the asymmetric and symmetric airfoil as well as typical design parameters. The chord line (black, dashed) connects the leading edge with the trailing edge, which are the geometric limiting points of the airfoil.

[1] https://www.nasa.gov/image-feature/langley/100/naca-airfoils

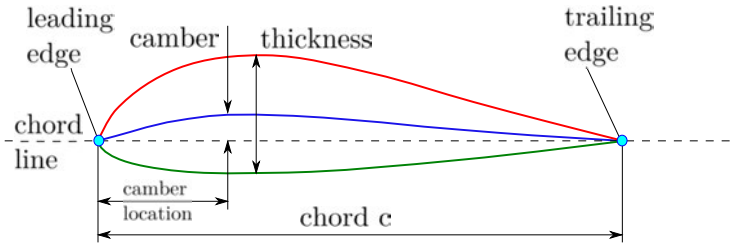

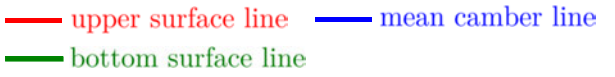

(a) Asymmetric airfoil

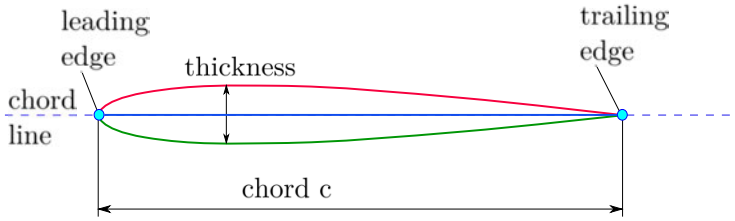

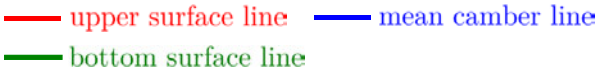

(b) Symmetric airfoil

Figure 2.1: Two types of the NACA airfoils with geometric parameters.

The chord line length is named as chord c. The mean camber line (blue) is the average line of the upper surface line (red) and the bottom surface line (green). The maximum distance between the mean camber line and the chord line is called camber. The horizontal distance from the leading edge to the camber is named camber location. Figure 2.1a shows for an asymmetric airfoil that the mean camber line proceeds above the chord line while Fig. 2.1b shows for a symmetric airfoil that the mean camber line is identical with the chord line. The camber location cannot be defined here and the camber is equal to zero. The thickness of an airfoil is the maximum vertical distance between the upper and bottom surface line. With these geometric parameters, the convention of numbers, for the *four-digits* NACA profiles, can be explained:

- The first digit is the camber magnitude in hundredths of the chord. For the symmetric case, such as the NACA 0012, it is obviously 0.

- The second digit is the camber location in tenths of the chord. For the symmetric case, such as the NACA 0012, it is defined as 0 as well.

- The third and fourth digit represent the thickness of the airfoil in hundredths of the chord. So in this case, it is $t = 0.12\,c$. With the chord of $c = 100\,\text{mm}$, the thickness results in $t = 12\,\text{mm}$.

2.1.2 Aerodynamic properties of the NACA 0012 airfoil

Considering the aerodynamic properties of the NACA 0012 airfoil, there are two main properties that are discussed here: the lift and the drag. These forces are depending on the Angle of Attack (AoA) or pitch angle of the airfoil and the free-stream velocity. First of all, Fig. 2.2 presents the schematic flow characteristics visualized by streamlines for an conventional airfoil as an allegory for the phenomena on the whole wing. Within the Reynolds number range of $10^4 \leq \mathrm{Re} \leq 5 \times 10^4$, the flow behavior is shown for two different AoA of the airfoil. For $\alpha \approx 0°$ (left image), the fluid flow forms a laminar boundary layer along the upper and lower surface of the profile, while the flow separates nearby the trailing edge. By increasing the AoA with $\alpha > 0°$ (right image), the separation moves upstream and takes place in the midst of the upper surface due to the unfavorable pressure increase along the upper surface resulting in a separated flow region with strong vortical structures and reducing the effect of the lift, while the drag is growing.

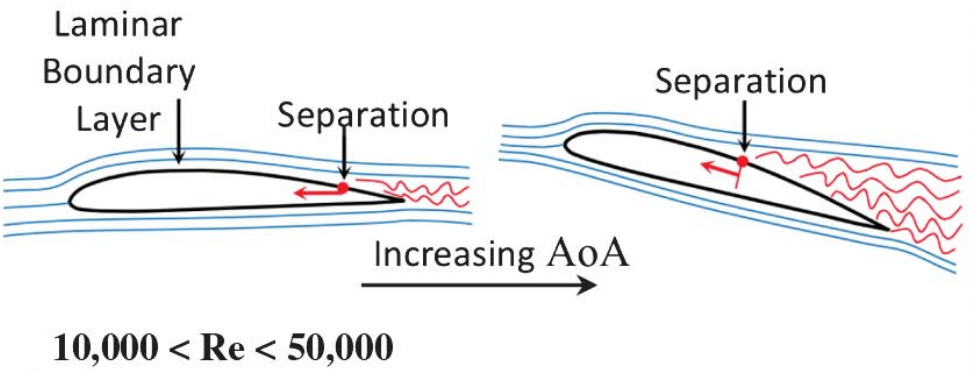

Figure 2.2: Schematic flow characteristics visualized by streamlines depending on the Angle of Attack (AoA) of a conventional airfoil at the Reynolds number regime of $10^4 \leq \mathrm{Re} \leq 5 \times 10^4$ from Winslow et al. [22].

The meaning of lift and drag shall be given by Fig. 2.3 according to the remarks of Anderson [2]. Again, the airfoil with the AoA α is exposed to a free-stream velocity U_∞ forming a boundary layer. The consequence is the normal pressure $p(s)$ and shear stress $\tau(s)$ distribution depending on the position s nearby the airfoil surface. The integration of these stresses over the upper and lower airfoil surface is the resultant force R', which can be splitted into the horizontal drag F'_D (skin friction and form drag) and the vertical lift F'_L. It has to be noted that these forces are all normalized by the unit span l of the wing with $[F/l] = [N/m]$. However, once these forces are determined, the non-dimensional quantities can be computed, which are the lift and drag coefficient C_L and C_D, yielding:

$$C_L = \frac{F_L}{q\,S} \equiv \frac{F_L}{\left(\frac{1}{2}\rho U_\infty^2\right) l\,c} = \frac{F'_L}{\left(\frac{1}{2}\rho U_\infty^2\right) c}\,, \tag{2.1}$$

$$C_D = \frac{F_D}{q\,S} \equiv \frac{F_D}{\left(\frac{1}{2}\rho U_\infty^2\right) l\,c} = \frac{F'_D}{\left(\frac{1}{2}\rho U_\infty^2\right) c}\ , \tag{2.2}$$

while q is the dynamic pressure $q = 1/2\,\rho U_\infty^2$ and S is the reference area of the wing span and the chord $S = l\,c$. These coefficients can be written based on the "per unit span"-format of the forces F'_L and F'_D on the airfoil.

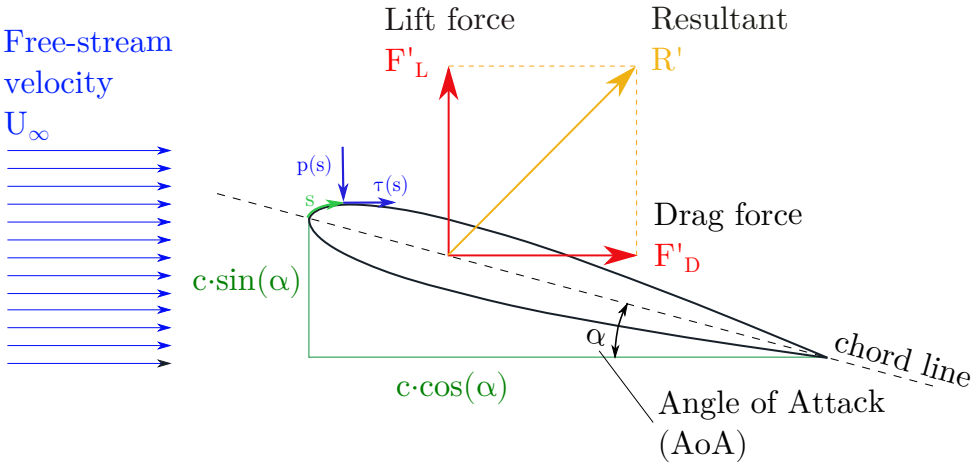

Figure 2.3: Schematic illustration of the lift F'_L and the drag F'_D forces per unit span $[F/l] = [N/m]$ at a certain Angle of Attack (AoA) α of the airfoil and a free-stream velocity U_∞. Indication of the pressure and shear stress distribution $p(s)$ and $\tau(s)$ depending on the position s on the airfoil as the origin of the forces mentioned by Anderson [2].

For the NACA 0012 airfoil, the lift and drag coefficients have been investigated by Winslaw et al. [22] at several angles of attack, which is depicted in Fig. 2.4. Thus, the free-stream velocity is adjusted for two Reynolds numbers $\mathrm{Re}_1 = 3 \times 10^5$ and $\mathrm{Re}_2 = 10^6$. Numerical results of the Transonic Unsteady Rotor Navier-Stokes 2D solver (TURNS2D, blue and red lines) solving the Reynolds-Averaged Navier-Stokes (RANS) equations are compared to experimental results (triangular and circular symbols). In the diagram of the lift (a, left) C_L initially increases linearly with the angle of attack within $\alpha = [0°; 10°]$, $C_L = [0; 0.95]$ for both Reynolds numbers. The lift coefficient at Re_1 reaches its maximum at $\alpha = 12°$, $C_L \approx 1$ and then decreases non-linearly which can be explained by the unfavorable stall of the wing due to the dominating flow separation on the upper surface. At Re_2 the lift coefficient reaches the AoA $\alpha = 14°$ with $C_L \approx 1.3$, until stall appears. In the drag diagram (b, right), C_D increases for both cases within the stall due to the fact that at the higher angle of attack the flow separates completely yielding a region of low pressure on the back side of the airfoil. Although the curve of Re_1 starts to increase earlier than the curve of Re_2 due to the prior entry of stall, the drag coefficient for both Re finally reaches a value of $C_D = 0.3$ for $\alpha \approx 20°$.

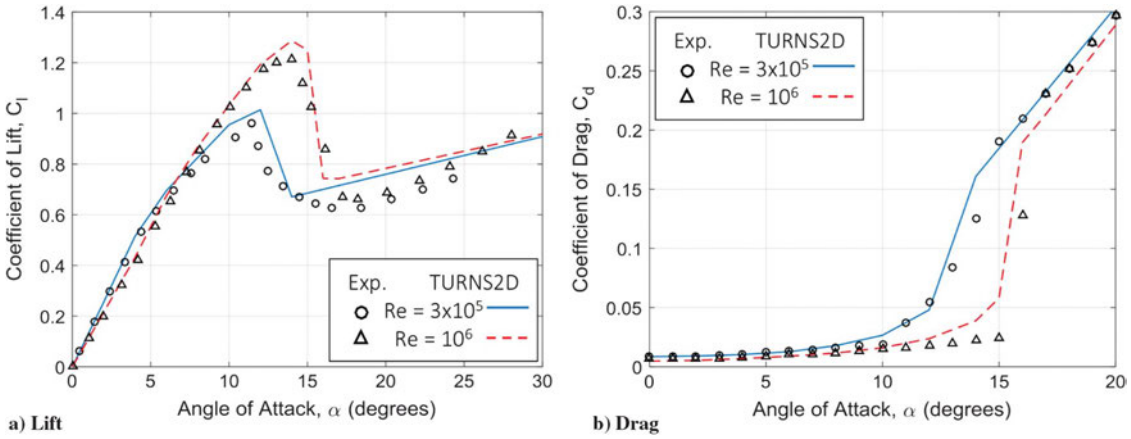

Figure 2.4: Aerodynamic airfoil properties presented by the diagrams of the lift (a) and drag (b) coefficients depending on the AoA of the NACA 0012 at Reynolds numbers between 3×10^5 and 5×10^4 from Winslow et al. [22].

2.1.3 Setup of the test case

In the following part, the setup design of the current NACA 0012 wing system with the elastic mounting is introduced. As a first impression, the structure-mechanical model is presented in Fig. 2.5. It is a two-dimensional illustration of the dynamic airfoil system, which is able to provide motions with two DOF. The NACA 0012 has the mass m_w and the mass moment of inertia I_α^E around the elastic axis E. It is elastically mounted at this elastic axis, which is marked as a red point here. The elastic axis is the center of the vertical heave motion (h) and the rotational pitch motion (α). It is located at $0.417\,c$ (41.7 mm) from the leading edge of the airfoil and its position cannot be shifted. The center of gravity (c.o.g., G) of the mass distribution of the airfoil, which is marked as a yellow-black point here, has the distance x_{EG} from the elastic axis. Its position is adjustable by adding an additional mass for different cases of the study, which will be explained later on. The mounting system is depicted as an equivalent network of a spring and viscous damper for both the translational and rotational DOF. The translational and rotational spring stiffnesses are declared as k_h and k_α, while b_h and b_α are the corresponding viscous damping coefficients. The concrete values are mentioned in detail and in comparison with the results of Wood et al. [23] in Section 5 (see Tab. 5.1 and 5.2), since a calculation with measurement results is partly necessary. As an environmental impact, the airfoil system is passed horizontally by a fluid flow with the density $\rho_{air} = 1.225\,\mathrm{kg/m^3}$, the dynamic viscosity $\mu_{air} = 18.72 \cdot 10^{-6}\,\mathrm{Pa\,s}$, the free-stream velocity U_∞ and the level of turbulence of $0.5\,\% \leq \mathrm{Tu} \leq 1\,\%$ which is provided by a wind tunnel.

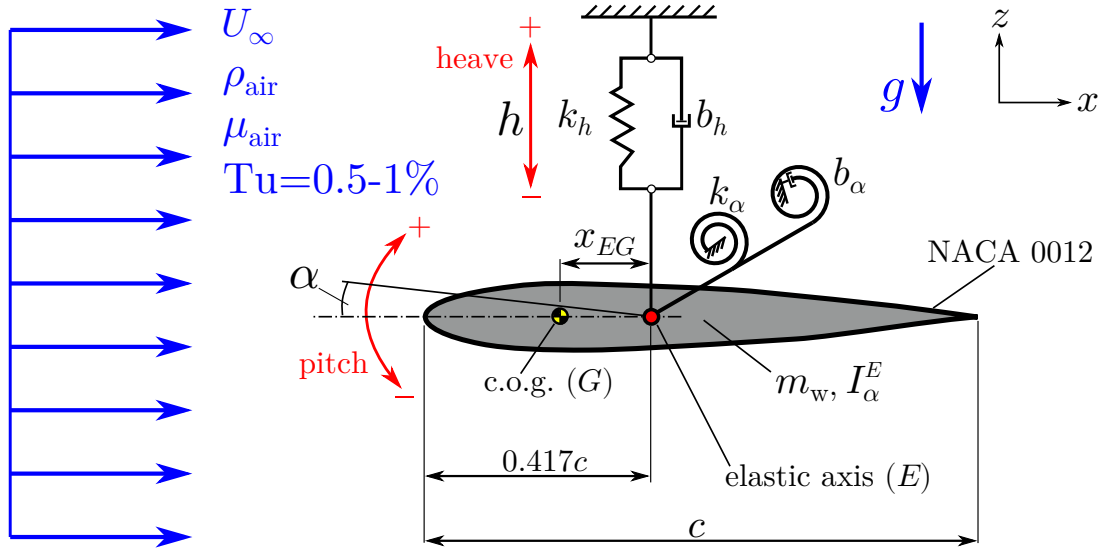

Figure 2.5: Setup of the test case and the structure-mechanical model [23].

Moving further to the real setup design, Fig. 2.6 shows the test stand with a global overview of the measuring devices with the laser, the PIV- and DIC-cameras on the right as well as a detailed image of the NACA 0012 airfoil system on the left. The wing is elastically mounted at both ends. The corresponding devices at both ends consist of two leaf springs each that are assembled with fixing elements, while one fixing element is mounted at the framework of the system. The leaf springs represent the network of the spring and the viscous damper for the heave motion of the structure-mechanical model. Additionally, there are torsional springs mounted in between each of the ends of the airfoil and the heave spring assemblies. Complementary to heave, the rotational springs represent the network of the spring and the viscous damper for the pitch motion of the structure-mechanical model.

Focusing on the components of the NACA 0012 system, the manufacturing details of the airfoil are explained as well as the details of the elastic mounting. The geometric dimensions of the airfoil are given by the chord length $c = 100\,\text{mm}$ and the thickness of 12 mm. The mass of the wing is at $m_{w,0} = 0.185\,\text{kg}$, Polylactic acid (PLA) is the chosen material offering light-weight properties. The manufacturing of the wing is realized by the adhesive technology of printing. However, three parts of the wing with $l = 200\,\text{mm}$ are separately printed and finally assembled by a bonded joint to the wing with the full span of $l = 600\,\text{mm}$. The shape of the wing is smoothed by a corrosive solution, reaching a mean surface roughness in the range of $8.9\,\mu\text{m} \leq \text{R}_a \leq 37.9\,\mu\text{m}$ measured by a high-resolution digital microscope (Keyence VHX-6000) [23]. Finally, the wing is varnished in black for the purpose of shading the measurement environment and preventing unfavorable illumination reflections.

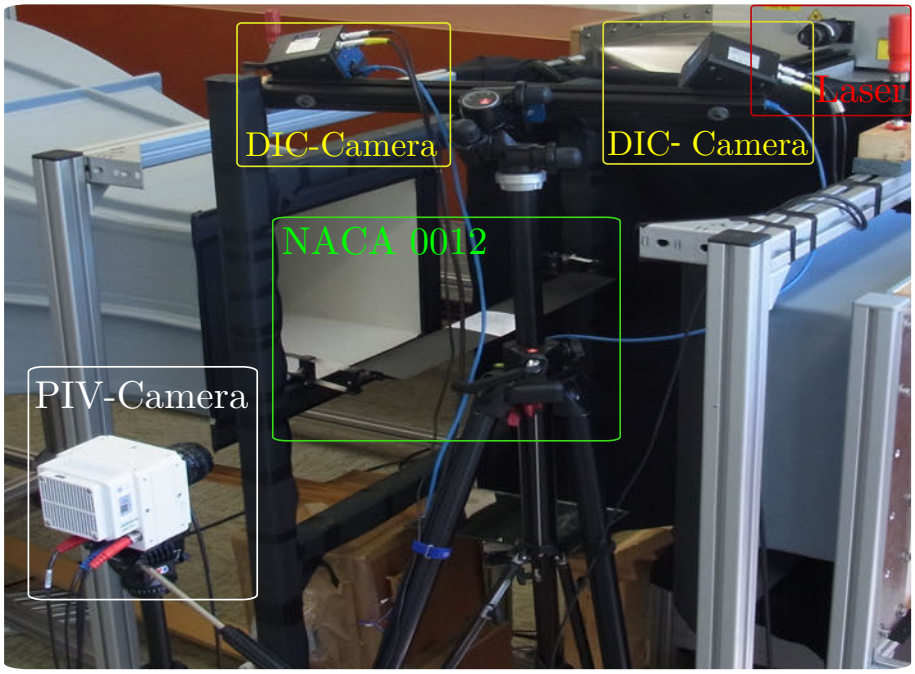

(a) Global overview.

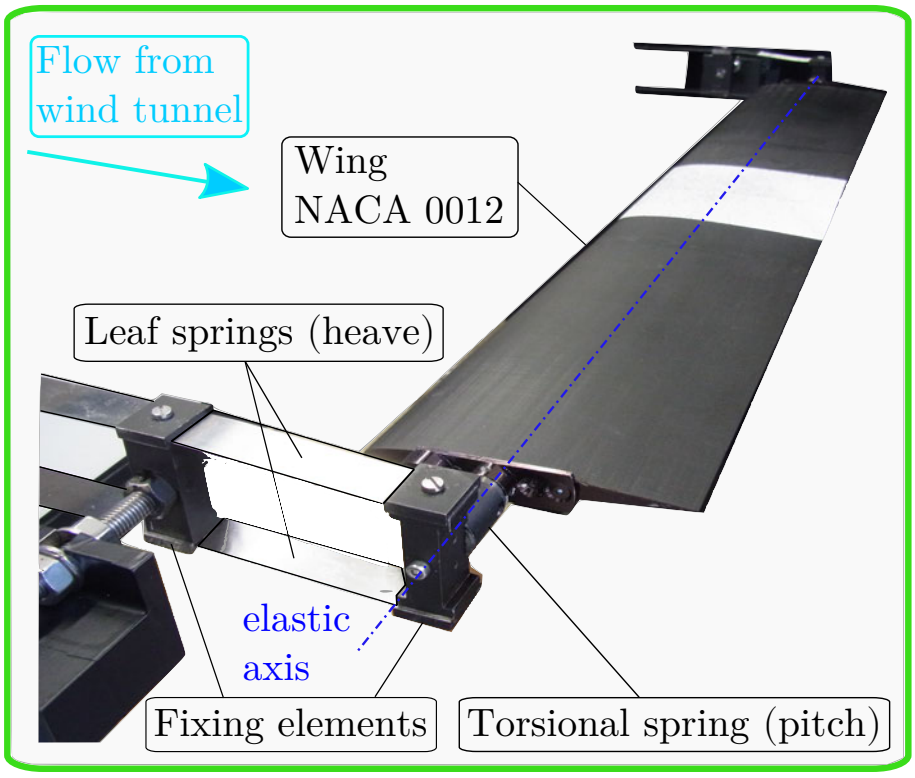

(b) Detailed view of the NACA 0012 wing system.

Figure 2.6: Experimental setup with a global overview (a) with the NACA 0012 wing system (green), the PIV-(white) and DIC-(yellow) cameras and the laser (red). The wing system with the mounting elements in detail (b).

Nevertheless, at both ends of the wing, there are several bore holes added to the airfoil, i.e., for the fixing of the additional masses or for the connection of the wing to the elastic mounting system. The detailed mounting system is depicted in Fig. 2.7. The leaf springs, which are connected in parallel, are clamped by the fixing elements, so that the effective spring length is at $l_h = 0.63\,\text{mm}$, see the top view of Fig. 2.7(a). The leaf spring packages are fixed to the solid support frame. Furthermore, there is a connection to each of the ends of the wing, which is realized by torsional springs (top view, yellow dashed line as the elastic axis). The schematic construction of the specific torsional spring from the company C-Flex Europa: GAD Elektronik-Komponenten Vertriebs GmbH is depicted in Fig. 2.7(b).

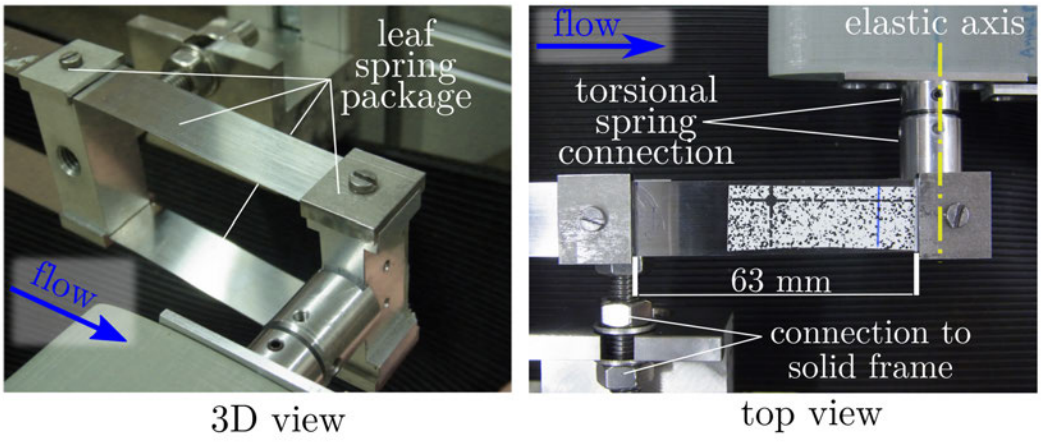

(a) 3D- and top-view of the construction.

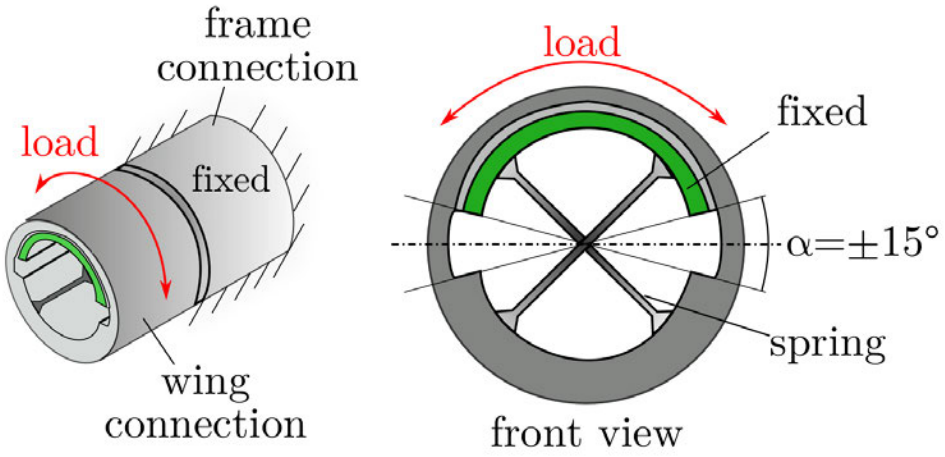

(b) Schematic construction of the torsional spring.

Figure 2.7: Elastic mounting of the wing system including the leaf spring package and the torsional spring connection [23].

The cylindrical bearing of the type "E-20C-Flex-Bearing" has a diameter of $D = 7.94\,\text{mm}$ and an overall length of $l = 12.70\,\text{mm}$. The angular rotation is limited to $\alpha_{max} = \pm 15°$, while the manufacturer recommends an angle of usage at $\alpha = \pm 7.5°$ for a long-lasting durability of the springs. The torsional spring stiffness is at $k_\alpha = 0.19162$ Nm/rad listed in the data sheet of the manufacturer[2]. Since there are two torsional springs at both ends of the wing, the total stiffness yields $k_\alpha^{tot} = 2\,k_\alpha = 0.38324$ Nm/rad. The bearing technique is a cross-connection spring with spring plates (X-form) that are fixed with two edges to the frame connection (green half shell) and with the other two edges to the wing connection (ring with loading). By applying a torque, the spring plates (X-form) are bent elastically to small spring "arcs" causing a rotation about the central axis, while the torque should be in the range of:

$$M_T(\alpha_{max}) = k_\alpha\,\alpha_{max} = \pm 5.017 \times 10^{-2}\ \text{Nm}\ . \tag{2.3}$$

After the previous investigations by Wood et al. [23], it has to be noted that the torsional springs of the wing setup were worn out, due to the fact that this torque tolerance $M_T(\alpha_{max})$ might have been exceeded at some points of measurement. Therefore, the torsional springs were replaced by new ones for the current measurements. These are identical in construction compared to the former torsional springs with the above mentioned classification and the spring stiffness k_α, for the purpose of providing equal measurement conditions.

Going further to the variation of the NACA 0012 setup for the current investigations, Fig. 2.8 depicts the two considered cases, whose center of gravity (c.o.g., G) is located at different positions within the chord line of the airfoil. Thus, in each test case, two extra masses (yellow circles) of the summed weight of $m_{w,e} = 0.034$ kg are fixed to both ends of the wing with varying positions. The following nomenclature of *case I* and *case III* originates from the previously published work of Wood et al. [23]. In *case I*, which is depicted in Fig. 2.8(a), the extra mass is horizontally positioned at the chord line at $0.22\,c$ related to leading edge of the airfoil. As a consequence, the c.o.g. (yellow-black semi-circle) coincides with the center of the rotational spring axis located at $0.417\,c$, which is called the elastic axis E (red semi-circle), so that $G = E$. In general, the elastic axis E is the reference for the pure heave displacement of the airfoil. In *case III*, which is depicted in Fig. 2.8(b), the extra mass is horizontally positioned at the chord line at $0.8\,c$ related to leading edge of the airfoil. As a consequence, the c.o.g. (yellow-black circle) is shifted towards the trailing edge with a distance ratio of $x_{EG}^{III}/c \approx +0.059$ from the position of E.

[2] https://g-a-d.de/files/kfg/Leitfaden%20Dimensionierung%20Kreuzfedergelenk_klein

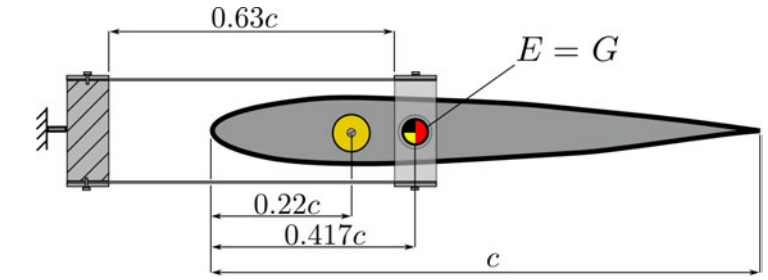

(a) $x_{EG}^{I}/c \approx 0$ (case I)

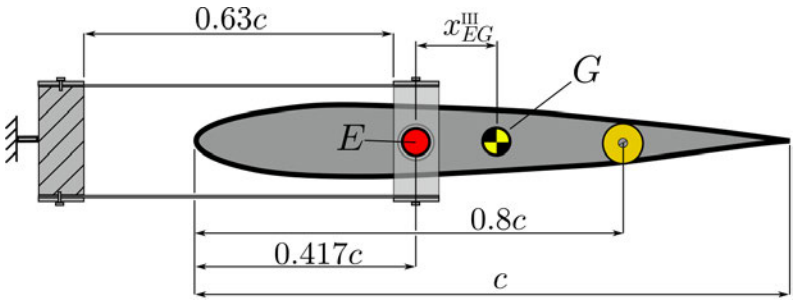

(b) $x_{EG}^{III}/c \approx +0.059$ (case III)

Figure 2.8: Setup with adding an extra mass (yellow circle) shifting the position of the center of gravity (G) for distinguishable test cases [23]. The position of the elastic axis E remains unchanged.

To conclude with the NACA 0012, the total mass of the wing system m_w is consisting of the mass of the wing $m_{w,0} = 0.185\,\text{kg}$, the mass of the elastic mounting $m_{w,m} = 0.12021\,\text{kg}$ and the extra mass of $m_{w,e} = 0.034\,\text{kg}$ yielding:

$$m_w = m_{w,0} + m_{w,m} + m_{w,e} = 0.33921\,\text{kg}\ . \tag{2.4}$$

The total mass of the wing is increased by 4 g compared to the former setup of Wood et al. [23]. This is due to the fact that the wing has been covered by the black varnish substance for the purpose of shading the setup for the current PIV measurements. Finally, as mentioned above, all other relevant parameters of the wing system are listed in Section 5 (see Tab. 5.1 and 5.2), since most of them are depending on the measurement results.

2.2 Wind tunnel system

The wind tunnel generates and recirculates the airflow, which is needed for the measurements. Thus, it is designed in the geometric form of a loop, which is known as Göttingen subsonic type [25]. A schematic representation of the top-view perspective is depicted in Fig. 2.9.

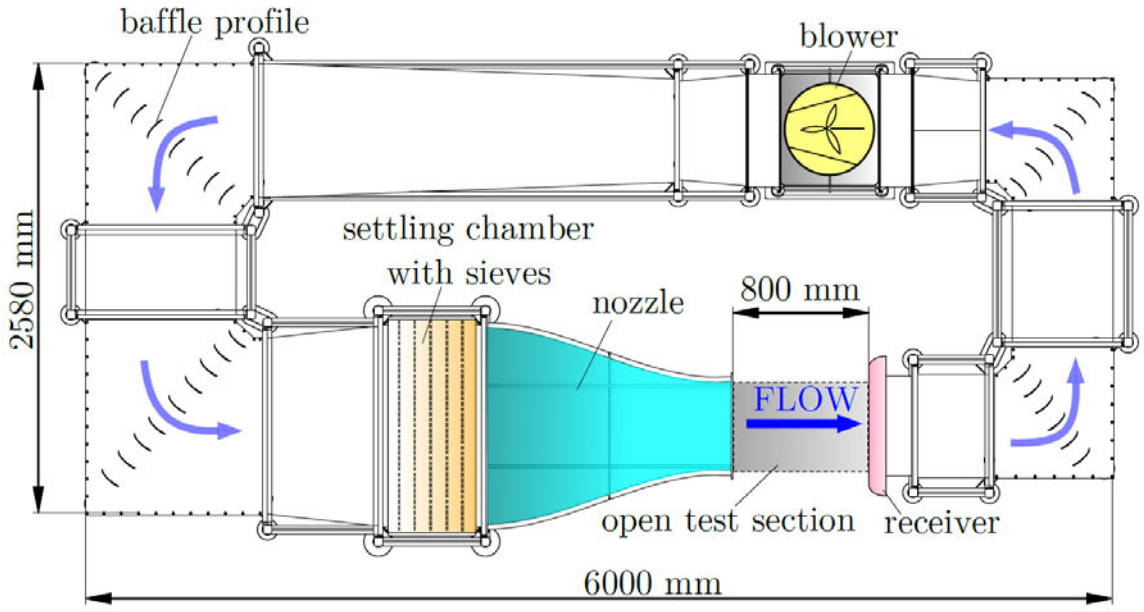

Figure 2.9: Top-view of the wind tunnel in schematic representation by courtesy of Wood [25].

The driving-unit is the air blower with a maximum performance of $P_{max} = 4.1 \times 10^3$ W and a rotation speed up to $n_{max} = 1400$ rpm generating flow velocities in the wind tunnel up to $U_{max} = 27$ m/s. The airflow is redirected by four baffle profiles, which are located at the corner elements of the wind tunnel. The velocity distribution in the cross-section is nearly uniform by removing turbulent fluctuations by passing the flow through a settling chamber including five sieves. Before entering the test section, a nozzle accelerates the airflow by reducing the cross-section with a contraction ratio of 5 : 1. The test section, which is also part of the wind tunnel loop and includes the object plane, has the dimensions 800 mm $\times$ 500 mm $\times$ 375 mm ($L \times W \times H$). After leaving the test section, a receiver collects the airflow to conserve its kinetic energy in the wind tunnel-loop.

Focussing on the flow characteristics within the test section, Fig. 2.10 shows the area of a "parallel" free-stream with a nearly constant velocity at the outlet section. The useable cross-section slightly diminishes while proceeding towards the end of the test section. This finding originates from the surrounding still air region ($u = 0\,\mathrm{m/s}$), resulting in the formation of a shear layer between the free-stream and the environment, which is schematically depicted in Fig. 2.10(a). Looking at the investigations of Wood [24], the streamwise velocity distribution U has been analyzed along the symmetry planes (xy and xz) of the test section at a rotation speed of $n = 540\,\mathrm{rpm}$ of the air blower, which is depicted in Fig. 2.10(b). The regions of reduced velocity have to be taken into account for the measurements at the borders of the test section.

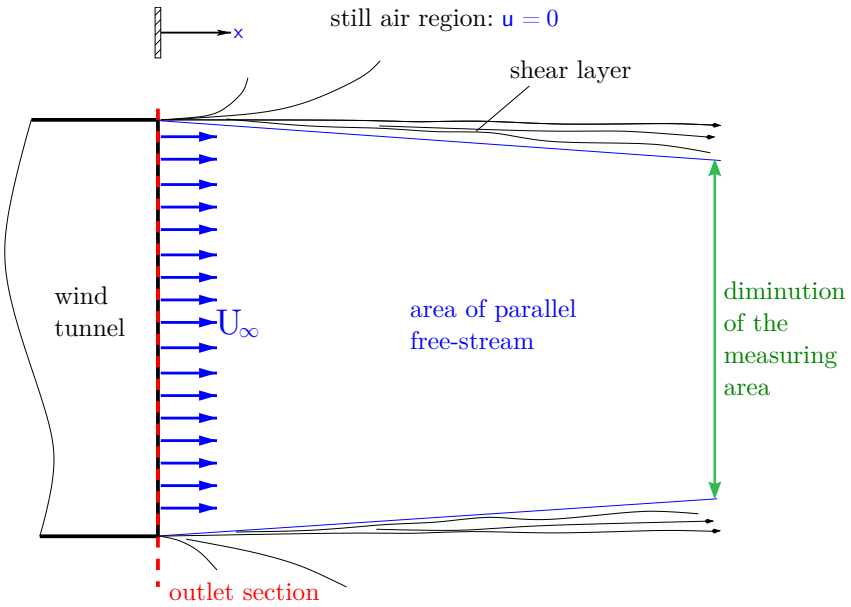

(a) Schematic illustration of the diminution of the measuring area.

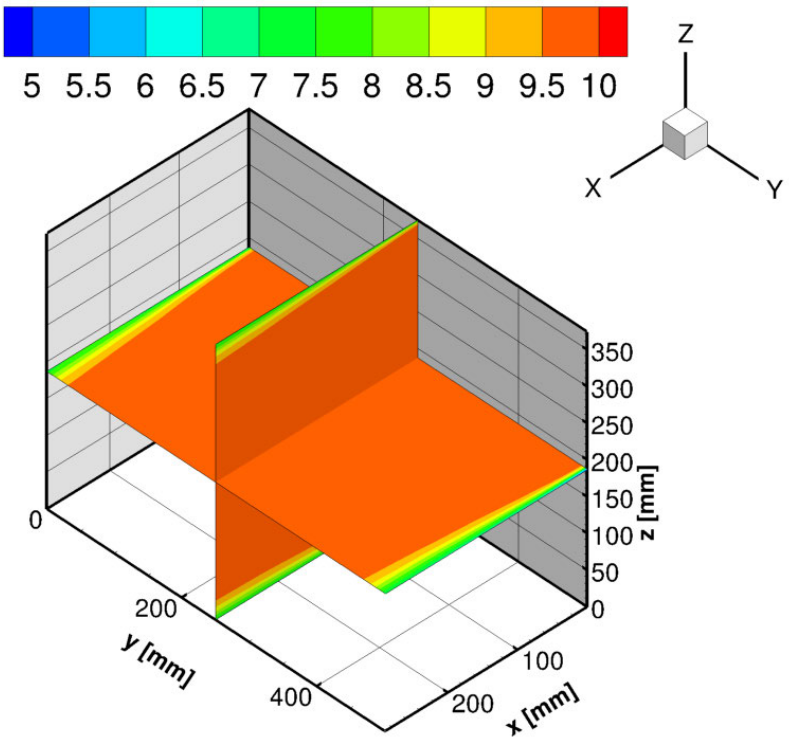

(b) Velocity distribution of U.

Figure 2.10: Experimental effects of free-stream in the open test section of the wind tunnel. Schematic presentation (a) and streamwise velocity distribution U in $[m/s]$ across the symmetry planes (xy and xz) at a rotation speed of $n = 540\,\text{rpm}$ of the air blower (b) from Wood [24].

The averaged streamwise velocity of the free-stream $U_\infty \equiv u_{\text{ref}}$ in [m/s] and the turbulence intensity Tu in [%] in the test section were determined by the CTA-measurements of Wood [28] shown in Fig. 2.11 as a function of the rotation speed n of the air blower within the range of 100 $\text{min}^{-1} \leq n \leq$ 1400 min^{-1}. Based on that, a linear regression curve (accuracy $R^2 = 0.9995$) is generated for the velocity measurement yielding the following relation:

$$u_{\text{ref}} = 0.02017 \, \frac{\text{min} \cdot \text{m}}{\text{s}} \cdot n \left[\frac{1}{\text{min}}\right] - 0.89995 \, \frac{\text{m}}{\text{s}} \, . \tag{2.5}$$

The turbulence intensity Tu is found mainly at 0.5-1 %. An exception is the rotation speed at 1100-1300 min^{-1}, whereas the maximum is at $Tu\,(n = 1200\,\text{min}^{-1}) = 1.55\%$.

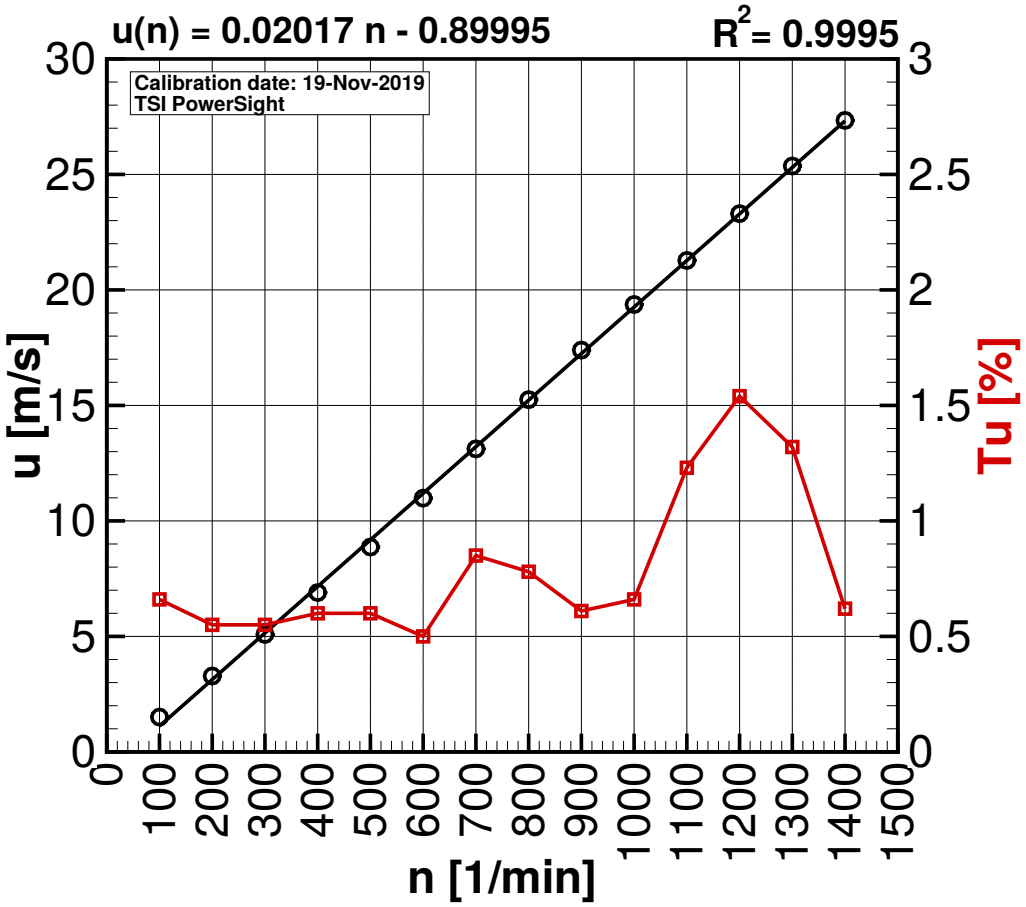

Figure 2.11: Averaged free-stream velocity U_∞ and turbulence intensity Tu in the test section of the wind tunnel without the application of Seiferth-wings at the nozzle. Linear relation between the rotation speed n of the air blower and the free-stream velocity U_∞ in the test section. CTA-measurements (sampling rate of 1000 Hz) with LDA calibration normal used as reference from Wood [28].

In the next chapter, the measurement techniques are explained for the analysis of the experimental setup according to the fluid flow in the wind tunnel and the structural behavior of the wing system.

Chapter 3

Measurement techniques

In the following part, the main measurement techniques are presented. The 2D-fluid velocity fields are measured by the High-Speed Particle-Image Velocimetry (HS-PIV), while the 3D-structural deformations of the wing system are measured by the Digital-Image Correlation (DIC). Both techniques have in common, that they are imaging methods, that are non-invasive, which means that the measurement sensors do not disturb the experimental flow or vibration process. After explaining both measurement techniques separately, the idea of synchronizing the HS-PIV and DIC is shown for the purpose of describing the FSI phenomena precisely. Finally, the main measurement quantities and resulting statistical quantities are presented.

3.1 Particle-image velocimetry

In this section, the High-Speed Particle-Image Velocimetry (HS-PIV) technique is introduced. It is a non-invasive method to determine the velocity field of fluid flows. Thus, the PIV-system has no impact on the fluid flow which is an advantage compared to standard measurement devices such as hot-film probes. A first impression of a PIV-system is given by Fig. 3.1. The basic idea is the imaging of micro-particles using a pulsed laser and a light sensitive camera in order to capture the displacements of the particles at two instances in time defined by the time interval Δt making it possible to measure the velocity field. By comparing the particle distribution of two images, velocity vectors can be reconstructed and assigned to the image plane of the camera using special algorithms.

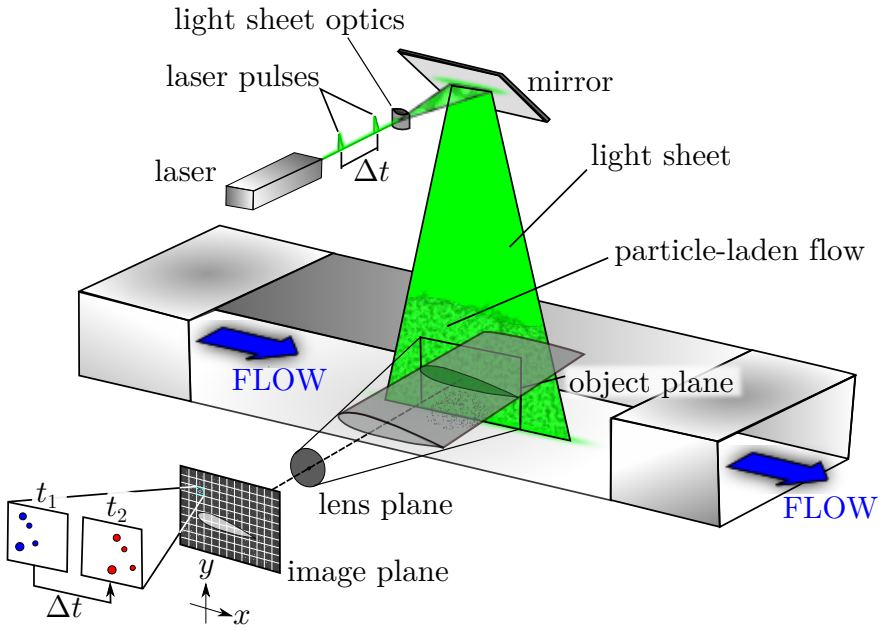

Figure 3.1: Technical setup of the PIV-system inspired by Wood [25].

3.1.1 Technical setup

In the following, the measurement technique is schematically presented in Fig. 3.2. A PC-software controls the laser and camera function. A synchronizer triggers the signals between the laser and the capturing of images by the digital camera. The high-speed laser Litron LD-527 PIV generates laser pulses which are expanded to a two-dimensional light sheet by a designated collimator optic and redirected by a mirror to illuminate a 2D-object-plane in the test section of the wind tunnel. The wind tunnel generates the fluid flow which is seeded by tracer particles produced by a TSI BG-1000 bubble generator. After capturing images of the 2D-object-plane with the camera Phantom VEO 640S, the software saves and evaluates the velocity field from the image data by specific processing algorithms described in Section 3.1.3.2.

3.1.1.1 PC-software and synchronizer

The measuring process is initiated by two PC-programs. The software Litron LD-527 Control is used to activate the laser system as a remote control tool via a Com-Port-cable from the PC to the designated port on the rear side of the laser power-unit. There are three main adjustments to consider: Firstly, after switching on the power-supply of the laser system, the software can connect with the laser by choosing the right Com-Port-pin of the computer. Secondly, while powering up the laser to the performance level, an internal cooling circuit has to be provided by the pump, which has to be turned on. Thirdly, the laser emission and the shutter optics can be activated.

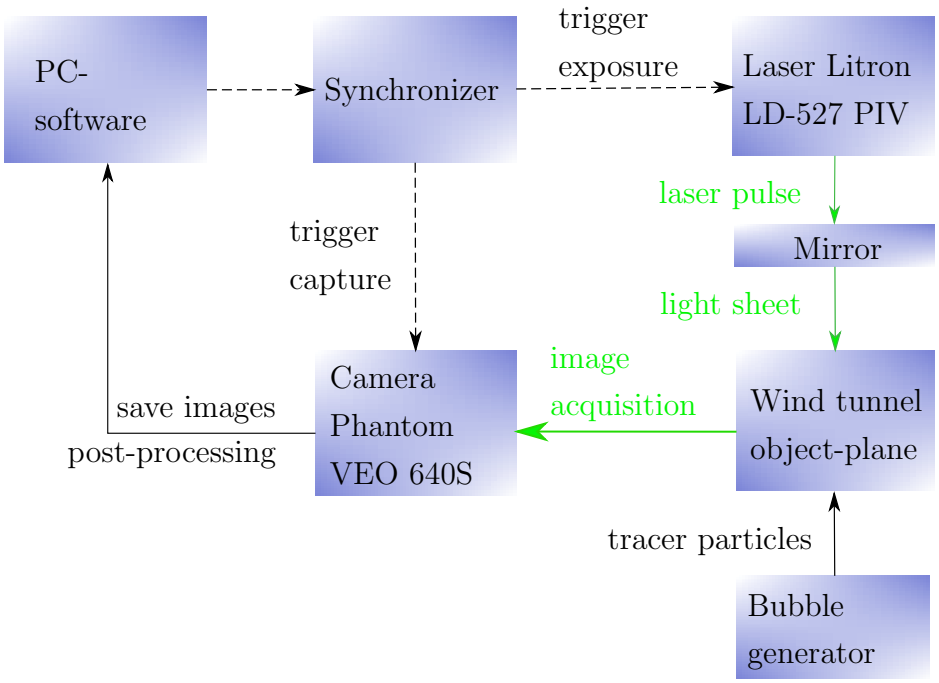

Figure 3.2: Logical sequence of the PIV-system

The software INSIGHT 4G from the company TSI organizes the following measurement tasks:

1. the hardware adjustment: laser alignment, camera focusing and image noise-balancing,
2. the experimental administration: preparing data folders and measurement presets,
3. the measuring procedure: double-laser-pulse exposure and double-image capturing in correct temporal sequence (see also Fig. 3.6). Here the following issues are relevant:
   (a) PIV sampling rate $1/\Delta t_{PR}$ in [Hz] (Pulse Repetition Rate of the double-image frames and the double-laser-pulses),
   (b) double-laser-pulse straddle time Δt_{PIV} in [μs] (temporal distance in between one double-laser-pulse),
   (c) automatic centering of the double-laser pulse within the double-capturing frame (Auto Center Laser Pulse).
4. the processing: image-data saving and calibration, evaluating tracer displacements, reconstructing velocity fields.

In Fig. 3.3 the capture tab (blue) of the graphical user interface of INSIGHT 4G is depicted which represents the mentioned item "3. the measuring procedure". There are three important riders that have to be considered for the measuring procedure: Application "PIV",

Exposure "Synchronized" (the double-pulsed laser with Δt_{PR}), Capture "Sequence" (the double-image frame with Δt_{PR}). In the timing setup the double-laser-pulse straddle time Δt_{PIV} is prescribed by the equivalent quantity "Delta T" (in μs). Additionally, the processing tab of the user interface is shown. The following topics are implemented: With "Define Processing Region" (magenta) the observed image is framed geometrically. By "2D Spatial Calibration" (green) the calibration factor C_{spat} for a line element is calculated, comparing the observed object size in mm with the amount of Pixel in px measured by the software. The "PIV Processor Setup" (yellow) is partitioned into the "Starting Spot Dimensions", for sizing the Interrogation Windows (IW) of the double-images, and the "PIV Plugins" for choosing the correlation algorithm and the type of subpixel algorithm. The processing with the calibration factor and the correlation algorithm are explained comprehensibly in Sections 3.1.3.1 and 3.1.3.2.

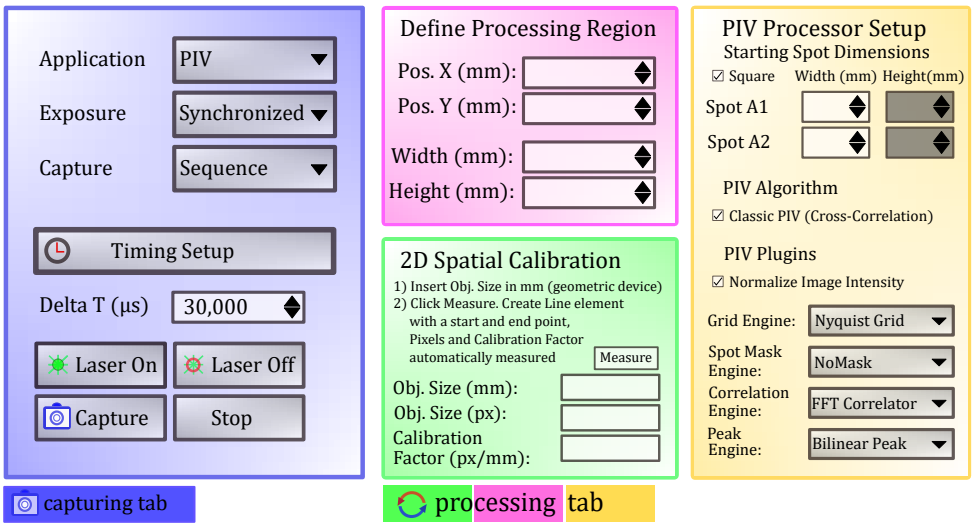

Figure 3.3: The measurement software `Insight 4G`.
The capture tab: *Delta T* (μs) (blue, Timing setup) is equivalent to Δt_{PIV}. The processing tab: "Define Processing Region" (magenta) with the region of interest in screen dimensions, "2D Spatial Calibration" (green) with C_{spat} for a line element, comparing the object size in mm with the amount of Pixel in px, "PIV Processor Setup" (yellow) with "Starting Spot Dimensions" for the size of the IW, PIV Plugins for the correlation algorithm and type of subpixel algorithm.

Furthermore, INSIGHT 4G manages the complete synchronization between laser and camera via USB connection with the synchronizer TSI 630036, which is coupled with the hardware setup using six BNC-ports, also depicted in Fig. 3.4:

- ports A, B, C, D with the pins of the laser-power-unit: SYNC 1/2, TRIG 1/2,
- ports E and H with the pins of the High-Speed-camera: 3 *I/O* (Frame SYNC), 1 TRIGGER.

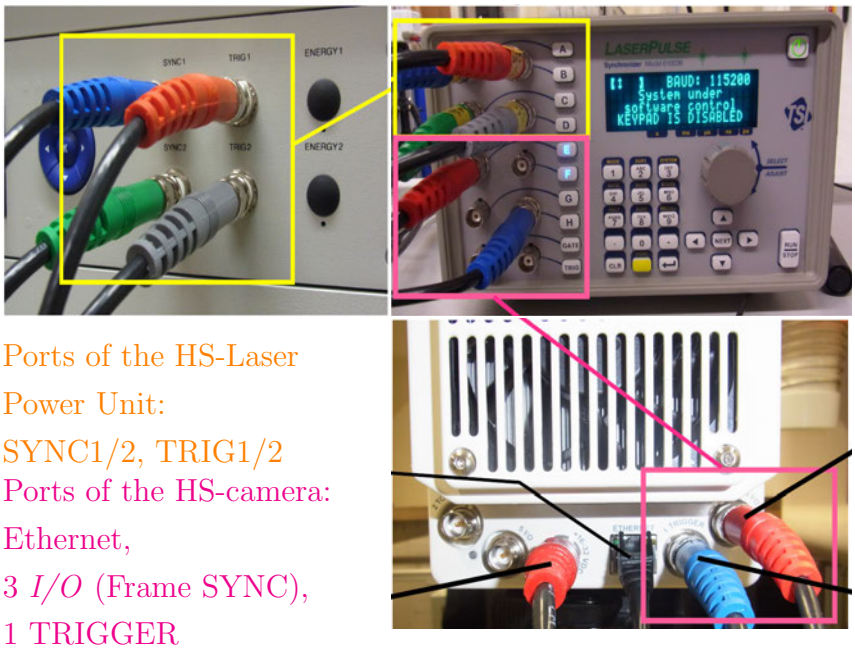

Figure 3.4: Connection ports of the HS-laser-power-unit (top-left), the synchronizer (top-right) and the HS-camera (bottom-right) from Wood [29].

3.1.1.2 High-speed laser Litron LD-527 PIV

For the illumination of the object plane, the High-Speed pulsed laser LITRON LD-527 PIV is used. The design consists of the power-unit and the laser head. The power-unit contains the cooling medium (distilled water) as well as the pump. Furthermore, it provides the energy for producing the laser beam. The laser head includes two identical solid-state lasers in the ND:YLF-configuration, which means that Neodym-Ions are implemented in Yttrium-Lithium-Fluorid crystals. By optical pumping, this composition produces infra-red laser light with a wave length up to $\lambda = 1053$ nm[1], which is beyond the perceptive spectrum of the human eye. Therefore, a crystal harmonic doubler is utilized to reduce the wave length to $\lambda = 527$ nm, which is in the visible green spectrum area. Leaving the laser head, the beam is conducted through externally mounted light-section optics, firstly, by a spherical lens to collimate the beam controlling the light intensity, and secondly, by a cylindrical lens to expand the beam creating a two-dimensional light-section [5]. With a specified output energy of 30 mJ the laser beam has spatially and temporally reproducible properties needed for high-speed-PIV applications. It is used as a pulse-laser, sending out two impulses per trigger signal (high-intense peaks) with the temporal distance Δt_{PIV} and the time lag Δt_{LD} between the trigger signal and the first laser impulse (see also Fig. 3.6).

[1] https://www.advatech-uk.co.uk/nd_ylf.html

3.1.1.3 High-speed camera Phantom VEO 640S

In order to capture images of the illuminated object plane, the HS-camera PHANTOM VEO 640S is used. It is a digital camera including a CMOS (complementary metal-oxide-semiconductor) chip with a spatial resolution of 4 MPx (2560 × 1600 Pixels) and a sample rate at this resolution of $f_{cam} = 1400$ frames/s yielding an exposition time for taking one picture of $\Delta t_{cam} = f_{cam}^{-1} = 7.1428 \cdot 10^{-4} s$. The camera is connected with the PC by an Ethernet-pin to safely transmit the image data to the software tool `Insight 4G` for saving and further evaluating.

3.1.1.4 Bubble generator TSI BG-1000 and aerosol generator for DEHS droplets

During the flow process, the test section is seeded by tracer particles, which are provided in form of small soap bubbles by the TSI BG-1000 bubble generator: The bubbles have a mean diameter of about $d_p = 10$ μm. Their surfaces scatter light appropriately for PIV-image acquisitions. The bubble generator, which is depicted schematically in Fig. 3.5, includes four main components:

- the fluid reservoir,
- the pump pre-connected in series with the filter,
- ten micro-nozzles,
- the supply of pressurized air.

The reservoir contains 65-70 liters of water mixed with three liters of liquid detergent. The mixture is aspirated by the pump and pre-filtered with regard to foreign particles. By generating a pressure range of 900 to 1000 psi (62.05 to 68.95 bar), the mixture is conducted via a metal hose to the reservoir-head. Passing through ten inserted micro-nozzles mounted to a pressure-tight ring-tube, the soap bubbles are generated. By an external supply of pressurized air, the bubbles are directed from the outlet of the reservoir via a flexible hose towards the test section of the wind tunnel.
For the purpose of detection and tracking, the right size of the generated soap bubbles is important in the measurements, which is defined as the most penetration particle size (MPPS). The higher the mean diameter and the larger the corresponding surface of a tracer particle, the better is the effect of scattering the laser light. This improves the quality of the captured images. However, the impact of gravitational and buoyancy forces is increasing, the larger the particle gets. This has a direct impact on the following behavior of the particle in the flow. In order to accurately measure the velocity of the flow based on the movement of the particles, the inertial effects of the particle have to be

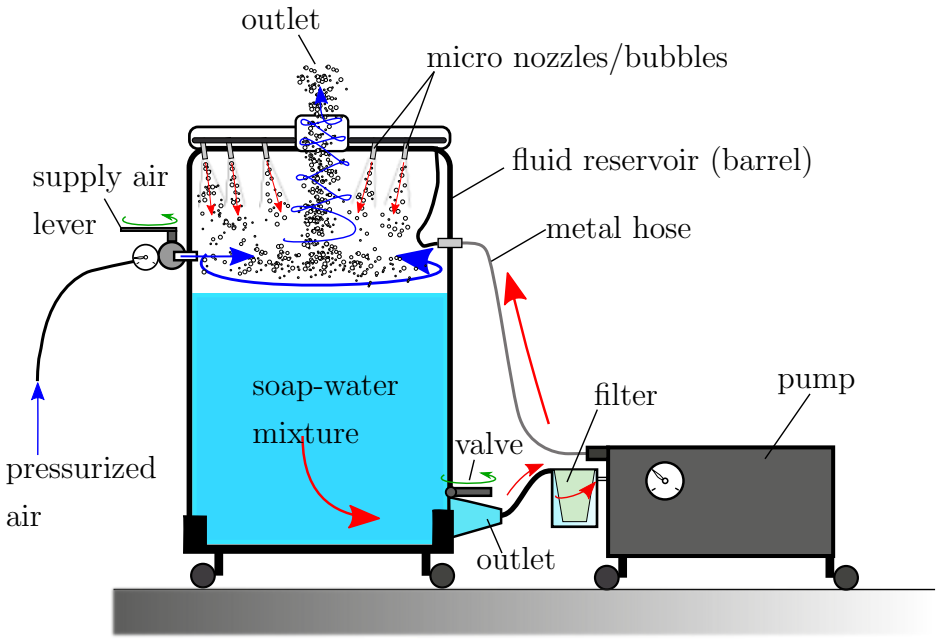

Figure 3.5: Schematic presentation of the bubble generator TSI BG-1000 from Wood [27].

as low as possible. Thus, the particles have to be large enough to scatter enough light to be detected by the camera and on the other hand they have to follow the flow as much as possible without affecting it.

For this purpose, there are two methods to characterize the suitability of tracers according to their dynamic behavior: Firstly, the Stokes number Sk defines whether the tracer particle represents the continuous fluid flow, without slipping off with its own velocity magnitude. Mathematically, it is the quotient of the particle response time τ_p, caused by the inertia effect, and of the fluid's characteristic time scale τ_f, based on the friction velocity u_τ. It follows that

$$\mathrm{Sk} = \frac{\tau_p}{\tau_f} = \frac{\rho_p\, d_p^2/(18\,\mu_f)}{\mu_f/(\rho_f\, u_\tau^2)} = \frac{\rho_p\, d_p^2\, \rho_f\, u_\tau^2}{18\,\mu_f^2} \quad , \tag{3.1}$$

where d_p and ρ_p are the tracer particle's diameter (MPPS) and the density of its chemical composition. The fluid flow properties are given by the density ρ_f and the dynamic viscosity μ_f. For ideal tracers, the Stokes number should tend towards zero ($\mathrm{Sk} \ll 1$).

Secondly, the settling velocity u_{ts} is a measure for spherical particles adapting to a quiescent environment. Its background is a force balance between Stokes drag, buoyancy and gravity. Thus, according to [25], it follows with the gravitational constant g, the tracer particle's diameter d_p (MPPS) and density ρ_p, as well as the fluid density ρ_f and the dynamic viscosity μ_f:

$$u_{ts} = g \cdot d_p^2 \cdot \frac{(\rho_p - \rho_f)}{18\,\mu_f} \quad . \tag{3.2}$$

For ideal tracers, the settling velocity should be much smaller than the airstream velocity ($u_{ts} \ll U_\infty$). The detailed calculations with the chosen parameters for the Stokes number and the settling velocity can be found in appendix A. Discussing the results, the Stokes number for the lowest and highest free-stream and friction velocity are in the range of $\mathrm{Sk}_a \leq \mathrm{Sk} \leq \mathrm{Sk}_b$:

$$\mathrm{Sk}_a = \frac{\rho_p \, d_p^2 \, \rho_f \, u_{\tau,a}^2}{18 \, \mu_f^2} = 0.1358 \quad , \tag{3.3a}$$

$$\mathrm{Sk}_b = \frac{\rho_p \, d_p^2 \, \rho_f \, u_{\tau,b}^2}{18 \, \mu_f^2} = 0.9780 \quad . \tag{3.3b}$$

To evaluate this estimation, the Stokes number range limited by Sk_a and Sk_b confirms the suitability of the soap bubble tracer particles for the given free-stream velocity range, whereas the higher limit still satisfies the condition $\mathrm{Sk} < 1$. The settling velocity of the tracer particle results in:

$$u_{ts} = g \cdot d_p^2 \cdot \frac{(\rho_p - \rho_f)}{18 \, \mu_f} = 2.9019 \cdot 10^{-3} \, \frac{\mathrm{m}}{\mathrm{s}} \tag{3.4}$$

and thus it is far smaller than the lower free-stream velocity with $U_{\infty,a} = 1.44\,\mathrm{m/s}$, which confirms the feasibility of using the soap bubbles as tracers.
An alternative to the soap bubbles are spherical droplets out of "Di-Ethyl-Hexyl-Sebacat" (DEHS), which is a water-insoluble chemical substance. These aerosol droplets are stable with a MPPS of less than $1\,\mu\mathrm{m}$ ($0.2 - 0.3\,\mu\mathrm{m}$) with a durability of 4 hours[2]. In the laboratory, the Six-Jet Atomizer 9306 from TSI[3] is used to generate the DEHS droplets, which offers a reliable seeding procedure with suitable tracers. Unfortunately, due to the irritation of the air ways after a longer treatment, the DEHS becomes uncomfortable for the experimenter. Therefore, a particulate-removing respirator is required here.

3.1.2 Measuring procedure

3.1.2.1 Triggering of measurements

For the purpose of PIV, there are at least two pictures necessary to describe a velocity field. This partitioning method is defined as straddle mode. Before measuring, this mode has to be adjusted by the software `Insight 4G` with regard to the camera and laser timings. Therefore, a schematic sequence of the signals is depicted in Fig. 3.6, which

[2] https://www.deha-gmbh.de/bilder/produkte/pdf/I_DEHS_Sicherheitsdatenblatt.pdf
[3] https://tsi.com/products/aerosol-generators-dispersers/seed-aerosol-generators/six-jet-atomizer-9306/

includes two double-images denoted here by $A_1 - A_2$ and $B_1 - B_2$, respectively. The acquisition procedure of the double-image $A_1 - A_2$ is as follows: The trigger signal of the synchronizer is the indicator for the laser exposition and image acquisition. The time lag between two trigger signals is called pulse repetition time Δt_{PR}. The temporal frame for capturing one image is defined as image acquisition time Δt_{cam}. Between each frame, a gap called inter-frame straddling-time Δt_{FS} occurs. The first laser beam, which is used to illuminate the first image A_1, is released with a delay time Δt_{LD} after the first trigger signal. Shortly after this event, the second laser beam associated with the illumination of the second image A_2 is generated. The two pulses within this double image $(A_1 - A_2)$ have a temporal gap Δt_{PIV}, which is an important parameter in PIV measurements. It is recommended that the first laser pulse is positioned closely to the end of the corresponding image acquisition time frame while the second laser pulse is positioned closely to the beginning of the following Δt_{cam} frame. The background of this procedure is found in the different illumination intensities within a double-image, which is used for the noise minimization. Additionally, in HS-PIV Δt_{PIV} should be positioned symmetrically with regard to the location of the inter-frame straddling-time Δt_{FS}, which also defines the temporal lowest limit of Δt_{PIV}. This centering of Δt_{PIV} is considered in the software settings by the command Auto Center Laser Pulse, see Section 3.1.1.1.

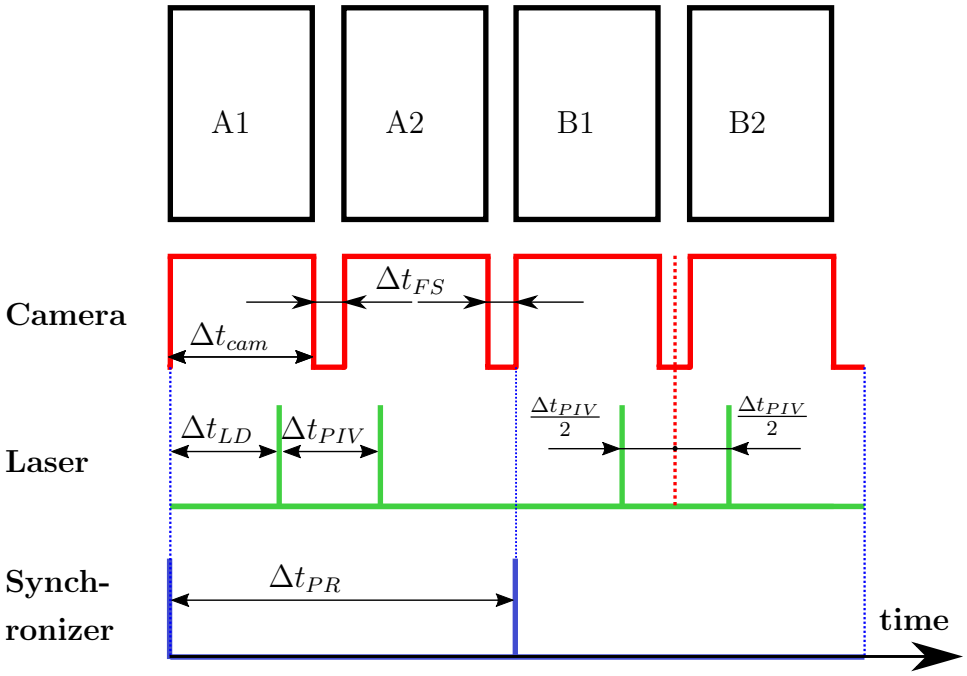

Figure 3.6: Trigger mechanism inspired by Wood [29].
Laser and camera signals controlled by synchronizer signal:
Δt_{cam}: image acquisition time, Δt_{FS}: inter-frame straddling-time,
Δt_{LD}: laser delay time, Δt_{PIV}: laser pulse straddling-time,
Δt_{PR}: pulse repetition time.

3.1.3 Processing: Image data analysis

3.1.3.1 Preparation

The analysis of the image data is based on the comparison of their grey scale values: PIV-cameras with standard CCD or CMOS-chips deliver 8-bit grey levels, so there are $2^8 = 256$ different grey scale values for each pixel possible [5]. Modern chips come with 12 up to 14 bits, which means $2^{12} = 4,096$ up to $2^{14} = 16,384$ grey scale values [25]. For the present PIV-camera, the CMOS chip is a 12-bit sensor[4]. These discrete pixel data are sent to the software `Insight 4G`. Before the processing begins, a preparation is necessary to balance the amount of pixels with the geometric dimensions of the image. Therefore, a spatial calibration is operated related to the actual camera position and focusing. For 2D-PIV applications a geometrical device, for example an inch rule, is placed and photographed in the object plane of the test section, as depicted in Fig. 3.7.

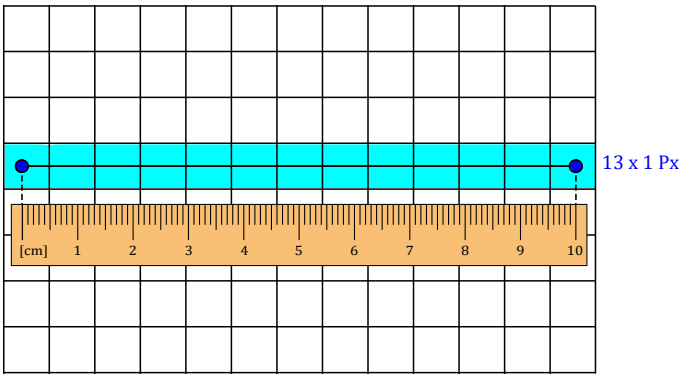

(a) Camera moved forward: $C_{spat} = 13\,\text{px}/100\,\text{mm} = 0.13\,\text{px/mm}$

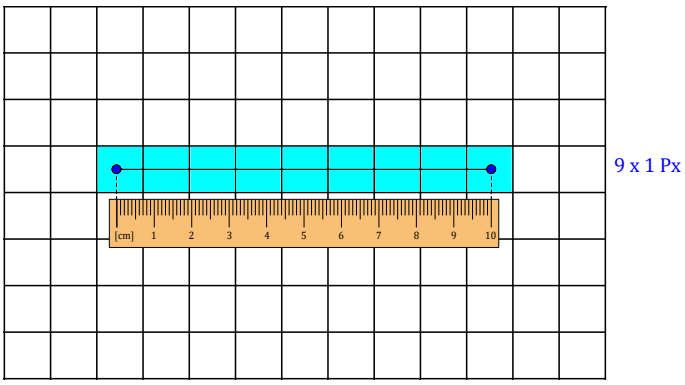

(b) Camera moved backward: $C_{spat} = 9\,\text{px}/100\,\text{mm} = 0.09\,\text{px/mm}$

Figure 3.7: Spatial calibration for the camera moving (a) towards and (b) away from the test section: A line element is generated by the scale of a lineal and its geometric dimension is compared to the amount of pixels (cyan).

[4] https://www.phantomhighspeed.com/products/cameras/veo/veo640

With the software tool a line element can be constructed virtually out of two points across the scale of the captured device in the image plane. The software measures the size of the line by counting the framed pixels while the user has to read the corresponding scale length. Both values can be typed in the tool and a calibration factor is calculated as follows:

$$C_{spat} = \frac{\text{Size of line element [px]}}{\text{Scale length of line element [mm]}} \quad . \tag{3.5}$$

This factor is characteristic for the spatial resolution: Expanding the image screen size (camera moved backward), the resolution and C_{spat} decrease. Reducing the image screen size (camera moved forward), the resolution and C_{spat} increase. These effects are also schematically presented in Fig. 3.7. The two statements have to be considered for the compromise between precise processing and available screen dimensions. However, after calibrating correctly, the borders of the images are often neglected for the processing since the entering and exiting tracers cannot be correlated properly by the applied algorithm. With the tab in the software `Insight 4G` called "Region of Interest", the image plane can be dimensioned by creating a (slightly) smaller frame or choosing a specific width and height manually. This can optimize the time for processing the images since only a fraction of the original image is taken into account.

3.1.3.2 Processing algorithms

In the processing of the PIV data, there are always double-images investigated, which are captured sequentially. Before starting the image data analysis, the region of interest is subdivided into a grid of quadratic cells, the so called "Interrogation Windows" (IW), which contain an equal amount of pixels. The distribution of the tracers within each IW is calculated by the cross-correlation algorithm. The schematic process is depicted in Fig. 3.8. There are two images $A_1(t)$ and $A_2(t + \Delta t_{PIV})$ taken at time t and $t + \Delta t_{PIV}$. A grid is generated by discretizing the original images into IWs. Each image in this tiny instance contains a (6×4) IW-structure, where each IW includes $(M \times N)$ pixels, usually with $M = N$. Exemplary, the IWs $(A_1^{(4,2)} - \overline{A}_1)$ and $(A_2^{(4,2)} - \overline{A}_2)$ are shown, where the nomenclature $(4, 2)$ refers to the (x, y)-coordinate system for counting IWs horizontally and vertically. $\overline{A}_1$ and $\overline{A}_2$ are the arithmetic mean of the grey values of all the pixels within the images A_1 and A_2 that are subtracted for the purpose of filtering out the common grey values of the IWs within each image A_1 and A_2, respectively. Furthermore, this is done for resolving and distinguishing the particles more clearly against the background noise. The IWs have their own local (i, j)-coordinate system, which is counting the pixels horizontally and vertically within $[1, M]$ and $[1, N]$. It is assumed that, during the PIV-process, the particle distribution of the compared IWs stays constant but is shifted slightly due to the

very short time lag Δt_{PIV} between both images. In order to find the displacements of the tracers, a statistical method is used. Both IWs are first superimposed. While the position of the first IW (blue) remains fixed, the second IW (red) is displaced arbitrarily by $|m| \leq 0.5\,M$ and $|n| \leq 0.5\,N$ [25].

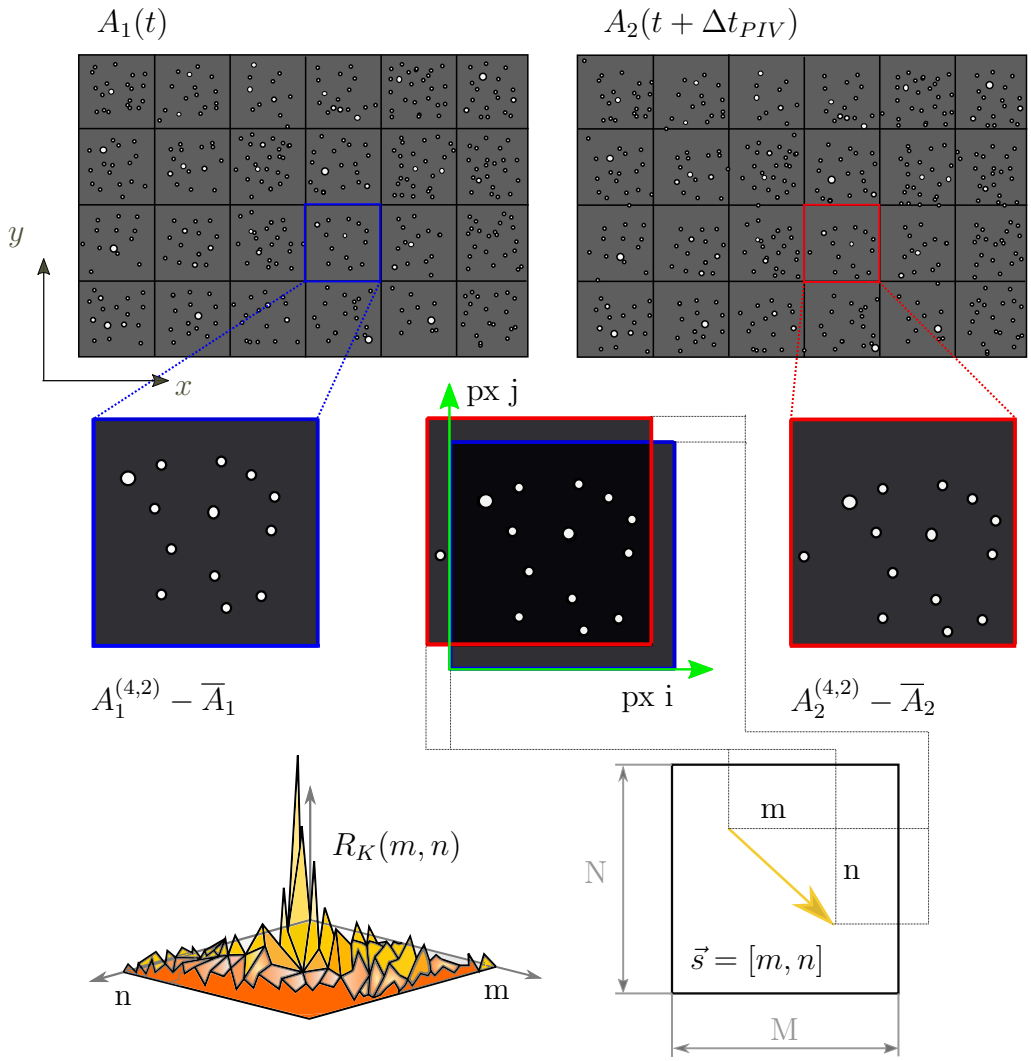

Figure 3.8: Schematic representation of the cross-correlation algorithm used for the displacement calculation of one grid cell pattern inspired by Wood [25].

Each pixel with its grey values at (i, j) (blue IW) is multiplied with the corresponding pixel at $(i+m, j+n)$ (red IW). All products are summarized. The corresponding mathematical procedure is the cross-correlation algorithm finding the optimum product value (peak) for the variables m and n:

$$R_K^{(4,2)}(m,n) = \max\left(\frac{1}{M \cdot N}\sum_{i=1}^{M}\sum_{j=1}^{N}(A_1^{(4,2)}(i,j) - \overline{A}_1)(A_2^{(4,2)}(i+m, j+n) - \overline{A}_2)\right) \quad . \tag{3.6}$$

This algorithm can be improved by optimizing the resolution of the IW. The discrete pixel values are smoothed by the so-called subpixel peak finding methods, which interpolate the interim values by different fitting functions, such as a bilinear fitting curve, a parabolic fitting curve or a Gaussian curve function [25].
The resulting displacement vector of the cross-correlation algorithm can be evaluated in pixels as:

$$\vec{s} = \begin{pmatrix} \mathrm{m} \\ \mathrm{n} \end{pmatrix} = \begin{bmatrix} \mathrm{px} \\ \mathrm{px} \end{bmatrix} \quad . \tag{3.7}$$

This information can be transformed in millimeters by using the calibration factor C_{spat} of Eq. (3.5). Thus, the velocity can be calculated by dividing this physical displacement by Δt_{PIV}. It follows:

$$\vec{v} = \frac{1}{C_{spat} \cdot \Delta t_{PIV}} \cdot \vec{s} \quad , \tag{3.8a}$$

$$= \frac{1}{C_{spat} \cdot \Delta t_{PIV}} \cdot \begin{pmatrix} \mathrm{m} \\ \mathrm{n} \end{pmatrix} \quad . \tag{3.8b}$$

This procedure is executed for each IW in the grid yielding the velocity vectors of the complete image forming a field distribution. Concluding this section, the accuracy of determining the velocity field of the object plane depends geometrically on the IW-size of the grid. Physically, the particle density plays an important role, since the tracer represent the fluid flow properties. Furthermore, the diameter of the particles defines the light-scattering characteristics and the ability of adaption to the fluid flow by the settling velocity. Finally, for measurement reasons, the correctness of the velocity field depends on the time lag Δt_{PIV} between two images due to the fact that the velocity field is calculated by the linear relation of the displacements and time $v = s/t$. Thus, the time Δt_{PIV} should be small enough here.

3.2 Digital-image correlation for deformation measurement

In this section, the Digital-Image Correlation technique (DIC) is introduced. It is a non-invasive imaging method to determine the structural dynamics of a system with regard to spatial displacements and local deformations. Practically, the DIC technique can be also used to measure complex curved surface geometries in order to export these data for CAD or 3D-printing purposes.
For the present investigations of the motion of the NACA-0012 airfoil, Fig. 3.9 shows the DIC-system and the wing system. By the stereoscopic arrangement of two DIC-cameras, three-dimensional surface deformations can be reconstructed. For the image acquisition a speckle pattern is placed on the area of interest of the wing. During the recording time, several images of the speckle pattern are captured. The evaluation is done by a processing tool, comparing the image series to a reference image by a correlation algorithm. Out of the results for the surface deformation, certain line elements (2D) or points (1D) can be extracted. Here, two monitoring points (1D) are considered on the speckle pattern with $P_{w,I}$ for case I and $P_{w,III}$ for case III, to characterize the oscillation of the wing.

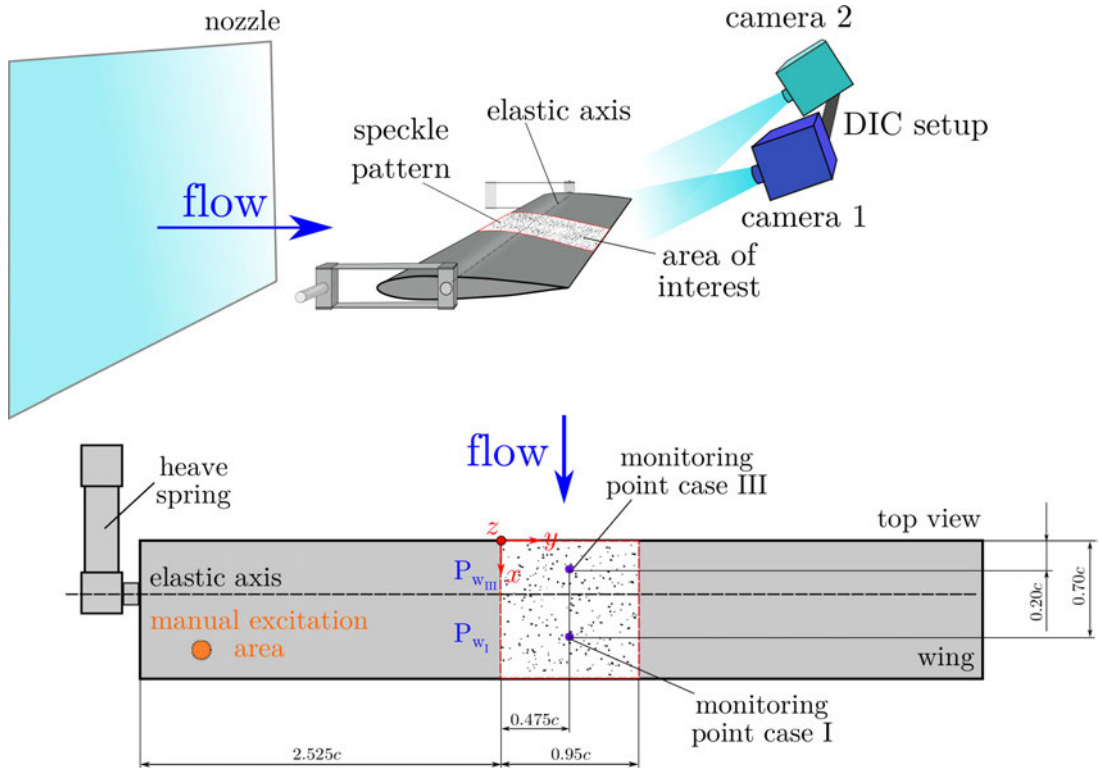

Figure 3.9: The principle of the DIC-system. Top view of the NACA-0012 airfoil with the speckle pattern and the location of the monitoring points for case I and III inspired by Wood et al. [23].

Focussing on the theory of the DIC-imaging, Fig. 3.10 shows the projection concept of the photogrammetry, especially the epipolar geometry [25]. Thus, 3D-objects can be captured from different perspectives by two 2D-cameras , which are stereoscopically positioned with a specified intersection angle, creating an "overlapping" observation area. Each camera is characterized by the image plane and the focal points O_l and O_r (left/right). The real world object point X is projected by the connection lines $\overline{XO_l}$ and $\overline{XO_r}$ on the left and right image planes with the projection points X_l and X_r. Together with the so-called baseline between the focal points $\overline{O_lO_r}$, the epipolar plane (green) is generated. Both image planes detect this epipolar plane as projected lines called epipolar line (red). While the right image plane shows the projection of all points $(x_1, x_2, x_3, ...)$ along $\overline{XO_l}$, the left image plane shows complementarily the projection of all points along $\overline{XO_r}$. The combination of both projections results in the three-dimensional surface image. For physically correct dimensions, a calibration is needed to set up a relation between the coordinate system of the focal points of the cameras, the image planes and the real world coordinate system. Details of the underlying correlation and calibration technique will be provided in Section 3.2.2.

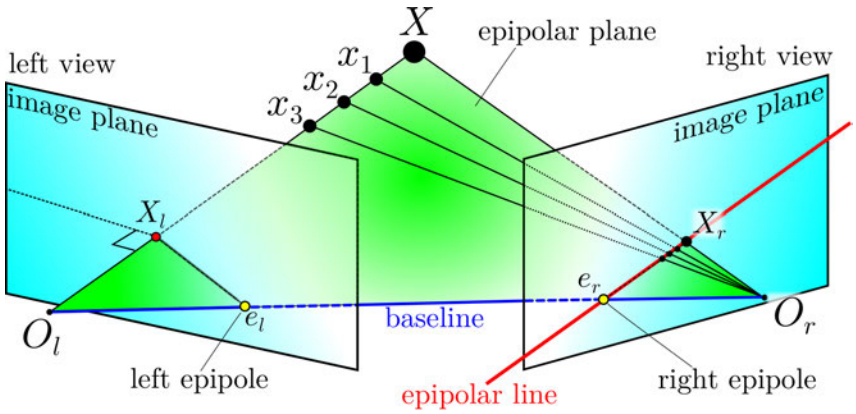

Figure 3.10: Concept of the epipolar geometry used for stereoscopic measurements (Wood [25]).

3.2.1 Technical setup

In the following, the technical setup of the DIC-system is presented. In Fig. 3.11, the hardware components are depicted. There are two identical high-speed cameras of the type *HSVision Speedcam MarcoVis Eo Sens* included. With a CMOS-sensor and a resolution of 1696 x 1710 pixels, images can be captured at a maximum frame rate of 526 fps. Reducing the resolution to 1472 x 1036 pixels, frame rates up to 1000 fps can be achieved[5]. The ring-memory of the CMOS-chip contains 8 GB, the recordings have a

[5] https://www.hsvision.de/images/pdf/MacroVis_EoSensD.pdf

BMP- or AVI-format, respectively. The Ethernet Cat 5e interface can submit the image data via a 5-port Ethernet-switch to the network interface card of the PC. Both cameras have a power supply connection and are synchronized by a whip wire lead. It includes a BNC-adaption of Sync-In and Sync-Out cords as well as a T-Link-adaption of two Trigg4 cords with a trigger button that can be pressed manually to start a measurement. For near-field applications of a 250 mm × 250 mm image plane, which is the case for the current investigation, two *Schneider-Kreuznach* object lenses (22 mm diameter) can be used. For 2000 mm × 2000 mm image planes, two wide-angle lenses can be mounted on the cameras. At critical capturing situations of extreme bright-dark differences, the camera can adjust the image acquisition dynamically, which is suitable for DIC-measurements due to the illumination of the moved speckle-pattern. Furthermore, the CMOS-sensor of the camera possesses a fixed pattern noise correction for precise, noise-reduced images. For three-dimensional measurements, both cameras are built up stereoscopically with a certain distance called *baseline vector* and a certain angle arrangement to each other: This is made possible by a square-cut profile which offers three boreholes at both ends and thus three adjustable *baseline vectors*. With the two camera projection lines an intersection angle of $25° \leq \Phi \leq 45°$ (see Fig. 3.12) is possible and recommended to adjust for a sufficiently large overlapping area. The square-cut profile is mounted via adapter on a *Manfrotto* 3-axes-stand offering a reliable stability for the camera system.

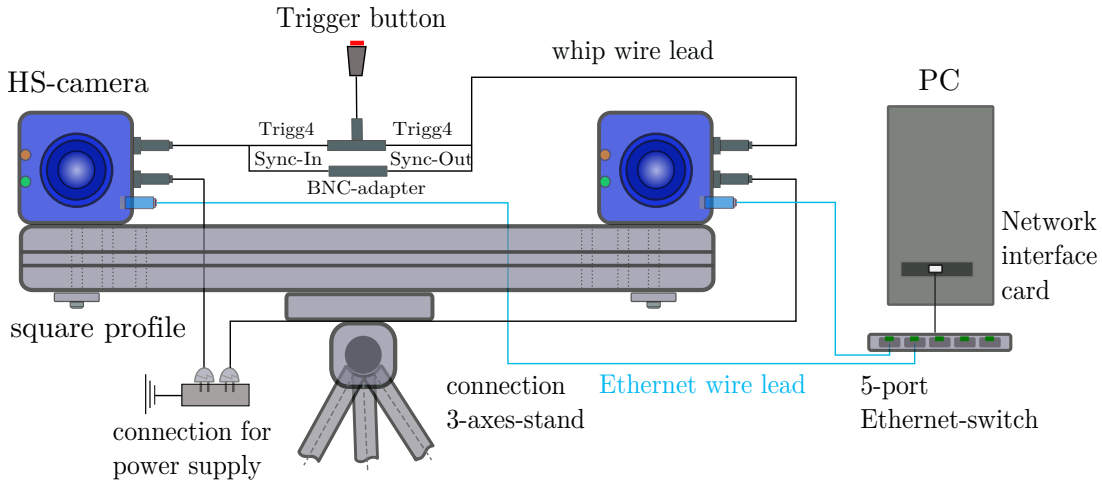

Figure 3.11: Connection schematic of the DIC-system inspired by Wood [26].

3.2.2 Camera calibration

The calibration of the DIC-system is necessary to describe the structural deformations of an object in space with correct dimensions. An approved method was introduced by Tsai [21] and revisited by Horn [11]. By means of a planar calibration target, which is

moved in the space of interest and captured in different positions, a relation between different coordinate systems (COS) is established. Thus, the calibration distinguishes between the *exterior orientation* and the *interior orientation*. The exterior orientation deals with the comparison of the outer positioning of the cameras in space, connecting the camera COS with the world COS of the calibration target, which is done by a coordinate transformation. The interior orientation deals with the comparison of the camera COS of the center of projection with the image plane COS of the CMOS-chip, which is based on the theorem of intersecting lines (photogrammetry). The resulting *extrinsic parameters* contain the rotational and translational values of the camera orientation, while the *intrinsic parameters* contain the information about the internal camera settings and image distortion effects. The identification of these parameters is the main task of the calibration, which can be subdivided in two steps. First, an estimation is done by means of solving an overdetermined system of equations with the least-square fitting method. Second, the provisionally calculated parameters are refined by an iterative procedure of a nonlinear optimization using the Levenberg-Marquardt method. In the following, this calibration concept is presented elaborately. A first impression shall be given by Fig. 3.12.

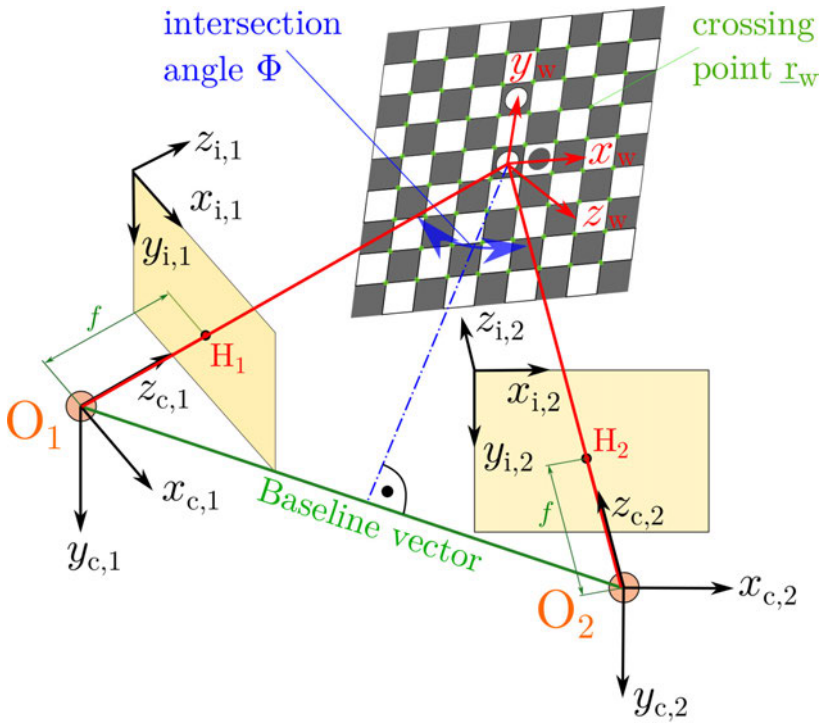

Figure 3.12: Exterior orientation: Calibration scheme of connecting different coordinate systems (COS): World COS (Calibration target plane with x_w, y_w, $z_w = 0$), image plane COS (x_i, y_i, z_i), camera COS (x_c, y_c, z_c). Arrangement of the DIC-cameras with the baseline as connection between the focal points O_1 and O_2 and the intersection angle of the projection lines Φ inspired by Wood [26].

The calibration target, which is presented in the form of a planar chessboard, includes the world COS (red) in its center with the coordinates $\underline{r}_w = (x_w, y_w, z_w)^T$. These are the physical coordinates which refer to the real dimensions of the displacements of the later investigated objects. The two DIC-cameras focus on the calibration target from different perspectives with the intersection angle Φ of the projection lines. The connection line $\overline{O_1O_2}$ of their focal points (the center of projection) was already introduced as the *baseline vector*. Each focal point has its camera COS with the coordinates $\underline{r}_{c,1} = (x_{c,1}, y_{c,1}, z_{c,1})^T$ for O_1 and $\underline{r}_{c,2} = (x_{c,2}, y_{c,2}, z_{c,2})^T$ for O_2, respectively. The components $z_{c,1}$ and $z_{c,2}$ are directed normally to the corresponding image planes of the CMOS-chip. The distance along this direction is called *focal length* f. The intersection point of the collinear projection lines with the image planes are the principle points H_1 and H_2, which are usually positioned centrally on the image plane. Each image plane has the COS with the in-plane components $x_{i,1}$, $y_{i,1}$ and the normal component $z_{i,1}$ for O_1 and $x_{i,2}$, $y_{i,2}$, $z_{i,2}$ for O_2, respectively.

3.2.2.1 Exterior orientation

Describing the calibration procedure, the calibration target has to be manually moved in space with different angles in the area of interest, while the DIC-cameras capture several images of the scenario. Due to the regular chessboard pattern by the alternating black and white squares, there are several crossing points within the target plane having the normed positions in the world COS $\underline{r}_w = (x_w;\, y_w,\, z_w = 0)$. For each image of the target, a coordinate transformation of its captured crossing points is calculated. Thus, the world COS of the calibration target is mapped on the camera COS, which is defined as the *exterior orientation*. The transformation of the coordinates of a point in the world COS $\underline{r}_w$ to the corresponding camera COS $\underline{r}_c$ can be subdivided into the rotation and translation as follows:

$$\underline{r}_c = \underline{\underline{R}}(\underline{r}_w)\, \underline{r}_w + \underline{t} \quad . \tag{3.9}$$

First, by the rotation matrix $\underline{\underline{R}}(\underline{r}_w)$, the world coordinates are turned by the Euler angles yaw $\theta(x_w)$, pitch $\alpha(y_w)$ and tilt $\psi(z_w)$ depending on their instantaneous position. The rotation matrix is orthonormal fulfilling the condition:

$$\underline{\underline{R}}(\underline{r}_w)^T \underline{\underline{R}}(\underline{r}_w) = \underline{\underline{R}}(\underline{r}_w) \underline{\underline{R}}(\underline{r}_w)^T = \underline{\underline{I}} \quad , \tag{3.10}$$

which means that the included row vectors are orthogonal to each other and normalized by their absolute value. Second, the COS is shifted by the translational vector $\underline{t}$ towards the position of the camera COS.

In three-dimensional space, the transformation can be written as

$$\begin{pmatrix} x_c \\ y_c \\ z_c \end{pmatrix} = \begin{pmatrix} R_{11} & R_{12} & R_{13} \\ R_{21} & R_{22} & R_{23} \\ R_{31} & R_{32} & R_{33} \end{pmatrix} \begin{pmatrix} x_w \\ y_w \\ z_w \end{pmatrix} + \begin{pmatrix} t_x \\ t_y \\ t_z \end{pmatrix} \quad . \tag{3.11}$$

3.2.2.2 Interior orientation

The projection of a real world object point onto the image plane is influenced by internal parameters of the camera such as the positioning of the focal point and the resulting focal length. Thus, the COS of the image plane is associated to the COS of the camera, which is declared as *interior orientation*. The explicit relation shall be explained by means of Fig. 3.13 presenting the intersect theorem.

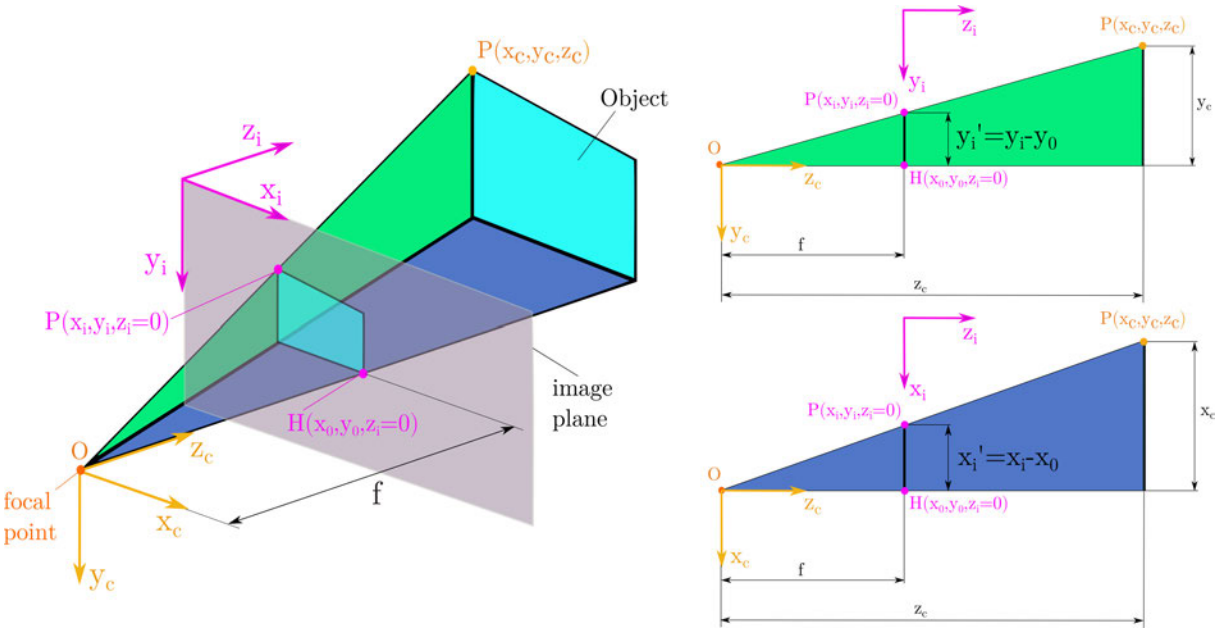

Figure 3.13: Interior orientation: Relation between the camera COS and image plane COS. Projection of an object point onto the image plane. Application of the intersect theorem on different perspectives inspired by Wood [26].

The image plane (grey) has its COS on the top-left corner (pink) with the components (x_i, y_i, z_i). At the focal point O, which is the center of projection, the camera COS (orange) is located with (x_c, y_c, z_c). Both COS have in common that $z_i||z_c$. The focal length f is the perpendicular distance between the focal point and the image plane along z_c, resulting in the principle point in the camera coordinates $\underline{H}(c) = [0; 0; f]^T$. In image coordinates the principle point is at $\underline{H}(i) = [x_0; y_0; 0]^T$, which usually is at the center of the CMOS chip. The object plane (turquois) is projected onto the image plane.

Perspectively, it results from several connection lines which are created between the object points and the focal point and intersecting the image plane. An example may be the object point $\underline{P}(c) = [x_c; y_c; z_c]^T$ that can be found on the image plane with $\underline{P}(i) = [x_i; y_i; 0]^T$. This projection can be subdivided in two triangular forms, regarding the x-z-coordinates (blue) and the y-z-coordinates (green), resulting in two intersect theorem equations:

$$x\text{-}z\,(\text{blue}): \quad \frac{x_i'}{f} \equiv \frac{x_i - x_0}{f} = s\,\frac{x_c}{z_c}\,, \tag{3.12a}$$

$$y\text{-}z\,(\text{green}): \quad \frac{y_i'}{f} \equiv \frac{y_i - y_0}{f} = \frac{y_c}{z_c}\,. \tag{3.12b}$$

The factor s in Eq. (3.12a) is the horizontal scale factor which originates from the digitization of the smooth, low-pass filtered analogous signal to the discrete image, resulting in a horizontal spacing difference in between each column of the sensor cells and the pixels. In the vertical direction, this sampling problem can be prevented by the camera controlling the equal spacing of rows of the sensor cells and the pixels.
A further influencing factor on the projection is the radial distortion on the image plane, which is caused by the spherical design of the camera lenses. Figure 3.14 depicts two different types: The left one shows the pincushion distortion expanding the ideal image projection (green square) forming distortion wedges at the corners.

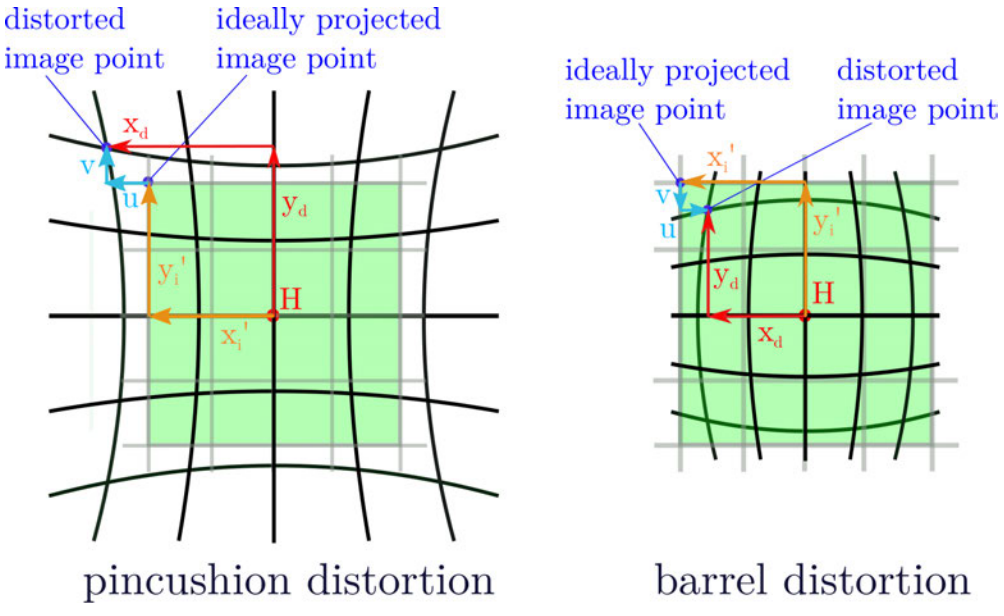

Figure 3.14: Two different types of radial distorted image projections caused by different lenses. The green square symbolizes the ideal projection on the image plane. Measured from the principle point H, one example point at $r^2 = x_i'^2 + y_i'^2$ is presented as ideal and distorted with the displacements $u = f(r)$, $v = f(r)$. Left: Pincushion distortion for "near-field application" lenses. Right: Barrel distortion for "far-field application" wide-angle lenses.

This effect happens for telephoto lenses or "near-field application" lenses, i.e., the Schneider-Kreuznach object lenses (22 mm) for the currently used lenses. The right type is the barrel distortion contracting the ideal projection forming curvatures at the corners. This effect appears for "far-field application" lenses. Exemplarily for both types of distortion, one point measured from the principle point H is presented in the ideal and distorted configuration of the image coordinates at $(x_i'; y_i')$ (idealized for calibration procedure) and $(x_d; y_d)$ (measured in the actual image plane) with the following relation:

$$x_d = x_i' + u \ , \tag{3.13a}$$

$$y_d = y_i' + v \ . \tag{3.13b}$$

The horizontal and vertical displacements $u = f(x_i', r)$ and $v = f(y_i', r)$ can be mathematically described in the form of even polynomial functions depending on the radial distance $r^2 = x_i'^2 + y_i'^2$ from the principle point H as follows:

$$u = x_i'(\kappa_1\, r^2 + \kappa_2\, r^4) \ , \tag{3.14a}$$

$$v = y_i'(\kappa_1\, r^2 + \kappa_2\, r^4) \ . \tag{3.14b}$$

The radial lense error coefficients κ_1 and κ_2 (intrinsic parameters) are determined by the deviations u and v between (x_d, y_d) and (x_i', y_i'). This can be done after the main calibration procedure with (x_i', y_i') is finished.

3.2.2.3 Combining exterior and interior orientation

Apart from the radial distortion effect, the main calibration procedure with (x_i', y_i') is continued in the following. The concepts of exterior and interior orientation can be combined by substitution and modification of the former Eqs. (3.11), (3.12a) and (3.12b), yielding:

$$\frac{x_i'}{y_i'} = s\,\frac{R_{11}\,x_w + R_{12}\,y_w + R_{13}\,z_w + t_x}{R_{21}\,x_w + R_{22}\,y_w + R_{23}\,z_w + t_y} \ , \quad \text{with } s = 1. \tag{3.15}$$

For the planar calibration target, it is assumed that $s = 1$ since the image coordinates have been balanced according to the horizontal scaling differences. Due to the fact that every crossing point of the calibration target is at $z_w = 0$, this former equation can be simplified:

$$\frac{x_i'}{y_i'} = \frac{R_{11}\,x_w + R_{12}\,y_w + t_x}{R_{21}\,x_w + R_{22}\,y_w + t_y} \quad . \tag{3.16}$$

By cross-multiplying, it follows:

$$(x_w\,y_i')R_{11} + (y_w\,y_i')R_{12} + y_i'\,t_x - (x_w\,x_i')R_{21} - (y_w\,x_i')R_{22} - x_i'\,t_y = 0 \quad . \tag{3.17}$$

The unknowns in this equation are the entities of the rotation matrix $\underline{\underline{R}}$ and the translation vector $\underline{t}$. At this point, it might be remarked that the focal length f is omitted in Eq. (3.17), though it is an unknown parameter that has to be determined later on.

3.2.2.4 Solving the equation system

The small planar calibration target for the near-field application possesses $n = 64$ crossing points with its specified positions $(x_w; y_w; z_w = 0)$ in the world COS, which is depicted in Fig. 3.15. According to the scanning procedure, for each of the crossing points, Eq. (3.17) can be set up forming a homogeneous linear system of equations. It includes the six unknowns (R_{11}, R_{12}, R_{21}, R_{22}, t_x, t_y). Since there are more equations ($n = 64$) than the six unknowns, the linear system of equations is over-determined with a non-invertible system matrix. For the solving, an approximation method is used, which is called the *least-square fitting*-method. This procedure searches for the minimum of the squared residual function (squared error function) by subtracting the exact y_k-values of a series of measurement (x_k, y_k) from a linear approach $\tilde{y} = f(x_k)$ and by subsequently squaring [1]. First of all, this approximation method requires an inhomogeneous linear system of equations. Therefore, the current homogeneous system of equations is slightly modified. One parameter is set arbitrarily to a certain value, here $t_y^* = 1$, which means one unknown less.

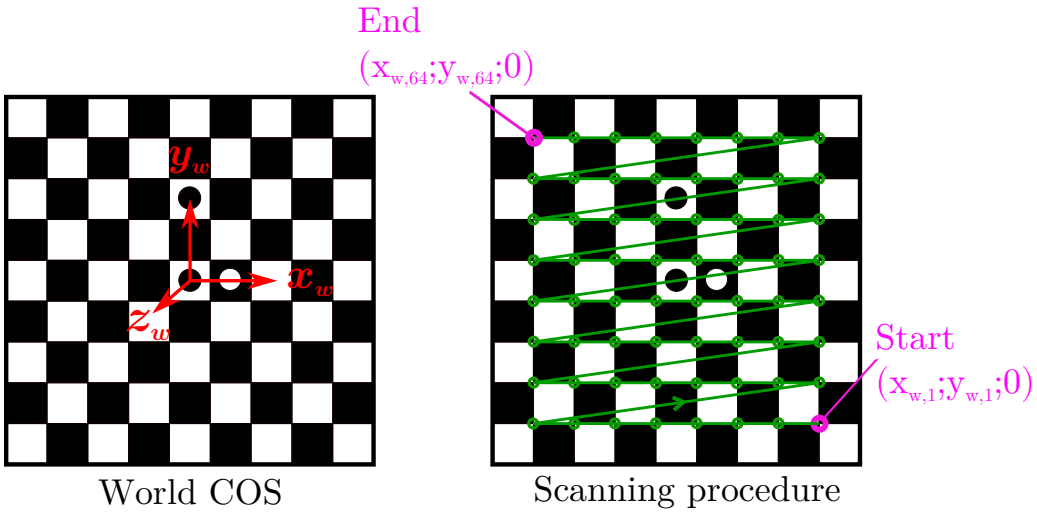

Figure 3.15: "Small size" planar calibration target with a chessboard pattern with 81 black/white squares of 11 mm×11 mm size. Left: world COS in the middle of the board. Right: Scanning procedure with start and end crossing point ($N \leq 64$) for building up the linear system of equations (3.18) inspired by Wood [26].

Then, the inhomogeneous system of equations follows with:

$$\underbrace{\begin{pmatrix} (x_w\,y_i')_1 & (y_w\,y_i')_1 & (y_i')_1 & -(x_w\,x_i')_1 & -(y_w\,x_i')_1 \\ (x_w\,y_i')_2 & (y_w\,y_i')_2 & (y_i')_2 & -(x_w\,x_i')_2 & -(y_w\,x_i')_2 \\ \vdots & \vdots & \vdots & \vdots & \vdots \\ \vdots & \vdots & \vdots & \vdots & \vdots \\ (x_w\,y_i')_n & (y_w\,y_i')_n & (y_i')_n & -(x_w\,x_i')_n & -(y_w\,x_i')_n \end{pmatrix}}_{\underline{\underline{P}}^{(n\times 5)}} \underbrace{\begin{pmatrix} R_{11}^* \\ R_{12}^* \\ t_x^* \\ R_{21}^* \\ R_{22}^* \end{pmatrix}}_{\underline{q}^{*(5\times 1)}} = \underbrace{\begin{pmatrix} (x_i')_1 \\ (x_i')_2 \\ \vdots \\ \vdots \\ (x_i')_n \end{pmatrix}}_{\underline{x_i'}^{(n\times 1)}} \quad . \tag{3.18}$$

From the minimum value problem of the *least-square fitting*-method, the "normal system of equations" results in:

$$\underline{\underline{P}}^T\,\underline{\underline{P}}\,\underline{q}^* = \underline{\underline{P}}^T\,\underline{x_i'}\ , \tag{3.19a}$$

$$\underline{q}^* = (\underline{\underline{P}}^T\,\underline{\underline{P}})^{-1}\,\underline{\underline{P}}^T\,\underline{x_i}\ . \tag{3.19b}$$

Thus, the current system is multiplied by the transposed matrix $\underline{\underline{P}}^T$ and can be solved now by taking the so-called pseudo-inverse $(\underline{\underline{P}}^T\,\underline{\underline{P}})^{-1}\,\underline{\underline{P}}^T$, which consists mainly of the former non-invertible matrix $\underline{\underline{P}}$ [1,12]. Hence, a first solution is generated with the vector $\underline{q}^* = (R_{11}^*; R_{12}^*; t_x^*; R_{21}^*; R_{22}^*)^T$ and $t_y^* = 1$, respectively [11]. With these results, the elements of the rotation matrix R_{13}^*, R_{23}^* can be recovered by two orthonormal constraints:

$$R_{11}^{*2} + R_{12}^{*2} + R_{13}^{*2} = k^2\ , \tag{3.20a}$$

$$R_{21}^{*2} + R_{22}^{*2} + R_{23}^{*2} = k^2\ . \tag{3.20b}$$

By the provisional solution components (*), the squared absolute values of the first and second row vector of the rotation matrix yield a scaling factor $k^2 \neq 1$. For the converged solution, it would be finally at $k^2 = 1$ (ideally normed row vectors). Furthermore, the first and second row vector are orthogonal. Thus, their scalar product follows with:

$$R_{11}^* R_{21}^* + R_{12}^* R_{22}^* + R_{13}^* R_{23}^* = 0\ . \tag{3.21}$$

From Eqs. (3.20*a*), (3.20*b*) and (3.21), it results:

$$R_{13}^* = \pm\sqrt{k^2 - (R_{11}^{*2} + R_{12}^{*2})}\ , \tag{3.22a}$$

$$R_{23}^* = \pm\sqrt{k^2 - (R_{21}^{*2} + R_{22}^{*2})}\ , \tag{3.22b}$$

$$R_{13}^* R_{23}^* = -(R_{11}^* R_{21}^* + R_{12}^* R_{22}^*)\ , \tag{3.22c}$$

with the value for the scaling factor:

$$k^2 = \frac{1}{2}\left[(R_{11}^{*2} + R_{12}^{*2} + R_{21}^{*2} + R_{22}^{*2}) + \sqrt{((R_{11}^{*} - R_{22}^{*})^2 + (R_{12}^{*} + R_{21}^{*})^2)((R_{11}^{*} + R_{22}^{*})^2 + (R_{12}^{*} - R_{21}^{*})^2)}\right] . \quad (3.23)$$

Unfortunately, the sign of R_{13}^{*} and R_{23}^{*} can not be clearly defined, instead the sign of the product $R_{13}^{*}R_{23}^{*}$ is unique. Hence, there are two options for the sign combination of R_{13}^{*} and R_{23}^{*} which is done with the *trial-and-error method*. However, the right sign can be proven afterwards with the scalar product condition of the "predicted", retransformed point vector $P_p = (x'_p; y'_p)^T$ and the real measured point vector $P = (x'_i; y'_i)^T$ from the principle point $H(x_0; y_0)$ within the image plane. If the following result appears with

$$\sum_{j=1}^{n} (x'_{i,j} x'_{p,j} + (y'_{i,j} y'_{p,j}) < 0 , \quad (3.24)$$

then the same orientation of the image vectors is not given and the signs of R_{13}^{*} and R_{23}^{*} have to be inverted in retrospect. This procedure might be possibly repeated, until the right signs are found. Nevertheless, the third row vector $(R_{31}^{*}; R_{32}^{*}; R_{33}^{*})$ of the rotation matrix results from the cross-product of the first and second row vector:

$$(R_{31}^{*}; R_{32}^{*}; R_{33}^{*}) = ((R_{11}^{*}; R_{12}^{*}; R_{13}^{*})^T \times (R_{21}^{*}; R_{22}^{*}; R_{23}^{*})^T)^T . \quad (3.25)$$

The missing parameters, the translational vector component t_z and the focal length f can be calculated based on Eq. (3.12b):

$$\frac{y'_i}{f} = \frac{y_c}{z_c} \equiv \frac{R_{21}^{*}\, x_w + R_{22}^{*}\, y_w + R_{23}^{*}\, z_w + t_y^{*}}{R_{31}^{*}\, x_w + R_{32}^{*}\, y_w + R_{33}^{*}\, z_w + t_z^{*}} , \quad (3.26a)$$

$$(R_{21}^{*}\, x_w + R_{22}^{*}\, y_w + R_{23}^{*}\, z_w + t_y^{*})\, f - y'_i t_z^{*} = (R_{31}^{*}\, x_w + R_{32}^{*}\, y_w + R_{33}^{*}\, z_w)\, y'_i . \quad (3.26b)$$

Again, an inhomogeneous system of equations can be developed by inserting the coordinates $\underline{r}_w = (x_w; y_w; z_w)^T$ and $\underline{r}_i = (x_i; y_i; z_i)^T$ of the crossing points into this equation and applying the method of *least-square fitting*. Practically for defining t_z and f appropriately, it is recommended to capture several images of the moved calibration target with different angles in the space of interest (not only normal to the image plane) and with slight deviations in the depth.

After all necessary parameters are provisionally defined in the first step of solving the linear system of equations, the second step is a nonlinear optimization to improve these parameters by:

$$\min \left\{ \sum_{j=1}^{N} (x_{d,j} - x'_{i,j})^2 + \sum_{j=1}^{N} (y_{d,j} - y'_{i,j})^2 \right\} , \tag{3.27}$$

Every crossing point ($j = 1...N$) of the target ($x_w, y_w, z_w = 0$) with the "predicted" image plane positions (x'_i, y'_i) is compared to the corresponding "real" image plane positions (x_d, y_d) by taking the sum of the squared component differences. This error function is iteratively minimized by applying the modified Levenberg-Marquardt method [16]. Precise results are delivered for the elements of the Rotation matrix $\underline{\underline{R}}$ as well as for the elements of the translation vector $\underline{t}$ (inclusively the optimized t_y) at a low CPU-time and effort. Afterwards, by the remaining residuals within the optimization u (horizontal residual) and v (vertical residual), the radial distortion coefficients κ_1 and κ_2 can be determined (see therefore Fig. 3.14).

To summarize this section, all parameters of the calibration, which the DIC-system requires for the measurement processing (evaluation), are listed in Tab. 3.1.

Table 3.1: Extrinsic, intrinsic and stereoscopic parameters of the camera system [26].

Parameter	**Classification**	**Unit**	**Description**
R_x	extrinsic	[rad]	rotation of x_w-axis with yaw angle θ
R_y	extrinsic	[rad]	rotation of y_w-axis with pitch angle α
R_z	extrinsic	[rad]	rotation of z_w-axis with tilt angle ψ
t_x	extrinsic	[mm]	translation in x_w-direction
t_y	extrinsic	[mm]	translation in y_w-direction
t_z	extrinsic	[mm]	translation in z_w-direction
f	intrinsic	[mm]	effective focal length
C_x	intrinsic	[pixel]	$x_i = x_0$ position of the principle point H′
C_y	intrinsic	[pixel]	$y_i = y_0$ position of the principle point H′
s	intrinsic	[-]	horizontal scale factor
κ	intrinsic	[1/mm^2]	radial lense distortion coefficient
Φ	stereoscopic	[°]	Intersection angle of the projection lines
Baseline vector	stereoscopic	[mm]	Absolute distance of the focal points

A classification into extrinsic and intrinsic parameters is given, distinguishing the origin from the exterior orientation (relation of world COS and camera COS) and interior orientation (relation of camera COS and image COS with distortion and scaling effects).

3.2.3 Measuring procedure

The measurement software of the DIC system is called "Visart" from *HSVision*. The controlling of high-speed cameras is supported for the two available cameras *HSVision Speedcam MarcoVis Eo Sens*. An impression of the software user interface design is given in Fig. 3.16. Two cameras with the labels "A3" and "EF" are registered, while the former

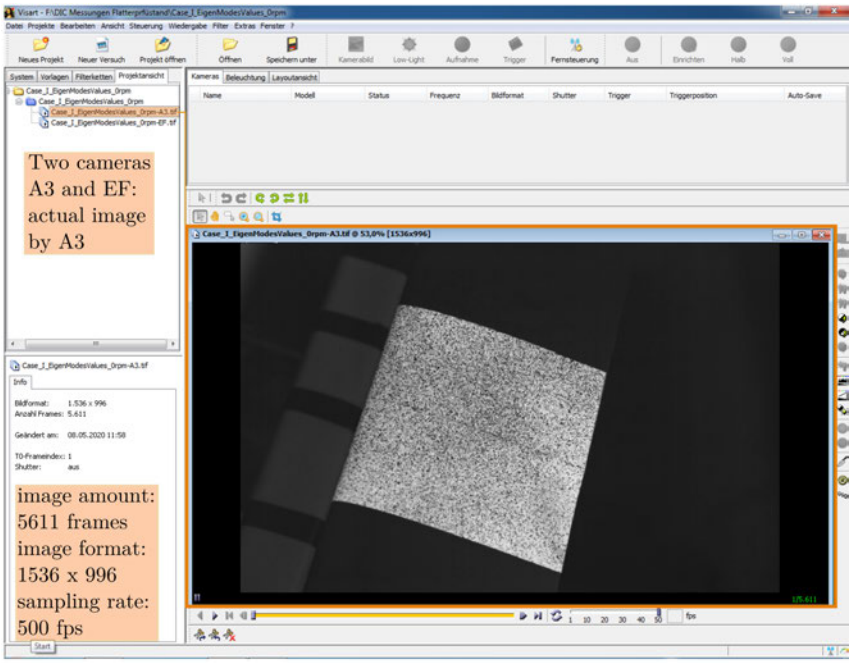

Figure 3.16: DIC-measuring software "Visart" from HSVision. Two cameras A3 and EF registered. Actual image (.tif-format) of the speckle pattern by camera A3. Image format, frame rate and number of frames are presented.

one is the "slave" and the last mentioned is the "master". This means that the trigger signal controls the master, which enables the slave shortly after to record the images (Sync-In/Out, see also Fig. 3.11). For the measurement procedure, the software provides a time period where the trigger can be manually pressed. The captured images are sent via an Ethernet wire and the 5-port Ethernet-switch to the network interface card. The actual image of the speckle pattern of the wing is shown in Visart by the perspective of camera A3. The image format is adjusted to 1536×996 pixels. The frame sampling rate is set to 500 fps resulting in an amount of 5611 frames. Usually, the sequence of images is saved by the format of binary video data called "Advanced Recording File" (.arf). In a further step, this has to be manually converted to the format of raster graphics images called "Tagged Image File" (.tif), which is necessesary for the processing. Detailed information about the software properties can be found on the homepage of HSVision[6].

[6] https://www.hsvision.de/de/produkte/software/steuersoftware-visart

3.2.4 Image data analysis and processing

The processing software of DIC is called "Istra4D" from *Dantec Dynamics GmbH*. An impression of the software user interface design is given in Fig. 3.17. The profile is target-oriented by offering six main processing steps which are briefly introduced (see below on the right side of Fig. 3.17):

- "Input data selection": The image data (format ".tif") from the software Visart are loaded in Istra4D, which is separately done for the data of camera "A3" and "EF". Furthermore, the calibration data, which are determined by capturing the calibration target, are loaded here.

- "Evaluation Settings": For the correlation algorithm of DIC, there are several adjustment parameters necessary, i.e., the grid spacing and the facet size, which divide the observed surface area into facets for correlation. This is explained later on.

- "Mask Definition": The area for implementing the correlation algorithm of DIC is framed, which can be done by a polygon with several support points. In this case, a rectangular area is applied on the observed surface. Here, it is important to frame the highly resolved areas. At the small areas around the leading and trailing edge, the resolution is critical due to the fact that the arching of the wing surface is relatively high there. Thus, these small areas are excluded from the correlation frame.

- "Startpoints": Within the framed mask, the correlation of DIC needs a startpoint for executing the algorithm. Ideally, the user has to choose a distinguishable speckle of larger size or a merged number of smaller speckles. The software shows in retrospect, if the starting point leads to a successful correlation.

- "Control": The correlation is started after the adjustments above have been finished.

- "Visualization Settings": After the correlation has been done, several visualization parameters can be analyzed. In this case, the displacement field in the direction of $z/[\mathrm{mm}]$ is presented in Fig. 3.17. Thus several images can be compared to the reference image, which is structured in steps. "Step 0" is the undeformed reference pattern, which usually is the first image. "Step 7" is exemplarily analyzed and shows the instantaneous surface deformations of the 8th image, which can be seen by the colored surface area. Within this area, line elements or point elements can be extracted by the Tab "Gauge" to further investigate the deformations in reduced dimensions. Here, two monitoring points, point 1 and 2, are chosen for

case I and III, respectively. The locations are defined according to a COS, which has been positioned by the user at a distance of 20 mm from the leading edge with the x-axis directed in free-stream direction and the z-axis directed vertcially downwards. From these monitoring points, the time history of the oscillations in z-direction can be exported for all correlated images to a file in "ASCII"-format to generate diagrams in special visualization softwares like "Tecplot".

Detailed information about the software properties can be found on the homepage of Dantec Dynamics GmbH[7].

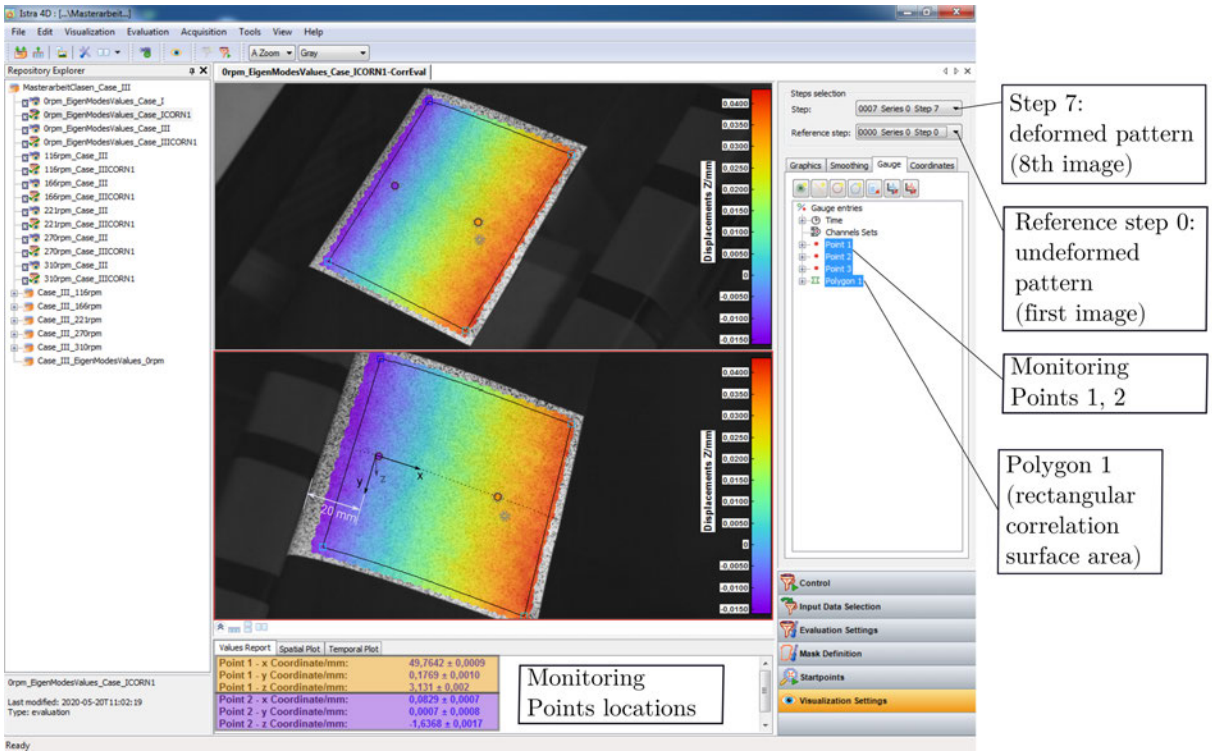

Figure 3.17: DIC-processing software "Istra 4D" from Dantec Dynamics GmbH. Visualization of the correlated results for the z-displacement of the 8th image of the speckle pattern on the wing. Coordinate system, monitoring points 1,2 with locations (orange, violet) and the rectangular correlation area (in general "polygon").

3.2.4.1 Image digitization and intensity interpolation

The image data of DIC, which are generated by Visart and loaded into Istra 4D for processing, contain discrete light intensity distributions. This fact originates from the image capturing by the DIC-cameras and the digitized mapping on the image sensor plane with discrete pixel subdivisions. An example by Sutton [20] is depicted in Fig. 3.18.

[7] https://www.dantecdynamics.com/new-release-of-istra4d-4-4-7/

A three-dimensional bar diagram of discrete values of image intensity is presented for an image sensor plane with the discrete pixel-COS $[X_s, Y_s] = [(0, 10)\ \text{px}; (0, 10)\ \text{px}]$. Thus, every pixel has a certain light intensity height with a grey level value between 0 and 255, which is related to a 8 bit intensity resolution. This discrete distribution is problematic for the processing, due to the fact that the so-called "sub-pixel registration algorithm" by Newton-Raphson, which is explained later on, requires the displacements in between neighboring pixels [3, 20]. Therefore, *sub-pixel estimates* are done to compensate this deficit by converting the discrete pattern (integer values) into a continuous intensity distribution (non-integer values). Usually, *bicubic splines* provide reliable results which is indicated in Fig. 3.18 at the borders. With the intensity interpolation, the correlation algorithm of DIC delivers well-converged deformation results with a high registration accuracy even at small local displacement gradients [3, 20].

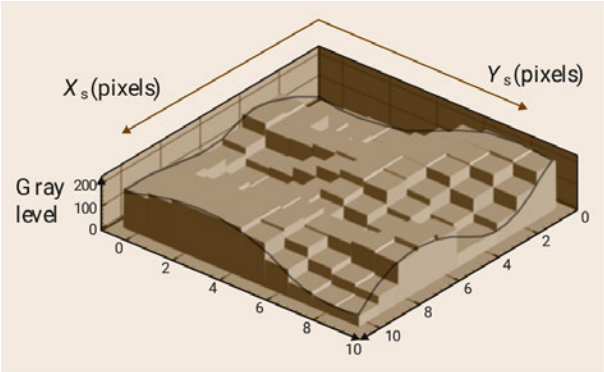

Figure 3.18: Three-dimensional plot of discrete image intensity values. The height represents grey level value (8 bit, 0...255) at pixel locations $[X_s, Y_s] = [(0, 10)\ \text{px}; (0, 10)\ \text{px}]$ from Sutton [20]. Additional indication of bicubic splines as subpixel interpolation lines.

3.2.4.2 Grid cell displacements and correlation method

For the calculation of the deformations by DIC, the observed surface geometry is subclassified into *facets*. Exemplarily, Fig. 3.19 depicts a facet on the left side, which is again subdivided into 9 grid cells, containing a certain amount of pixels. Each grid cell has its grid point at the center (green). The corners of intersection of the grid cells within the facet are the facet-points (blue). While the grid points (green) serve as the basis for the calculation with the information of longitudinal strain, the 4 facet-points include the information of shear and longitudinal strain, which is significant for the deformation by DIC. Hence, the facet points are also called DIC-points. On the right side of Fig. 3.19 the correlation parameters are listed that have been used here. The grid spacing (discrete edge length of the grid cell) is set with 9 pixels (green), while the

facet size (discrete edge length of the facet) results in 27 pixels (blue). Further parameters (yellow) are the "correlation accuracy" of 0.1 pixels of the sub-pixel analysis based on the intensity interpolation, the maximum acceptable value of the residuum of 30 grey values and the maximum acceptable deviation of the pixel position found by the correlation and the back projected object points within 1 pixel.

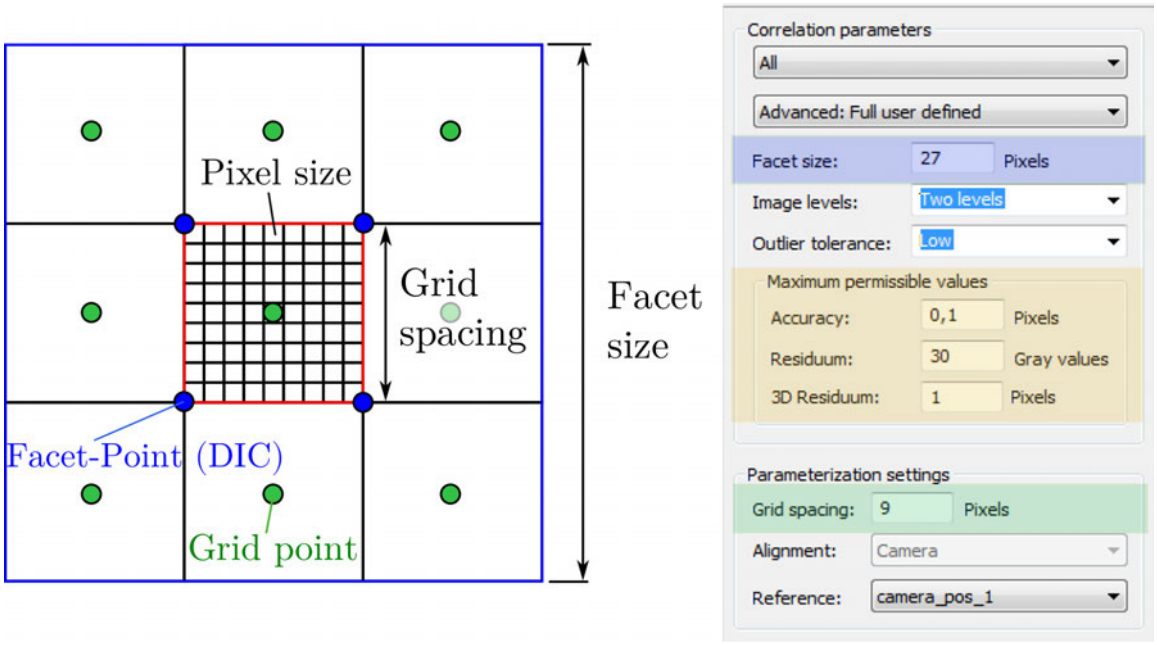

Figure 3.19: Overview of a facet which is a subset of the speckle pattern. The facet consists of 9 grid cells with one grid point (green) in the middle and 4 intersecting facet points (blue) characteristic for the DIC-deformation. Further parameters: Accuracy, residuum, 3D-residuum (yellow) inspired by Wood [26].

Focussing on the correlation algorithm of DIC, the calculation method for the displacement field is introduced according to Bing et al. [3]. In Fig. 3.20, one grid cell of a facet is shown for simplicity. The undeformed grid cell contains the grid point P(x,y) in the center and another point Q$(x + \Delta x, y + \Delta y)$ is decentralized. Actually, Q can be seen as the generalization of the facet points (see Fig. 3.19). The deformed grid cell shows the grid point P', which has been shifted by the translational stretching parameters κ (horizontal) and ψ (vertical). The facet point Q'(x',y') is shifted with the same values and due to the decentralized effect, the shear deformation has to be considered, additionally. Thus, the governing equations are presented in vector form:

$$\begin{pmatrix} x' \\ y' \end{pmatrix} = \begin{pmatrix} x \\ y \end{pmatrix} + \begin{pmatrix} \kappa \\ \psi \end{pmatrix} + \begin{pmatrix} \frac{\partial \kappa}{\partial x} & \frac{\partial \kappa}{\partial y} \\ \frac{\partial \psi}{\partial x} & \frac{\partial \psi}{\partial y} \end{pmatrix} \begin{pmatrix} \Delta x \\ \Delta y \end{pmatrix} \tag{3.28}$$

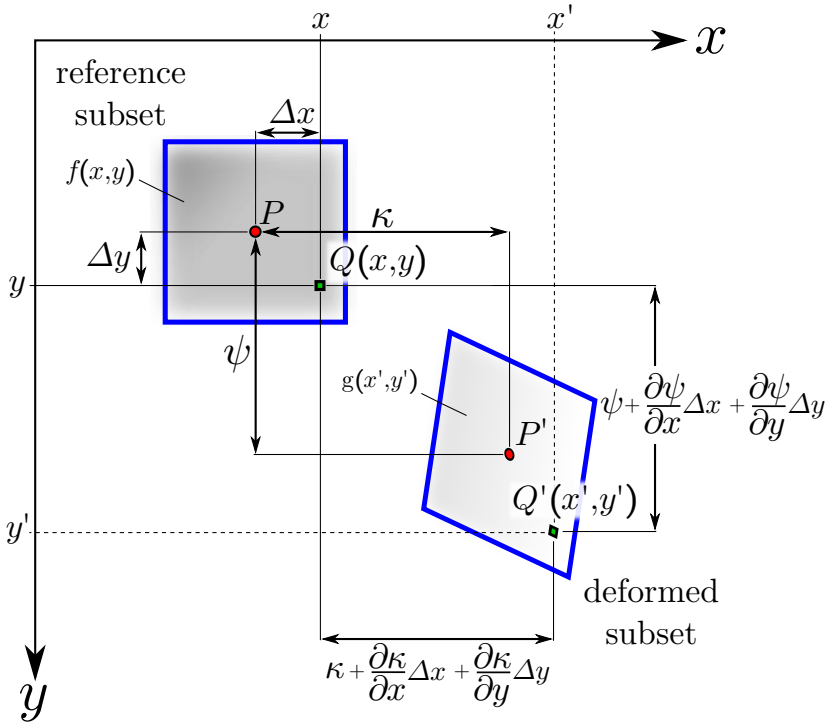

Figure 3.20: DIC registration of a subset from the reference to the deformed image according to the sub-pixel algorithm (Wood [25]).

For the purpose of a successful correlation, the minimum of the sum of the squared differences of the deformed and undeformed grid cells with the size of $(2M+1)\times(2M+1)$ pixels is searched:

$$\min\left(C(\underline{P})\right) = \min\left(\sum_{x=-M}^{M}\sum_{y=-M}^{M}\left[f(x,y)-g(x',y')\right]^2\right) \quad . \tag{3.29}$$

$f(x,y)$ and $g(x',y')$ represent the discrete grey value fields of the undeformed and deformed images, respectively, which have been interpolated by the *bicubic splines*. Hence, $(C(\underline{P}))$ is a multidimensional, bicubic function, containing the unknown vector:

$$\underline{P} = \left(\kappa,\ \frac{\partial\kappa}{\partial x},\ \frac{\partial\kappa}{\partial y},\ \psi,\ \frac{\partial\psi}{\partial x},\ \frac{\partial\psi}{\partial y}\right)^T \quad . \tag{3.30}$$

The correlation function of Eq. (3.29) can be solved iteratively by the Newton-Raphson method, while an iteration guess is executed at the start, using the provisional vector $\underline{P}^*$ and the following equation of iteration:

$$\underline{P} = \underline{P}^* - \underline{\underline{H}}^{-1}\,\nabla C(\underline{P}^*)\ , \tag{3.31a}$$

$$\underline{P} = \underline{P}^* - \left(\nabla\nabla C(\underline{P}^*)\right)^{-1}\,\nabla C(\underline{P}^*)\ . \tag{3.31b}$$

The subtrahend stands for the correction term of $\underline{P}^*$. The vector $\nabla C(\underline{P}^*)$ is the gradient of the correlation function, while the matrix $\underline{\underline{H}} = \nabla\nabla C(\underline{P}^*)$ stands for the second-order derivative of the correlation function or *Hessian matrix* [4]. By using Eq. (3.31) in the further iteration process, $\underline{P}^*$ relates always to the result $\underline{P}$ of the former iteration step. After the correlation is converged and all displacement paramaters are determined for the grid cells and facets, the displacement field is assembled to the whole correlation area corresponding to the defined polygon mask in Istra4D. To conclude, the Newton Raphson method provides high accuracy considering the sub-pixel displacement registration at a moderate computational efficiency.

3.3 Idea of synchronizing the DIC- and PIV-techniques

Until now, the DIC and PIV techniques have been used separately for the structural deformation and fluid velocity measurement. To describe the FSI precisely, a synchronization of these techniques is necessary. This is a challenge considering the synchronous control of PIV and DIC, with the adequate interfaces, cable connections and the right illumination source for both. During this master thesis, a concept has been developed to make a synchronization of PIV and DIC possible.

Focussing on the hardware combination, the basic idea is depicted in Fig. 3.21, while Fig. 3.21(a) visualizes the information or signal flow path and Fig. 3.21(b) visualizes the cable connections. The PIV-setup is framed by a pink rectangular frame, while the DIC-setup is framed by a blue one, respectively. The PIV-setup remains unchanged compared to the unsynchronized setup. The DIC-system is slightly changed. The illumination source is now the PIV-laser instead of the former headlight. Furthermore, the DIC-trigger button is replaced by a connection between the PIV- and DIC-setups. This is realized by an "I/O-link" cable which is commonly called *single-drop digital communication interface for small sensors and actuators* (SDCI) according to the norm ISO 61131-9. Thus, the "I/O-link"-master, which is the mono PIV-camera Phantom VEO HS-Camera here, triggers the "I/O-link"-device, which are the stereoscopic DIC-cameras HSVision Speedcam connected by the trigg4 and BNC-adapter. The trigger signal works as an electronic switching mode with the signal "0" (Off, 0 V) and "1" (On, 24 V). When the PIV-camera is triggered by the synchronizer, the same trigger signal is immediately sent to the DIC-cameras. This guarantees a synchronous recording mechanism of the cameras of both systems.

For the purpose of synchronized image data, some internal parameters have to be respected. The laser pulse repetition rate with $f_{PR} = 500\,\text{pps}$ (pulses per second) has to be adjusted to the camera frame rates of the PIV and DIC with $f_{DIC} = f_{PIV} = 500\,\text{fps}$

(frames per second). This ensures a constantly high illumination intensity in the captured images of PIV and DIC. By choosing the same recording time, every result of the image sequence of PIV can be compared chronologically to the result of the image series of DIC, due to the fact, that the same number of images are generated.

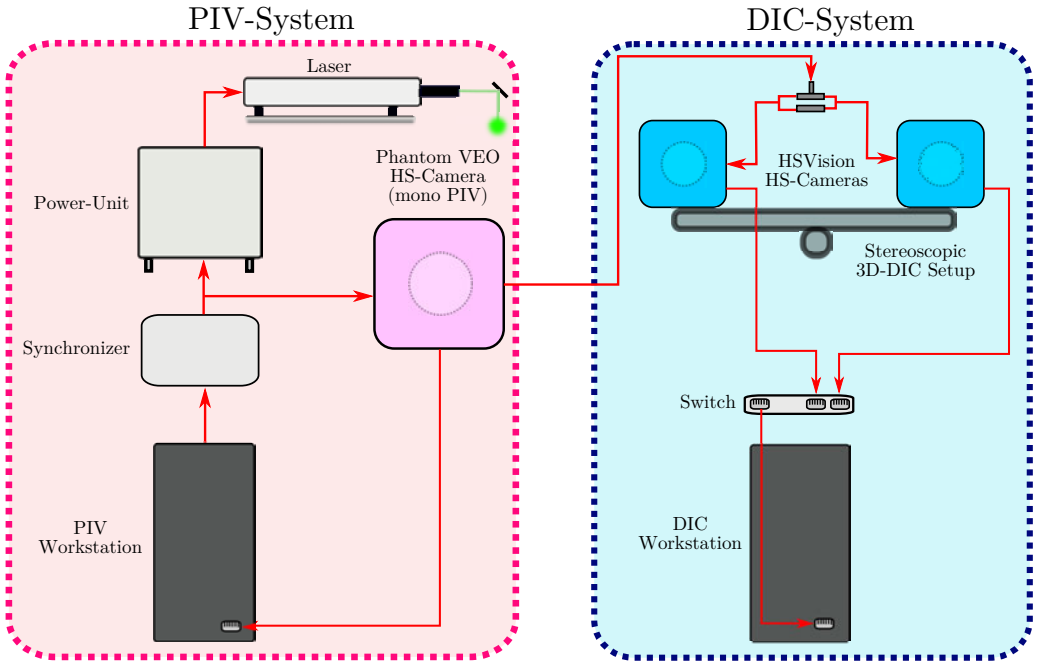

(a) Visualization by the information flow path.

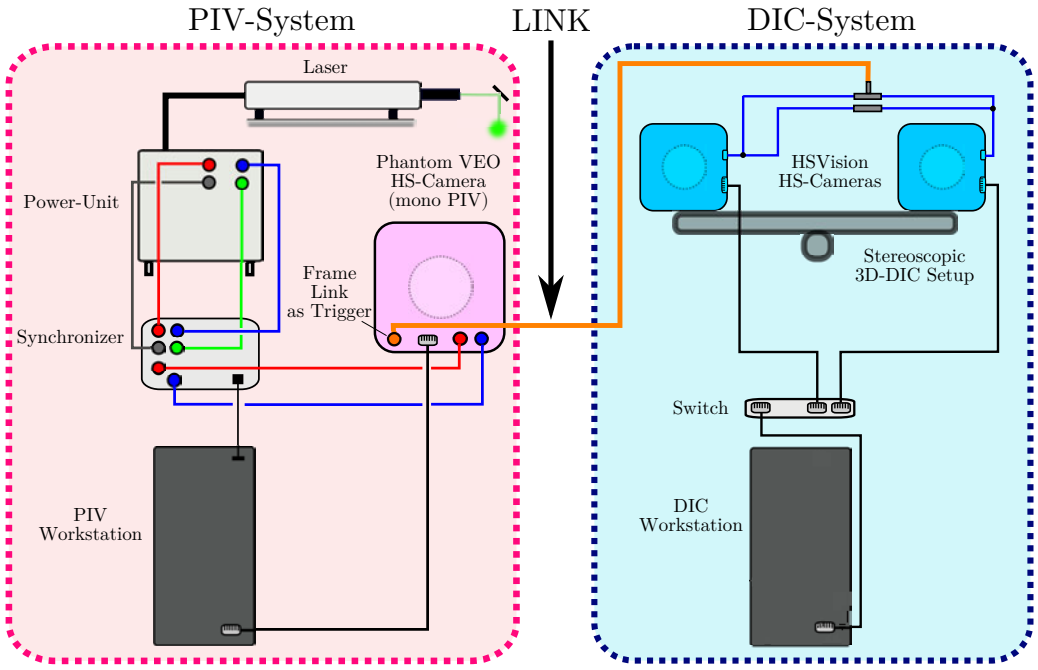

(b) Visualization by the cable connections.

Figure 3.21: Idea of synchronizing the DIC- and PIV-system.

A further challenge is the adequate illumination by the PIV laser, due to the fact that the DIC technique requires a wider field of illumination of the speckle pattern with moderate light intensity and the PIV requires a rather thin and concentrated light sheet for the 2D test section. Thus, the effective usability of a concentrated light sheet for PIV and an evenly illuminated speckle pattern for DIC is desirable. According to these ambiguous criteria, Fig. 3.22 presents the comparison between the unsynchronized illumination with a standard light source (headlight) and the synchronized illumination. For this purpose, the standard light sheet optics (LSO) from *iLA 5150 GmbH*[8] is mounted on the PIV-laser. It is a conventional LSO with the aperture of 50×10^{-3} m consisting of an extendable unit. This enables the adjustment of the thickness of the light sheet with at least 5×10^{-4} m, while a wider light sheet is adjusted here with 12×10^{-3} m. The divergence angle of the light sheet can be set up to 50°. The unsynchronized illumination under standard light conditions is depicted in Fig. 3.22a. It is shown that this source of light leads to a moderate light intensity, which is evenly distributed across the whole speckle pattern.

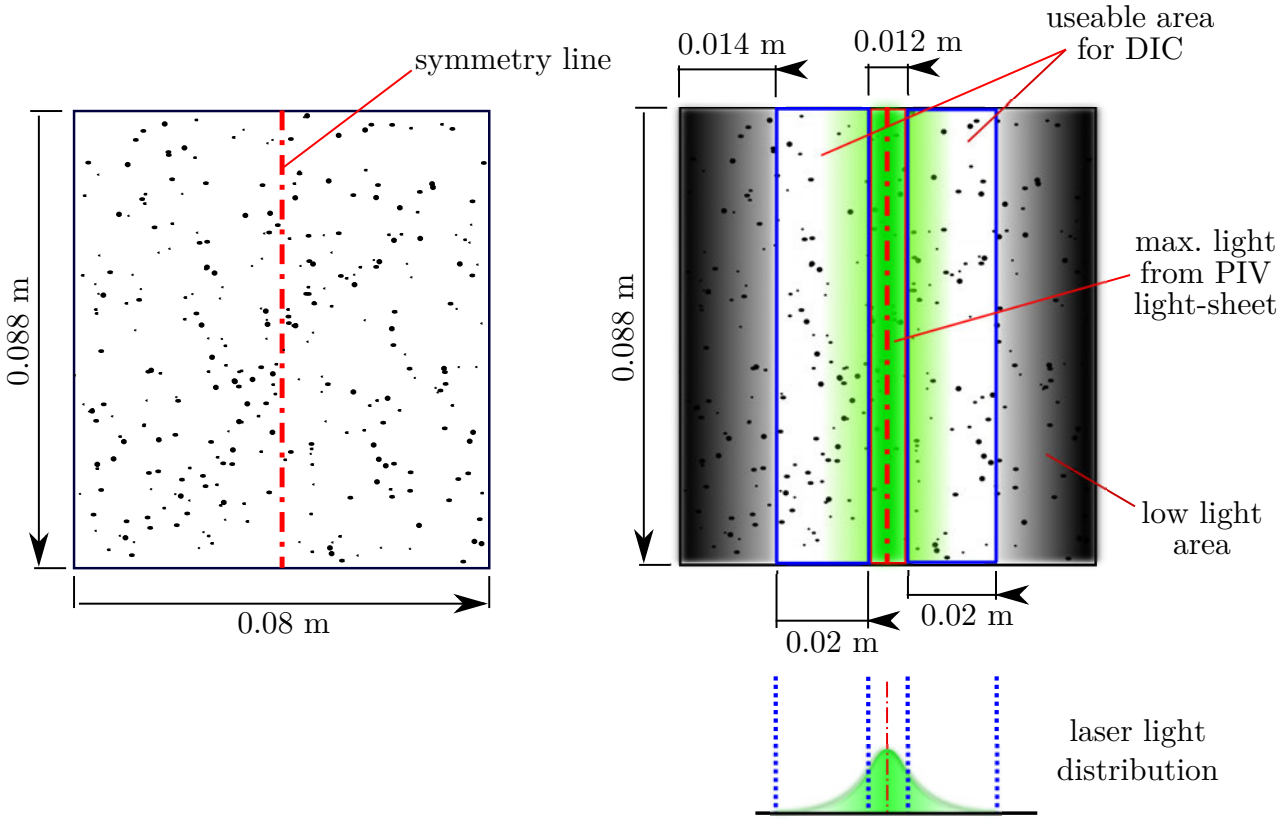

(a) Illumination by a standard light source.

(b) Illumination by PIV-laser-light.

Figure 3.22: Comparison of the useable area of the speckle pattern illuminated by different sources of light.

[8] https://www.ila5150.de/en/components/optical-component/standard-lso

This becomes visible by the useable, nearly quadratic, white area $A_{\text{ref}}^{\text{DIC}} = 0.08\,\text{m} \cdot 0.088\,\text{m} = 7.04 \times 10^{-3}\,\text{m}^2$. In contrast, the illumination of the useable speckle pattern by the laser with the mounted LSO is shown in Fig. 3.22b. Here, the intensity of the laser light is symmetrically distributed across the area of the speckle pattern, whereas the light distribution follows a Gaussian bell: The laser sheet is located at the symmetry line of the speckle pattern (= symmetry-line of the wing) representing the maximum light intensity with a thickness of $12 \times 10^{-3}\,\text{m}$. This area is overexposed by light and therefore not usable for the DIC-processing. In the adjacent regions, there are two areas of 0.02 m thickness each that are illuminated by the decreasing laser light intensity, which is sufficiently bright in order to illuminate the speckle pattern. These areas are considered for the correlation in the DIC-processing. It has been determined by means of the DIC-software that the totally useable area is $A_{\text{Laser}}^{\text{DIC}} \approx 2 \cdot 0.02\,\text{m} \cdot 0.88\,\text{m} = 3.52 \times 10^{-3}\,\text{m}^2 = A_{\text{ref}}^{\text{DIC}}/2$. Thus, the useable area of the speckle pattern illuminated by the laser is half compared to the illumination by the standard light. However, in the present quasi 2-D setup the laser illumination delivers satisfactory correlation results within the limited speckle pattern area, so that displacement measurements of profile line elements or of monitoring points can be extracted successfully. In the case of a 3-D setup, a limited speckle pattern area would be problematic for the measurements, since a symmetric displacement behavior like in the current case of the airfoil (representing the whole wing span) is not coercively given. Thus, information about important areas, which can not be sufficiently illuminated, might get lost. Hence, a future challenge can be the investigation of optics that solve this limitation in the illumination by the PIV-laser.

3.4 Statistical measuring quantities

The DIC and PIV measurement softwares allow the calculation of several statistical measuring quantities, whose background is briefly introduced here.

3.4.1 Structural deformation measurement quantities by DIC

For the structural deformation measurements, the DIC processing software can compute measurement uncertainties on the basis of a Gaussian normal distribution. Figure 3.23 depicts the density function $f(z)$ of the Gaussian normal distribution with the estimated expectation value $\mu \approx \overline{z}$ and the standard deviation $\sigma \approx s$. The estimation is due to the fact that the real values are unknown. By the estimation of the standard deviation range below and above the expectation value, a relative amount of 68.3 % of all measurement data are represented (orange area). According to Papula [17],

the density function can be mathematically described by:

$$f(z) = \frac{1}{\sqrt{2\pi}\,\sigma}\,\mathrm{e}^{-\frac{1}{2}\left(\frac{z-\mu}{\sigma}\right)^2}\ , \tag{3.32}$$

while the estimated expectation value $\mu \approx \overline{z}$ (arithmetic mean value) and the standard deviation $\sigma \approx \overline{\Delta\tilde{z}} = s$ (mean variation) yield:

$$\mu \approx \overline{z} = \frac{1}{n}\sum_{i=1}^{n} z_i\ , \tag{3.33}$$

$$\sigma \approx \overline{\Delta\tilde{z}} = s = \sqrt{\frac{1}{n-1}\sum_{i=1}^{n}(z_i - \overline{z})^2}\ . \tag{3.34}$$

The standard deviation s in Eq. (3.34) is the measurement uncertainty calculated by the DIC-software for the purpose of presenting reliable and accurate results. Thus, every measured displacement point in z is measured n-times, while the coefficient in the formula is normalized by $1/(n-1)$, which is due to the unbiased estimation of the standard deviation. It says that the expectation value of the squared standard deviation is equal to the variance $E(\overline{\Delta\tilde{z}}^2 = s^2) = \sigma^2$ [17].

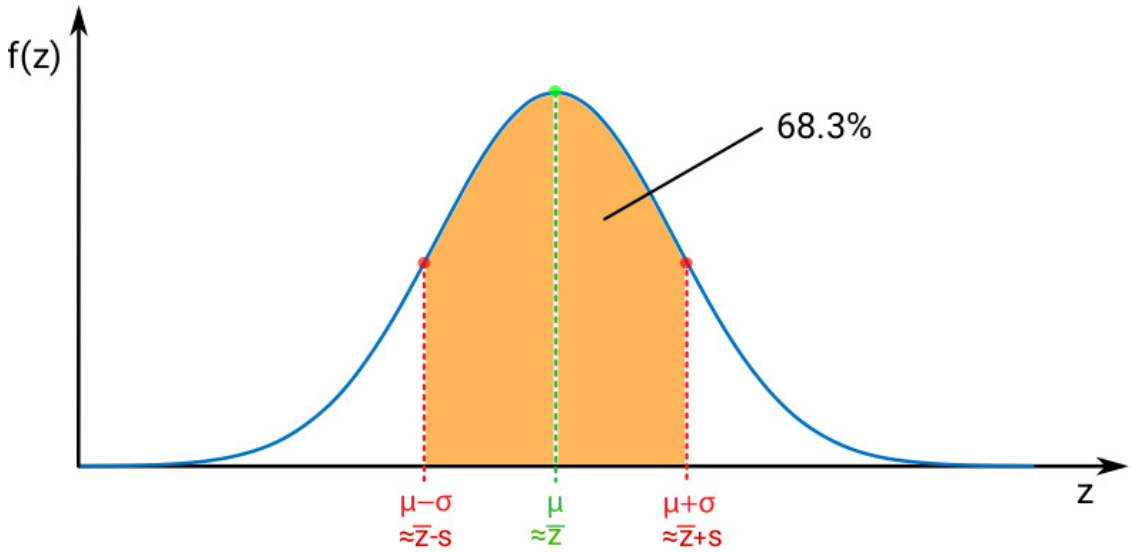

Figure 3.23: Density function $f(z)$ of the Gaussian normal distribution with the estimated expectation value $\mu \approx \overline{z}$ and the standard deviation $\sigma \approx s$ while an amount of 68.3 % of all measurement data are represented (orange area).

3.4.2 Fluid mechanical measurement quantities by PIV

For the fluid mechanical measurements, the PIV processing software can generate velocity distributions. For a 2D-plane the velocity field of the horizontal component $u(\vec{x},t)$ as well as the vertical components $w(\vec{x},t)$ can be presented as a vector function depending on space $\vec{x}=[x,y]$ and time t. Furthermore, the software is able to calculate statistical quantities on the basis of the Reynolds averaging approach. For this purpose, the velocity fields are separated into time-averaged mean values and fluctuations (Reynolds separation):

$$u(\vec{x},t) = \overline{u}(\vec{x}) + u'(\vec{x},t) \ , \tag{3.35a}$$

$$\overline{u}(\vec{x}) = \lim_{T\to\infty} \frac{1}{T} \int_0^T u(\vec{x},t)\,\mathrm{d}t \ , \tag{3.35b}$$

and

$$w(\vec{x},t) = \overline{w}(\vec{x}) + w'(\vec{x},t) \ , \tag{3.36a}$$

$$\overline{w}(\vec{x}) = \lim_{T\to\infty} \frac{1}{T} \int_0^T w(\vec{x},t)\,\mathrm{d}t \ , \tag{3.36b}$$

respectively. $\overline{u}(\vec{x})$ and $\overline{w}(\vec{x})$ are the temporally averaged mean values, while $u'(\vec{x},t)$ and $w'(\vec{x},t)$ are the fluctuations. This is depicted schematically in Fig. 3.24. The corresponding discrete formulation of Reynolds separation can be formulated by:

$$u_k = \overline{u} + u'_k \ , \tag{3.37}$$

and

$$w_k = \overline{w} + w'_k \ , \tag{3.38}$$

respectively. $\overline{u}$ and $\overline{w}$ are the temporally averaged mean values, while u'_k and w'_k are the fluctuations at a discrete local position k within the image frame of the PIV control window. The mean fluid velocity value is the *arithmetic mean value* related to the measured velocities at all discrete locals $k = 1...n$:

$$\overline{u} = \frac{1}{n} \cdot \sum_{k=1}^{n} u_k \ , \tag{3.39}$$

$$\overline{w} = \frac{1}{n} \cdot \sum_{k=1}^{n} w_k \ . \tag{3.40}$$

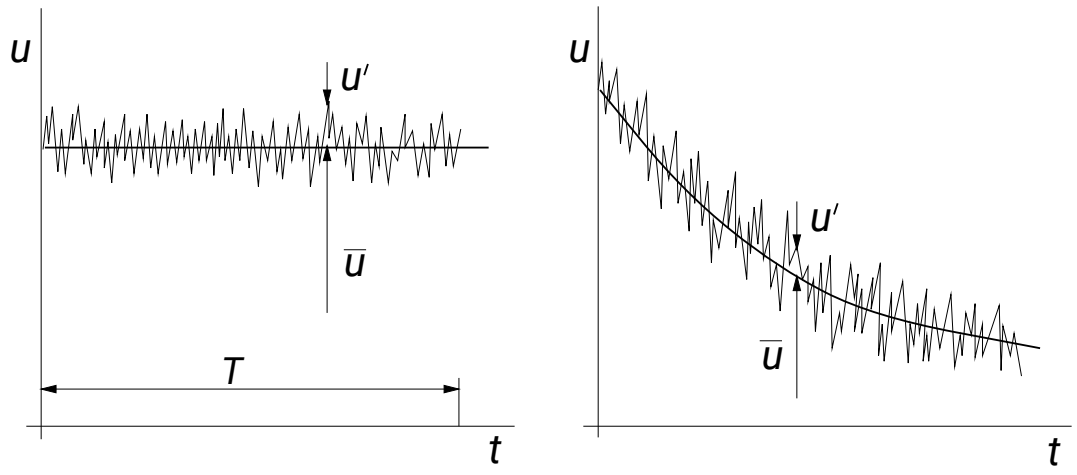

Figure 3.24: The time averaging of a statistically steady fluid flow (left) and the ensemble averaging of a statistically unsteady fluid flow (right) from Ferziger and Peric [8].

According to Ferziger and Peric [8], these Reynolds separated values can be inserted into the conservation equation of mass and momentum for incompressible fluid flows without body forces. After time averaging the corresponding equations read with Cartesian coordinates and in index notation ($i = 1...3,\ j = 1...3$):

$$\frac{\partial(\rho\,\overline{u}_i)}{\partial x_i} = 0\ , \tag{3.41a}$$

$$\frac{\partial(\rho\,\overline{u}_i)}{\partial t} + \frac{\partial}{\partial x_j}\left(\rho\,\overline{u}_i\overline{u}_j + \rho\,\overline{u_i'u_j'}\right) = -\frac{\partial\overline{p}}{\partial x_i} + \frac{\partial\overline{\tau}_{ij}}{\partial x_i}\ , \tag{3.41b}$$

while $\overline{p}$ is the mean pressure and $\overline{\tau}_{ij}$ the viscous stress tensor. Here, the Reynolds stress tensor $\rho\,\overline{u_i'u_j'}$ shall be pointed out, which contains second-order moments of the velocity data [25]. It describes the effect of the fluctuations occuring in the flow field associated with turbulence on the mean flow. The 2D-tensor with the velocity components $u_1 = u$ (horizontal) and $u_2 = w$ (vertical) follows with:

$$\rho\,\overline{u_i'u_j'} = \rho\begin{pmatrix} \overline{u_1'u_1'} & \overline{u_1'u_2'} \\ \overline{u_2'u_1'} & \overline{u_2'u_2'} \end{pmatrix} = \rho\begin{pmatrix} \overline{u'u'} & \overline{u'w'} \\ \overline{w'u'} & \overline{w'w'} \end{pmatrix} \quad . \tag{3.42}$$

The main diagonal elements of the tensor can be seen as the quadratic standard deviations of u and w, respectively. The normal Reynolds stress component in streamwise direction is given by:

$$\overline{u'u'} = \frac{1}{n-1}\cdot\sum_{k=1}^{n}(u_k - \overline{u})^2\ , \tag{3.43}$$

and the normal Reynolds stress component in vertical direction reads:

$$\overline{w'w'} = \frac{1}{n-1} \cdot \sum_{k=1}^{n} (w_k - \overline{w})^2 \ . \tag{3.44}$$

The shear stress component follows with:

$$\overline{u'w'} = \overline{w'u'} = \frac{1}{n-1} \cdot \sum_{k=1}^{n} (u_k - \overline{u})(w_k - \overline{w}) \ , \tag{3.45}$$

while it reveals the dependency of the fluctuations between the different velocity components. Finally, the intensity of turbulence can be computed within a flow field out of the main diagonal elements of the Reynolds stress tensor. For a 2-D flow field it reads:

$$\mathrm{Tu} = \frac{1}{U_\infty} \cdot \sqrt{\frac{1}{2} \left(\sigma_u^2 + \sigma_w^2\right)} \tag{3.46}$$

$$= \frac{1}{U_\infty} \cdot \sqrt{\frac{1}{2} \left(\overline{u'u'} + \overline{w'w'}\right)} \ . \tag{3.47}$$

To conclude, the PIV-data allow to determine the following parameters:

- The time-averaged velocity fields $\overline{u}/U_\infty$, $\overline{w}/U_\infty$,
- the Reynolds stress components $\overline{u'u'}/U_\infty^2$, $\overline{w'w'}/U_\infty^2$, $\overline{u'w'}/U_\infty^2$,
- the intensity of turbulence Tu.

It has to be considered that the measurement results in this thesis are normalized by the free-stream velocity U_∞ and U_∞^2, respectively.

Chapter 4

Measurement planning and conditions

In this chapter, the measurement planning and the conditions for the measuring procedures are presented. Therefore, all parameters are mentioned, which are necessary for the adjustment of the measuring techniques, such as the parameters of the laser-timing (PIV), the cameras, the calibration and the software processing parameters. Finally, the agenda of the measurements is summarized with the relevant measuring quantities giving an overview of the discussed results in Section 5.

4.1 Measurement conditions for DIC

In the following, the conditions for the DIC-measurements are presented.

4.1.1 Camera and calibration parameters

Beginning with the two identical DIC-cameras of type *HSVision Speedcam MarcoVis Eo Sens*, Tab. 4.1 contains the main properties.

Table 4.1: Main properties of the DIC-cameras of type *HSVision Speedcam MarcoVis Eo Sens*.

Property	**Unit**	**Value/Name**
Resolution	[px]	1472 x 1036
Frame rate	[fps]	500 (synchronized), 250 (unsynchronized)
Objective lense	[-]	Schneider-Kreuznach Xenoplan 2.0/28-0901
Adjusted f-number (lense)	[-]	6.2 (min. 2.8)
Adjusted aperture (lense)	[mm]	4.5

For the purpose of synchronization with the PIV-laser, the frame rate of 500 fps is adjusted for all DIC-measurements, whereas a maximum frame rate of 1000 fps would be possible. The f-number of the Schneider-Kreuznach objective lenses, which is the aperture ratio standing for the light intensity in the image plane, is set to 6.2 and the aperture (diameter) results in 4.5 mm.
Focusing on the calibration data of the two DIC-cameras related to Section 3.2.2.4, the extrinsic and the stereoscopic parameters are summarized in Tab. 4.2, while the intrinsic parameters are listed in Tab. 4.3. For the extrinsic parameters, the translation and rotation data are related to the first acquired image of the calibration target. The components of rotation R_x, R_y, R_z are the eigenvalues of the rotation matrix $\underline{\underline{R}}^{3\times3}$ representing the rotation angles of each axis of the COS. It may be mentioned here that the numbers behind the "±" are the uncertainties of the determined parameters. According to the characteristics of the stereoscopic setting, the intersection angle of the projection lines is found at $\Phi = 42.8°$ and the baseline vector, which is the absolute distance of the focal points, is set to 466.2 mm.

Table 4.2: Extrinsic parameters of the cameras "EF" and "A3" as well as the stereoscopic parameters of the camera system.

Position	Parameter	Unit	Description	Value
Camera "EF"	R_x	[rad]	rotation of x_w-axis with yaw angle θ	2.7054 ± 0.0009
	R_y	[rad]	rotation of y_w-axis with pitch angle α	-0.4630 ± 0.0004
	R_z	[rad]	rotation of z_w-axis with tilt angle ψ	-0.3950 ± 0.0016
	t_x	[mm]	translation in x_w-direction	-33.8 ± 0.7
	t_y	[mm]	translation in y_w-direction	-1.6 ± 0.5
	t_z	[mm]	translation in z_w-direction	606.81 ± 0.19
Camera "A3"	R_x	[rad]	rotation of x_w-axis with yaw angle θ	2.7727 ± 0.0006
	R_y	[rad]	rotation of y_w-axis with pitch angle α	-0.6642 ± 0.0005
	R_z	[rad]	rotation of z_w-axis with tilt angle ψ	0.6418 ± 0.0015
	t_x	[mm]	translation in x_w-direction	13.4 ± 0.6
	t_y	[mm]	translation in y_w-direction	-0.3 ± 0.4
	t_z	[mm]	translation in z_w-direction	542.22 ± 0.16
Stereoscopic EF/A3	Φ	[°]	Intersection angle of the projection lines	42.7988
	Baseline vector	[mm]	Absolute distance of the focal points	466.2342

4.1.2 Processing parameters

The processing parameters of the "Evaluation settings" within the DIC-software Istra4D are listed in Tab. 4.4 (related to Fig. 3.19 in Section 3.2.4.2). The measured object surface is subdivided into subsets with the "facet size" (edge length) of 27 pixels, while

Table 4.3: Intrinsic parameters of the camera system.

Position	Parameter	Unit	Description	Value
Camera "EF"	f	[mm]	effective focal length	3848.95 ± 1.2
	C_x	[px]	$x_i = x_0$ position of the principle point H′	763 ± 5
	C_y	[px]	$y_i = y_0$ position of the principle point H′	540 ± 3
	s	[-]	horizontal scale factor	0.00171 ± 0.00017
	κ_1	[1/mm^2]	radial lense distortion coefficient	-0.054 ± 0.004
	κ_2	[1/mm^2]	radial lense distortion coefficient	-0.9 ± 0.11
Camera "A3"	f	[mm]	effective focal length	3856.7 ± 1.1
	C_x	[px]	$x_i = x_0$ position of the principle point H′	762 ± 4
	C_y	[px]	$y_i = y_0$ position of the principle point H′	557 ± 3
	s	[-]	horizontal scale factor	0.00228 ± 0.00014
	κ_1	[1/mm^2]	radial lense distortion coefficient	-0.033 ± 0.005
	κ_2	[1/mm^2]	radial lense distortion coefficient	-0.9 ± 0.3

the further sub-classified grid cell has a "grid spacing" (edge length) of 9 pixels. The "correlation accuracy" of the sub-pixel intensity interpolation is set to 0.1 pixels, while the "Residuum" of the correlation algorithm is chosen with the maximum acceptable number of 30 grey values. The "3D Residuum", which is the deviation of the correlated pixel positions and the back projected object points, is set to 1 pixel.

Table 4.4: Correlation parameters of DIC implemented in *Istra4D*.

Parameter	Unit	Value
Facet Size	[Pixels]	27×27
Grid spacing	[Pixels]	9×9
Accuracy	[Pixel]	0.1
Residuum	[Grey values]	30
3D Residuum	[Pixel]	1

4.2 Measurement conditions for PIV

In the following, the conditions for the PIV-measurements are presented.

4.2.1 Laser and camera adjustment

The properties of the PIV-camera are listed in Tab. 4.5. For the purpose of synchronization with the PIV-laser, the frame rate of 500 fps is adjusted for all PIV-measurements, whereas a maximum frame rate of 1400 fps would be possible. The f-number of the

"Nikon AF Nikkor" objective lenses is set to 2.8 and the aperture results in 18 mm.

Table 4.5: Properties of the HS-PIV-camera of type *Phantom VEO 640S*.

Property	Unit	Value/Name
Resolution	[Px]	2560 x 1600
Frame rate	[fps]	500 (max. 1400)
Objective lense	[-]	Nikon AF Nikkor 50 mm 1:1.8D
Adjusted f-number (lense)	[-]	2.8 (min. 1.8)
Adjusted aperture (lense)	[mm]	18

According to Fig. 3.6 in Section 3.1.2.1, the timing parameters of the PIV-laser and the PIV-camera are listed in Tab. 4.6. The laser delay time Δt_{LD}, which is not registered here, is internally calculated by the software with choosing the command *Auto Center Laser Pulses*. Additionally, it is important to mention that the pulse straddling-time with $\Delta t_{PIV} = 0.1 \times 10^{-3}$ is larger than the inter-frame straddling-time with $\Delta t_{FS} = 1.73 \times 10^{-6}$ guaranteeing the acquisition of double-images that are sufficiently illuminated by the double-pulsed laser.

Table 4.6: Timing-parameter for the adjustment of the PIV-laser and the PIV-camera.

Device	Timing-parameter	Unit	Description	Value
PIV-laser Litron LD-527	f_{PR}	[pps]	Pulse rate per second	500
	Δt_{PR}	[s]	Pulse repetition time	2×10^{-3}
	Δt_{PIV}	[s]	Pulse straddling-time	0.1×10^{-3}
PIV-camera Phantom VEO 640S	f_{cam}	[fps]	Frame rate per second	500
	Δt_{cam}	[s]	Image acquisition time	1.998×10^{-3}
	Δt_{FS}	[s]	Inter-frame straddling-time	1.73×10^{-6}

4.2.2 Processing parameters

The PIV-processing requires certain parameters for the calibration and the grid size of the observed processing region. According to Sections 3.1.3.1 and 3.1.3.2, the important parameters implemented in the software *Insight 4G* are listed in Tab. 4.7. The 2D spatial calibration factor is calculated as $C_{spat} = 126.03\,\mu$m/px. The observed processing region has the digital dimensions of (W × H) = (2224 px × 1249 px) and the corresponding geometric dimensions of (W × H) = (280 mm × 157 mm). The grid subdivides the processing region in squared interrogation windows (IW). The meshing begins with the so-called starting spots forming a coarse grid for the first processing step. The starting spot sizes of the double images A1 and A2 are set to 48 px (edge length). The result is

a coarse vector field at first. Then, these processed data are optimized by a "recursive ensemble processing", which is able to reduce the IW-size to

- 16 px $\equiv$ 2.016 mm (edge length), leading to a grid of (139 $\times$ 78) IW for higher-resolved vector fields, suitable for unsteady phenomena like the vortex formation and convection, see Fig. 5.20 in Section 5.3.1, or the velocity signal spectra measured in Section 5.3.3,

- 32 px $\equiv$ 4.032 mm (edge length), leading to grid of (69 $\times$ 39) IW for a global vector field in the processing region (standard software adjustment) used for the synchronized PIV-DIC-measurements in Section 5.4.

In the software *Insight 4G*, the correlation algorithm settings are implemented by plugin engines, which are listed in Tab. 4.8. The "Nyquist Grid" is the standard PIV-grid while the deformation vectors are positioned in the center of each IW. Furthermore, the Nyquist sampling criterion shall be fulfilled: The matching IWs within one double image, which are shifted in time by the time lag Δt_{PIV}, are still overlapping by 50% of their size (for the schematic overlapping of the IWs, see Fig. 3.8 in Section 3.1.3.2). However, according to the cross-correlation function of Eq. (3.6) in Section 3.1.3.2, the "Zero Pad Mask" is a filter that minimizes the image noise by subtracting the averaged grey value intensity of the processed image from each IW. The "FFT Correlation" is the *Fast Fourier Transform* method for solving the cross-correlation function. The "Bilinear Peak" is a sub-pixel algorithm that locates the correlation peak within the correlation map by fitting linear spline functions in between the highest pixel and the nearest neighboring pixels. To sum up, these plugin engines are necessary for the PIV processing algorithms.

4.3 Measurement planning for case I and III

In this part, the planning of the measurements is briefly summarized and structured. The specifications "case I" and "case III" of the added extra mass to the wing system are mentioned and visualized in Section 2.1.3 (see Fig. 2.8).
Beginning with the free-stream adjustment in the wind tunnel, there is a linear relation between the rotation speed n_{air} of the air blower and the free-stream velocity U_∞ and the Reynolds number, respectively. This has been discussed in Section 2.2 with the diagram in Fig. 2.11 and the Eq. (2.5) of the regression curve. According to that, the adjustments of the rotation speed and the corresponding free-stream velocities are listed in Tab. 4.9.

Table 4.7: Processing parameters implemented in the software *Insight 4G*.

Classification	**Parameter**	**Unit**	**Description**	**Value**
2D spatial calibration	C_{spat}	[μm/px]	Calibration factor	126.03
Processing region	W	[px]	Width (digital dimension)	2224
	W	[mm]	Width (geometric dimension)	280
	H	[px]	Height (digital dimension)	1249
	H	[mm]	Height (geometric dimension)	157
Processor setup: Square starting spots	Spot A1	[px]	Edge length (digital dimension)	48
	Spot A1	[mm]	Edge length (geometric dimension)	6.049
	Spot A2	[px]	Edge length (digital dimension)	48
	Spot A2	[mm]	Edge length (geometric dimension)	6.049
Final square size of interrogation windows (IW) (higher-resolved regions for unsteady phenomena)	IW A1	[px]	Edge length (digital dimension)	16
	IW A1	[mm]	Edge length (geometric dimension)	2.016
	IW A2	[px]	Edge length (digital dimension)	16
	IW A2	[mm]	Edge length (geometric dimension)	2.016
	IW-Array	[IW × IW]	Processing region subdivided in IWs	139 × 78
Final square size of interrogation windows (IW) (standard adjustment for PIV)	IW A1	[px]	Edge length (digital dimension)	32
	IW A1	[mm]	Edge length (geometric dimension)	4.032
	IW A2	[px]	Edge length (digital dimension)	32
	IW A2	[mm]	Edge length (geometric dimension)	4.032
	IW-Array	[IW × IW]	Processing region subdivided in IWs	69 × 39

Table 4.8: PIV-correlation plugins implemented in the software *Insight 4G*.

Classification	**Parameter**	**Description**	**Name**
PIV-correlation plugins	Grid engine	Grid generation (IW-subdivision)	"Nyquist Grid"
	Spot mask engine	Mask/filter for noise minimization	"Zero Pad Mask"
	Correlation engine	Computation of the cross-correlation	"FFT Correlation"
	Peak engine	Curve fitting, finding correlation peak	"Bilinear Peak"

Table 4.9: Conversion table for the rotation speed n_{air} of the air blower, the free-stream velocity U_∞ and the Reynolds number Re in the wind tunnel based on the chord length of the profile.

$\mathbf{n}_{\text{air}}$ [rpm]	$\mathbf{U}_\infty$ [m/s]	**Re** [−]
116	1.44	9.66×10^3
166	2.46	1.65×10^4
221	3.56	2.39×10^4
270	4.56	3.06×10^4
310 (for CTA)	5.06	3.39×10^4
325 (flutter)	5.37	3.60×10^4

The transitional Reynolds regime of $9.66 \times 10^3 \leq \mathrm{Re} \leq 3.60 \times 10^4$ is subdivided into 5 steps with $n_{\mathrm{air}} = [116, 166, 221, 270, 325]\,\mathrm{rpm}$, while $n_{\mathrm{air}} = 310\,\mathrm{rpm}$ is the rotation speed for the CTA measurements of Wood et al. [23], which is mentioned later on.

According to the results in Section 5, the planning of the measurements is given by Tab. 4.10. The involved section is indicated as well as the measurement type (PIV/DIC), the Reynolds number Re and a brief description of the measurement content.
In Sections 5.1.1 and 5.1.2, the free-oscillation characteristics for the heave and pitch are separately investigated (1-DOF) by the DIC measurements to calculate the structure-mechanical properties of the wing system, i.e., the viscous damping coefficients or spring stiffnesses. These data are compared to the results of Wood et al. [23]. Additionally, the combined heave and pitch movements (2-DOF) are presented in comparison with [23]. In Sections 5.2.1 and 5.2.2 the DIC measurements (2-DOF) are carried out for the still air case as well as several free-stream velocities. The unsynchronized results (under standard light as the illumination source of the DIC-system) are compared to the synchronized results (under the PIV-laser as the illumination source of the DIC-system). Furthermore, the feasibility of the PIV-laser as illumination source for DIC is investigated. In Sections 5.3.1 to 5.3.3 the PIV measurements are carried out to analyze the wake flow behind the airfoil. The formation and convection of vortices is visualized for $\mathrm{Re} = 2.39 \times 10^4$, while for several other Re numbers, the vortex shedding frequencies and Strouhal numbers are calculated. Furthermore, pointwise signal spectra of the fluid velocities u and w are extracted from the PIV measurements in the format of time histories and FFT plots. This is done to point out the influence of the structural oscillations of the wing on the wake flow as well as to show the "independent frequencies" of the flow instability. In Section 5.4 the synchronized PIV-DIC measurements are done for a single period of the flutter motion of the wing system. Structural displacement data of the airfoil motion and the corresponding fluid velocity fields u/U_∞, w/U_∞ are superimposed. Finally, in Sections 5.5.1 and 5.5.2, the phase-averaged velocity fields are determined by PIV for the flutter test case. The fluid velocity fields $\overline{u}/U_\infty$, $\overline{w}/U_\infty$ and the Reynolds stress fields $\overline{u'u'}/U_\infty^2$, $\overline{w'w'}/U_\infty^2$, $\overline{u'w'}/U_\infty^2$ are discussed.

Table 4.10: Measurement planning with indication of the measurement type, the involved section, the rotation speed of the air blower n_{air} (for conversion see Tab. 4.9) and the summarized description of the measurement.

Section	**Technique**	**Re** $[\times 10^4]$	**Description**
5.1.1	DIC	still air	Free-oscillation characteristics with 1-DOF. Comparison to the results of Wood et al. [23] including time histories and FFT plots of the vertical displacements in z-direction. Structure-mechanical parameters of the elastically mounted wing system.
5.1.2	DIC	still air	Free-oscillation characteristics with 2-DOF. Comparison to the results of Wood et al. [23] including time histories and FFT plots of the vertical displacements in z-direction.
5.2.1	DIC	still air, 0.966, 1.65, 2.39, 3.06, 3.60	Eigenfrequency analysis of case I and III including time histories and FFT plots of the vertical displacements in z-direction. Comparison of unsynchronized with synchronized results.
5.2.2	DIC	still air, 3.60	Comparison of the DIC illumination sources for case I: Standard light (unsynchronized measurements) and laser light (synchronized measurements). Time histories of the vertical displacements in z-direction with measurement uncertainties.
5.3.1	PIV	2.39	Unsteady wake flow analysis of case I: Visualized vortex convection. Fluid flow velocity w/U_∞ in a sequence of time (single period time $T = 0.032$ s).
5.3.2	PIV	0.966, 1.65, 2.39, 3.06, 3.60	Unsteady wake flow analysis of case I and III: Calculated shedding frequencies and Strouhal numbers.
5.3.3	PIV	0.966, 1.65, 2.39, 3.06, 3.60	Fluid flow velocities u and w extracted from a monitoring point in the wake flow. Time histories and frequency spectra (FFT).
5.4	PIV/DIC	3.60	Synchronized measurements for case I and III: Single period wing motion and corresponding fluid flow velocities u/U_∞, w/U_∞ in a sequence of time (time period $T = 0.12$ s).
5.5.1	PIV	3.60	Phase-averaged velocity field for case I and III: Fluid flow velocities $\overline{u}/U_\infty$, $\overline{w}/U_\infty$ in a sequence of time (time period $T = 0.12$ s).
5.5.2	PIV	3.60	Phase-averaged velocity field for case I and III: Reynolds stresses $\overline{u'u'}/U_\infty^2$, $\overline{w'w'}/U_\infty^2$ and $\overline{u'w'}/U_\infty^2$ in a sequence of time (time period $T = 0.12$ s).

Chapter 5

Measurement results and evaluation

In this chapter, the results of the DIC- and PIV-measurements are presented. By the unsynchronized DIC-measurements, the structure-dynamic behavior of the wing-system is compared to the results of Wood et al. [23] dealing with the characteristic parameters of the system. Furthermore, the synchronized DIC-measurements are discussed in their compatibility with the unsynchronized measurements. Finally, the light sources of both methods are compared according to the measurement uncertainties and effective usage of the speckle pattern to evaluate the quality of the synchronization with the PIV-laser as the illumination source. By the synchronized PIV-measurements, the behavior of the fluid flow is investigated, corresponding to the airfoil motion. A comparison to the numerical results of De Nayer et al. [15] is presented. Moreover, unsteady wake flow phenomena are analyzed and finally, phase-averaged velocity fields are discussed.

5.1 Unsynchronized DIC-measurements

Beginning with the unsynchronized DIC-measurements, the results have to be verified according to the corresponding results of Wood et al. [23]. This is done due to the background that the wing system was slightly renewed in some elements. Firstly, the rotational springs were worn out after the investigation series of [23] and had to be renewed with springs of the identical type with the rotational spring stiffness of $k_\alpha = 0.3832\,\mathrm{Nm/rad}$ according to the data sheet of the manufacturer. Secondly, the total mass of the wing has slightly changed, since it was varnished in black for PIV-issues, which raised the total mass by 0.004 kg to $m_w = 0.33921\,\mathrm{kg}$. Apart from the constructional reasons, some measurement conditions have changed. For the comparison with the synchronized measurement, the speckle pattern was positioned symmetrically in the middle of the wingspan. Furthermore, the camera frame rate of the current DIC-measurements is set with 500 fps

(frames per second), while the frame rate of the measurements in [23] was 250 fps. It has been changed due to comparison with the synchronized measurements and the fact, that the previously published CTA-measurements have shown relevant frequencies in the fluid up to 230 Hz. According to the *Nyquist–Shannon sampling theorem*, exact measurement results are given if the sampling rate is at least twice as large as the maximum of the expected frequencies. The consequence of the higher frame rate is that the recording time is reduced. While the measurement time in [23] lasts until $t \approx 20\,\mathrm{s}$, the current recording time is limited to $t \approx 10\,\mathrm{s}$. This has also an influence on the computation of the frequency based FFT-plot, which is dependent on the amount of data in the time history of the oscillation. These are the reasons that may authorize a comparison of the current measurements to the previously published results.

5.1.1 Comparison of free-oscillation characteristics with 1-DOF in still air with previously published results

In the following, the properties of the renewed wing system is investigated according to characteristic parameters. Therefore, several values of stiffness and damping are calculated which physically refer to 1-DOF-oscillations of the analogous spring-damper-mass-system. The 1-DOF investigations are made possible either by stiffening the translational leaf springs or by blocking the rotational springs.
Figure 5.1 presents the separate 1-DOF-oscillations of heave and pitch for case I with the comparison to the results of Wood et al. [23]. The motion itself is induced by an impulse excitation. The monitoring point of the measured displacements is located at 0.7 m far from the leading edge of the airfoil, the background is explained later on for the synchronized measurements. Considering the heave motion, the time history in Fig. 5.1(a) shows exponentially decaying oscillations. The results from the current measurements and the previously published results are in good agreement, while the FFT-plot in Fig. 5.1(b) reveals that the corresponding eigenfrequencies are nearby with $f_\mathrm{h} = 7.398\,\mathrm{Hz}$ (current) and $f_\mathrm{h} = 7.263\,\mathrm{Hz}$ (Wood et al. [23]). The slight deviation can be deduced to the individual measurement condition by removing and installing the renewed wing system out of and into the support frame, respectively. Therefore, the prestressing forces of the bolted joints between the heave clamps and the support frame can vary. Regarding the pitch motion, the former heave oscillation behavior can be observed as well for pitch in the time history of Fig. 5.1(c). Furthermore, the eigenfrequencies are nearly identical with $f_\alpha = 8.378\,\mathrm{Hz}$ (current) and $f_\alpha = 8.333\,\mathrm{Hz}$ (Wood et al. [23]).

Moreover, the frequencies of the FFT give information about the properties of the dynamic wing system. The total damping ratios $D_h^{1-\mathrm{DOF,tot}}$ and $D_\alpha^{1-\mathrm{DOF,tot}}$ can be determined by the method of the *logarithmic decrement* related to the amplitude ratios of the oscillations in the time histories.

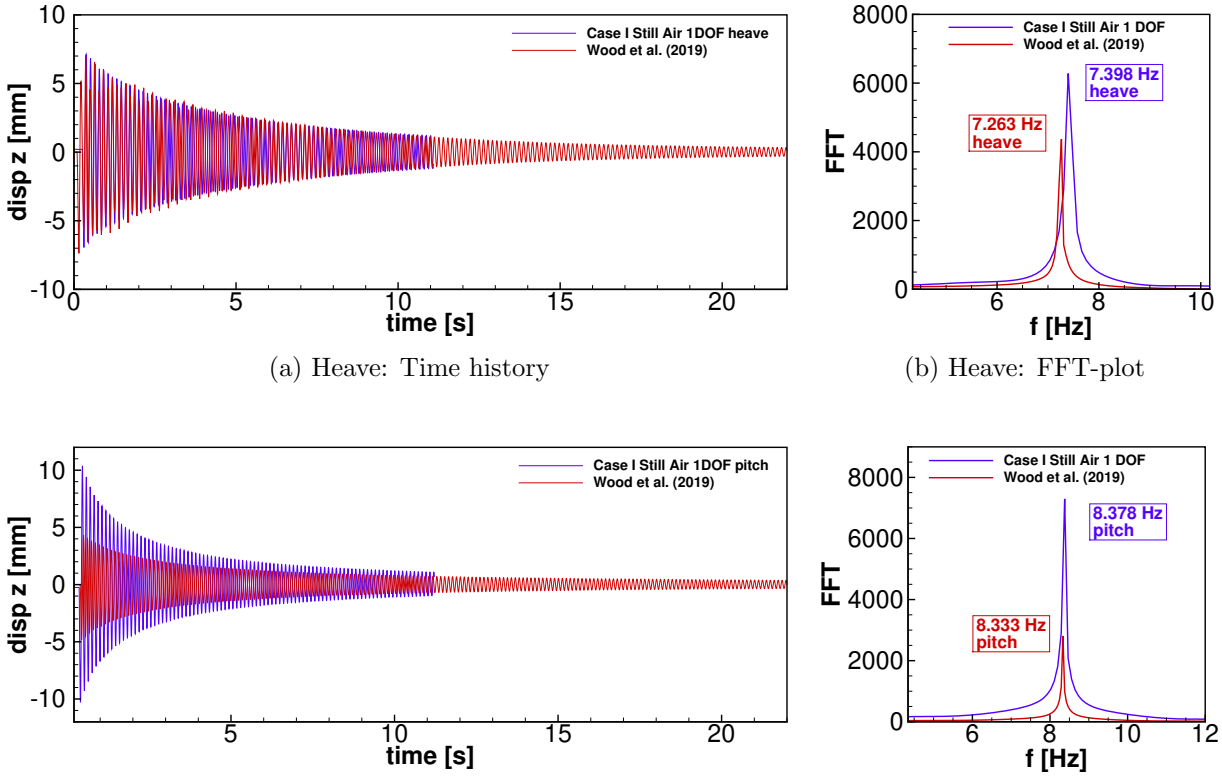

(a) Heave: Time history

(b) Heave: FFT-plot

(c) Pitch: Time history

(d) Pitch: FFT-plot

Figure 5.1: Case I: Comparison of the unsynchronized DIC-data of the still air analysis with the corresponding results from [23] including the time history and frequency-plot (FFT) of the 1-DOF-oscillations separately for heave and pitch.

The detailed calculations can be found in appendix B. The results are listed in Tab. 5.1, which also contains parameters like the mass moment of inertia I_α^E of the wing, the bending and torsional stiffnesses k_h and k_α of the heave and rotational springs of the elastic mounting and the translational and rotational damping $b_h^{1-\mathrm{DOF,tot}}$ and $b_\alpha^{1-\mathrm{DOF,tot}}$. Comparing these values with the data of Wood et al. [23], the results are in the same order of magnitude and corresponding well. The quotient of the total translational damping ratios yields $D_h^{1-\mathrm{DOF,tot}}/D_h^{1-\mathrm{DOF,tot}}$(Wood et al. [23])$= 1.013$ and the quotient of the total rotational damping ratios yields $D_\alpha^{1-\mathrm{DOF,tot}}/D_\alpha^{1-\mathrm{DOF,tot}}$(Wood et al. [23])$= 1.245$. Thus, the translational damping stays nearly constant, while the rotational damping is slightly increased.

Table 5.1: Parameters calculated from the free-oscillation behavior of case I. Comparison with results of Wood et al. [23].

Parameter	Symbol	Unit	Case I (1-DOF) [23]	Case I (1-DOF)
mass moment of inertia	I_α^E	$\mathrm{kg \cdot m^2}$	1.399×10^{-4}	1.383×10^{-4}
mass of dynamic system	m_w	kg	0.33521	0.33921
bending stiffness	k_h	N/m	698	732.92
torsional stiffness	k_α	Nm/rad	0.3832	0.3832
translational damping	$b_h^{1-\mathrm{DOF,tot}}$	Ns/m	9.72×10^{-2}	10.16×10^{-2}
rotational damping	$b_\alpha^{1-\mathrm{DOF,tot}}$	Nm/s	3.70×10^{-5}	4.59×10^{-5}
translational damping ratio	$D_h^{1-\mathrm{DOF,tot}}$	–	3.18×10^{-3}	3.22×10^{-3}
rotational damping ratio	$D_\alpha^{1-\mathrm{DOF,tot}}$	–	2.53×10^{-3}	3.15×10^{-3}

Complementary to case I, Fig. 5.2 presents the separate 1-DOF-oscillations of heave and pitch for case III and the comparison with the results of Wood et al. [23]. The monitoring point of the measured displacements is located at 0.2 m far from the leading edge of the airfoil. The reason for this choice is explained later on for the synchronized measurements. The time history of the heave motion can be seen in Fig. 5.2(a) which shows the good agreement of both oscillations. It is considerable that the exponential decay in the time history of the current measurement is decreased compared to the result in [23]. However, the frequencies of the FFT-plot in Fig. 5.2(b) are nearby with $f_\mathrm{h} = 7.398\,\mathrm{Hz}$ (current) and $f_\mathrm{h} = 7.175\,\mathrm{Hz}$ (Wood et al. [23]), while the heave frequency of the current measurement is identical with the heave frequency of case I. Regarding the pitch motion, the time history in Fig. 5.2(c) shows the same behaviour as well as the coincident exponential decay of both oscillations. The FFT-plot in Fig. 5.2(d) delivers similar frequencies with $f_\mathrm{h} = 7.576\,\mathrm{Hz}$ (current) and $f_\mathrm{h} = 7.487\,\mathrm{Hz}$ (Wood et al. [23]). By the results of the FFT-plot, the main structural parameters for case III are calculated in appendix B and listed in Tab. 5.2. By comparison with the published values, the order of magnitude is identical. It is noticeable that the currently calculated damping parameter of heave is decreased related to the results of [23], which is caused by the varying prestressing forces of the bolted joints, as mentioned above for case I. The damping parameters of pitch are close-by. Hence, the quotient of the total translational damping ratios yields $D_h^{1-\mathrm{DOF,tot}}/D_h^{1-\mathrm{DOF,tot}}$(Wood et al. [23])$= 0.6485$ and the quotient of the total rotational damping ratios follows with $D_\alpha^{1-\mathrm{DOF,tot}}/D_\alpha^{1-\mathrm{DOF,tot}}$(Wood et al. [23])$= 0.9355$.

To conclude the findings of the 1-DOF free-oscillations, the structural parameters of the wing system are comparable to the parameters of the wing system in [23] with the exception that for case I and III there is a slight deviation in the translational damping ratio.

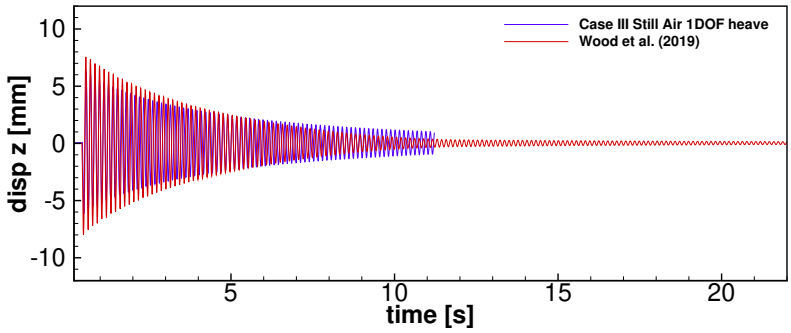

(a) Heave: Time history

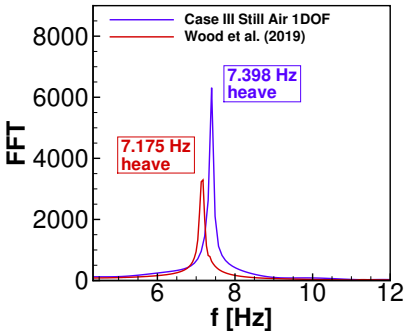

(b) Heave: FFT-plot

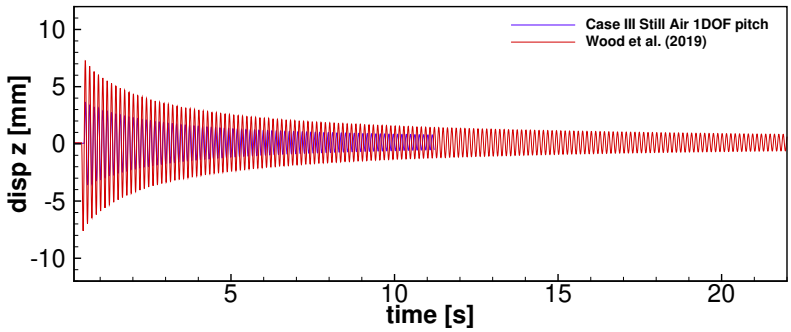

(c) Pitch: Time history

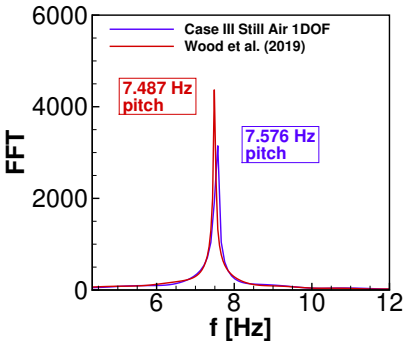

(d) Pitch: FFT-plot

Figure 5.2: Case III: Comparison of the unsynchronized DIC-data of the still air analysis with the corresponding results from [23] including the time history and frequency-plot (FFT) of the 1-DOF-oscillations separately for heave and pitch.

Table 5.2: Parameters calculated from the free-oscillation behavior of case III. Comparison with results of Wood et al. [23].

Parameter	Symbol	Unit	Case III (1-DOF) [23]	Case III (1-DOF)
mass moment of inertia	I_α^E	$\mathrm{kg \cdot m^2}$	1.730×10^{-4}	1.69×10^{-4}
mass of dynamic system	m_w	kg	0.33521	0.33921
bending stiffness	k_h	N/m	698	732.92
torsional stiffness	k_α	Nm/rad	0.3832	0.3832
transitional damping	$b_h^{1-\mathrm{DOF,tot}}$	Ns/m	16.28×10^{-2}	10.88×10^{-2}
rotational damping	$b_\alpha^{1-\mathrm{DOF,tot}}$	Nm/s	4.54×10^{-5}	4.21×10^{-5}
transitional damping ratio	$D_h^{1-\mathrm{DOF,tot}}$	–	5.32×10^{-3}	3.45×10^{-3}
rotational damping ratio	$D_\alpha^{1-\mathrm{DOF,tot}}$	–	2.79×10^{-3}	2.61×10^{-3}

In general, the replacement of the rotational springs and the slight increase of the total mass by the varnishing of the wing does not yield a significant change in the 1-DOF measurement results.

5.1.2 Comparison of free-oscillation characteristics with 2-DOF in still air with previously published results

In this section, the free-oscillation characteristics of the 2-DOF heave and pitch motion are presented by enabling the elastic mounting of the translational heave springs and the rotational springs likewise. A comparison with the results of [23] shall confirm the former findings.

Figure 5.3 shows the characteristics of the free-oscillation for case I with 2-DOF without fluid flow (still air). The motion itself is induced by an impulse excitation. The monitoring point of the measured displacements is located at 0.7 m far from the leading edge of the airfoil as for the 1-DOF test case. Describing the time history in Fig. 5.3(a), both results exhibit a similar exponential decay of the motion, which is caused by structural damping in the elastic mounting and fluid damping by the surrounding air. The amplitudes of the current measurement are slightly higher than in [23], which is due to the different intensity of the manual impulse excitation of the system. Furthermore, regarding the oscillation behavior, the amplitudes proceed in the form of waves. This can be explained by the physical effect of *beat*, which is caused by the superposition of oscillations with slightly different frequencies. Here, a periodic exchange of energy between the heave and pitch movement takes place. An indicator for the energy transfer are points with oscillatory cancellations. Focussing on the FFT-plot of Fig. 5.3(b), the beat frequency can be determined, which is the absolute difference of the heave and pitch frequency. The current results show a beat frequency of $\Delta f^{2-DOF,I} = 0.98\,\text{Hz}$, which is in good agreement with the results of [23] ($\Delta f^{2-DOF,I} = 1.07\,\text{Hz}$). Furthermore, the frequency ratios of the heave- and pitch-frequency are also similar with $f_h^{2-DOF,I}/f_\alpha^{2-DOF,I} = 0.872$ of [23] and $f_h^{2-DOF,I}/f_\alpha^{2-DOF,I} = 0.884$ of the current measurement.

Now, focussing on case III, Fig. 5.4 shows the complementary characteristics to case I with the same measurement conditions. The monitoring point of the measured displacements is located at 0.2 m far from the leading edge of the airfoil as for the 1-DOF test case. The time history in Fig. 5.4(a) shows the exponential decay of the motion, caused by structural damping of the elastic mounting and fluid damping by the surrounding air. In the beginning, the amplitudes of the measurement of [23] are about 3 mm higher compared with the current measurement due to different excitation magnitudes in the experimental handling. However, this difference decreases with time, until both amplitudes level out at $t = 11\,\text{s}$.

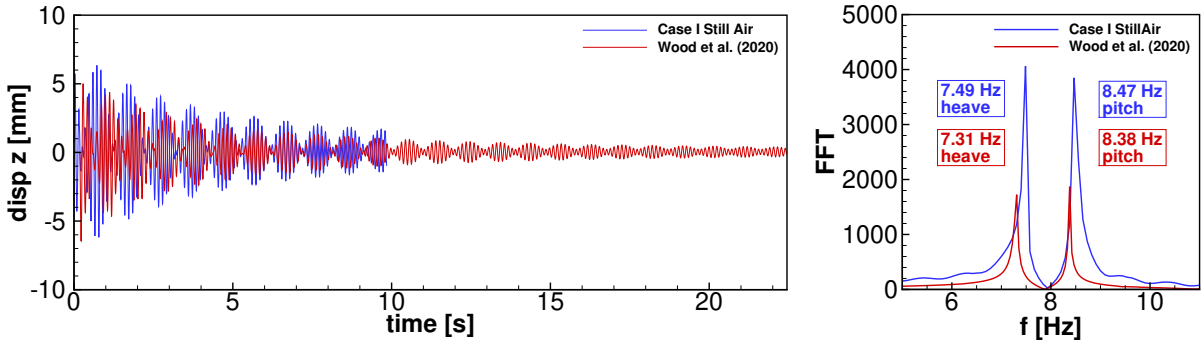

(a) Time history (b) FFT-plot

Figure 5.3: Case I: Comparison of the unsynchronized DIC-data of the still air analysis with the corresponding results from [23] including the time history and frequency-plot (FFT) of the oscillations.

This marks the end of the recording time of the current measurements with a camera frame rate of 500 fps, while the measurement in [23] has a recording time of $t \geq 20\,\mathrm{s}$ with a frame rate of 250 fps. In contrast to case I, the effect of the *beat* is still visible in the time history, but the oscillatory cancellation is more difficult to observe. Regarding the FFT-plot in Fig. 5.4(b), this fact can be deduced to the increased beat frequency of $\Delta f^{2-DOF,I} = 2.05\,\mathrm{Hz}$, which is doubled compared to case I and corresponds well with the published value ($\Delta f^{2-DOF,I} = 1.96\,\mathrm{Hz}$). Additionally, the frequency ratio of $f_h^{2-DOF,I}/f_\alpha^{2-DOF,I} = 0.770$ of Wood et al. [23] is confirmed by the current ratio of $f_h^{2-DOF,I}/f_\alpha^{2-DOF,I} = 0.765$.

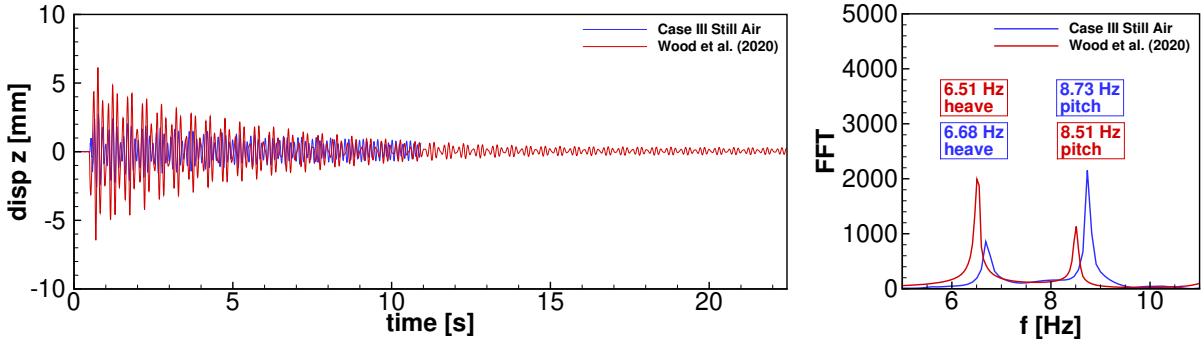

(a) Time history (b) FFT-plot

Figure 5.4: Case III: Comparison of the unsynchronized DIC-data of the still air analysis with the corresponding results from [23] including the time history and frequency-plot (FFT) of the oscillations.

To conclude this section, the results of the unsynchronized measurements mostly correspond to the results of Wood et al. [23]. The replacement of the rotational springs has

no significant effect on the behavior of the 2-DOF-setup. Furthermore, the position of the monitoring points in the symmetry plane of the wing shows no effect on the DIC-measurements, i.e., the decay of motion. The slight deviations in the FFT-plots can be explained by the difference in the length of the data sets of the time histories, from which the FFT-plots are generated. However, the resonance frequencies of heave and pitch are well comparable with the published values.

5.2 Synchronized DIC-measurements

Besides the comparison of the DIC-results with the data of Wood et al. [23], it is of great interest to verify the feasibility of the synchronized measurements, which has not been possible until now. By using the PIV-laser as the illumination source for the DIC-measurements with a pulse rate of 500 pps and a frame rate of the DIC-camera of 500 fps, the synchronized DIC-results are compared with the unsynchronized results for different flow velocities. Due to the limited amount of camera memory, especially for the PIV-system, and the fact that the synchronized measurements consider PIV- as well as DIC-data at the same time, the recording time is shorter than in case of the unsynchronized DIC-measurements. The main objective is to prove the feasibility of the synchronized PIV-DIC-measurements. However, the changed setup considering the laser light as the illumination source shall be qualified by a comparison with unsynchronized DIC-measurements under standard illumination, in order to assure reproducibility.
Before presenting the first results, it has to be determined for the synchronized measurements, where the monitoring point for the acquisition of displacements has to be located in order to deliver meaningful oscillations. Therefore, Fig. 5.5 shall give information about the general motion of the airfoil within one period of oscillation at the extreme phenomenon of flutter. This is shown for case I in Fig. 5.5(a) and for case III in Fig. 5.5(b). By the DIC-method, the three-dimensional displacements of the speckle pattern on the upper wing surface are measured. In the processing, a two-dimensional line element is extracted out of this surface. The result is the airfoil line element which can be seen in the diagrams while the heave- and pitch-movements are superimposed here.
The coordinate systems in both diagrams are normalized in terms of the chord length of the airfoil with $c = 100\,\text{mm}$, so that the axis values x/c and z/c are dimensionless. At the position $x/c = 0$, the leading edge of the airfoil is found at the pitch angle of $\alpha = 0°$, while the trailing edge with the same pitch angle is located at $x/c = 1$. The size of the visible airfoil line elements is slighty reduced compared to the scale of the diagrams, which is due to the fact, that the acquisition of the speckle pattern was difficult at the region of the leading and the trailing edge, respectively. So the DIC-software limited the con-

trol surface for the correlation of displacements. At the position $x/c = 0.417$, the elastic axis is located. It is assumed that its position is horizontally constant and that it offers pure heave displacements during the period of oscillation due to the congruence with the rotational springs. Focussing on the amplitudes, by the blue and red line, the extreme airfoil displacements are visible. On the one hand, the largest amplitude of oscillation with $\Delta z/c \approx 0.32$ is found for case I at $x/c \approx 0.975$ and for case III at $x/c \approx 0.15$. Thus, in case I, where the position of the center of gravity and the elastic axis are equal, the airfoil oscillates strongly up- and downwards at its trailing edge. In contrast to this finding, in case III, where the center of gravity is shifted behind the elastic axis, the airfoil oscillates intensively at the leading edge and less at its trailing edge. On the other hand, the lowest amplitude of oscillation for case I with $\Delta z/c \approx 0.1$ is found at $x/c \approx 0.3$ and for case III with $\Delta z/c \approx 0.04$ at $x/c \approx 0.675$.

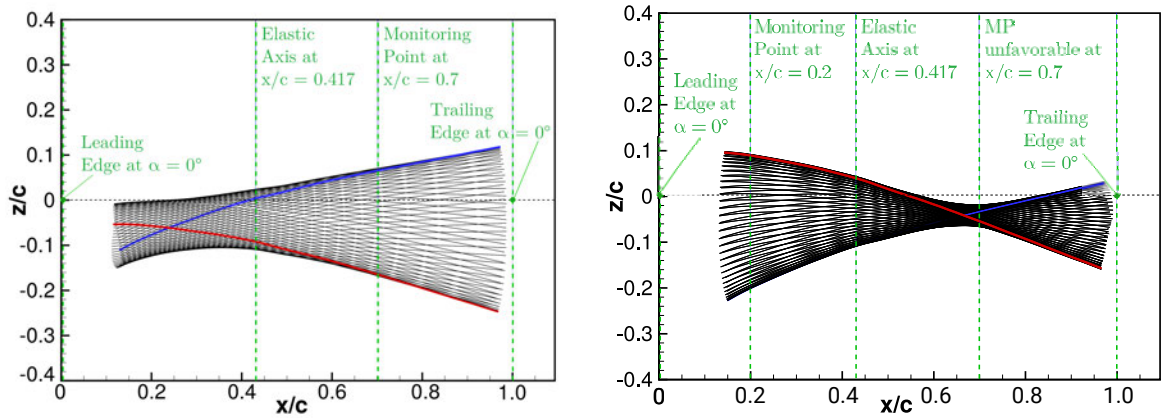

(a) Case I (b) Case III

Figure 5.5: Comparison of synchronized DIC: NACA-0012-profile positions during one period of flutter oscillation: Red/Blue line-elements represent the upper surface line at maximum/minimum pitch angles.

To conclude the findings, the regions of lowest amplitude are rather unfavorable for the monitoring points of the measurement series due to the fact, that for lower velocities below flutter the amplitudes further decrease. To find a compromise of rather high and equal amplitudes of oscillations for both cases, the monitoring point for case I is chosen at $x/c = 0.7$ and for case III at $x/c = 0.2$. This is done for all of the following measurement series.

5.2.1 Comparison of synchronized with unsynchronized DIC-results

5.2.1.1 Case I: Eigenfrequency analysis at several fluid flow velocities

Regarding the free-oscillations in still air for case I, Fig. 5.6 shows the superposition of the synchronized and unsynchronized DIC-data. In the time history in Fig. 5.6(a), an in-phase behavior of the data obtained by both methods is visible. The amplitudes of the synchronized data are slightly higher due to the randomness of the manual excitation. The exponential decay of the oscillation, caused by structural and fluid damping, is recognizable as well as the effect of the *beat* with its typical curve showing oscillatory cancellation as an effect of the transfer of energy between the heave and pitch motion. Furthermore, the beat frequency $\Delta f^{2-DOF,I} = 0.98\,\text{Hz}$ for the unsynchronized method and $\Delta f^{2-DOF,I} = 1.25\,\text{Hz}$ for the synchronized method are similar. The difference in the FFT-plot can be at least partially explained by the varying length of the data sets in the time range caused by the diverse frame rates of 250 fps (unsynchronized) and 500 fps (synchronized), respectively. The ratios between the heave- and pitch-frequency are nearby with $f_h^{2-DOF,I}/f_\alpha^{2-DOF,I} = 0.884$ for the unsynchronized method and $f_h^{2-DOF,I}/f_\alpha^{2-DOF,I} = 0.853$ for the synchronized method.

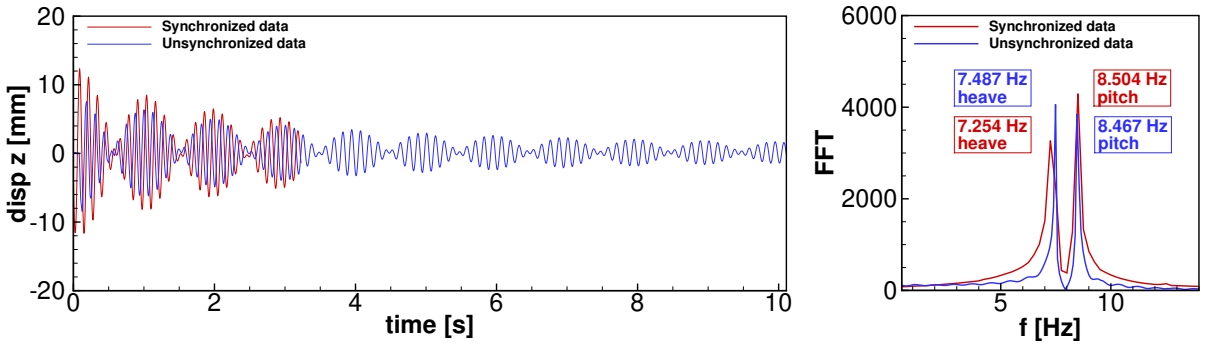

(a) Time history (b) FFT-plot

Figure 5.6: Case I: Comparison of the synchronized and the unsynchronized DIC-data in still air including the time history and frequency-plot (FFT) of the oscillations.

Moving to fluid flow velocities in the Reynolds number range of $9.66 \times 10^3 \leq \text{Re} \leq 2.39 \times 10^4$ (Fig. 5.7 to Fig. 5.9), it can be stated in general that the effect of fluid damping is increasing, the higher the free-stream velocity is. Additionally, the oscillations are in-phase and the effect of the beat is recognizable in the progression of the curves of both the synchronized and unsynchronized data, but its characteristic of amplitude cancellation is diminishing with higher flow velocities. Beginning with $\text{Re} = 9.66 \times 10^3$ in the time history

in Fig. 5.7(a), the oscillation amplitudes start at $\Delta z^{\text{sync}} = 11\,\text{mm}$ for the synchronized method and $\Delta z^{\text{unsync}} = 9\,\text{mm}$ for the unsynchronized method. The difference in these values originates from the individual, manual excitation. Both curves proceed in-phase and assimilate by their amplitudes, until the motion of the unsynchronized measurement is decayed at about $t = 9\,\text{s}$. Looking at the FFT-plot in Fig. 5.7(b), the amplitudes are decreased compared with those of the free-oscillation analysis, whereas the beat frequency $\Delta f^{2-DOF,I} = 0.98\,\text{Hz}$ for the unsynchronized method remains unchanged and for the synchronized method it decreased to $\Delta f^{2-DOF,I} = 1\,\text{Hz}$.

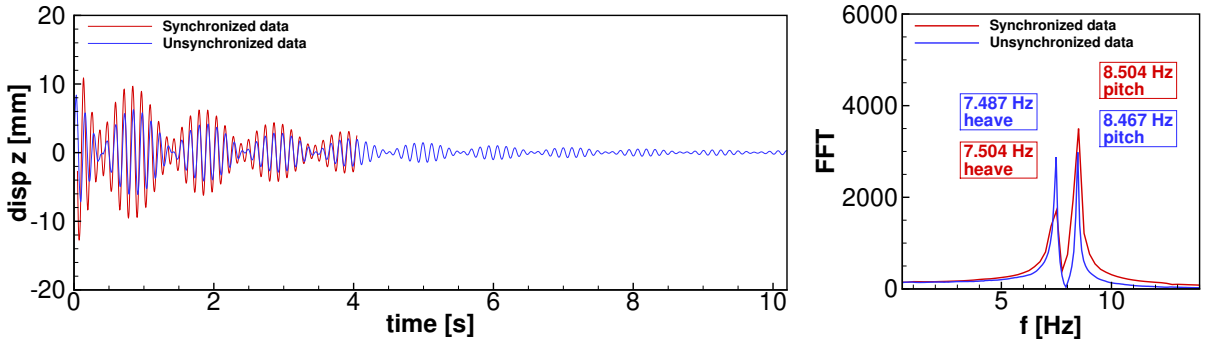

(a) Time history (b) FFT-plot

Figure 5.7: Case I: Comparison of the synchronized and the unsynchronized DIC-data of the analysis at Re $= 9.66 \times 10^3$ ($U_\infty = 1.44\,\text{m/s}$) including the time history and frequency-plot (FFT) of the oscillations.

In Fig. 5.8, the Reynolds number is raised to Re $= 1.65 \times 10^4$. In the time history in Fig. 5.8(a), the amplitudes of the unsynchronized and synchronized measurement converge with proceeding time. The motion of the unsynchronized measurement decays until $t = 10\,\text{s}$. Regarding the FFT-plot in Fig. 5.8(b), the amplitudes are decreased in comparison to those at the former Reynolds number and the heave peak is dominated by the pitch peak. The beat frequencies $\Delta f^{2-DOF,I} = 0.891\,\text{Hz}$ for the unsynchronized and $\Delta f^{2-DOF,I} = 0.75\,\text{Hz}$ for the synchronized measurement are further decreased.
In Fig. 5.9, the Reynolds number is raised to Re $= 2.39 \times 10^4$. In the time history in Fig. 5.9(a), the motion of the unsynchronized method is nearly decayed at $t = 6\,\text{s}$, whereat small amplitude oscillations (SAO) are remaining with $\Delta z = \pm 0.5\,\text{mm}$. Regarding the FFT-plot in Fig. 5.9(b), the pitch amplitude remains unchanged compared to the former Reynolds number and the heave amplitude is further decreased in the unsynchronized data and strongly damped in the synchronized data. The beat frequency $\Delta f^{2-DOF,I} = 0.802\,\text{Hz}$ for the unsynchronized measurement is further decreased, while the synchronized method can not be clearly evaluated anymore. It may be mentioned here, that due to different data lengths of the unsynchronized and synchronized measurements, the FFT-plots are

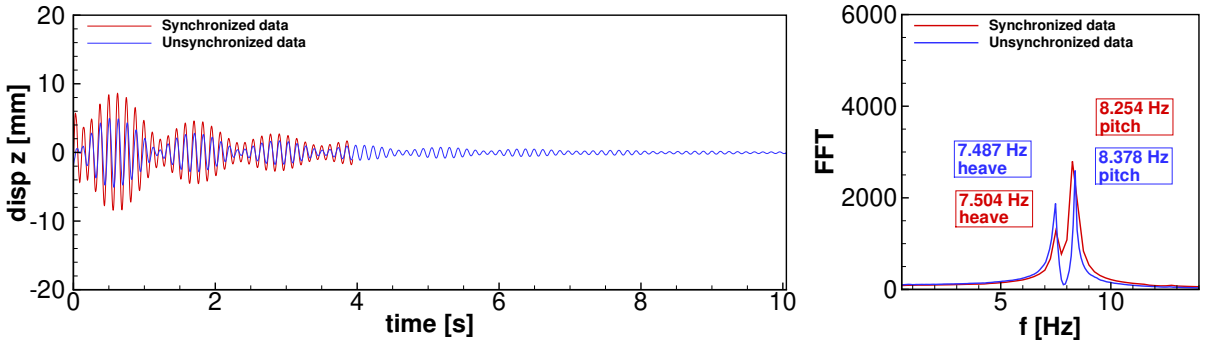

(a) Time history (b) FFT-plot

Figure 5.8: Case I: Comparison of the synchronized and the unsynchronized DIC-data of the analysis at Re $= 1.65 \times 10^4$ ($U_\infty = 2.46\,\mathrm{m/s}$) including the time history and frequency-plot (FFT) of the oscillations.

generated with slight deviations in the frequency and amplitude values. Hence, in the Discrete Fourier Transform (DFT), which is the background of the FFT, the sampling points of the time history are interpolated by complex polynomials as a summation of multiple trigonometric functions dependent on the amount of time data points. In the time history of the synchronized measurements, which does not show the whole decay of motion, the nodes are limited as well as the trigonometric content of the interpolation curve.

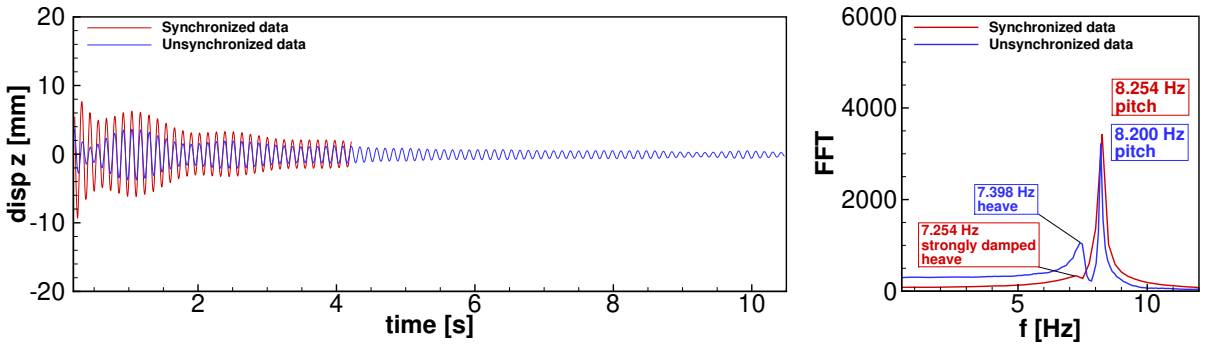

(a) Time history (b) FFT-plot

Figure 5.9: Case I: Comparison of the synchronized and the unsynchronized DIC-data of the analysis at Re $= 2.39 \times 10^4$ ($U_\infty = 3.56\,\mathrm{m/s}$) including the time history and frequency-plot (FFT) of the oscillations.

Going further to the Reynolds number range of $3.06 \times 10^4 \leq \mathrm{Re} \leq 3.66 \times 10^4$ (Fig. 5.10 to Fig. 5.11), the impact of fluid damping on the oscillations is not present here. Instead, fluid flows at these velocities induce structural oscillations of the airfoil with high amplitudes such as LAO. Thus, an initial excitation is not necessary anymore. By further increasing

the flow velocity, flutter instability of the wing system is provoked. In the following, the synchronized measurements were conducted at fully developed structural oscillations, due to the short measurement time. First, at $\mathrm{Re} = 3.06 \times 10^4$, the time history in Fig. 5.10(a) initially reveals SAO with an amplitude of $\Delta z = \pm 1\,\mathrm{mm}$ that develop into LAO with an amplitude of $\Delta z = \pm 2.5\,\mathrm{mm}$, while the synchronized method shows only the LAO at an amplitude of $\Delta z = \pm 4\,\mathrm{mm}$. This difference in the amplitude of the time history is peculiar, since the surrounding free-stream velocity is equal for both. However, those measurements are not repeated, so statistical deviations due to individual measurement conditions, i.e., coincidentally exaggerated wing motions, can be a reason here. However, the constant, sinusoidal course of the oscillation is visible by the synchronized and unsynchronized measurements. Both have in common, that the frequency of the so called *limit-cycle oscillations* (LCO) is represented in the FFT-plot in Fig. 5.10(b) with a single frequency peak at $f_{\mathrm{LCO}} = 8.111\,\mathrm{Hz}$ for the unsynchronized and $f_{\mathrm{LCO}} = 8.004\,\mathrm{Hz}$ for the synchronized method. Physically, it can be deduced that the dominating pitch and the reduced heave motion frequencies have merged.

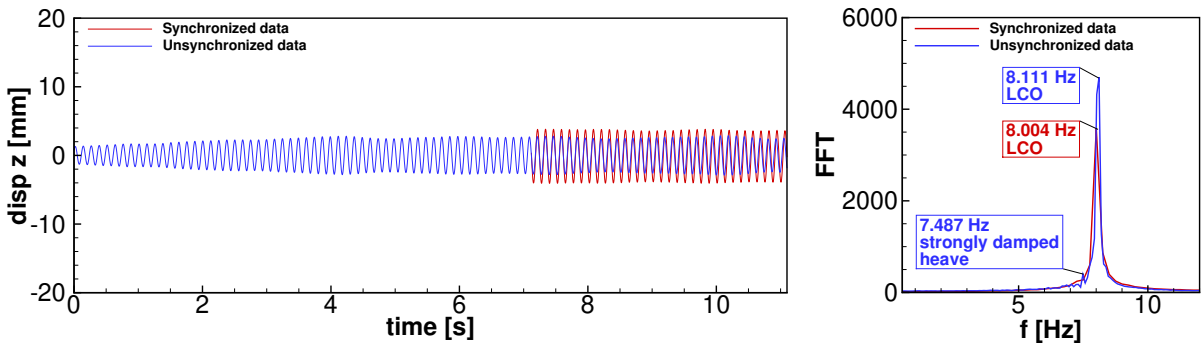

(a) Time history (b) FFT-plot

Figure 5.10: Case I: Comparison of the synchronized and the unsynchronized DIC-data of the analysis at $\mathrm{Re} = 3.06 \times 10^4$ ($U_\infty = 4.56\,\mathrm{m/s}$) including the time history and frequency-plot (FFT) of the oscillations.

Second, at a Reynolds number of $\mathrm{Re} \geq 3.66 \times 10^4$, the time history in Fig. 5.11(a) shows the flutter phenomenon for the unsynchronized method by an exponentially increasing oscillation with amplitudes up to $\Delta z = \pm 16\,\mathrm{mm}$, while the synchronized data are captured at constantly high amplitudes of $\Delta z = \pm 14\,\mathrm{mm}$. Looking at the FFT-plot in Fig. 5.11(b), a flutter frequency of $f_{\mathrm{flutter}} = 7.932\,\mathrm{Hz}$ is found for the unsynchronized method and $f_{\mathrm{flutter}} = 8.004\,\mathrm{Hz}$ for the synchronized method. To avoid a structural damage in the elastic mounting of the wing system, which may be caused by the fanned amplitudes of the flutter oscillation, the fluid flow was stopped after 11 seconds related to the unsynchronized measurement.

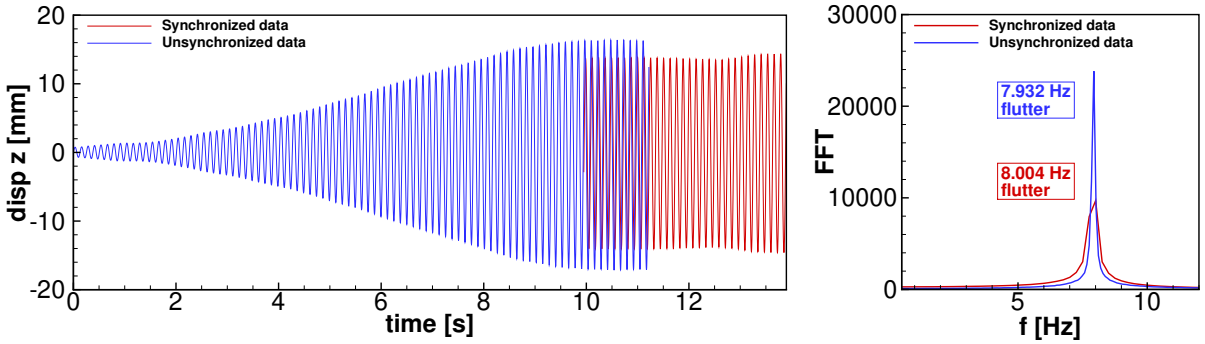

(a) Time history (b) FFT-plot

Figure 5.11: Case I: Comparison of the synchronized and the unsynchronized DIC-data of the analysis at flutter Re $= 3.60 \times 10^4$ ($U_\infty = 5.37\,\mathrm{m/s}$) including the time history and frequency-plot (FFT) of the oscillations.

5.2.1.2 Case III: Eigenfrequency analysis at several fluid flow velocities

Focussing on the dynamic behavior of case III, firstly, the free-oscillation characteristics are considered and depicted in Fig. 5.12. As for case I, the time history of case III in Fig. 5.12(a) shows the in-phase behavior of the oscillations of the synchronized and unsynchronized measurements, whereas the amplitudes start with $z = 7\,\mathrm{mm}$ for the synchronized data and $z = 3\,\mathrm{mm}$ for the unsynchronized data due to different manual excitation magnitudes. The exponential decrease of the oscillation is not as steep as for case I in Fig. 5.6(a), which means that the damping on the dynamic system is smaller. Furthermore, the exact decay time for the unsynchronized data is difficult to determine, due to the fact that there are oscillations of $\Delta z = \pm 1\,\mathrm{mm}$ remaining between $7\,\mathrm{s} \leq t \leq 10\,\mathrm{s}$. However, the effect of the beat is recognizable in the time history for both methods, although the cancellation of the oscillations are not as sharply distinguishable as in case I. Instead, there are reduced amplitudes with no clearly visible zero crossings. The repetition rate of the energy transfer is higher than in case I (Fig. 5.6(a)). This finding becomes clearer by looking at the FFT-plot in Fig. 5.12(b). The beat frequencies of $\Delta f^{2-DOF,I} = 2.05\,\mathrm{Hz}$ for the unsynchronized data and $\Delta f^{2-DOF,I} = 2.001\,\mathrm{Hz}$ for the synchronized method are increased compared to those in Fig. 5.6(b). The frequency ratio of heave and pitch of the current measurement is at $f_h^{2-DOF,I}/f_\alpha^{2-DOF,I} = 0.765$ for the unsynchronized method, which is nearby the frequency ratio of $f_h^{2-DOF,I}/f_\alpha^{2-DOF,I} = 0.771$ for the synchronized method.

Now, by adjusting the fluid flow velocities within the Reynolds number range of $9.66 \times 10^3 \leq \mathrm{Re} \leq 3.06 \times 10^4$ (Fig. 5.13 to Fig. 5.16), the fluid damping increases, while the effect of the beat decreases, the higher the streamwise free-stream velocity is. Starting with the

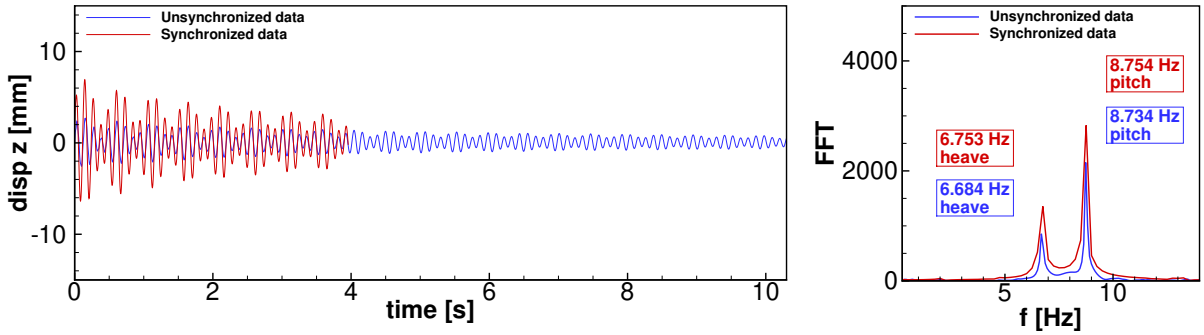

(a) Time history (b) FFT-plot

Figure 5.12: Case III: Comparison of the synchronized and the unsynchronized DIC-data of the still air analysis including the time history and frequency-plot (FFT) of the oscillations.

Reynolds number of $\mathrm{Re} = 9.66 \times 10^3$, the structural response of the airfoil is depicted in Fig. 5.13. The time history in Fig. 5.13(a) shows the collinear course of the curves for the synchronized and unsynchronized method, due to the fact that the oscillation behavior is identical and the amplitudes are nearly matching. The characteristic beat and the oscillatory cancellation are visible for $t \leq 4\,\mathrm{s}$, then the oscillation is continuously decreasing by the influence of fluid damping. Nevertheless, it is noteworthy for the unsynchronized data that oscillations of $\Delta z = \pm 1.5\,\mathrm{mm}$ remain at the end, which results in a ratio of $\Delta z_{\mathrm{end}} / \Delta z_{\mathrm{start}} = 0.375$ related to the displacements in the beginning of the recording. So the damping process is extended in time here.

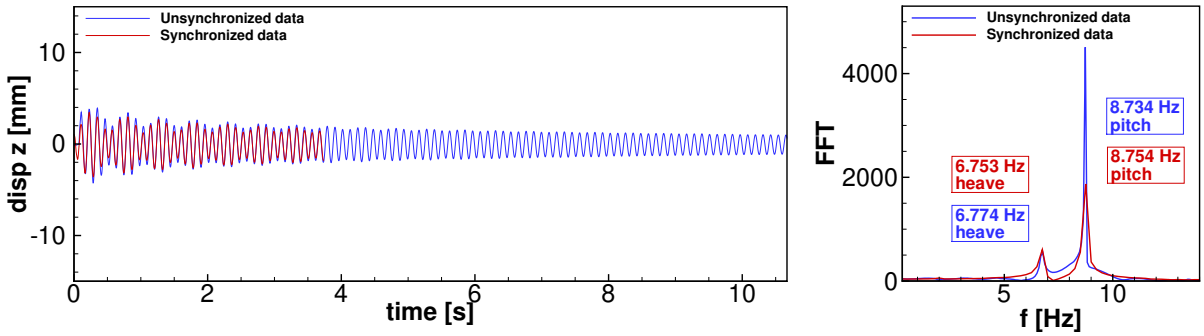

(a) Time history (b) FFT-plot

Figure 5.13: Case III: Comparison of the synchronized and the unsynchronized DIC-data of the analysis at $\mathrm{Re} = 9.66 \times 10^3$ ($U_\infty = 1.44\,\mathrm{m/s}$) including the time history and frequency-plot (FFT) of the oscillations.

Looking at the FFT-plot in Fig. 5.13(b), a similar behavior of the synchronized and unsynchronized curve is confirmed by the matching heave and pitch frequency peaks,

while the amplitude of the pitch frequency is larger. This disparity may explain the reduction of the beat effect in the course of the amplitudes. However, the beat frequency of the synchronized method stays constant with $\Delta f^{2-DOF,III} = 2.001\,\text{Hz}$ compared to still air, while the beat frequency for the unsynchronized method is slightly decreased with $\Delta f^{2-DOF,III} = 1.96\,\text{Hz}$.

Increasing the fluid flow velocity to $\text{Re} = 1.65 \times 10^4$ in Fig. 5.14, the characteristics of the fluid-damped oscillations are further developed, which can be seen in the time history in Fig. 5.14(a). Already at the beginning, the amplitudes of the unsynchronized data are limited to $\Delta z = \pm 2\,\text{mm}$, while the amplitudes of the synchronized data are slightly higher. At the end of the recording time, there are remaining oscillations of $\Delta z = \pm 0.5\,\text{mm}$ for the unsynchronized data. Regarding the corresponding frequencies, the FFT-plot in Fig. 5.14(b) reveals that the pitch motion is dominating by its large amplitude peak. The beat frequency of the synchronized method is decreased to $\Delta f^{2-DOF,III} = 1.75\,\text{Hz}$ compared to the one at the former free-stream velocity, while the beat frequency of the unsynchronized method stays constant with $\Delta f^{2-DOF,III} = 1.96\,\text{Hz}$.

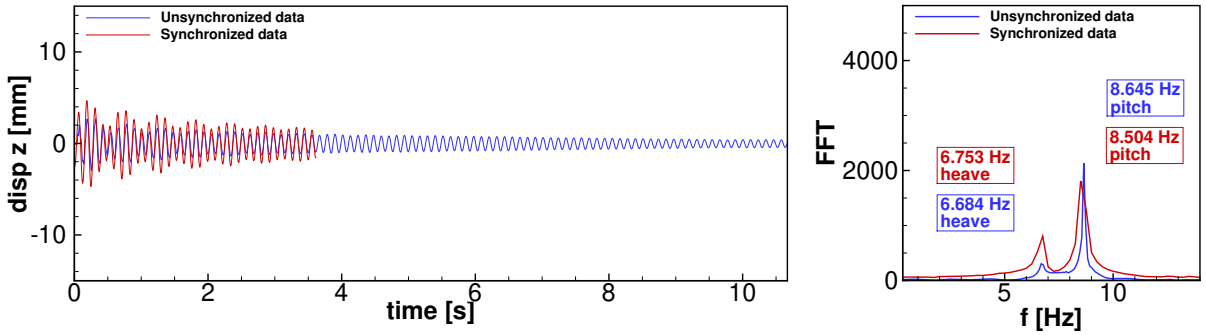

(a) Time history (b) FFT-plot

Figure 5.14: Case III: Comparison of the synchronized and the unsynchronized DIC-data of the analysis at $\text{Re} = 1.65 \times 10^4$ ($U_\infty = 2.46\,\text{m/s}$) including the time history and frequency-plot (FFT) of the oscillations.

Adjusting the Reynolds number further to 2.39×10^4 in Fig. 5.15, the free-stream damping increases leading to a visible decay of the motion within $t = 10\,\text{s}$ in the time history in Fig. 5.15(a). The FFT-plot in Fig. 5.15(b) reveals the reduced heave frequency and the further dominating effect of the pitch frequency, while the beat frequency of the synchronized data is unchanged and the beat frequency of the unsynchronized data is further decreased to $\Delta f^{2-DOF,III} = 1.78\,\text{Hz}$.

Finally, the fluid damping is maximized in Fig. 5.16 showing the oscillatory behavior at the fluid flow velocity according to $\text{Re} = 3.06 \times 10^4$. Within $t = 2\,\text{s}$ the decay process has ended in the unsynchronized measurement, though the synchronized measurement still

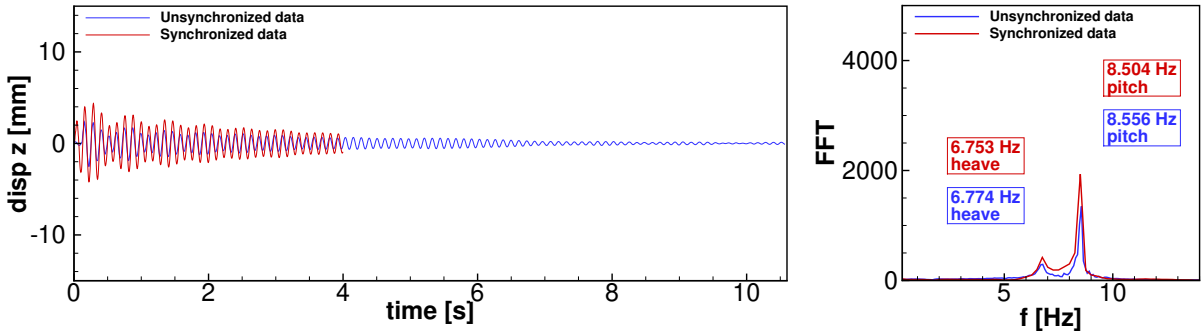

(a) Time history (b) FFT-plot

Figure 5.15: Case III: Comparison of the synchronized and the unsynchronized DIC-data of the analysis at Re $= 2.39 \times 10^4$ ($U_\infty = 3.56\,\mathrm{m/s}$) including the time history and frequency-plot (FFT) of the oscillations.

reveals small oscillations. The FFT-plot in Fig. 5.16(b) shows that the amplitude peaks for both methods are reduced, while the data determined by the synchronized method consists mainly of the pitch motion due to the fact that the heave frequency is strongly damped. The unsynchronized method shows equal characteristics for heave and pitch with a beat frequency of $\Delta f^{2-DOF,III} = 1.52\,\mathrm{Hz}$.

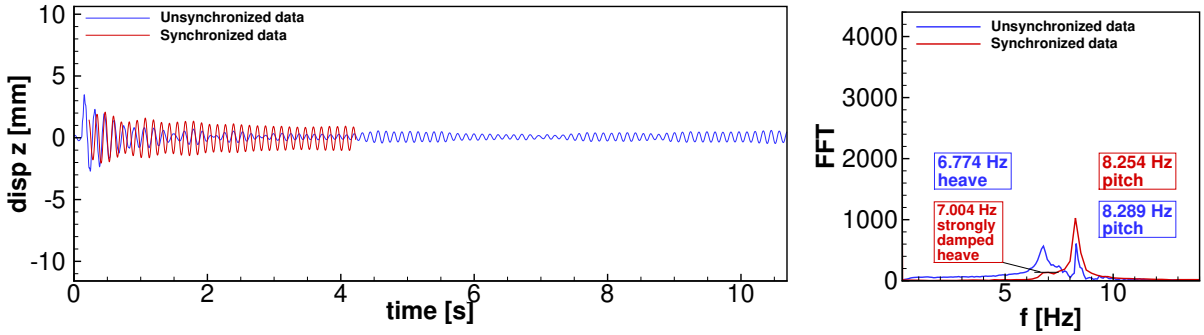

(a) Time history (b) FFT-plot

Figure 5.16: Case III: Comparison of the synchronized and the unsynchronized DIC-data of the analysis at Re $= 3.06 \times 10^4$ ($U_\infty = 4.56\,\mathrm{m/s}$) including the time history and frequency-plot (FFT) of the oscillations.

Concentrating on the last measurement in Fig. 5.17, the flutter phenomenon is depicted. In the time history in Fig. 5.17(a) there are constantly high amplitudes of about $\Delta z = \pm 11\,\mathrm{mm}$ for both methods reached at $t \geq 7\,\mathrm{s}$, whereat the unsynchronized method reveals the amplitude progression slightly within $0\,\mathrm{s} \leq t \leq 6\,\mathrm{s}$. Besides, the FFT-plot in Fig. 5.17(b) reveals for both methods a similar distribution of the flutter peak with $f_{\mathrm{flutter}} = 8.111\,\mathrm{Hz}$ for the unsynchronized and $f_{\mathrm{flutter}} = 8.004\,\mathrm{Hz}$ for the synchronized method.

This single resonance peak represents the merging of the dominating pitch and the reduced heave frequency.

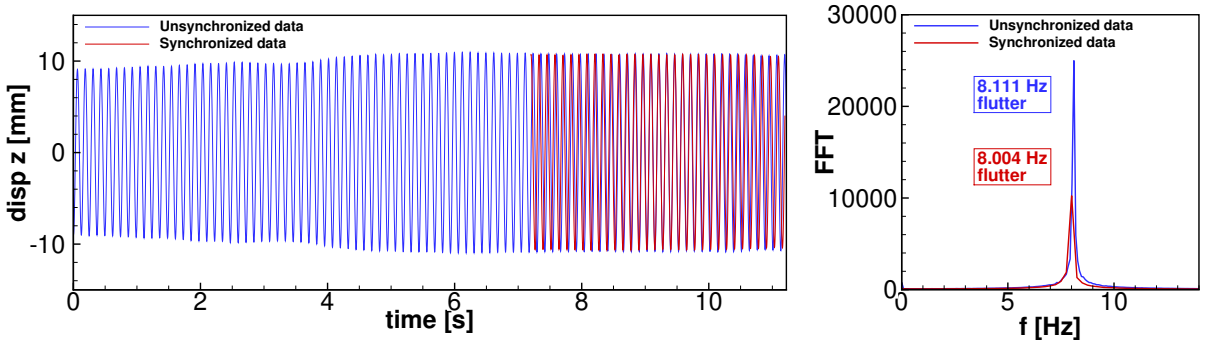

(a) Time history (b) FFT-plot

Figure 5.17: Case III: Comparison of the synchronized and the unsynchronized DIC-data of the analysis at flutter Re $= 3.60 \times 10^4$ ($U_\infty = 5.37\,\mathrm{m/s}$) including the time history and frequency-plot (FFT) of the oscillations.

To summarize the feasibility of the synchronized DIC-measurements, the results correspond well with those of the unsynchronized DIC-measurements. The time histories reveal oscillations that are usually in-phase and show the typical characteristics of the beat for the lower free-stream velocities. Due to the individual manual excitation of the wing, the amplitudes of the synchronized and unsynchronized measurements are different at the beginning of the recording, though the decaying course of the curves is similarly recognizable. The flutter phenomenon shows at the higher free-stream velocities, where an initial excitation is not necessary, a slight difference in the amplitudes for case I in Fig. 5.11(a) that may be caused by statistical variations. This assumption could be proven by a repetition of the concerned measurement beyond this thesis. Nevertheless, for case III, the flutter amplitudes in Fig. 5.17(a) correspond well for the synchronized and unsynchronized measurements. The FFT-plots, which are calculated from the time histories, are also similar according to their frequency distributions, which can be exemplarily seen for the flutter phenomenon of case III in Fig. 5.17(b). In general, due to the fact that the DIC-camera frame rates and therefore the recording times are different for the synchronized and unsynchronized method, the FFT uses different data set lengths, which can lead to slightly varying frequency and amplitude values. However, the results of the synchronized measurements can be evaluated as satisfactory. Thus, the usage of the PIV-laser as illumination source for DIC has been successfull. In the following, this finding shall be confirmed by the investigation of the different illumination sources due to measurement uncertainties and effectively illuminated areas of the speckle pattern.

5.2.2 Comparison of the DIC-illumination sources: standard light and laser light

In this section, the synchronized and unsynchronized DIC-measurements are compared with regard to their sources of illumination. Besides the measurement of the displacements, it is possible to determine the uncertainties to evaluate the quality of the illumination sources. Figure 5.18 shows the time histories of the DIC-measurements and the uncertainties of case I for the free-oscillation analysis in still air.

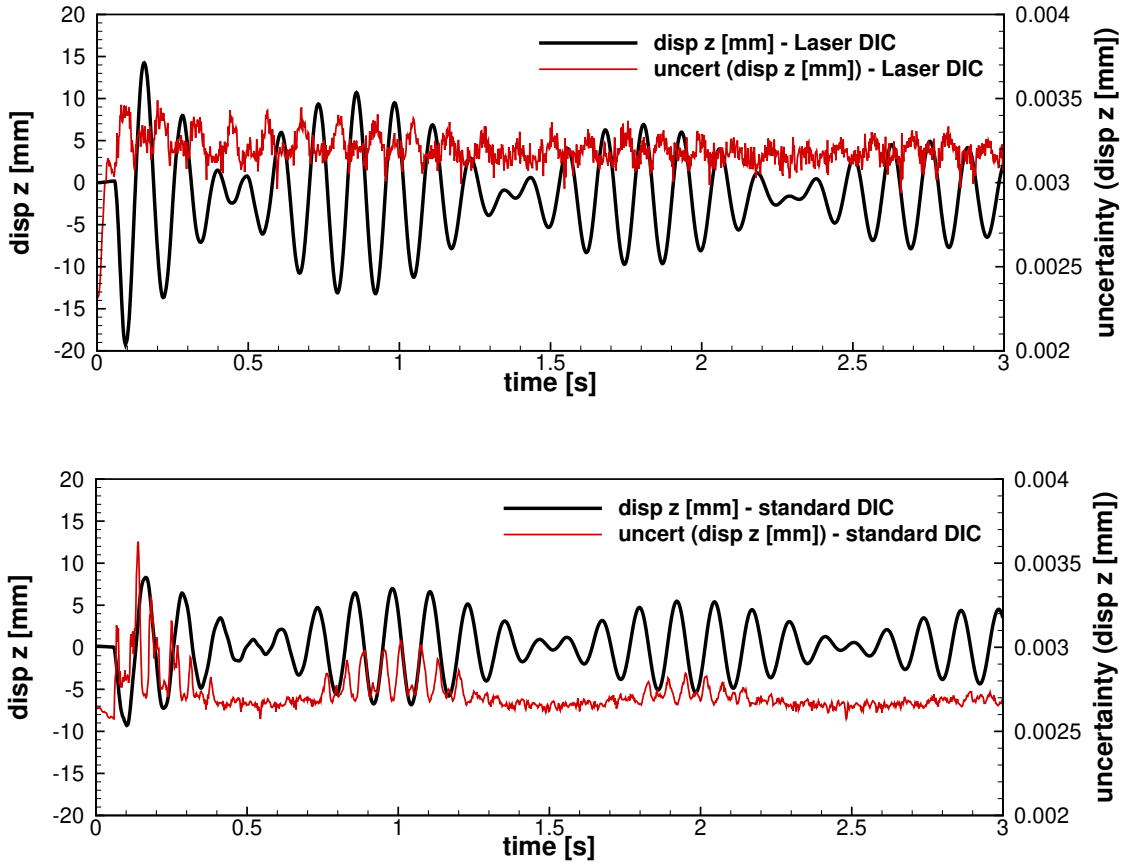

Figure 5.18: DIC-measurement results and uncertainties for the still air analysis of case I. Comparison of the illumination by laser light (above) and by standard light (below).

In the upper diagram, the synchronized measurements are investigated using the laser of the PIV-system as illumination source. The black curve represents the displacements Δz in z-direction of the wing system. The oscillations proceed in the form of waves, which is already known as the effect of the beat. The mean value of the amplitude is found at $\mathrm{rms}(\Delta z) \approx 7\,\mathrm{mm}$. Here the *root mean square* value (rms) is applied on the amplitudes due to the fact that the oscillation proceeds across $z = 0\,\mathrm{mm}$, which is the classical mean value here. Therefore, the rms-value is suitable for a further comparison

of mean amplitude ratios or relative mean errors. The red curve, which represents the uncertainty of this measurement, oscillates along its mean value of $\overline{\Delta\tilde{z}} \approx 3.2\,\mu$m, while the deviation is limited to $\Delta\tilde{z} = \overline{\Delta\tilde{z}} \pm 0.2\,\mu$m. The relative mean error can be calculated as $\overline{\Delta\tilde{z}}/\mathrm{rms}(\Delta z)\cdot 100\,\% = 0.046\,\%$. The maximum uncertainty with $\max(\Delta\tilde{z}) = 3.5\,\mu$m can be seen at $t = 0.1\,$s and $t = 0.2\,$s, respectively. At these instants of time, the z-displacements of the free-oscillation reach their minimum values. Furthermore, it is globally noticeable that the uncertainty values are evenly distributed along the recording time. Thus, the PIV-laser seems to deliver a constant light intensity of the illuminated speckle pattern, which is minimally effected by the movement position of the wing system. It can be evaluated as satisfactory for the operation of the synchronized DIC-method. In the lower diagram of Fig. 5.18, the complementary investigations are shown for the unsynchronized method using standard light as illumination source. The uncertainty distribution has a mean value of $\overline{\Delta\tilde{z}} \approx 2.8\,\mu$m with the upper and lower limit of $\Delta\tilde{z} = \overline{\Delta\tilde{z}} \pm 0.2\,\mu$m. With the rms value of the amplitude of the z-displacements $\mathrm{rms}(\Delta z) \approx 4\,$mm, the relative mean error results in $\overline{\Delta\tilde{z}}/\mathrm{rms}(\Delta z) \cdot 100\,\% = 0.07\,\%$ which is higher than for the synchronized measurements. Furthermore, the uncertainty distribution seems to be dependent on the z-displacements. Thus, the oscillations of the uncertainty are increased in the regions of higher displacement amplitudes. By looking at the local maxima at $t = 0.95\,$s, $t = 1.0\,$s and $t = 1.1\,$s with similar uncertainty values of $\Delta\tilde{z} \approx 3.0\,\mu$m, it is remarkable that the peaks are located at the zero crossing of the measured displacements in z. These are the time points of the highest temporal alteration rate in which the wing system has maximum speed. A possible explanation is that the intensity of illumination by the standard light source is fluctuating there, which may lead to undesirable blurring effects of the rapid wing movement.

Moving further to the evaluation of the measurement reliability at higher fluid flows, three different types of illumination are depicted in Fig. 5.19 examined on the example of the flutter phenomenon of case I considering two periods of oscillation. Figure 5.19(a) shows the illumination of the dynamic wing system with a standard light source for the unsynchronized measurements. The red curve depicts the measurement of the two oscillation periods of flutter with an amplitude of $\Delta z = 5.5\,$mm with the rms-value of $\mathrm{rms}(\Delta z) = \Delta z/\sqrt{2} = 3.889\,$mm, assuming a zero-crossing sine wave function. The black curve shows the accompanied uncertainty with a mean value of $\overline{\Delta\tilde{z}} = 2.5\,\mu$m which is evenly distributed along the recording time. The relative mean error according to the rms-value of the black curve results in $\overline{\Delta\tilde{z}}/\mathrm{rms}(\Delta z)\cdot 100\,\% = 0.064\%$, which shows that the unsynchronized illumination source delivers sufficiently accurate measurement results. Complementary to the findings of the standard illumination, Fig 5.19(b) presents the results of the synchronized method using the PIV-laser as illumination source. The synchronization

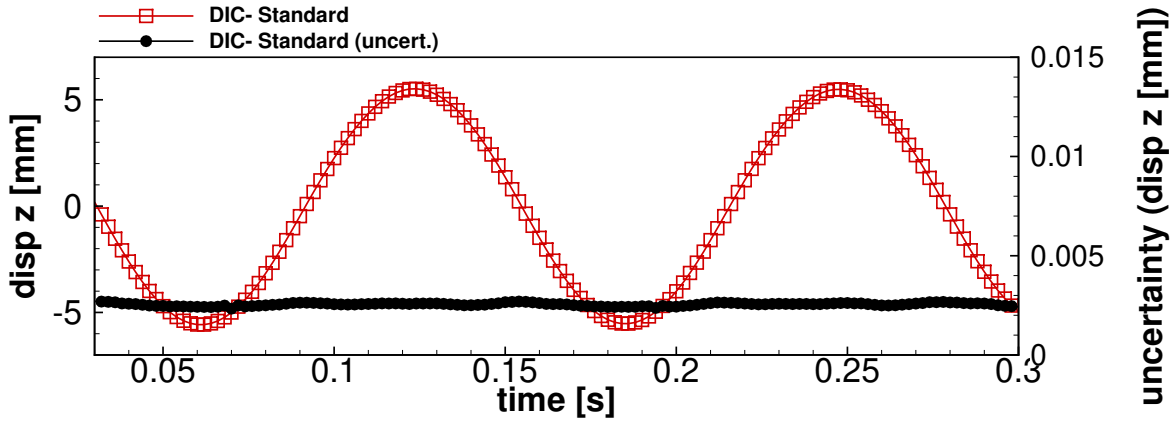

(a) Unsynchronized DIC: Standard light illumination.

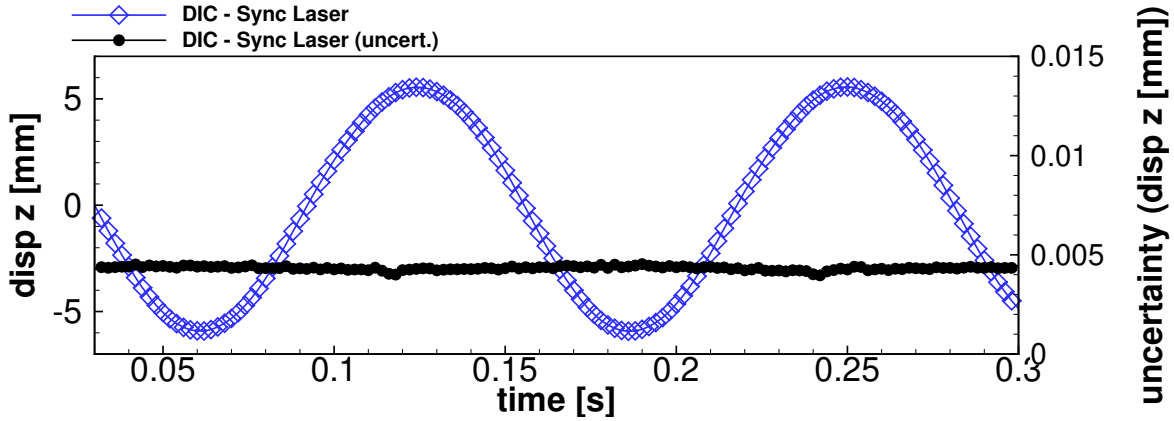

(b) Synchronized DIC: Laser with a pulse rate of 500 pps at the camera frame rate of 500 fps.

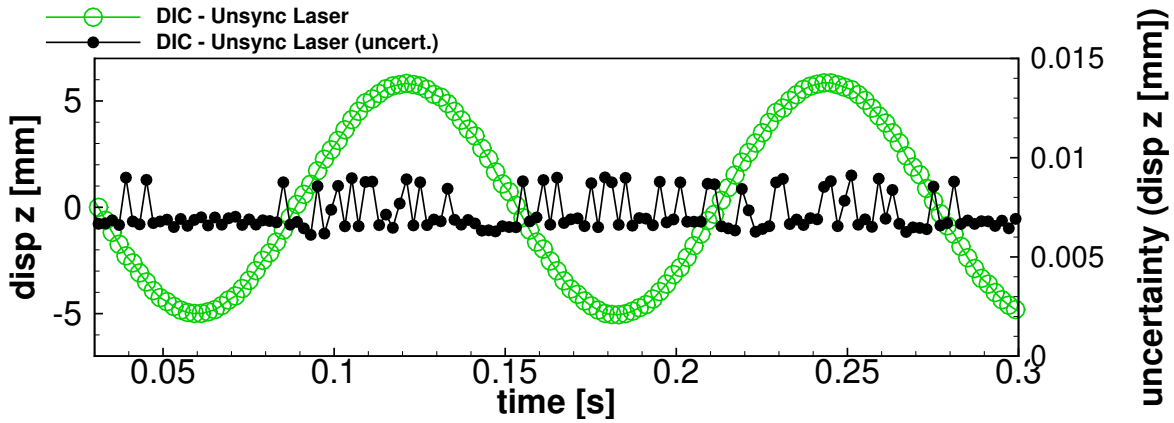

(c) Unsynchronized DIC: Laser with a pulse rate of 700 pps at the camera frame rate of 500 fps.

Figure 5.19: DIC-measurement results and uncertainties of Δz for two cycles of the flutter phenomenon analysis of case I. Comparison of the illumination by standard light and by laser light with synchronized and unsynchronized pulse rates.

is characterized by the fact that the laser pulse repetition rate is the same as the frame rate of the DIC-camera, here with 500 pps (pulses per second) and 500 fps (frames per second), respectively. The amplitude of the blue curve is identical according to the former value of standard light. The mean measurement uncertainty of the black curve is determined as $\overline{\Delta\tilde{z}} = 4\,\mu$m leading to a relative mean error of $\overline{\Delta\tilde{z}}/\mathrm{rms}(\Delta z) \cdot 100\,\% = 0.103\,\%$. This is slightly higher compared to the unsynchronized method, but still in the same order of magnitude and sufficiently small. Thus, the synchronized method delivers reliable measurement results for the flutter case. Finally, the illumination by the PIV-laser is used in an unsynchronized way in order to investigate the influence of insufficient synchronization on the DIC-measurements. For this purpose, the laser pulse repetition rate is set to 700 pps and therefore differs from the camera frame rate of 500 fps. Although Fig. 5.19(c) shows the qualitative characteristic of the flutter oscillation with the same displacement amplitude as in the former results, the measurement uncertainties are not evenly distributed, but instead, fluctuate in the limits of $7\,\mu\mathrm{m} \leq \Delta\tilde{z} \leq 9\,\mu$m with a mean value of $\overline{\Delta\tilde{z}} = 7.5\,\mu$m leading to a relative mean error of $\overline{\Delta\tilde{z}}/\mathrm{rms}(\Delta z) \cdot 100\% = 0.193\%$. This varying uncertainty is caused by the camera capturing the lambency of the laser. The higher-frequent laser pulses generate strongly varying illumination conditions for the image acquisition by the camera, which is rather unfavorable.

5.3 PIV measurements

The following section contains the unsteady wake flow analysis by the PIV measurements. Using the example of the flow at the Reynolds number of $\mathrm{Re}_c = 2.39 \times 10^4$, the adjusted fluid velocity is sufficiently high compared with the flutter case, so that unsteady phenomena like the development and convection of vortices can be observed in the wake. In addition, the captured images show high-resolution properties without blurring effects. Out of the image data, fluid-mechanical parameter are calculated. In an analogous manner, this is done for the other Reynolds numbers as well. Finally, point-wise extractions are taken from the HS-PIV-measurements in the wake, comparing the results (FFT of the velocity oscillations in time) with the previously published CTA measurements results by Wood et al. [23]. Furthermore, a relation to the structural heave and pitch motion of DIC is presented by opposing the time histories and corresponding frequencies.

5.3.1 Unsteady wake flow analysis of case I at $\mathrm{Re}_c = 2.39 \times 10^4$

Beginning with the analysis of the unsteady wake flow, Fig. 5.20 shows a time sequence of images at the freestream velocity of $U_\infty = 3.56\,\mathrm{m/s}$ corresponding to $\mathrm{Re}_c = 2.39 \times 10^4$,

where the detachment and convection of several vortices is visible. The geometry of the observed wake region has the dimensions $[x \times z] = [170\,\text{mm} \times 80\,\text{mm}]$, while the diagrams are normalized by the chord length $c = 100\,\text{mm}$ of the NACA-0012 airfoil. The trailing edge at zero angle of attack forms the geometric offset $[x, y] = [0, 0]$ of the coordinate system of the velocity field. The vertical black line in each image indicates the position of the trailing edge of the airfoil. For the velocity field of the dimensionless component w/U_∞ a resolution of $16 \times 16\,\text{px}$ is chosen for each interrogation window (IW) of the grid for the PIV-processing algorithm. During the recording time, the airfoil experiences only small amplitude oscillations (SAO), which are assumed in [23] to be the effect of the laminar separation of the boundary layer occuring successively at the upper and lower surface of the airfoil. Here, the generation of several vortices can be seen by the alternating negative (blue, $w/U_\infty = -0.10$) and positive (red, $w/U_\infty = +0.15$) velocity regions. Exemplarily, the development and convection of a vortex is followed within the image sequence, which can be noticed by the dashed black square in each snapshot. In Fig. 5.21 the distance between the trailing edge and the dashed square is plotted over the convection time of the traced vortex. There are twice as much data points included in the plot, compared with the image sequence showing the wake flow of the observed vortex: Sufficiently for the visualization purpose of convection, every second data point is presented in Fig. 5.20 as a snapshot of the wake. Exceptionally, Fig. 5.20(b) with $t = t_0 + \Delta t$ is added due to the presentation of the vortex development nearby the trailing edge. With the data points in Fig. 5.21, it is possible to calculate several characteristic parameters. Beginning with the vortex convection velocity, a linear regression reveals the relation between the vortex position and the proceeding time in the form of:

$$x_v(t) = 3.184\,\frac{\text{m}}{\text{s}} \cdot t - 0.0009391\,\text{m} \quad . \tag{5.1}$$

Thus, the vortex convection velocity is estimated by the slope of the linear regression of $x_v(t)$ with $U_{\text{cv}} = \text{d}x_v/\text{d}t = 3.184\,\text{m/s}$, which is slightly decreased compared to the free-stream velocity of $U_\infty = 3.56\,\text{m/s}$.

Furthermore, it is of interest to determine the vortex shedding frequency from the HS-PIV-data. The approximate analysis method, which has been developed within this thesis, is introduced schematically in Fig. 5.22: There are four main eddies observed in the wake flow region. The distance of eddy 4 to the trailing edge is declared as Δs_{tot}, while the distance in between each eddy is $\overline{\Delta s}$. It is the mean convection length of a vortex until the following one is generated. It can be calculated by:

$$\overline{\Delta s} = \frac{\Delta s_{\text{tot}}}{n_{\text{Eddy}}} \quad . \tag{5.2}$$

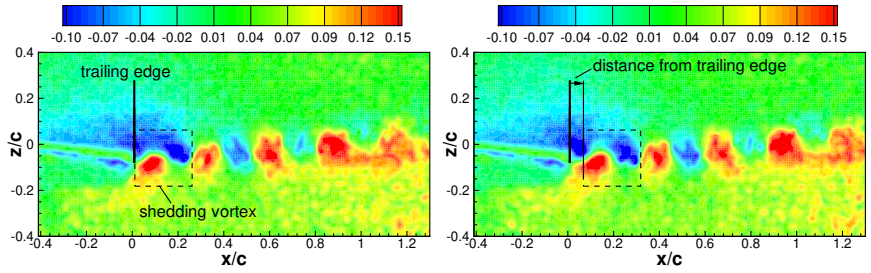

(a) t_0

(b) $t_0 + \Delta t$

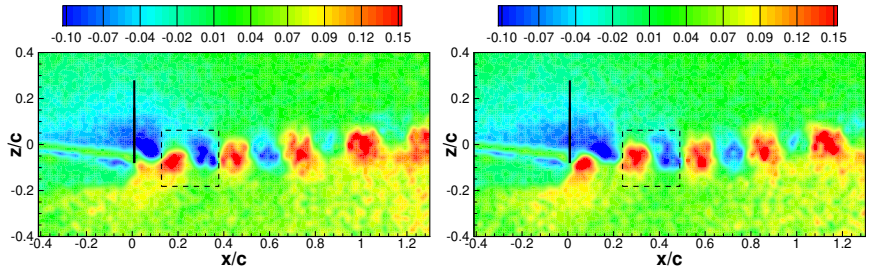

(c) $t_0 + 2\Delta t$

(d) $t_0 + 4\Delta t$

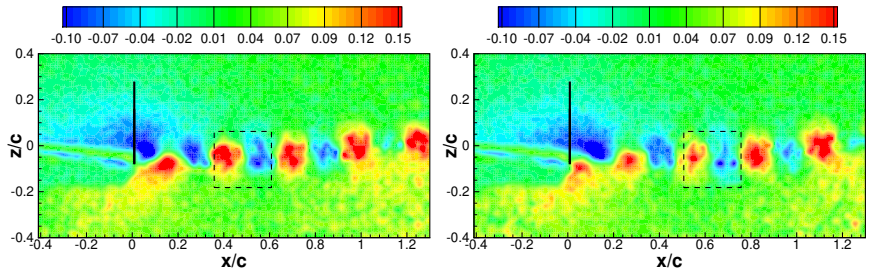

(e) $t_0 + 6\Delta t$

(f) $t_0 + 8\Delta t$

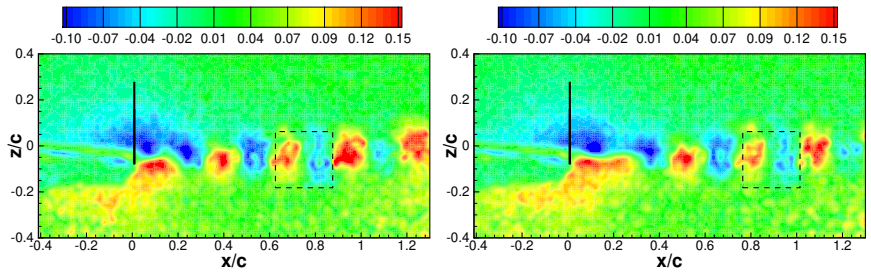

(g) $t_0 + 10\Delta t$

(h) $t_0 + 12\Delta t$

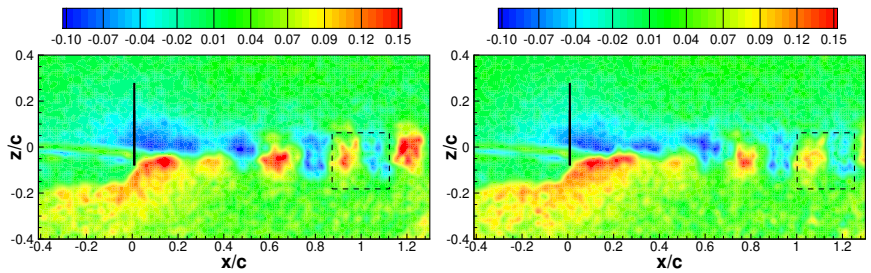

(i) $t_0 + 14\Delta t$

(j) $t_0 + 16\Delta t$

Figure 5.20: Case I: Time series of vortex shedding in the wake flow visualized by w/U_∞ at $U_\infty = 3.56\,\mathrm{m/s}$ ($\mathrm{Re}_c = 2.39 \times 10^4$) with the time step $\Delta t = 0.002\,\mathrm{s}$.

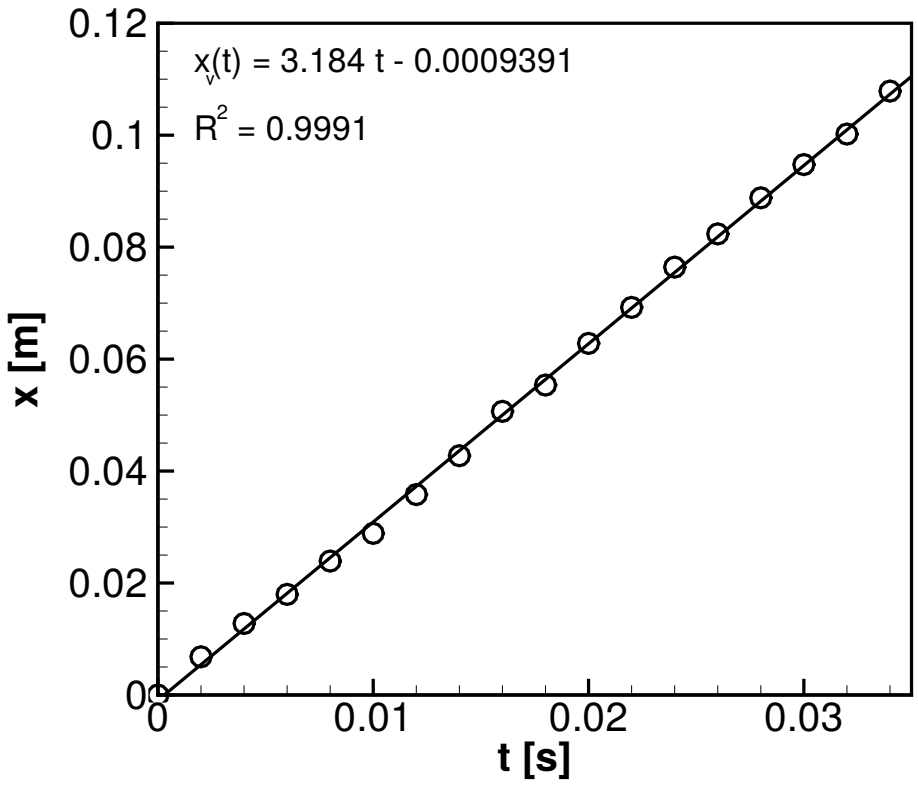

Figure 5.21: x_v-t-diagram as a linear regression across the positions of the traced shedding vortex during several instants in time. The distance x_v is measured from the trailing edge of the airfoil.

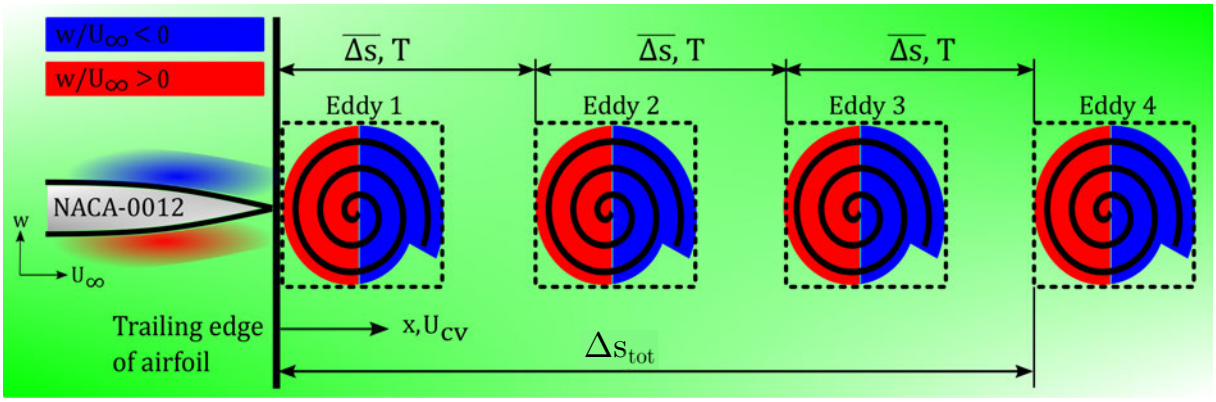

Figure 5.22: Principle of vortex shedding frequency calculation.

n_{Eddy} is the number of vortices with the last one included (eddy 4 in Fig. 5.22), that has the total distance Δs_{tot} to the trailing edge. Exemplarily according to Fig. 5.20(j), which is the 17th data-point with $t = t_0 + 16\,\Delta t$ in Fig. 5.21, it yields that

$$\overline{\Delta s} = \frac{\Delta s_{\text{tot}}(t_0 + 16\,\Delta t)}{n_{\text{Eddy}}(t_0 + 16\,\Delta t)} = \frac{0.101\,\text{m}}{4} = 0.02525\,\text{m} \quad . \tag{5.3}$$

Corresponding to the mean distance $\overline{\Delta s}$, it can be stated that the proceeding time of a vortex is the vortex shedding period T, until a following one is generated. The vortex shedding frequency f is the reciprocal value of T. The fraction can be expanded by $\overline{\Delta s}$ and rewritten with $U_{cv} = \overline{\Delta s}/T$ as follows:

$$f = \frac{1}{T} = \frac{\overline{\Delta s}}{\overline{\Delta s} \cdot T} = \frac{U_{\text{cv}}}{\overline{\Delta s}} \quad . \tag{5.4}$$

With these parameters, the dimensionless Strouhal [1] number can be calculated to characterize the unsteady wake flow and vortex shedding process. Mathematically it is defined by

$$\text{Sr} = \frac{f \cdot L}{U_\infty} \quad , \tag{5.5}$$

with the diameter or thickness L of an obstacle. According to the NACA-0012 airfoil, it is the maximum profile thickness, which results in 12% of the chord length $c = 0.1\,\text{m}$:

$$L = 0.12 \cdot c = 0.012\,\text{m} \quad . \tag{5.6}$$

Inserting Eqs. (5.6) and (5.4), the Strouhal number of Eq. (5.5) can be transformed in the current case as follows:

$$\text{Sr} = \frac{U_{\text{cv}}}{U_\infty} \cdot \frac{0.12 \cdot c}{\overline{\Delta s}} \quad . \tag{5.7}$$

Obviously, there is a relation between the vortex convection velocity and the upstream fluid velocity, as well as the profile thickness and the vortex shedding distance. For this exemplary case, the Strouhal number results in

$$\text{Sr} = \frac{U_{\text{cv}}}{U_\infty} \cdot \frac{0.12 \cdot c}{\overline{\Delta s}} = \frac{3.184\,\frac{\text{m}}{\text{s}}}{3.56\,\frac{\text{m}}{\text{s}}} \cdot \frac{0.012\,\text{m}}{0.02525\,\text{m}} = 0.4251 \quad . \tag{5.8}$$

This Strouhal number is similar to the result of the CTA-measurements of Wood et al. [23] with Sr = 0.48 at $\text{Re}_c = 3.06 \times 10^4$, where it is deduced to occuring flow instabilities in the wake, such as the shear layer roll-up with local velocity gradients nearby the trailing edge. It is a consequence of the laminar separation of the boundary layer, alternating

[1] Vincent Strouhal. Czech experimental physicist (10 April 1850 Seč - 26 January 1922 Prague).

at the upper and lower surface of the airfoil. To summarize this section, it is possible to calculate dimensionless fluid-mechanic parameters like the Strouhal number out of the spatio-temporal HS-PIV velocity measurements, which are exemplarily shown in the image sequence for the velocity component w/U_∞ in Fig. 5.20. Several vortices can be distinguished well by the alternating increased and decreased velocity regions, while their positions can be traced during the proceeding time. Thus, the High-Speed PIV-measurements are qualified for this purpose of visualization offering a precise, temporal resolution with a camera frame rate of 500 fps.

5.3.2 Characteristic parameters in the wake flow at several free-stream velocities

The exemplary calculation of the Strouhal number has been extended for the free-stream flow velocities in the range of $1.443\,\mathrm{m/s} \leq U_\infty \leq 5.665\,\mathrm{m/s}$. The airfoil's angle of attack is held at $\alpha \approx 0°$ and the position at $z = 0\,\mathrm{mm}$ to observe the pure flow instability in the wake without the influence of structural motion. The results for the Strouhal numbers as well as the intermediate results (U_{cv}, $\overline{\Delta s}$, f) are presented in Tab. 5.3 for case I and in Tab. 5.4 for case III, respectively. In Fig. 5.23, the Strouhal numbers are plotted over the corresponding Reynolds number, while the data points are connected linearly.

Table 5.3: Case I: Vortex shedding frequency and Strouhal number for different free-stream flow velocities generated by the rotation rate n of the air blower.

n [rpm]	Re_c [$\times 10^4$]	U_∞ [m/s]	U_{cv} [m/s]	$\overline{\Delta s}$ [m]	L [m]	f [Hz]	Sr [−]
116	0.966	1.443	1.372	0.01829	0.012	75.01	0.6237
166	1.65	2.453	2.057	0.01712	0.012	120.1	0.5876
221	2.39	3.560	3.184	0.02525	0.012	126.1	0.4251
270	3.06	4.554	3.814	0.01709	0.012	223.2	0.5882
325	3.60	5.665	4.611	0.01133	0.012	407.0	0.8622

Table 5.4: Case III: Vortex shedding frequency and Strouhal number for different free-stream flow velocities generated by the rotation rate n of the air blower.

n [rpm]	Re_c [$\times 10^4$]	U_∞ [m/s]	U_{cv} [m/s]	$\overline{\Delta s}$ [m]	L [m]	f [Hz]	Sr [−]
116	0.966	1.443	1.363	0.01848	0.012	73.78	0.6134
166	1.65	2.453	2.204	0.02420	0.012	91.09	0.4456
221	2.39	3.560	3.202	0.02009	0.012	159.4	0.5366
270	3.06	4.554	4.011	0.02059	0.012	194.8	0.5132
325	3.60	5.665	4.718	0.01887	0.012	250.0	0.5296

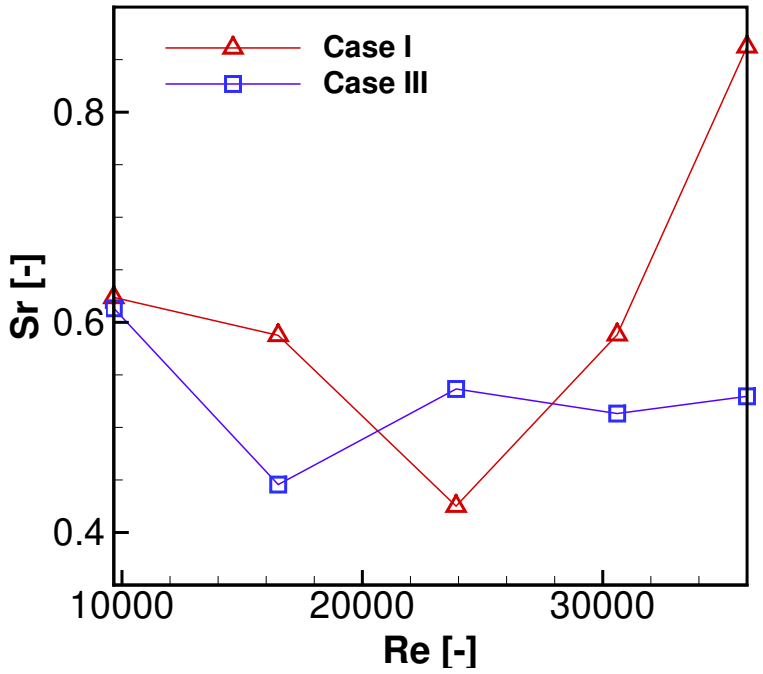

Figure 5.23: Strouhal number development at various Reynolds numbers for case I and III. Discrete data points are connected by linear lines.

In case I (red curve), the Strouhal number begins with Sr = 0.6237 at Re = 9.66×10^3. After exceeding a local maximum at Re = 1.25×10^4, it decreases with the increasing fluid velocity and reaches the global minimum with Sr = 0.4251 at Re = 2.39×10^4, which is identical with Eq. (5.8). However, the Strouhal number is increasing up to Sr = 0.8622 at the Reynolds number of Re = 3.60×10^4, which is the flutter case. For case III (blue curve), the Strouhal number begins at Sr = 0.6134 at Re = 9.66×10^3, which is similar to case I. The global minimum with Sr $\approx$ 0.43 at Re = 1.5×10^4 is reached faster. Then it increases until it levels off to Sr = 0.5296 at Re = 3.60×10^4, which is lower than in case I. It can be explained by the fact that the center of gravity is shifted backwards in case III, stabilizing the airfoil. However, it can be expected that the Strouhal number increases for higher Reynolds numbers in both cases, causing stronger structural oscillations and flow instabilities of higher frequency. At this point it may be mentioned that the results are calculated from the instationary observation of the vortex convection in the wake by HS-PIV. For each Reynolds number, one PIV-measurement was executed. Due to the fact that there are no replication measurements, which means an expenditure of time and storage capacity, statistical deviations can occur within the results. Nevertheless, a comparability with the results in [23] is given and can be seen also in the following subsections.

5.3.3 Frequency spectra in the wake flow at several free-stream velocities

In this part, the fluctuations of the velocity field in the wake region are discussed for a defined monitoring point based on the high-speed PIV-measurements. This point-wise fluid analysis is compared with the point-wise structural analysis of the DIC- and with the CTA-measurements, which have been published by Wood et al. [23]. It is of interest to find out, if similar frequencies can be observed in the PIV-measurements and which of them are mainly influencing the oscillations or the flow instability. To give a brief overview of all monitoring points, Fig. 5.24 depicts the locations of DIC, PIV and CTA [23]: The DIC monitoring point is located on the upper surface of the airfoil, which has a distance of $x = 0.07\,\mathrm{m}$ to the leading edge for case I or $x = 0.02\,\mathrm{m}$ for case III, respectively, measuring the displacements in z-direction. The PIV monitoring point is positioned at $x = 0.15\,\mathrm{m}$ from the leading edge measuring the velocity fluctuations in horizontal direction u and vertical direction w in [m/s]. The CTA-sensor [23] is located one chord length from the trailing edge, in other words at $x = 0.2\,\mathrm{m}$ revealing the averaged power spectral density of the fluid fluctuations in the wake of the airfoil.

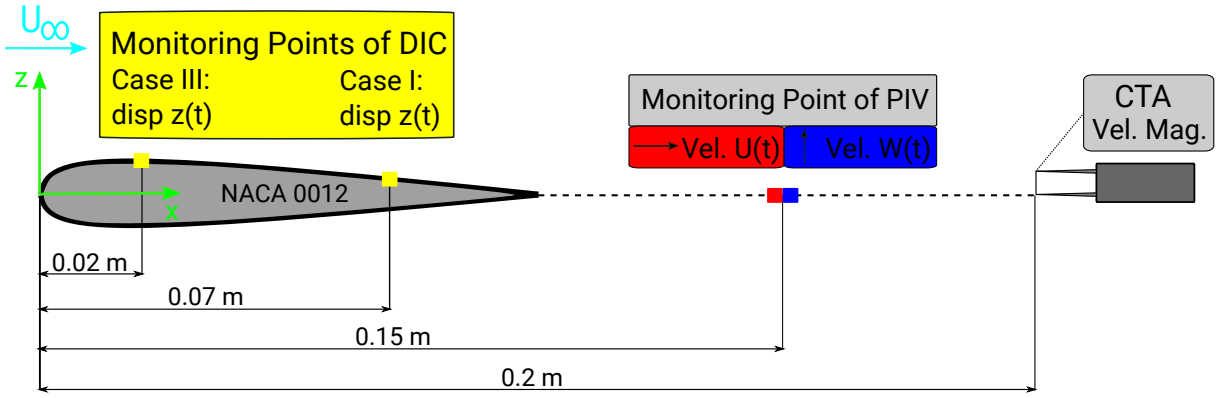

Figure 5.24: Position of the monitoring points for all measurement series (DIC: disp z of case I/III, PIV: vel. u and vel. w, CTA-sensor [23]).

5.3.3.1 Case I

The point-wise PIV-measurements for case I are depicted in Fig. 5.25 up to Fig. 5.31 for the known free-stream velocity range $1.443\,\mathrm{m/s} \leq U_\infty \leq 5.665\,\mathrm{m/s}$. There are time histories and FFT-plots of the fluid velocity component u (red curve, above) as well as w (blue curve, below).

Beginning with Fig. 5.25 the rotation rate of the blower in the wind tunnel is adjusted to $n = 116\,\mathrm{rpm}$, so the free-stream velocity is $U_\infty = 1.443\,\mathrm{m/s}$. A first impression is given by

the time histories. Especially for the vertical velocity component w, the characteristic of the curve is associated with the time history of the structure measured by DIC depicted in Fig. 5.7 showing the damped oscillation and the beat phenomenon. Considering the FFT-plots, the velocity component u shows a main frequency peak at $f_u = 8.43\,\mathrm{Hz}$. This frequency is also visible in the FFT-plot of the velocity component w. Comparing with the corresponding DIC-measurements, this is very similar to the pitch-frequency of the oscillating structure, which is $f_\alpha = 8.467\,\mathrm{Hz}$ for the unsynchronized and $f_\alpha = 8.504\,\mathrm{Hz}$ for the synchronized DIC-measurements. It is comprehensible that it is a rotational movement including displacements in x- and z-direction. This has an impact on both of the velocity components u and w in the wake. Furthermore, the heave frequency of the DIC-measurements relates to the pure displacement in the vertical z-direction, which is $f_h = 7.487\,\mathrm{Hz}$ for the unsynchronized and $f_h = 7.504\,\mathrm{Hz}$ for the synchronized DIC-measurements. It matches the first frequency of $f_{w,1} = 7.41\,\mathrm{Hz}$ in the FFT-plot of the vertical velocity component w. Regarding the graph of both FFT-plots, the course of the curve at higher frequencies shows a turbulent decay effect. The background of this lays in the oscillating airfoil structure, which causes several high-frequency local velocity fluctuations in different directions that are captured point-wise by the monitoring point in the wake. The FFT results in many high-frequency and tightly neighbored peaks. Especially in the FFT-plot of the w-component, there are two higher frequencies pointing out of the blurring curve with $f_{w,3} = 98\,\mathrm{Hz}$ and a duplicate one with $f_{w,4} = 196\,\mathrm{Hz}$. These are usually indications for flow instabilities, i.e., a shear layer roll-up in the wake, as explained by Wood et al. [23].

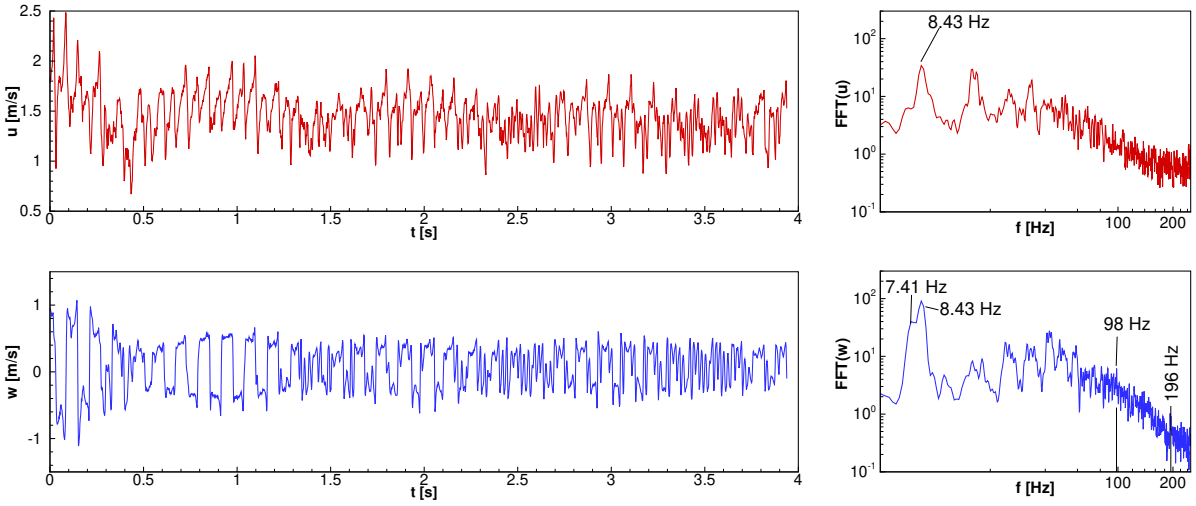

Figure 5.25: Oscillation of fluid velocity components u (above) and w (below) recorded at a fixed wake monitoring point $[x, z] = [150, 0]\,\mathrm{mm}$ by high-speed PIV. Time and FFT-plots of case I, $n = 116\,\mathrm{rpm}$, $U_\infty = 1.443\,\mathrm{m/s}$, $\mathrm{Re}_c = 9.66 \times 10^3$.

Continuing with Fig. 5.26 with the free-stream velocity $U_\infty = 2.46\,\mathrm{m/s}$ ($n = 166\,\mathrm{rpm}$), the time history of the velocity component w has similar characteristics as the DIC-measurements in Fig. 5.8 showing the temporal oscillation of the structure in z-direction (damping, beat). The FFT of the velocity components u and w contain again the pitch-frequency of $f_u = f_{w,2} = 8.43\,\mathrm{Hz}$, which is nearly equivalent to the unsynchronized DIC-measurement with $f_\alpha = 8.378\,\mathrm{Hz}$ and to the synchronized one with $f_\alpha = 8.254\,\mathrm{Hz}$, respectively. Furthermore, the heave frequency, which is $f_h = 7.487\,\mathrm{Hz}$ (unsynchronized DIC) and $f_h = 7.504\,\mathrm{Hz}$ (synchronized DIC), is present in the FFT of the vertical velocity component w with $f_{w,1} = 7.41\,\mathrm{Hz}$. Additionally, in the high-frequency course of the curve a peak at $f_{w,3} = 131\,\mathrm{Hz}$ is observed, which is matching approximately with the vortex shedding frequency in Tab. 5.3 with $f(n = 166\,\mathrm{rpm}) = 120.1\,\mathrm{Hz}$.

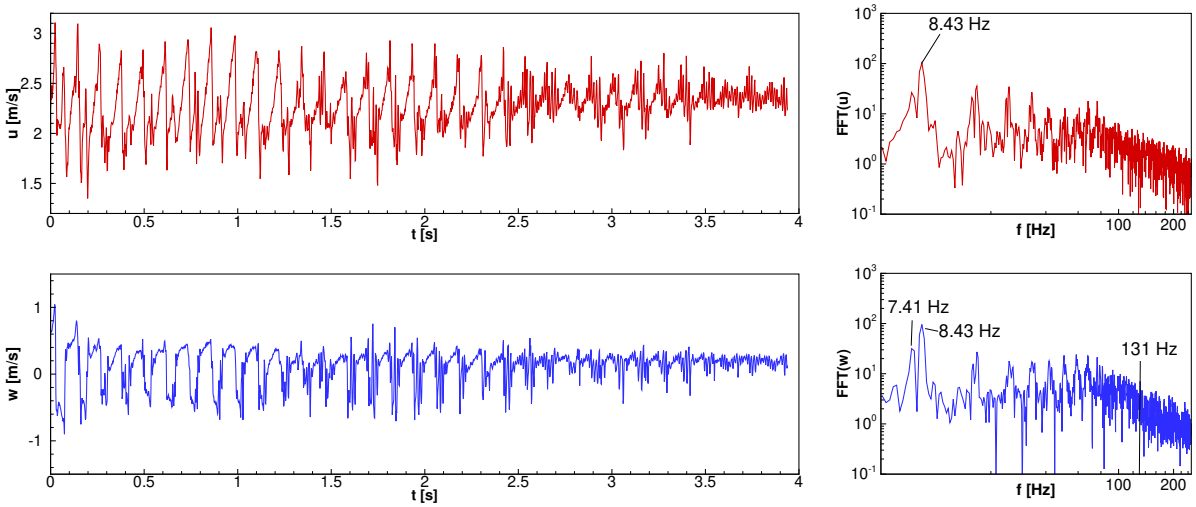

Figure 5.26: Oscillation of fluid velocity components u (above) and w (below) recorded at a fixed wake monitoring point $[x, z] = [150, 0]\,\mathrm{mm}$ by high-speed PIV. Time and FFT-plots of case I, $n = 166\,\mathrm{rpm}$, $U_\infty = 2.46\,\mathrm{m/s}$, $\mathrm{Re}_c = 1.65 \times 10^4$.

Going on with Fig. 5.27 with the free-stream velocity $U_\infty = 3.56\,\mathrm{m/s}$ ($n = 221\,\mathrm{rpm}$), the time histories are rather difficult to compare with the corresponding structural oscillations of the DIC-measurements in Fig. 5.9. However, the FFT-plots give information about the main frequencies. Like in the former investigations, the pitch frequencies of DIC with $f_\alpha = 8.2\,\mathrm{Hz}$ (unsynchronized) and $f_\alpha = 8.254\,\mathrm{Hz}$ (synchronized) are represented as frequency peaks in the FFT-plots of the u- and w-velocity component $f_{u,2} = f_{w,1} = 8.27\,\mathrm{Hz}$. The heave frequency peak in the FFT of the DIC-measurements with $f_h = 7.398\,\mathrm{Hz}$ (unsynchronized) and $f_h = 7.254\,\mathrm{Hz}$ (synchronized) is strongly decreased. Remarkable here is that it appears in the FFT of the horizontal velocity component u with $f_{u,1} = 7.27\,\mathrm{Hz}$. The frequency peak is also strongly decreased. In the FFT-plot of the w-component, a much smaller peak at this specific frequency is also visible. It can be assumed that because

of the increased free-stream velocity the vertical heave motion of the structure has an impact on both velocity components in the wake. Additionally, in the high-frequency range of the FFT, the turbulent decay is visible. The separated flows are sent out in several directions of the wake as a trace of the trailing edge of the airfoil. Due to the fact that the PIV-measurement is done at a fixed point in the wake, which is not moving with the airfoil it leads to the blurring effect in the FFT. Nevertheless, there are two frequencies highlighted, $f_{u,3} = 154\,\mathrm{Hz}$ and $f_{w,2} = 121\,\mathrm{Hz}$. The second one is nearly identical to the calculated frequency in Tab. 5.3 with $f(n = 221\,\mathrm{rpm}) = 126.1\,\mathrm{Hz}$, which is characteristic for the shear layer roll-up in the wake.

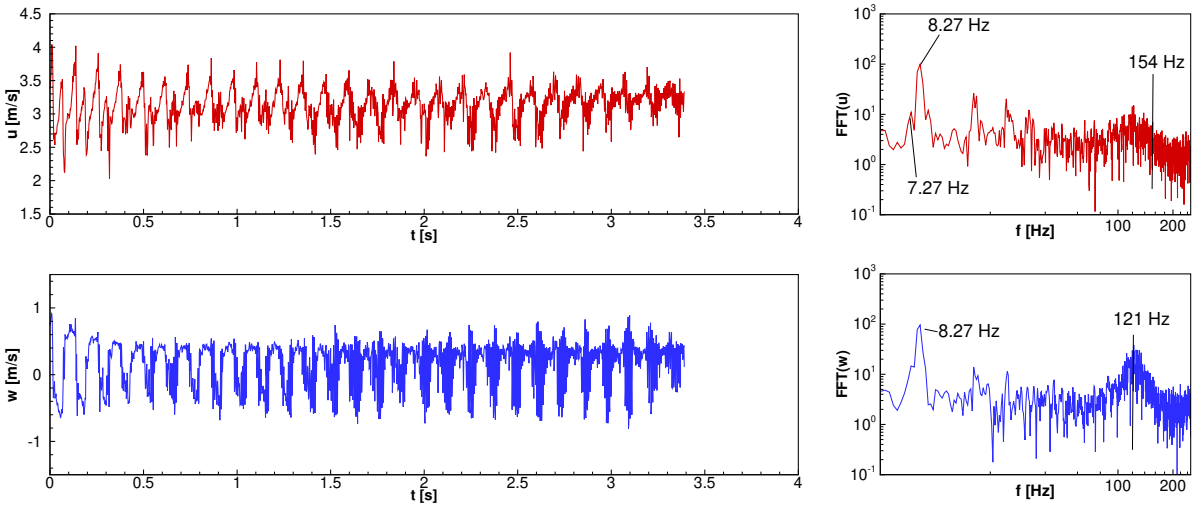

Figure 5.27: Oscillation of fluid velocity components u (above) and w (below) recorded at a fixed wake monitoring point $[x, z] = [150, 0]\,\mathrm{mm}$ by high-speed PIV. Time and FFT-plots of case I, $n = 221\,\mathrm{rpm}$, $U_\infty = 3.56\,\mathrm{m/s}$, $\mathrm{Re}_c = 2.39 \times 10^4$.

Before discussing the characteristics of Fig. 5.29 with the free-stream velocity of $U_\infty = 4.56\,\mathrm{m/s}$ ($n = 270\,\mathrm{rpm}$), it may be indicated to take a look at the data of Wood et al. [23] containing point-wise hot-film CTA-measurements in the wake flow. This has been realized by applying the Constant Temperature Anemometer (CTA), which is located at $[x, z] = [200, 0]\,\mathrm{mm}$ and has the sampling rate of 2000 Hz and the recording time span of 500 s. In the post-processing the temporal fluctuations of the fluid velocity are transformed into a power spectral density plot, which reveals the characteristic frequencies. The diagrams can be seen in Fig. 5.28: In Fig. 5.28(b), the CTA-measurement is done for the rigid airfoil, which does not allow any pitch or heave motion of the structure. Looking at this PSD-diagram, there is a frequency peak at $f_{CTA,CV} = 183\,\mathrm{Hz}$ and higher harmonic ones. From the perspective that the airfoil does not move here, these frequencies can be related only to the flow instabilities that are generated by the shear layer rolling up behind the trailing edge of the airfoil, i.e., the shedding of vortices in the wake. In Fig. 5.28(a) it can

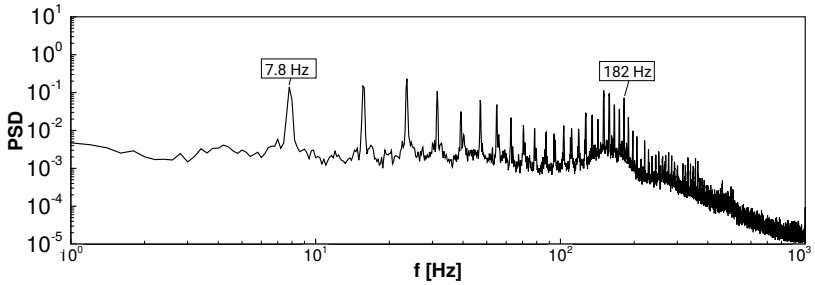

(a) Oscillating airfoil.

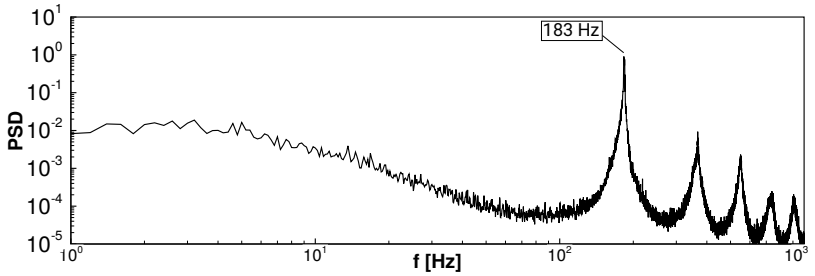

(b) Rigid airfoil at $\alpha = 0°$.

Figure 5.28: CTA measurements of the LAO phenomenon for case I by Wood et al. [23]. Monitoring point location $[x, z] = [200, 0]\,\text{mm}$, $n = 270\,\text{rpm}$, $U_\infty = 4.55\,\text{m/s}$, $\text{Re}_c = 3.06 \times 10^4$.

be seen that these high frequencies are still visible, unfortunately there appears the already known blurring effect. As already mentioned, this can be deduced to the motion of the airfoil, which has a blurring impact on the CTA-measurement, disturbing the pure flow instability oscillations as in the rigid airfoil case. However, in the lower frequency range, there is one frequency peak clearly visible, which is $f_{CTA,LCO} = 7.8\,\text{Hz}$. It can be assumed that its origin lays in the structural motion of the airfoil. The corresponding DIC-measurements in Fig. 5.10 show a limit-cycle-oscillation (LCO) with a frequency of $f_{DIC,LCO} = 8.111\,\text{Hz}$ and a strongly damped heave peak at $f_h = 7.487\,\text{Hz}$ for the unsynchronized method. The synchronized method delivers one LCO-frequency at $f_{DIC,LCO} = 8.004\,\text{Hz}$. Comparing these results to the point-wise measurements of the velocity components u and w in Fig. 5.29, both time histories show a constant large amplitude oscillation (LAO). Both FFT-plots contain the LCO-frequency at $f_{u,1} = f_{w,2} = 8.14\,\text{Hz}$. The w-component has also a strongly damped frequency at $f_{w,1} = 7.24\,\text{Hz}$, which is similar to the strongly damped heave frequency f_h mentioned above for the unsynchronized DIC method. Furthermore, in the higher frequency range the blurring effect is increased in both FFT-plots: The u-component shows a frequency peak of $f_{u,2} = 182\,\text{Hz}$, while the w-component shows one at $f_{w,3} = 149\,\text{Hz}$. Remarkable here is that the frequency of the streamwise velocity component u is confirmed by $f_{CTA,CV} = 183\,\text{Hz}$ of the CTA-measurement, which stands for the pure shear layer roll-up.

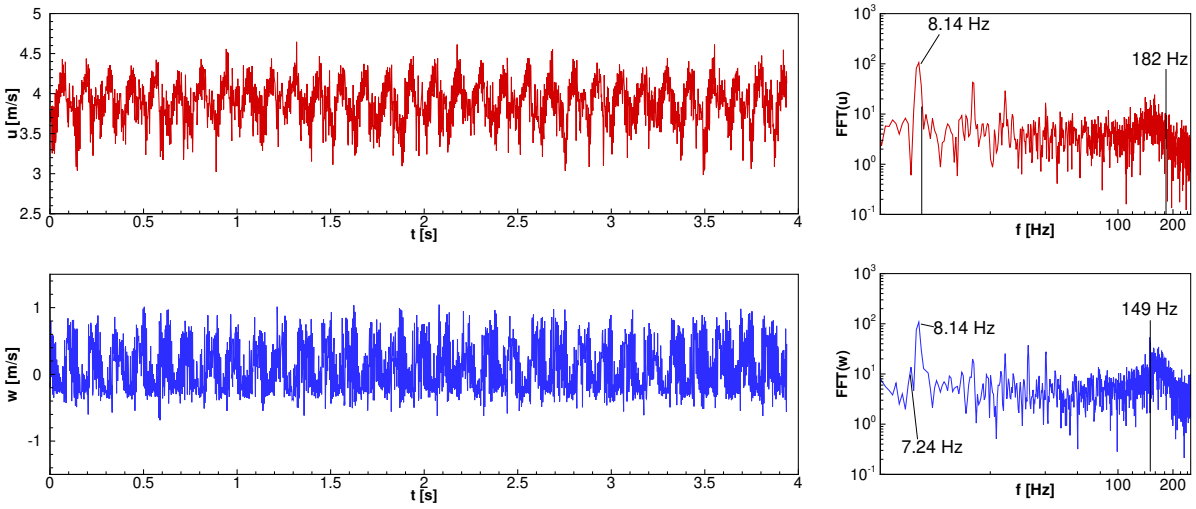

Figure 5.29: Oscillation of fluid velocity components u (above) and w (below) recorded at a fixed wake monitoring point $[x, z] = [150, 0]$ mm by high-speed PIV. Time and FFT-plots of case I, $n = 270$ rpm, $U_\infty = 4.55$ m/s, $\mathrm{Re}_c = 3.06 \times 10^4$.

Before concluding with the analysis of Fig. 5.31, the corresponding CTA-results of Wood et al. [23] in Fig. 5.30 are focused. The measuring location stays the same as for the LAO case. The free-stream velocity is adjusted to $\mathrm{Re} = 3.60 \times 10^4$. In Fig. 5.30(b), the flow instability due to the roll-up of the shear layer behind the trailing edge of the airfoil is characterized by the frequency $f_{CTA,CV} = 222$ Hz and higher harmonics. Removing the

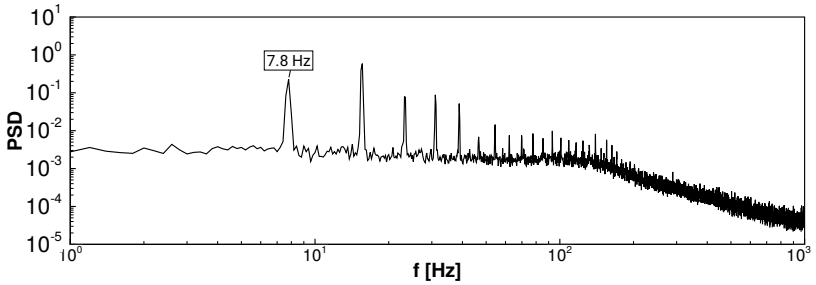

(a) Oscillating airfoil.

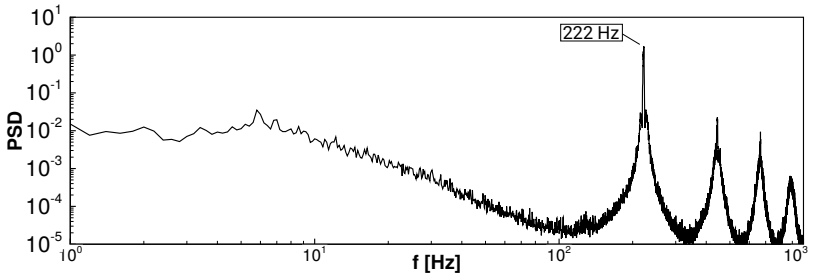

(b) Rigid airfoil at $\alpha = 0°$.

Figure 5.30: CTA measurements of the flutter phenomenon for case I by Wood et al. [23]. Monitoring point location $[x, z] = [200, 0]$ mm. $U_\infty = 5.665$ m/s, $\mathrm{Re} = 3.60 \times 10^4$.

motion blocking, Fig. 5.30(a) shows the expected blurring effect. There is no frequency peak visible in the region between 10^2 Hz and 10^3 Hz. The reason is the flutter motion with highly increased amplitudes of the airfoil, causing flow instabilities in the wake region. The fixed point-wise CTA-measurements denote high-frequent velocity fluctuations. At the lower frequency range of Fig. 5.30(a), one first peak with $f_{CTA,flutter} = 7.8\,\text{Hz}$ identical to $f_{CTA,LCO}$ from Fig. 5.28(a) is found. This frequency is representative for the structural flutter motion of the airfoil, which has an impact on the fluid flow oscillations in the wake. In the DIC-measurements of Fig. 5.17, there are structural flutter frequencies analyzed at $f_{DIC,flutter} = 7.932\,\text{Hz}$ (unsynchronized) and $f_{DIC,flutter} = 8.004\,\text{Hz}$ (synchronized), which are very similar to $f_{CTA,flutter}$ of the CTA-measurement. Now, comparing these results with the point-wise PIV-measurements for the velocity components u and w in Fig. 5.31 with $U_\infty = 5.665\,\text{m/s}$ ($n = 325\,\text{rpm}$), the blurring effect in the higher frequency range confirms the CTA-result of Fig. 5.30(a). However, the structural flutter frequency of the airfoil is visible in both FFT-plots with $f_u = f_w = 7.79\,\text{Hz}$. This identical result for u and w is comprehensible since the flutter frequency is a merging of the former separated heave and pitch frequencies. Thus, it contains horizontal as well as vertical displacements, which influences the horizontal and vertical velocity components in the wake flow in an equal manner.

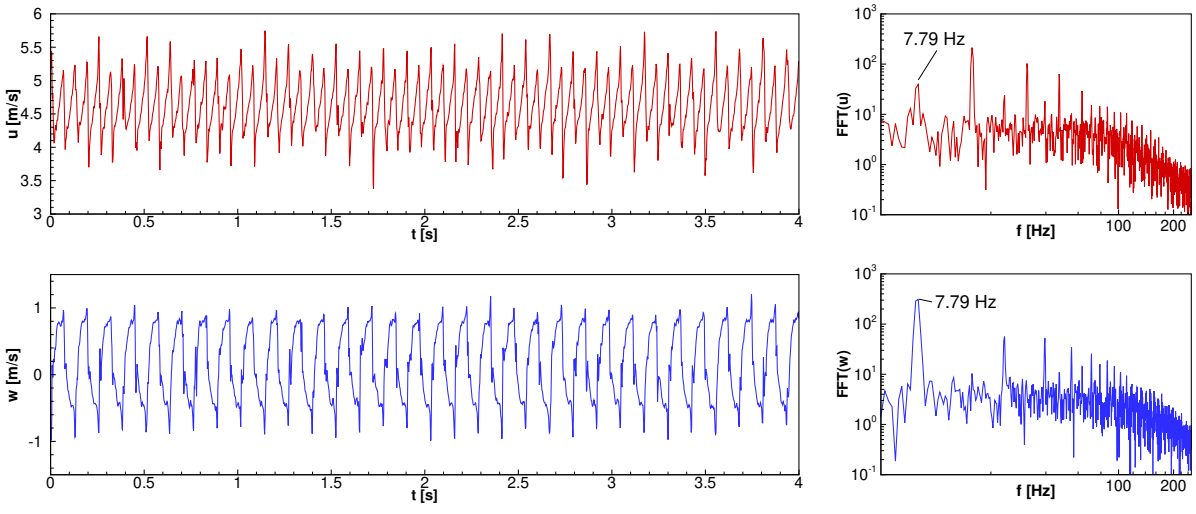

Figure 5.31: Oscillation of fluid velocity components u (above) and w (below) recorded at a fixed wake monitoring point $[x, z] = [150, 0]\,\text{mm}$ by high-speed PIV. Time and FFT-plots of case I, $n = 325\,\text{rpm}$, $U_\infty = 5.665\,\text{m/s}$, $\text{Re}_c = 3.60 \times 10^4$.

5.3.3.2 Case III

Complementary to case I, the point-wise PIV-measurements are recorded for case III in Fig. 5.32 up to Fig. 5.37 in the identical free-stream velocity range. Again, the time- and FFT-plots are shown for the fluid velocity component u (red curve, above) as well as w (blue, below).
Starting with Fig. 5.32 with the free-stream velocity of $U_\infty = 1.443\,\mathrm{m/s}$ ($\mathrm{Re}_c = 9.66 \times 10^3$), the time histories are difficult to compare with the corresponding DIC-measurement results of Fig. 5.13 according to the damping and beat phenomena. Nevertheless, the FFT-plots reveal the main frequencies of the oscillations in the fluid. In the lower frequency range, there are two dominating peaks visible for the velocity component w, from which the second frequency appears also at the velocity component u, with $f_{w,1} = 6.65\,\mathrm{Hz}$ and $f_{w,2} = f_{u,1} = 8.72\,\mathrm{Hz}$. In comparison with the FFT-results of the DIC-measurement in Fig. 5.13(b), $f_{w,1}$ is close to the structural heave frequency of $f_h = 6.753\,\mathrm{Hz}$ (synchronized) and $f_h = 6.774\,\mathrm{Hz}$ (unsynchronized). Since the pitch oscillation of the airfoil is of rotational kind with $f_\alpha = 8.754\,\mathrm{Hz}$ (synchronized) and $f_\alpha = 8.734\,\mathrm{Hz}$ (unsynchonized), the pitch frequency f_α has an impact on the vertical and horizontal fluid velocity oscillations with $f_{w,2} = f_{u,1}$. In the higher frequency range of w, although the turbulent decay process is present, one frequency of $f_{w,3} = 115\,\mathrm{Hz}$ is still observable, assuming the flow instability due to the shear layer roll-up in the wake.

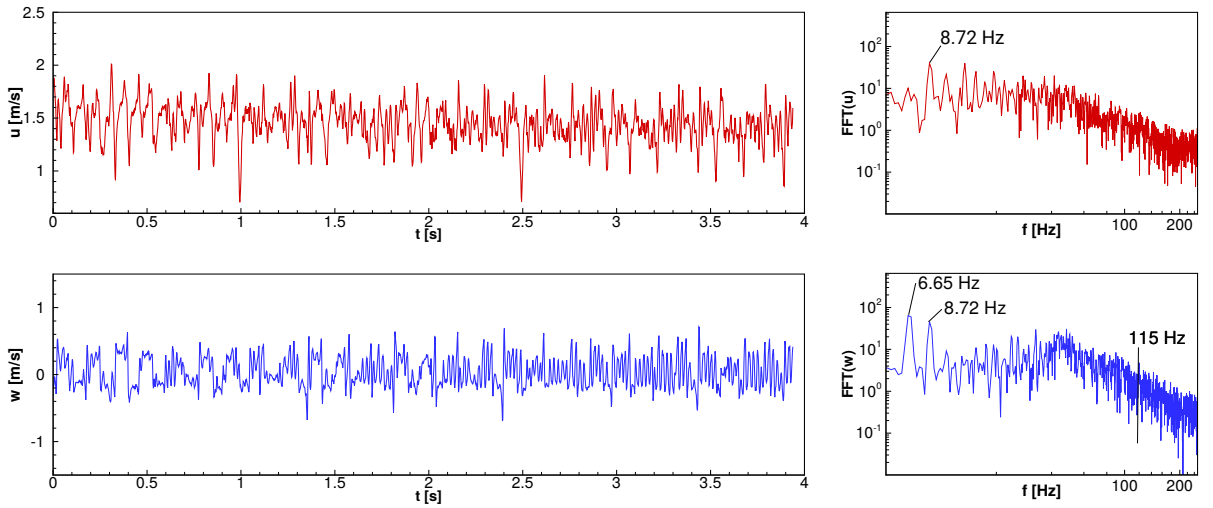

Figure 5.32: Oscillation of fluid velocity components u (above) and w (below) recorded at a fixed wake monitoring point $[x, z] = [150, 0]$ mm by high-speed PIV. Time and FFT-plots of case III, $n = 116\,\mathrm{rpm}$, $U_\infty = 1.443\,\mathrm{m/s}$, $\mathrm{Re}_c = 9.66 \times 10^3$.

Going on with Fig. 5.33 with $U_\infty = 2.46\,\mathrm{m/s}$ ($\mathrm{Re}_c = 1.65 \times 10^4$), the time history oscillations of u and w exhibit velocity fluctuations, which are difficult to compare with the

DIC-measurements of Fig. 5.14. However, it is remarkable that the FFT-plots reveal two identical frequency peaks for both velocity components. The first frequency of u and w with $f_{u,1} = f_{w,1} = 6.85\,\text{Hz}$ can be assigned to the heave frequency of the DIC-results in Fig. 5.14(b) with $f_h = 6.753\,\text{Hz}$ (synchronized) and $f_h = 6.684\,\text{Hz}$ (unsynchronized). The second frequency of u and w with $f_{u,2} = f_{w,2} = 8.60\,\text{Hz}$ is influenced by the pitch frequency of the DIC-results with $f_\alpha = 8.504\,\text{Hz}$ (synchronized) and $f_\alpha = 8.645\,\text{Hz}$ (unsynchronized). The higher frequency range denotes again a turbulent decay process, which though reveals two significant frequencies at $f_{w,3} = 128\,\text{Hz}$ and $f_{w,4} = 167\,\text{Hz}$ which can be related again to the flow instabilities.

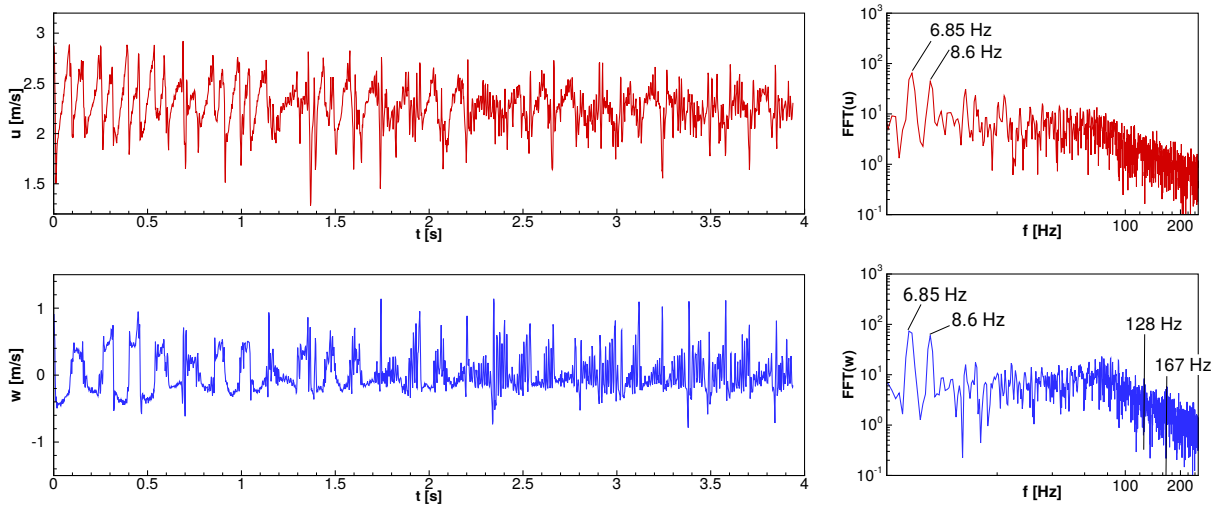

Figure 5.33: Oscillation of fluid velocity components u (above) and w (below) recorded at a fixed wake monitoring point $[x, z] = [150, 0]$ mm by high-speed PIV. Time and FFT-plots of case III, $n = 166\,\text{rpm}$, $U_\infty = 2.46\,\text{m/s}$, $\text{Re}_c = 1.65 \times 10^4$.

Moving on with Fig. 5.34 with $U_\infty = 3.56\,\text{m/s}$ ($\text{Re}_c = 2.39 \times 10^4$), both time histories show an almost regular oscillation starting at $t = 1.5\,\text{s}$ with high-frequency contents, while the magnitude of the horizontal velocity component is dominating with $u = (3.2 \pm 0.5)\,\text{m/s}$ and the vertical velocity component is at $w = (0.3 \pm 0.7)\,\text{m/s}$. Considering the FFT-plots, as for the former set flow velocity, the first and second frequency peaks are visible for u as well as for w with $f_{u,1} = f_{w,1} = 6.74\,\text{Hz}$ and $f_{u,2} = f_{w,2} = 8.56\,\text{Hz}$, which correspond to the DIC-results of Fig. 5.15. The heave frequencies $f_h = 6.753\,\text{Hz}$ (synchronized) and $f_h = 6.774\,\text{Hz}$ (unsynchronized) are similar to $f_{u,1}$ and $f_{w,1}$. The pitch frequencies $f_\alpha = 8.504\,\text{Hz}$ (synchronized) and $f_\alpha = 8.556\,\text{Hz}$ (unsynchronized) are similar to $f_{u,2}$ and $f_{w,2}$, respectively. From the turbulent decay process in the higher frequencies, two significant frequencies at $f_{u,3} = f_{w,3} = 128\,\text{Hz}$ and $f_{u,4} = f_{w,4} = 238\,\text{Hz}$ can be observed for u and w due to the flow instabilities.

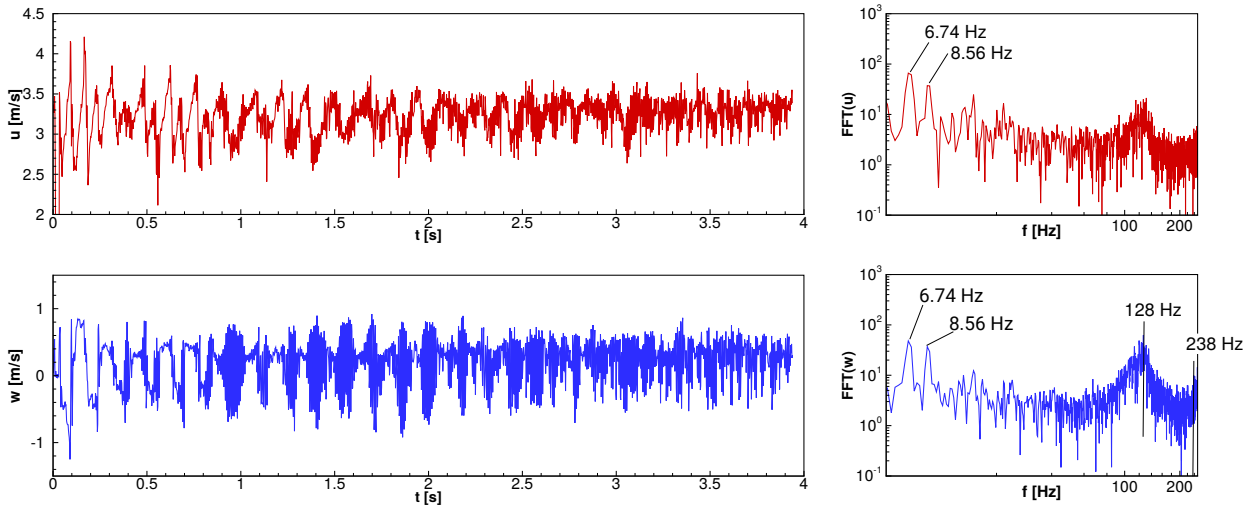

Figure 5.34: Oscillation of fluid velocity components u (above) and w (below) recorded at a fixed wake monitoring point $[x, z] = [150, 0]$ mm by high-speed PIV. Time and FFT-plots of case III, $n = 221$ rpm, $U_\infty = 3.56$ m/s, $\mathrm{Re}_c = 2.39 \times 10^4$.

In Fig. 5.35 with $U_\infty = 4.56$ m/s $\mathrm{Re}_c = 3.06 \times 10^4$, both time histories show regular oscillations starting at $t = 1.0$ s with lower-frequency contents, while the magnitudes slightly increased compared to the former case with $u = (4.25 \pm 0.25)$ m/s and $w = (0.4 \pm 0.2)$ m/s. Regarding the FFT-plots, again, the first and second frequency peaks are visible for u as well as for w with $f_{u,1} = f_{w,1} = 6.64$ Hz and $f_{u,2} = f_{w,2} = 8.27$ Hz, which can be related to the DIC-results of Fig. 5.16. While the heave frequency peak of the synchronized method is strongly damped at $f_h = 7.004$ Hz, the unsychronized one at $f_h = 6.774$ Hz is comparable to $f_{u,1}$ and $f_{w,1}$. The pitch frequency $f_\alpha = 8.254$ Hz (synchronized) and $f_\alpha = 8.289$ Hz (unsynchronized) coincide with $f_{u,2}$ and $f_{w,2}$, respectively. In the higher frequency range, one significant frequency at $f_{u,3} = f_{w,3} = 170$ Hz can be observed and compared to the calculated vortex detachment frequency $f(n = 270\,\mathrm{rpm}) = 194.8$ Hz listed in Tab. 5.4.
Finally, before presenting the results for the flutter phenomenon, CTA-measurements by Wood et al. [23] are discussed in the wake at the flutter velocity of $\mathrm{Re} = 3.39 \times 10^4$, from which the PSD-results are depicted in Fig. 5.36. Considering the case of the rigid airfoil in Fig. 5.36(b), which is bound in the heave and pitch DOF with a fixed pitch angle of $\alpha = 0°$, there are several peaks measured in the higher frequency range at $f_{CTA,rigid} = 208$ Hz and multiple higher harmonics. The calculated Strouhal number of $\mathrm{Sr} = 0.49$ is similar to the currently calculated result of $\mathrm{Sr} = 0.5296$ listed in Tab. 5.4. Those higher frequencies can be related to the shear-layer instability originating from the detachment of the boundary layer from the trailing edge. In contrast, Fig. 5.36(a) shows the results in the wake for the case of the oscillating airfoil. Here, the higher frequency peaks vanish, due to the fact that the airfoil is able to move and the flow instabilities can not develop continuously

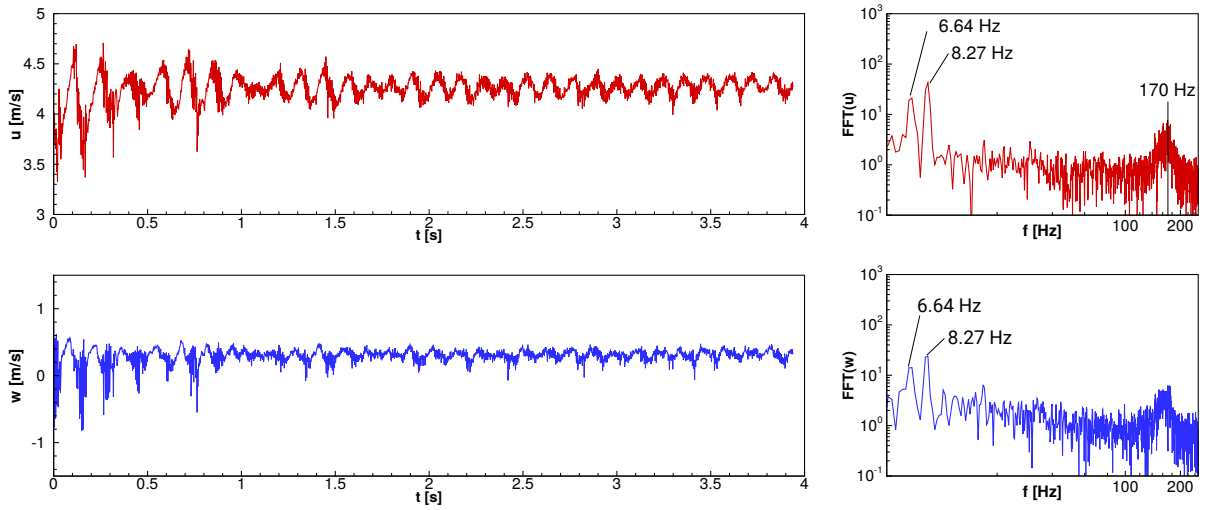

Figure 5.35: Oscillation of fluid velocity components u (above) and w (below) recorded at a fixed wake monitoring point $[x, z] = [150, 0]$ mm by high-speed PIV. Time and FFT-plots of case III, $n = 270$ rpm, $U_\infty = 4.56$ m/s, $\mathrm{Re}_c = 3.06 \times 10^4$.

in the direction of the the fixed CTA-probe like in the case of the rigid airfoil. Instead, the shear layer adapts with the airfoil motion, causing a blurring effect in the point-wise CTA-measurement results. However, in the lower frequency range, there are frequency peaks of similar harmonics visible. The first one is at $f_{CTA,oscillate} = 7.8$ Hz, which can be deduced from the flutter frequency of the oscillating wing system: The correspondent DIC-measurements of Fig. 5.17 reveal the flutter frequencies $f_{DIC,flutter} = 8.004$ Hz (synchronized) and $f_{DIC,flutter} = 8.111$ Hz (unsynchronized).

Now, focussing on the point-wise PIV-measurements in the wake with $U_\infty = 5.665$ m/s ($\mathrm{Re}_c = 3.60 \times 10^4$), Fig. 5.37 shows for the velocity components u and w regular oscillations in the time histories with $u = (4.5 \pm 1.0)$ m/s and $w = (0.1 \pm 1)$ m/s. The FFT-plots reveal the expected blurring effect in the higher frequency range as for the CTA-measurements [23]. Looking at the lower frequency range, there is one frequency visible at $f_u = f_w = 8.02$ Hz which is the dominating frequency of the oscillations in the time history for u and w and conforms to the flutter frequencies determined by DIC, mentioned above. To conclude, the flutter movement of the airfoil influences entirely the measured velocity fluctuations in vertical and horizontal direction, here.

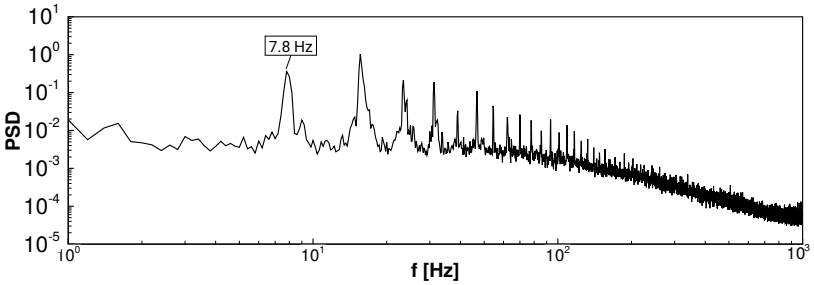

(a) Oscillating airfoil.

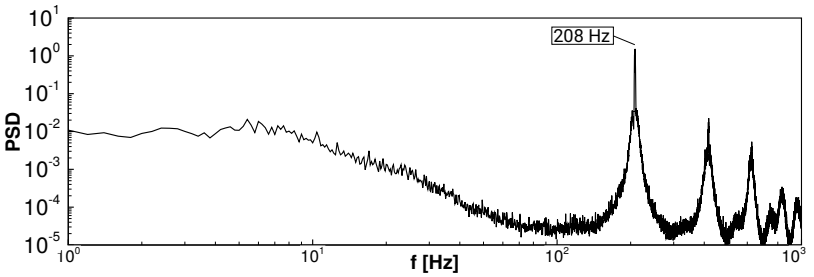

(b) Rigid airfoil at $\alpha = 0°$.

Figure 5.36: CTA measurements of the flutter phenomenon for case III by Wood et al. [23]. Monitoring point location $[x, z] = [200, 0]$ mm, $U_\infty = 5.068$ m/s, Re $= 3.39 \times 10^4$.

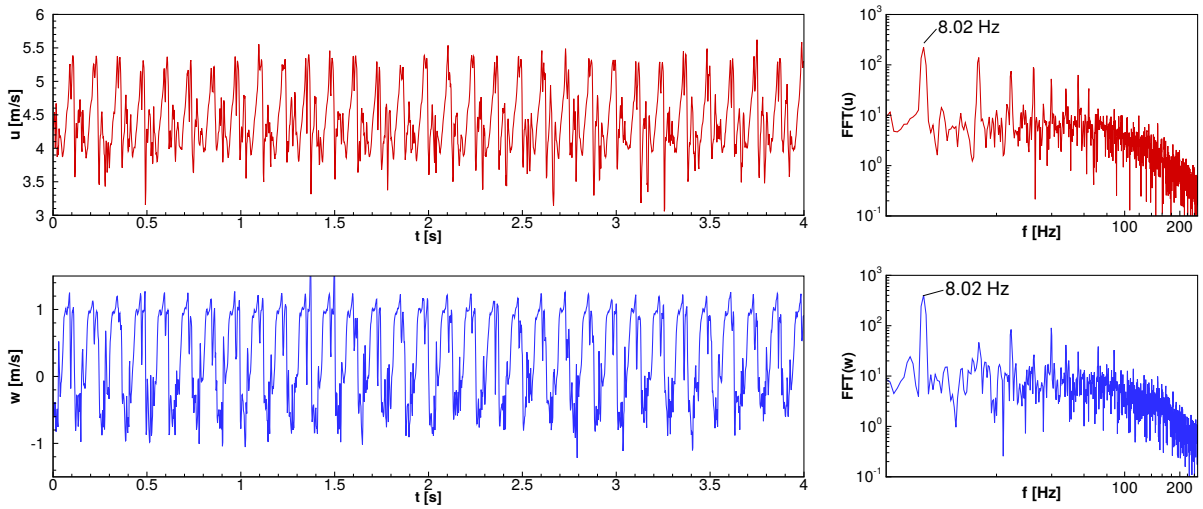

Figure 5.37: Oscillation of fluid velocity components u (above) and w (below) recorded at a fixed wake monitoring point $[x, z] = [150, 0]$ mm by high-speed PIV. Time and FFT-plots of case III, $n = 325$ rpm, $U_\infty = 5.665$ m/s, Re$_c = 3.60 \times 10^4$.

5.4 Synchronized PIV-DIC results

By the synchronization of PIV and DIC-measurements, it is experimentally possible to investigate and describe the FSI precisely. For this purpose, there are some factors that have to be considered: The illumination source for the fluid flow and the structure deformation measurements is the PIV-laser with a pulse repetition rate of 500 pps. Thus, for guaranteeing an equal light intensity for each captured image, the PIV-camera and the DIC-cameras have the same frame rate of 500 fps. The post-processing of the synchronized results shows some difficulties, as can be seen schematically in Fig. 5.38. The PIV-camera is positioned and centered on the same height as the wing system at rest, resulting in a 2D-capturing of the mounted airfoil and the clamp (blue). The first difficulty is that the front-view is enlarged compared to the real airfoil dimensions. This is due to the fact that the PIV-calibration is done at half of the span length of the wing behind the front-view, where the light sheet is located, which is the test section area for the current 2D-FSI investigations. The physically real airfoil dimensions are determined by DIC, since the upper airfoil line is extracted out of the surface measurements in the region of the light sheet which is calibrated by DIC. Now, by comparing the size of the upper airfoil line from DIC to the size of the blue front-view from PIV, it is a perspective fallacy that the DIC profile seems to be scaled down. The second difficulty is the motion of the airfoil, i.e., at minimum heave position, the static PIV camera is not centered to the instantaneous height of the airfoil anymore. As a consequence, the former 2D-airfoil shape is distorted and a 3D-projection of the wing system is generated, focussing on the vanishing point of the PIV-camera. According to the precise synchronization of the PIV and DIC data, the DIC-profile line is superimposed and fitted on the enlarged PIV-front-view of airfoil, so that the 2D-view of the wing contour is reconstructed within the velocity field.
In the following, the synchronized PIV-DIC measurements are presented for the flutter phenomenon at $\mathrm{Re}_c = 3.60 \times 10^4$. For one entire time period of a single oscillation with a time span of $T = 0.12\,\mathrm{s}$, the motion of the wing is investigated as well as the 2D fluid flow behavior: For this purpose, the dimensionless fluid velocity component u/U_∞ in streamwise direction and the vertical dimensionless fluid velocity component w/U_∞ are presented for case I and case III.

5.4.1 Investigation of case I

According to the synchronization of the DIC and PIV measurements, Figs. 5.40 and 5.42 depict the combined investigations on the structural motion of the airfoil with the corresponding fluid flow fields u/U_∞ and w/U_∞. The test section has the dimensions $x/c = [-1.55; 1.1]$ and $z/c = [-0.95; 0.95]$ related to the chord length $c = 0.1\,\mathrm{m}$ of the

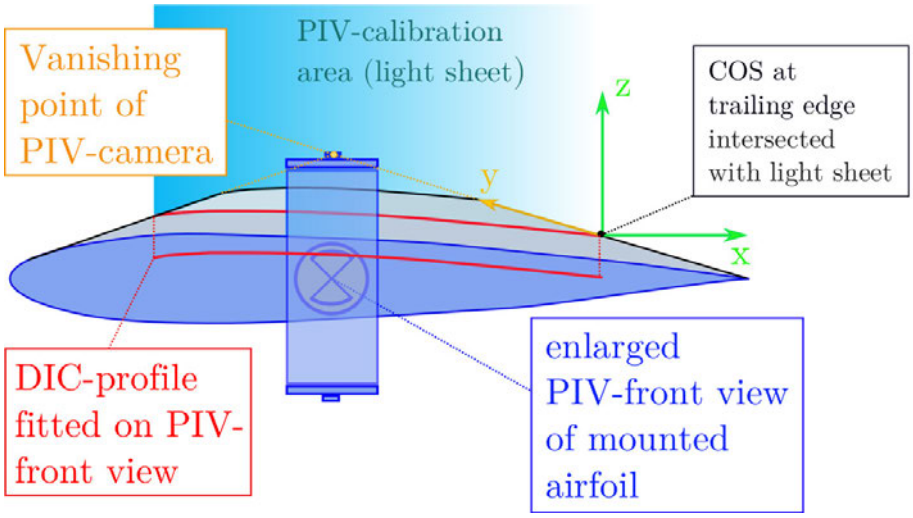

Figure 5.38: Vanishing point projection by PIV with an enlarged front view of the airfoil (blue) and a fitted DIC-surface line (red) of real size.

airfoil. Representing the characteristic flutter behavior, one period corresponds to the temporal length $T = 0.12\,\mathrm{s}$ and is depicted as 11 snapshots of the field of view. The recording sequence of images starts at t_0 and ends at $t_0 + 10\Delta t$, which means that the time step is $\Delta t = 0.012\,s$. Beginning with the structural motion of the airfoil, the image content includes the upper side of the symmetric airfoil marked as a black curve: This line element is extracted from the upper surface of the wing, measured by the 3D-DIC technique. With the aid of two-point-measurements along this line element, the movement is separated into heave and pitch. The principle is depicted in Fig. 5.39.

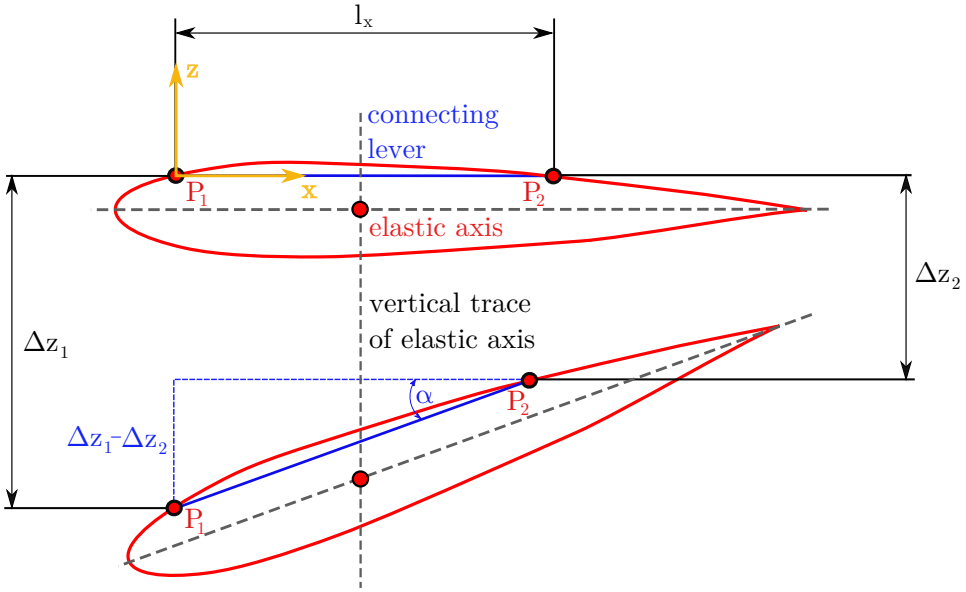

Figure 5.39: Principle of separate calculations of heave and pitch from the displacements at two points.

From the difference of the displacements $\Delta z_1 - \Delta z_2$ of the two points P_1 and P_2, the pitch angle can be calculated:

$$\alpha = \arcsin\left(\frac{\Delta z_1 - \Delta z_2}{l_x}\right) \quad . \tag{5.9}$$

The elastic axis is the center of rotation located at $x = l_x/2 \approx$ const related to the length of the connection lever l_x. Its vertical trace position contains mainly the information on the heave displacement, which can be approximately calculated with two methods:

$$\mathrm{h} \approx \Delta z_1 - \frac{l_x}{2} \cdot \tan(\alpha) \quad , \tag{5.10a}$$

$$\mathrm{h} \approx \Delta z_2 + \frac{l_x}{2} \cdot \tan(\alpha) \quad . \tag{5.10b}$$

Regarding the results of these calculations, the graphs at the lower right of the image sequence in Figs. 5.40(l) and 5.42(l) show the history of the heave and pitch oscillation for every snapshot marked by the corresponding symbols, where the separated DOFs oscillate sinusoidally and are separated by a phase shift angle of $\varphi = 125°$. The markers (red diamonds, blue circles) represent each of the 11 time steps with the associated heave and pitch values. Comparing the oscillations with the previously published results, the phase shift angles of $\varphi = 149°$ (De Nayer et al. [15]) and $\varphi = 137°$ (Wood et al. [23]) for case I are similar to the current one. Furthermore, the heave and pitch amplitudes can be seen in Tab. 5.5. They are of the same magnitude and confirm the previously published results [15, 23]. The slight differences in the heave amplitudes can be explained by the wearing of the heave springs during the measurement series.

Table 5.5: Comparison of two-point measurements: Previously published results [15, 23] and current results of the heave and pitch oscillations and the phase angle shift for case I.

	Δz_h [mm]	α [°]	φ [°]
Case I (De Nayer et al. [15])	±7.5	± 11.5	149
Case I (Wood et al. [23])	± 4.7	± 14	137
Case I (present)	± 6.5	± 14.5	125

Taking the fluid flow field into consideration, the driving mechanism for the airfoil motion can be analyzed by the velocity characteristics. In Fig. 5.40, there are some regions which are not processed by the PIV software due to insufficient resolution of the tracer droplets in this region and thus are blanked out in white in the post-processing. Additionally, the perspective effects mentioned in Fig. 5.38 are visible. The front-view of the airfoil with the mounting clamp (blue area) is visualized enlarged, compared to the DIC-line

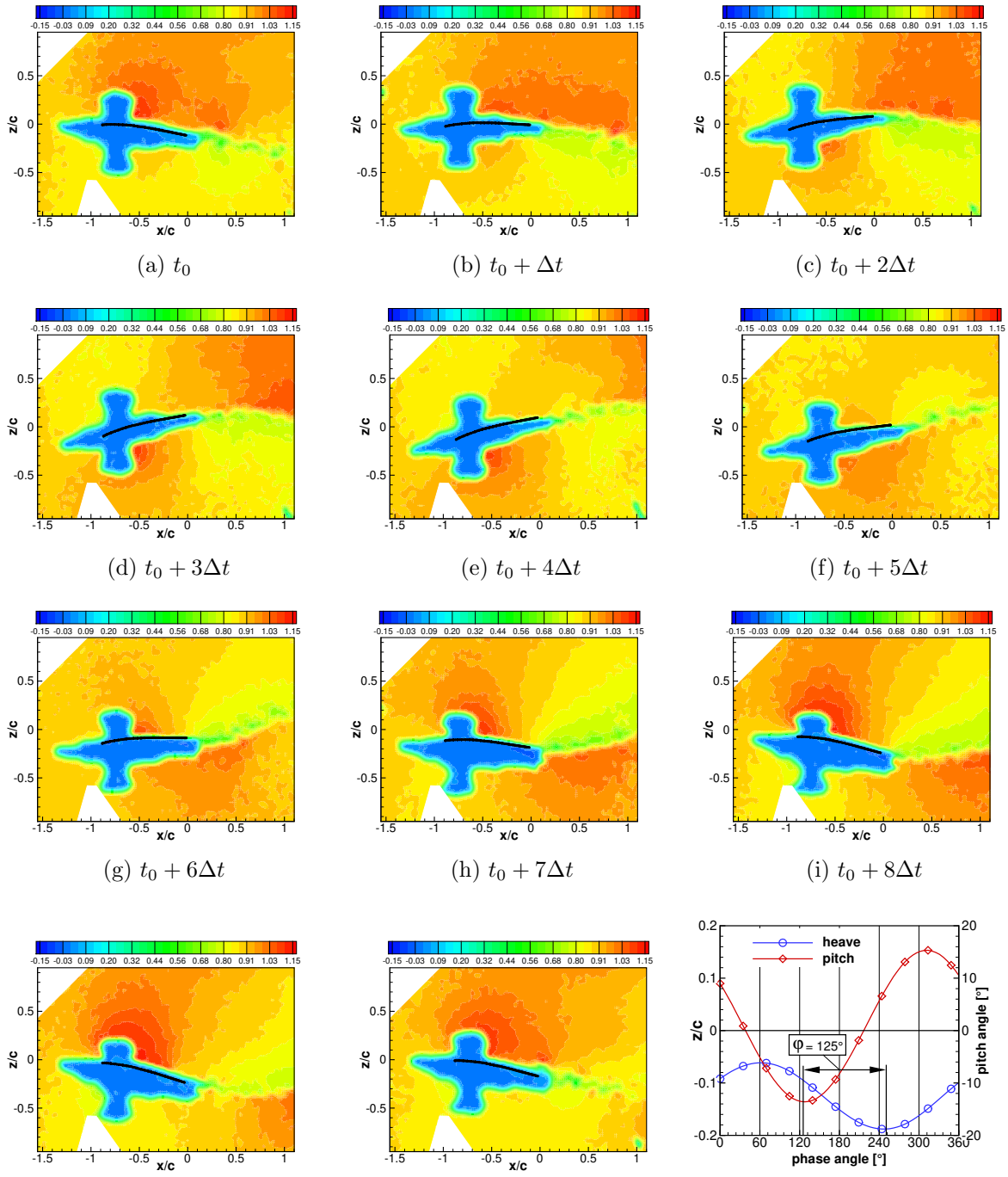

(a) t_0 (b) $t_0 + \Delta t$ (c) $t_0 + 2\Delta t$

(d) $t_0 + 3\Delta t$ (e) $t_0 + 4\Delta t$ (f) $t_0 + 5\Delta t$

(g) $t_0 + 6\Delta t$ (h) $t_0 + 7\Delta t$ (i) $t_0 + 8\Delta t$

(j) $t_0 + 9\Delta t$ (k) $t_0 + 10\Delta t$ (l) DIC: phase-shift (heave/pitch)

Figure 5.40: Synchronized PIV-DIC for case I: Wing flutter motion and corresponding fluid flow velocity component u/U_∞ in a time period of $[t_0; t_0 + 10\Delta t]$ with $\Delta t = 0.012\,s$.

element (black) that is superimposed and fitted to the images. However, focussing on the component u/U_∞, it can be noticed that for the extreme values of the pitch motion in Fig. 5.40(e) (minimum amplitude) ($\alpha_{min} = -14°$, $z/c_{min} = -0.11$) and 5.40(j) (maximum amplitude) ($\alpha_{max} = 15°$, $(z/c)_{max} = -0.15$) the local velocity is increased on the lower side of the airfoil or on the upper one, respectively, which means that the fluid is strongly accelerated along the curved surface of the wing. Assuming potential theory in this region, it can be deduced that the local pressure behaves reversely to the local velocity. A practical device for proving is the dimensionless pressure coefficient c_p, which considers the difference of the local pressure $p(x)$ and the surrounding far-field pressure p_∞ to the stagnation pressure[2]. It can be formulated as follows:

$$c_p = \frac{p(x,y,z) - p_\infty}{\frac{\varrho}{2} U_\infty^2} = 1 - \frac{u^2 + v^2 + w^2}{(U_\infty)^2} \ , \tag{5.11}$$

$$c_p \approx 1 - \left(\frac{u}{U_\infty}\right)^2 \ , \tag{5.12}$$

with the assumption that $v/U_\infty \ll 1$ and $w/U_\infty \ll 1$ due to the dominating velocity component u/U_∞ in free-stream direction. Exemplarily for Fig. 5.40(e), the top side region of the airfoil reveals a mean velocity component of $u/U_\infty = 0.91$ at $x/c = -0.3$, $z/c = +0.25$, whereas the bottom side region shows that $u/U_\infty = 1.09$ at $x/c = -0.5$, $z/c = -0.3$. The pressure coefficients result in

$$c_{p,(5.40(e))}^{\text{top}} = 1 - 0.91^2 = 0.172 \ , \tag{5.13a}$$

$$c_{p,(5.40(e))}^{\text{bottom}} = 1 - 1.09^2 = -0.188 \ . \tag{5.13b}$$

Thus, in the bottom part of the airfoil, a low pressure region exists and in the top part a high pressure region, which confirms the potential theory in this region and furthermore explains the downward lift force and heave motion in the following snapshots. This tendency can also be seen by the negative slope of the tangent line at the inflection point (phase angle $\approx 140°$) of the corresponding time history of the heave in Fig. 5.40(l). One the other hand, the upward lift force and heave motion can be noticed in Fig. 5.40(j) by

$$c_{p,(5.40(j))}^{\text{top}}(x/c = -0.6,\ z/c = 0.2) = 1 - 1.14^2 = -0.300 \ , \tag{5.14a}$$

$$c_{p,(5.40(j))}^{\text{bottom}}(x/c = -0.6,\ z/c = -0.5) = 1 - 0.86^2 = 0.260 \ , \tag{5.14b}$$

and the positive slope of the tangent line at the inflection point (phase angle $\approx 320°$) of the corresponding time history of the heave in Fig. 5.40(l). For comparison, the

[2]according to https://www.mb.uni-siegen.de/lfst/lehre/dokumente/maschinenlabor.pdf

schematic airfoil motion during one time period of oscillation is depicted in Fig 5.41 (De Nayer et al. [15]). The relation of lifting forces (red arrows) and heave directions (black arrows) are shown. At the position of the maximum pitch angle, the heave motion is directed upwards, which is observable in a positive slope at the tangent line of the blue oscillation curve. Here, the lift force is also upwardly directed. This corresponds well to the current findings. In the extreme heave positions of the airfoil, the lift force is directed in the opposite direction, having a repressing impact on the dynamic system. For example, at maximum heave position, the pitch angle of the airfoil is negative, which induces a downwards directed lift force. Globally regarded, the flutter motion develops by the positive work which is done by the lift force in cooperation with the direction of heave.

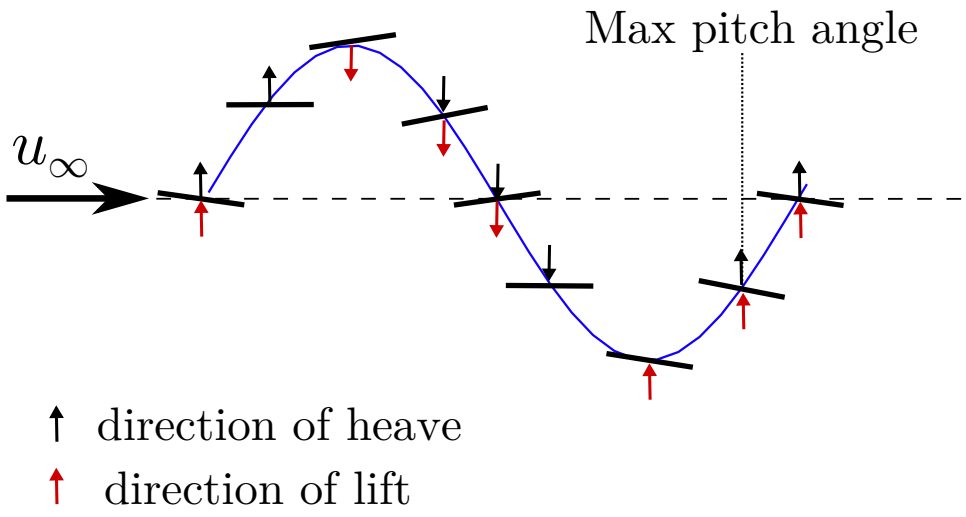

Figure 5.41: Case I: Schematic airfoil motion during one time period of oscillation with the heave (black arrow) and the lift force influence (red arrow) [15].

Characterizing the wake of the fluid flow behind the airfoil, a turbulent shear layer appears. This is remarkable in the images of extreme heave values or shortly before the extrema of the pitch values, respectively. Figure 5.40(c) shows, among other things, the contrast of the velocity fields in the wake along the imaginary extension of the symmetry line of the airfoil: The increased local velocity field from the upper side $u/U_\infty = 1.05$ ($x/c = 0.25$, $z/c = 0.2$), which has been necessary for the upward heave mechanism of the airfoil, is joined with the decreased velocity of the lower side $u/U_\infty = 0.82$ ($x/c = 0.25$, $z/c = -0.2$). In the green colored intersection part with $u/U_\infty = 0.58$ ($x/c = 0.25$, $z/c = 0.1$), the velocity is even more reduced than the adjoining ones. This is a sign for a turbulent shear layer. Thus, it proceeds in the form of a curved trace of the

trailing edge in the wake. In an analogous manner, Fig. 5.40(h) shows the reversed wake phenomenon of the increased local velocity field $u/U_\infty = 1.03$ $(x/c = 0.4,\ z/c = -0.3)$ from the lower side and the decreased field $u/U_\infty = 0.8$ $(x/c = 0.4,\ z/c = 0.1)$ from the upper side, having caused the downward lift mechanism of the airfoil. According to Fig. 5.40(l), it is the minimum of the heave oscillation curve. Nevertheless, considering the intersection part in the wake in Fig. 5.40(h), the velocity $u/U_\infty = 0.5$ $(x/c = 0.4,\ z/c = -0.1)$ is again decreased compared with the adjoining velocity fields. Obviously in this turbulent shear layer a sequence of vortices is generated and builds an oscillating trace behind the trailing edge, which can be distinguished in the velocity field of the vertical component w/U_∞ presented in the following.

Figure 5.42 depicts the image series of the vertical velocity distribution w/U_∞. Due to the fact that the flutter oscillation of the airfoil is very rapid in reaching high amplitudes, the flow development is not as regular as for lower Reynolds numbers. Thus, the capturing and visualization of vortices in the wake region is difficult to manage. However, the generation and shedding of vortices is mainly visible in those images taken at a short time after the extreme values of the dominating pitch movement. In Fig. 5.42(l) the minimum pitch appears at a phase angle of $\varphi \approx 125°$ while the maximum pitch is at $\varphi \approx 320°$. At these extreme values, the instantaneous rate of change is zero, so the pitch angle of the airfoil remains in this position for a while, and therefore, vortices can be captured that shed for a certain distance from the trailing edge. In Fig. 5.42(k), after the pitch maximum has been passed over, small vortices can be noticed by the fact that for each, there are two alternating local neighbored velocity regions, either directed in positive (red) or in negative (blue) direction. The vortex centers, positioned at $x/c = 0.2$, $z/c = -0.1$ and $x/c = 0.3$, $z/c = -0.2$, are placed in between those velocity pairs and should be ideally at $w/U_\infty = 0$. In Fig. 5.42(a), which is periodically short after the former image, only one large vortex is visible with the position of the center at $x/c = 0.3$, $z/c = -0.1$ which is the last distinguishable one. Additionally in Fig. 5.42(j), before the maximum pitch is reached and the vortex detaching happens, two locally increased velocity regions are visible: First, at the leading edge of the airfoil, the fluid flow overcomes the stagnation point and accelerates positively with $w/U_\infty = +0.25$ at $x/c = -1.05,\ z/c = 0.1$ along the upper side. Second, proceeding further in space, the fluid flow accelerates negatively with $w/U_\infty = -0.23$ $(x/c = -0.15,\ z/c = -0.1)$, which is due to the angle of attack of the airfoil and the downwards directed region of the trailing edge. This behavior of the fluid flow is analogous to the velocity field of u/U_∞ in Fig. 5.40(j), where the flow acceleration leads to a low pressure region on the upper side.

Complementary, the pitch minimum is reached in Fig. 5.42(e). The fluid flow, proceeding below the bottom airfoil line, shows a positive acceleration area with $w/U_\infty = +0.2$

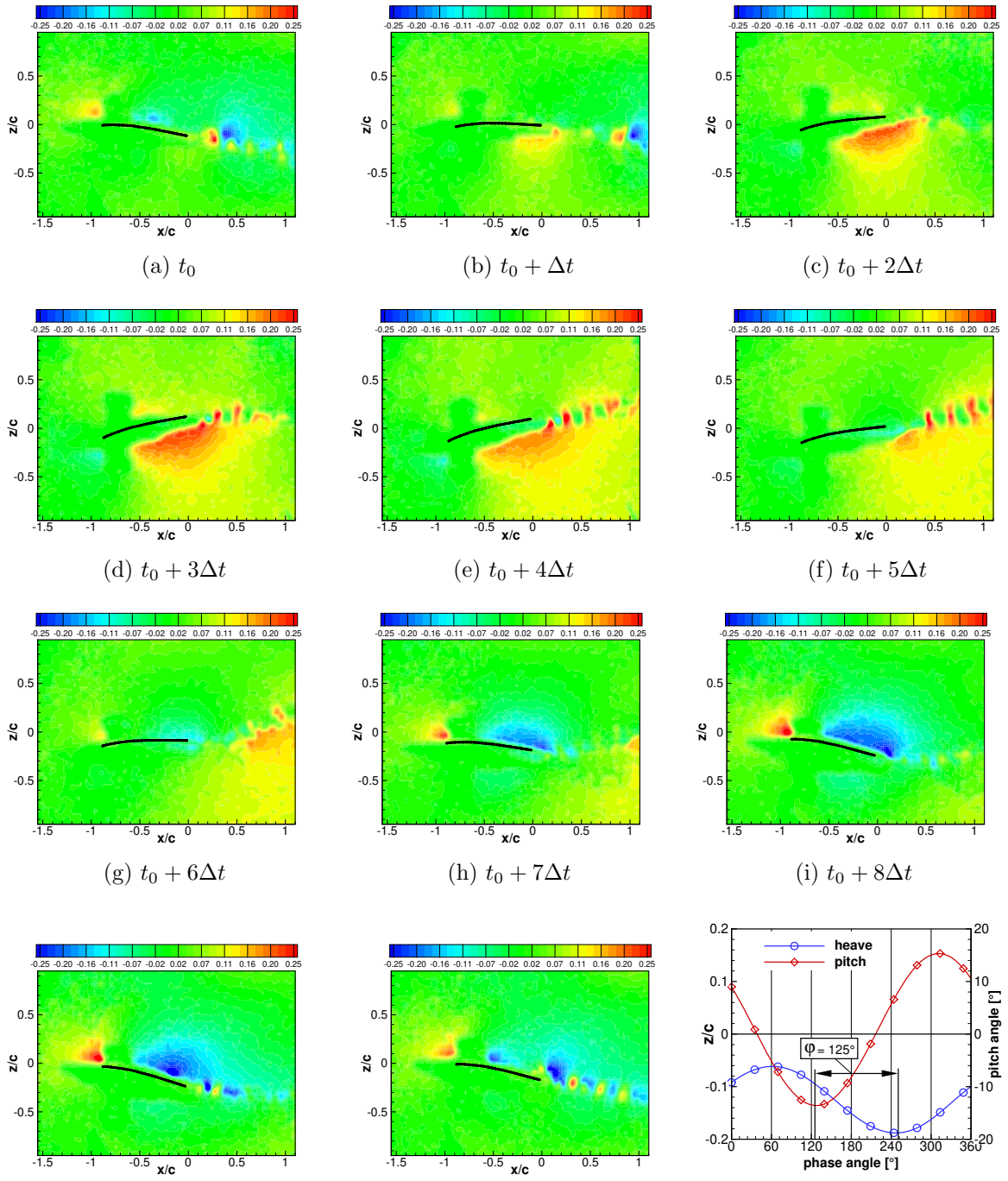

(a) t_0 (b) $t_0 + \Delta t$ (c) $t_0 + 2\Delta t$

(d) $t_0 + 3\Delta t$ (e) $t_0 + 4\Delta t$ (f) $t_0 + 5\Delta t$

(g) $t_0 + 6\Delta t$ (h) $t_0 + 7\Delta t$ (i) $t_0 + 8\Delta t$

(j) $t_0 + 9\Delta t$ (k) $t_0 + 10\Delta t$ (l) DIC: phase-shift (heave/pitch)

Figure 5.42: Synchronized PIV-DIC for case I: Wing flutter motion and corresponding fluid flow velocity component w/U_∞ in a time period of $[t_0; t_0 + 10\Delta t]$ with $\Delta t = 0.012\,s$.

(red) at ($x/c = 0,\ z/c = -0.15$) along the upwards directed region of the trailing edge. This results in a low pressure region, which is analogous to the velocity field of u/U_∞ in Fig. 5.40(e). Furthermore, in the wake region ($x/c = [0.1; 0.8],\ z/c = [0; 0.3]$) the velocity fluctuations denote the generation of vortices, which are convected downstream. Finally in Fig. 5.42(f), after the minimum pitch angle is overcome, the convection of the last vortices becomes visible.

5.4.2 Investigation of Case III

In the following, the dynamic structure and fluid behavior of case III is investigated, as depicted in Figs. 5.43 and 5.45. To begin with the structural characteristics, it can be seen in Fig. 5.43(l) that the oscillation of heave and pitch are rather synchronous. From a detailed perspective, the pitch precedes the heave motion with a phase shift angle of $\varphi = 23°$, which is in good agreement with the previously published results of De Nayer et al. [15] ($\varphi = 25°$) and Wood et al. [23] ($\varphi = 25°$). The heave and pitch amplitude values, Δz_h and α, are listed in Tab. 5.6. It is remarkable, that there are differences in the amplitude values between the present results and the previously published ones. The heave amplitude Δz_h is increased compared to the corresponding values of [15, 23], which can be assigned to the wearing of the heave springs during the measurement series. A further background can be in the removal and installation of the wing system that there are slight differences in the preload forces connecting the mounting clamps with the support frame. However, the present pitch amplitude α is close to the average of the previously published values.

Table 5.6: Comparison of two-point measurements: Previously published results [15, 23] and current results of heave-pitch oscillation and phase angle shift for case III.

	Δz_h [mm]	α [°]	φ [°]
Case III (De Nayer et al. [15])	± 3	± 25	25
Case III (Wood et al. [23])	± 3.4	± 8.5	25
Case III	± 8.6	± 17.4	23

Considering the fluid characteristics, a slightly different behavior for case III than for case I can be seen. The flutter instability of the airfoil is supported intensively by the distribution of the local fluid velocity. At the extremal values of the heave and pitch motion, the lift forces try to extend the structural oscillations. Fortunately, this can be restricted by the heave and torsional springs for a certain level of the dynamic fluid loading. According to Fig. 5.43(l), the pitch motion has its maximum at $\alpha_{max} = 19°$, while the heave motion has nearly reached its maximum at $(z/c)_{max} = 0.17$.

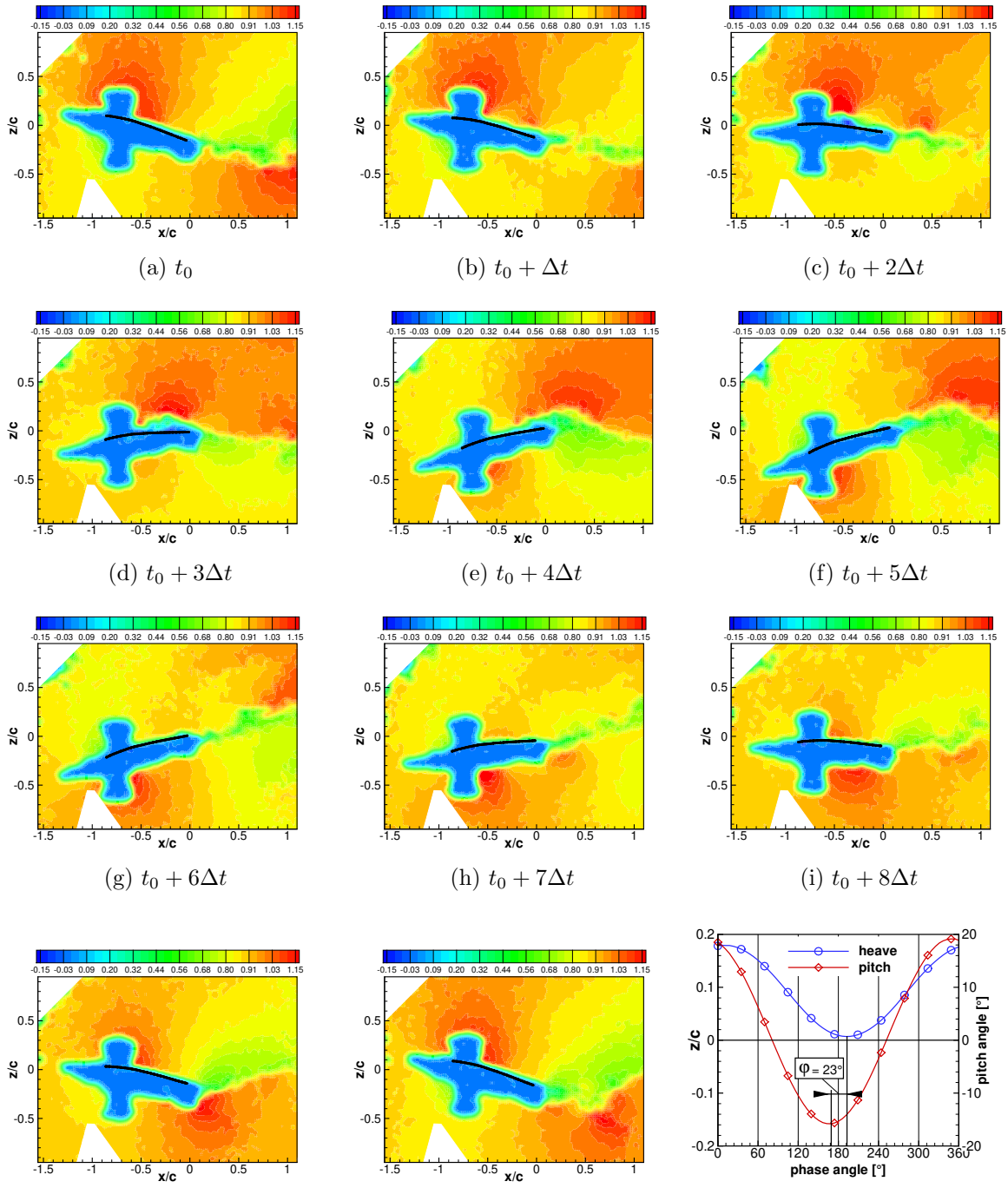

(a) t_0 (b) $t_0 + \Delta t$ (c) $t_0 + 2\Delta t$

(d) $t_0 + 3\Delta t$ (e) $t_0 + 4\Delta t$ (f) $t_0 + 5\Delta t$

(g) $t_0 + 6\Delta t$ (h) $t_0 + 7\Delta t$ (i) $t_0 + 8\Delta t$

(j) $t_0 + 9\Delta t$ (k) $t_0 + 10\Delta t$ (l) DIC: phase-shift (heave/pitch)

Figure 5.43: Synchronized PIV-DIC case III: Wing flutter motion and corresponding fluid flow velocity component u/U_∞ in a time period of $[t_0; t_0 + 10\Delta t]$ with $\Delta t = 0.012\,s$.

According to Fig. 5.43(k), the dimensionless pressure coefficient c_p in the region above and below the airfoil can be calculated by:

$$c^{\text{top}}_{p,5.43(k)}(x/c = -0.45,\ z/c = 0.15) = 1 - 1.12^2 = -0.2544\ , \tag{5.15a}$$

$$c^{\text{bottom}}_{p,5.43(k)}(x/c = -0.45,\ z/c = -0.35) = 1 - 0.84^2 = 0.2944\ . \tag{5.15b}$$

Obviously, due to the strong positive pitch angle of the airfoil, the fluid tends to accelerate at its upper side and generates a low pressure region there, whereas the bottom side reveals a high-pressure region with low flow velocities. So the adjusted surrounding fluid flow leads to a further lift of the wing system. In Fig. 5.44, this finding is confirmed by the extremal positions of the oscillation. At the maximum and minimum amplitudes of the blue curve, the lift forces (red arrows) are directed further upwards and downwards, respectively.

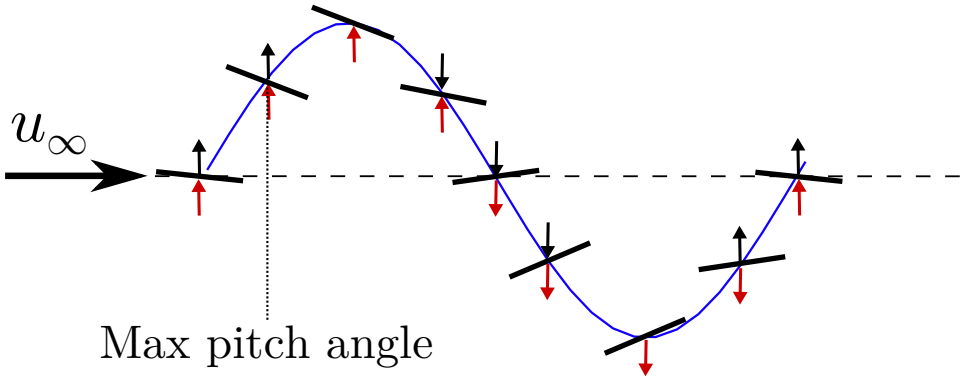

Figure 5.44: Case III: Schematic airfoil motion during one time period of oscillation with the heave (black arrow) and the lift force influence (red arrow) [15].

Thus, the fluid forces perform continuously positive work on the wing system, resulting in a rapid growth of amplitudes. This can be declared as negative damping. Fortunately, the structural leaf and torsional springs restrict the heave and pitch amplitudes during this period of oscillation. However, the springs are limited in their stiffnesses and repressing forces, so the oscillations at higher amplitudes should be avoided, if possible.
Complementary, looking at Fig. 5.43(f), the pitch and heave motion have their minimum at $\alpha_{min} = -16°$ and $(z/c)_{min} = 0.001$.

The dimensionless pressure coefficient c_p at the top and bottom side of the airfoil can be calculated by:

$$c^{\text{top}}_{p,5.43(f)}(x/c = -0.4,\ z/c = 0.1) = 1 - 0.84^2 = 0.2944\ , \tag{5.16a}$$

$$c^{\text{bottom}}_{p,5.43(f)}(x/c = -0.5,\ z/c = -0.45) = 1 - 1.09^2 = -0.1881\ . \tag{5.16b}$$

Again, the tendency that a lift force is still generated, here in the opposite direction (downward), can be observed by the low pressure at the bottom side of the airfoil and the high pressure on the upper side.
Discussing the wake of the fluid flow behind the airfoil, it is remarkable and in contrast to case I that the turbulent shear layer is not proceeding sinusoidally in alignment with the trailing edge. Instead, the flow starts to detach already on half of the chord length on the upper side of the airfoil, which can be seen in Fig. 5.43(c) and Fig. 5.43(d) by slight deceleration areas (green/blue) above the upper side. Thus, the local pressure is increased in that region within the region of $x/c = [-0.4, 0], z/c = [0, 0.1]$. Then, the detached flow on the upper side of the airfoil merges with the shear layer in the wake. This effect is visible in Figs. 5.43(e) and 5.43(f). However, in general, the turbulent shear layer separates the different velocity regions, which have moved along the upper and bottom side of the airfoil and detached into the wake region. The shear layer has the proceeding velocity of $u/U_\infty = 0.56$ at $x/c = [0.25, 0.8],\ z/c = [0, 0.2]$ according to Fig. 5.43(f).
Regarding the normalized vertical velocity component w/U_∞ in Fig. 5.45, there is a correspondence to the behavior of u/U_∞. The snapshot of the maximum pitch angle in Fig. 5.45(k) reveals the acceleration of the fluid at the leading edge of the airfoil, which can be seen by the red colored area at $x/c = -0.9,\ z/c = 0.25$ with $w/U_\infty = +0.22$. Along the upper side of the airfoil, the fluid possesses a negative vertical velocity with $w/U_\infty = -0.22$ located in the region of $x/c = [-0.5, 0.2],\ z/c = [-0.1, 0.3]$. In the following diagrams, the detachment of vortices at the trailing edge becomes visible. Especially in Figs. 5.45(c) and 5.45(d), it can be seen that vortices are already generated at half length of the upper side, which can be noticed by the alternating local positive and negative velocity areas. Considering the complementary minimum pitch motion in Fig. 5.45(f), the acceleration at the leading edge of the airfoil is rather invisible. Instead, along the bottom side of the airfoil, a large local velocity region in positive vertical direction is visible. At the trailing edge, velocity fluctuations appear in the sequence of green and red colored areas. Therefore, it can be assumed that vortices are generated. Furthermore, the wake region behind the trailing edge is irregular, the acceleration region expands in a diffuse manner. This is matching with the analysis of Fig. 5.45(f) and the mixing between detached flow and the shear layer.

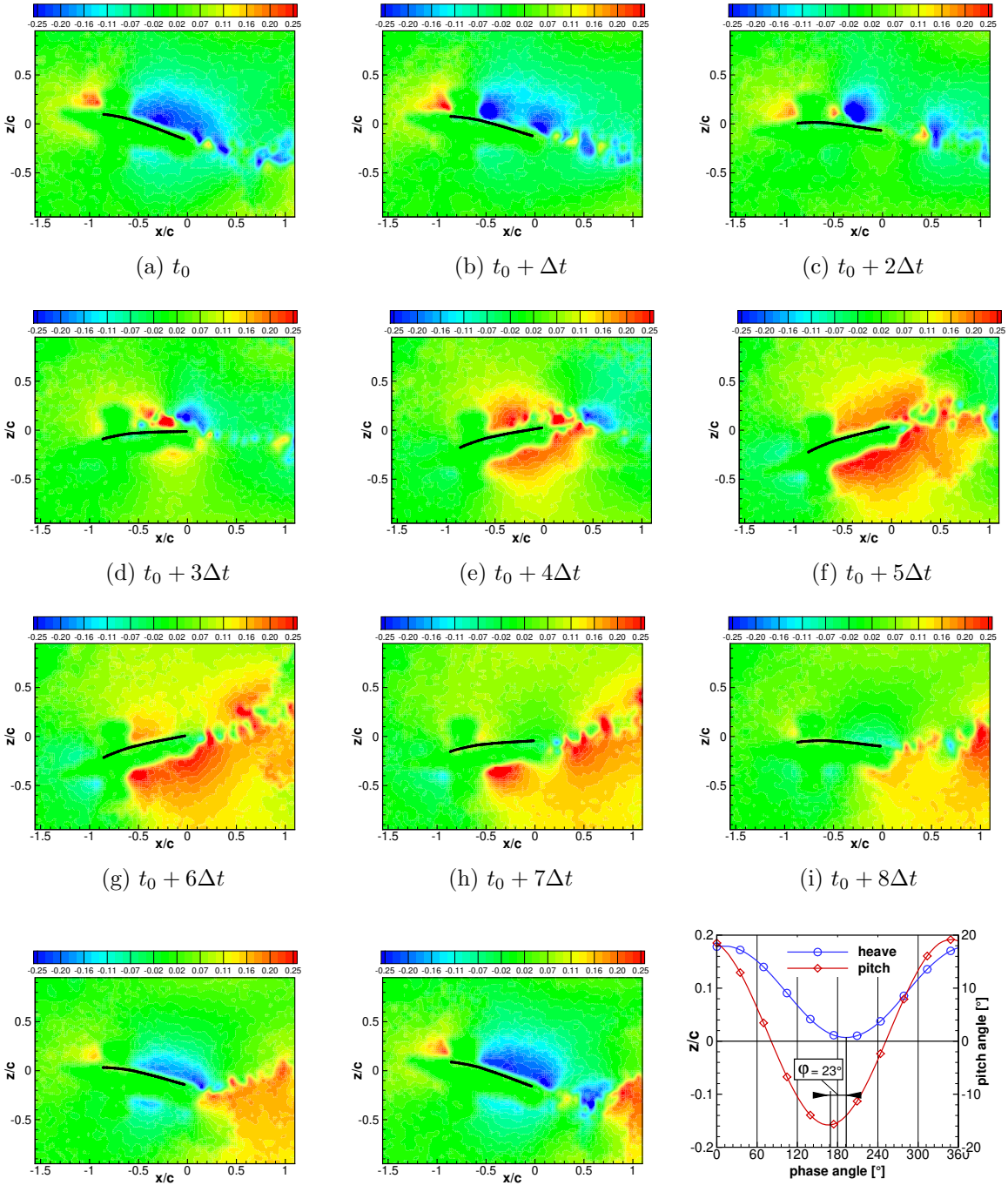

(a) t_0 (b) $t_0 + \Delta t$ (c) $t_0 + 2\Delta t$

(d) $t_0 + 3\Delta t$ (e) $t_0 + 4\Delta t$ (f) $t_0 + 5\Delta t$

(g) $t_0 + 6\Delta t$ (h) $t_0 + 7\Delta t$ (i) $t_0 + 8\Delta t$

(j) $t_0 + 9\Delta t$ (k) $t_0 + 10\Delta t$ (l) DIC: phase-shift (heave/pitch)

Figure 5.45: Synchronized PIV-DIC case III: Wing flutter motion and corresponding fluid flow velocity component w/U_∞ in a time period of $[t_0; t_0 + 10\Delta t]$ with $\Delta t = 0.012\,s$.

To conclude the results from Figs. 5.40 to 5.45, the structural oscillations of heave and pitch are shifted by a larger phase angle of $\varphi = 125°$ for case I and a smaller phase angle of $\varphi = 23°$ for case III. In a figurative language according to De Nayer et al. [15], the oscillation behavior in case I can be declared as a *swimming fish*, schematically depicted in Fig. 5.41. Case III can be called as a *flapping motion*, schematically depicted in Fig. 5.44. On the one hand, in case I, the extremal values of the pitch motion match with the inflection points of the heave motion related to the phase angle, see Fig. 5.40(l). On the other hand, in case III, the extremal values of heave and pitch are close to each other, see Fig. 5.43(l). Looking at the fluid flow surrounding the airfoil at certain angles of attack, locally increased velocity regions are measured either above the upper side or below the bottom side of the airfoil. At the extremal pitch angle positions, the dimensionless pressure coefficients c_p are calculated out of the velocity data in the regions of the upper and bottom airfoil line. By the difference of c_p, the quantitative effect of lift can be determined. The pressure coefficient is mainly influenced by the component u/U_∞ since its local velocities are higher than those of the component w/U_∞ due to the horizontal free-stream direction and the geometric properties of the obstacle: The design of the airfoil is stretched out horizontally over the chord length c, while the maximum thickness in vertical direction is $t = 0.12\,c$. Hence, although the surrounding fluid flow is lightly deflected vertically at certain pitch angles, it is mainly horizontally directed according to the free-stream. Finally presenting the results, at maximum pitch angles, for both cases, an upward lift is calculated. This can be seen in Eqs. (5.14a), (5.14b) and (5.15a), (5.15b) where the dimensionless pressure coefficient c_p is higher at the bottom airfoil line region than at the upper one. At minimum pitch angles, for both cases, a downward lift is calculated. This can be seen in Eqs. (5.13a), (5.13b) and (5.16a), (5.16b), where the dimensionless pressure coefficient c_p is higher at the upper airfoil line region than at the bottom one. Comparing the qualitative effect of lift at extremal heave positions, in case I, the lift forces tend to repress higher amplitudes of flutter, while in case III the lift forces tend to support an increase of the displacements.

5.5 Phase-averaged data of the wake flow field at flutter

Along one period of oscillation of the airfoil, that represents the characteristics of the flutter motion, the velocity is presented by phase-averaged data in the following. Phase-averaged data determine the mean value of the corresponding velocity fields at the same instant of time of each period of the oscillations, i.e., the same position of the airfoil. These quantities are presented here for the horizontal and vertical velocity component $\overline{u}/U_\infty$ and $\overline{w}/U_\infty$. Furthermore, the fluctuations or deviations from the mean values are calculated as Reynolds stress components $\overline{u'u'}$, $\overline{w'w'}$ and $-\overline{u'w'} = -\overline{w'u'}$, while the negative algebraic signs in the last components are pretended by the PIV-software. The detailed formula for the prediction of the Reynolds stresses are explained in Section 3.4. In the following, the mean values and Reynolds stresses are shown for the flutter velocity at $\mathrm{Re}_c = 3.60 \times 10^4$. For the overall measurement, there are 2000 images captured by the PIV-camera which means that, due to the frame rate of 500 fps, the recording time is 4 s. Representative for the whole airfoil motion, one time period of oscillation is divided into 63 bins, corresponding to the temporal length of $T = 0.12\,\mathrm{s}$, which is equivalent to the former time series results. Assuming that the period is perfectly described by 63 bins and the corresponding images, the 2000 images yield approximately 31 full periods within the complete measurement. Thus, each bin is phase-averaged by 31 unsteady PIV-pictures at the same instant of time. In the presented diagrams, the recording sequence of images starts at t_0 and ends at $t_0 + 12\Delta t$, which means that the time step is $\Delta t = 0.01\,s$. In order to distinguish the differences of each flutter case, case I and case III are compared taking the acceleration areas on the upper/lower airfoil surface, the shear layer roll up in the wake and the local turbulent fluctuation areas into account.

5.5.1 Comparison of mean velocity components in case I/III

Regarding the phase-averaged velocity components, Figs. 5.46 and 5.47 show the results for the streamwise velocity component $\overline{u}/U_\infty$. Case I and III have in common that there are acceleration areas proceeding alternately over the upper and lower airfoil surface into the wake, which can be seen by the orange-red marked velocity fields $\overline{u}/U_\infty = [1.03; 1.15]$. Additionally, in the region of the trailing edge at $x/c \leq 0$, $z/c = [-0.2; 0.2]$ there are blurring effects with green (case I, $\overline{u}/U_\infty = 0.56$) and blue (case III, $\overline{u}/U_\infty = -0.15$) areas around the airfoil, which are caused by the systematic resolution errors of the phase-averaging as well as the perspective difficulties of the PIV-camera. The systematic error originates from the idealization that a constant period of the oscillation

is assumed for the post-processing not taking into account that due to turbulence the length of the period is not necessarily constant. This restriction is executed successively for all periods within the measurement, although each flutter period is slightly different in its duration. Thus, the chosen 63 images naturally contain a small deviation in the position of the airfoil. During the averaging process, these positions are blurred in the diagrams, which is visible as broad blue velocity distribution, especially recognizable in the extreme positions. Furthermore, since the PIV-camera is fixed at one position, it also records a perspective error, as mentioned in the context of Fig. 5.38: As the airfoil moves up and down, the camera also focuses on the upper and lower side of the wing surface due to its vanishing point perspective. These "perspective errors" are most prominent in the extreme positions of the wing. However, discussing the flow properties in the wake, a difference in both cases is the development of the shear layer. This can be seen by the green-marked content in the wake ($\overline{u}/U_\infty = [0.4; 0.7]$). On the one hand, case I shows a shear layer of continuous thickness $\Delta z/c \approx 0.1$ that proceeds in the shape of an arch, which can be seen in Figs. 5.46(e) and 5.46(h). On the other hand, case III presents a shear layer of varying thickness, i.e., in Fig. 5.47(f) with $\Delta z/c \approx 0.1$ ($x/c = 0.4$) and in Fig. 5.47(h) with $\Delta z/c \approx 0.4$ ($x/c = 0.8$). Furthermore in case III, it develops irregularly and chaotically in the wake revealing curvatures in different directions.
Complementary, focussing on the results for the vertical velocity component $\overline{w}/U_\infty$, Figs. 5.48 and 5.49 show the acceleration areas alternating at the upper and lower airfoil surface near the trailing edge at the positions of extremal pitch angles. At minimum pitch, case I presents in Fig. 5.48(e) a local velocity region below the bottom airfoil surface that is directed upwards with $\overline{w}/U_\infty \approx 0.2$ at $x/c = [-0.4; 0.2]$, $z/c = [-0.4; 0.1]$. The corresponding velocity field of case III shows in Fig. 5.49(e) an increased local velocity region below the airfoil with $\overline{w}/U_\infty = 0.25$ at $x/c = [-0.4; 0.3]$, $z/c = [-0.5; 0.1]$ as well as a velocity region above the airfoil with $\overline{w}/U_\infty = 0.18$ at $x/c = [-0.4; 0.3]$, $z/c = [0.1; 0.3]$. At maximum pitch, case I reveals in Fig. 5.48(h) the acceleration region located above the upper airfoil surface and directed downwards with $\overline{w}/U_\infty \approx -0.2$ at $x/c = [-0.4; 0.2]$, $z/c = [-0.1; 0.2]$, while for case III in Fig. 5.49(h) an increased region can be observed with $\overline{w}/U_\infty \approx -0.25$ at $x/c = [-0.4; 0.2]$, $z/c = [-0.1; 0.4]$. The findings that the vertical acceleration areas are higher for case III than for case I, can be deduced from the higher pitch amplitudes caused by the backward shifted center of gravity for case III. Therefore, the local flow velocities and turbulence intensity around the airfoil are increased.

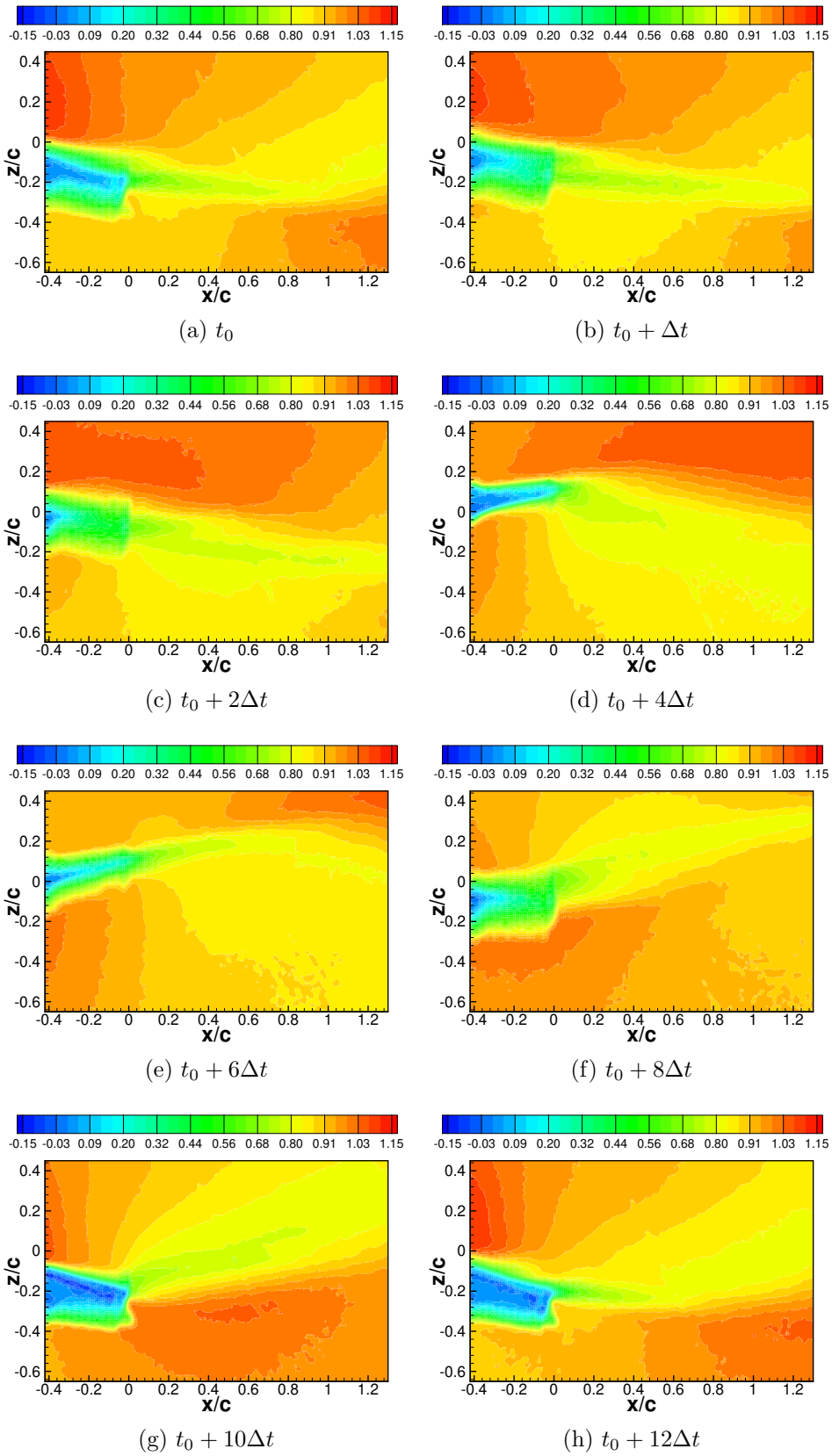

(a) t_0 (b) $t_0 + \Delta t$

(c) $t_0 + 2\Delta t$ (d) $t_0 + 4\Delta t$

(e) $t_0 + 6\Delta t$ (f) $t_0 + 8\Delta t$

(g) $t_0 + 10\Delta t$ (h) $t_0 + 12\Delta t$

Figure 5.46: Case I: Influence of the structural flutter phenomenon on the wake flow. Phase-averaged velocity field $\overline{u}/U_\infty$ normalized by the free-stream velocity.

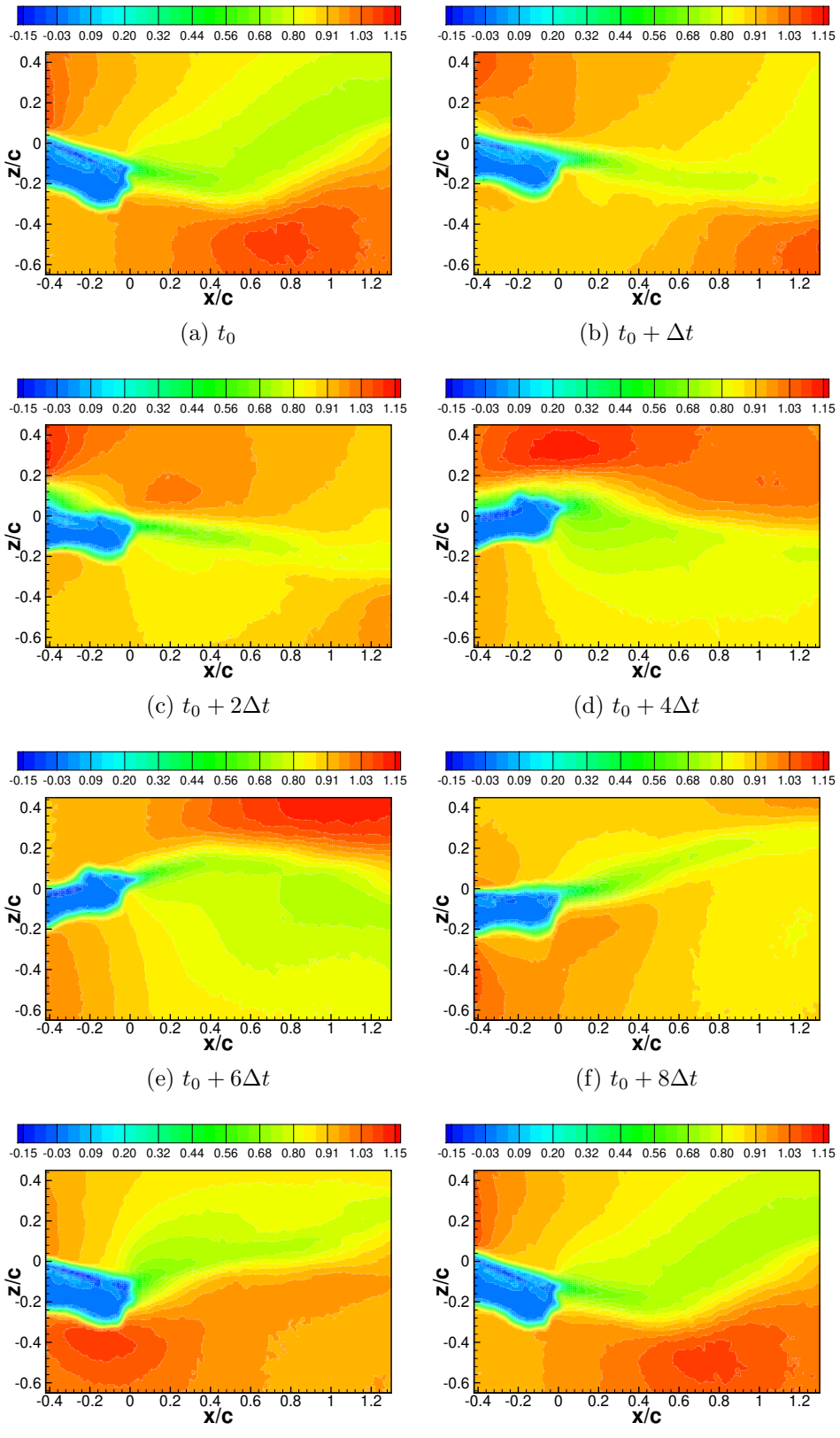

(a) t_0 (b) $t_0 + \Delta t$

(c) $t_0 + 2\Delta t$ (d) $t_0 + 4\Delta t$

(e) $t_0 + 6\Delta t$ (f) $t_0 + 8\Delta t$

(g) $t_0 + 10\Delta t$ (h) $t_0 + 12\Delta t$

Figure 5.47: Case III: Influence of the structural flutter phenomenon on the wake flow. Phase-averaged velocity field $\overline{u}/U_\infty$ normalized by the free-stream velocity.

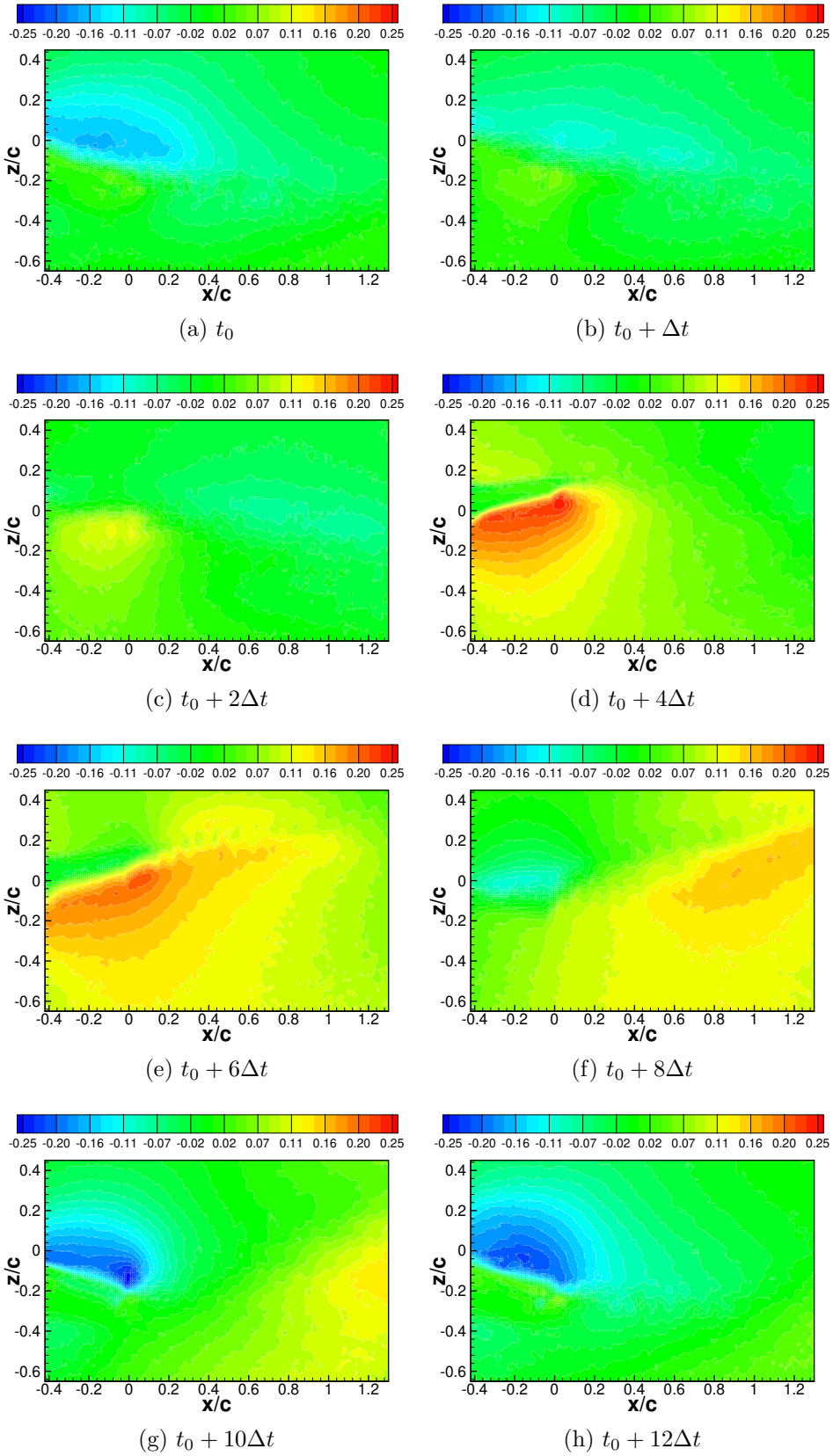

(a) t_0 (b) $t_0 + \Delta t$

(c) $t_0 + 2\Delta t$ (d) $t_0 + 4\Delta t$

(e) $t_0 + 6\Delta t$ (f) $t_0 + 8\Delta t$

(g) $t_0 + 10\Delta t$ (h) $t_0 + 12\Delta t$

Figure 5.48: Case I: Influence of the structural flutter phenomenon on the wake flow. Phase-averaged velocity field $\overline{w}/U_\infty$ normalized by the free-stream velocity.

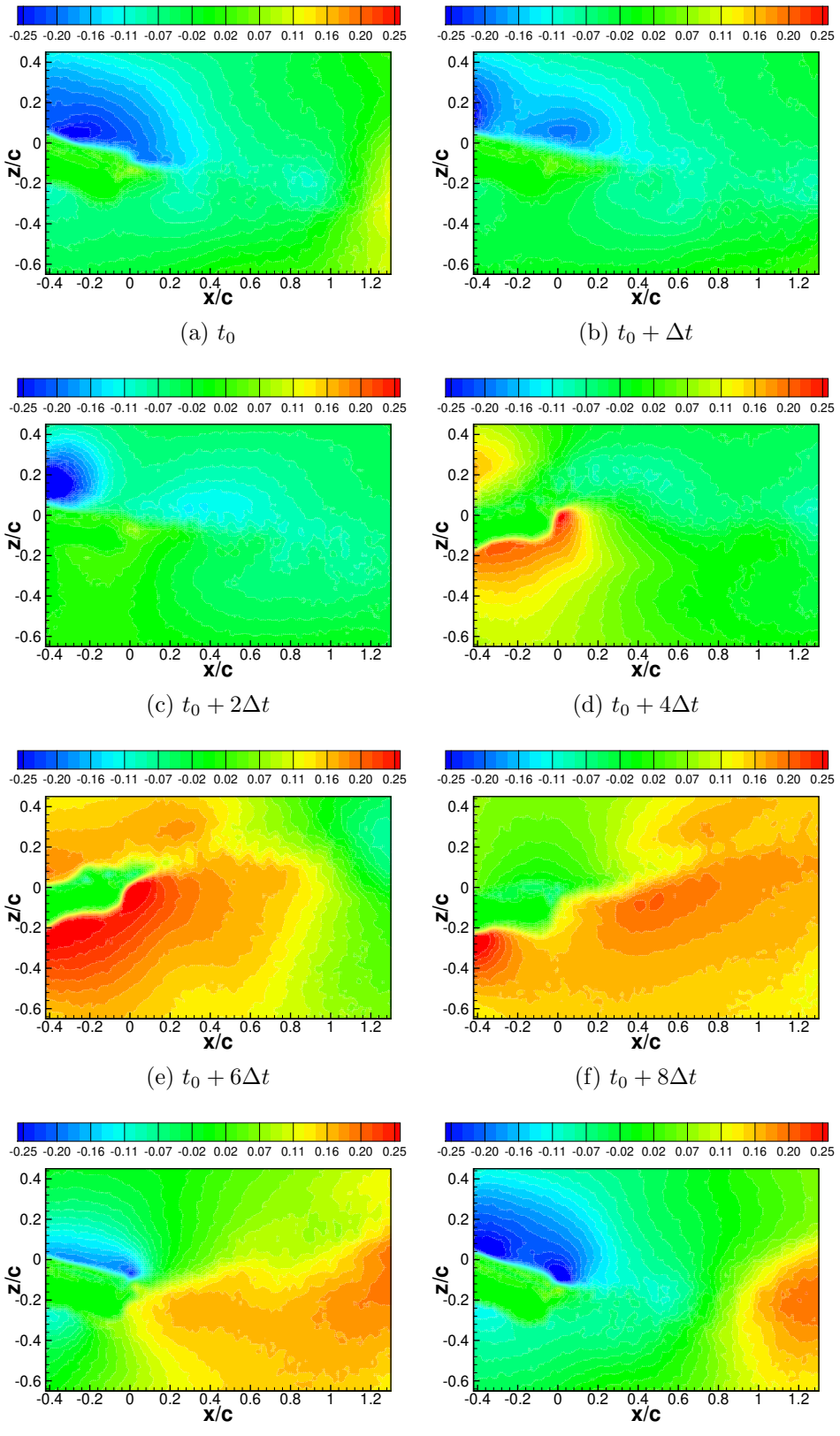

(a) t_0 (b) $t_0 + \Delta t$

(c) $t_0 + 2\Delta t$ (d) $t_0 + 4\Delta t$

(e) $t_0 + 6\Delta t$ (f) $t_0 + 8\Delta t$

(g) $t_0 + 10\Delta t$ (h) $t_0 + 12\Delta t$

Figure 5.49: Case III: Influence of the structural flutter phenomenon on the wake flow. Phase-averaged velocity field $\overline{w}/U_\infty$ normalized by the free-stream velocity.

5.5.2 Comparison of Reynolds stresses in case I/III

Going further to the phase-averaged fluctuations of the velocity components, the Reynolds stress tensor provides information about the turbulent behavior in the fluid flow that persists during the periods of oscillation and is not averaged out by phase-averaging. In contrast to that, coincidental phenomena like the appearance of a turbulent eddy at a definded position and time, are filtered out by the phase-averaging procedure and are thus not visible in the phase-averaged velocity fields.

Beginning with the normal tensor component $\overline{u'u'}/U_\infty^2$, it describes the averaged quadratic fluctuations in main flow direction normalized by the quadratic undisturbed free-stream velocity U_∞^2. Case I is depicted in Fig. 5.50. In the region around the airfoil, the systematic error of image acquisition by the PIV-camera can be seen in the red marked areas in each snapshot. However, in Fig. 5.50(d), there is a slightly red region with $\overline{u'u'}/U_\infty^2 = 0.024$ at $x/c = [0.1; 0.4]$, $z/c = 0.15$ that indicates a turbulence area, i.e., the shear layer roll-up behind the trailing edge. In the same image the shear layer is formed as a continuous green curvature in the wake with $\overline{u'u'}/U_\infty^2 = [0.012; 0.015]$. In the following Fig. 5.50(e), this shear layer proceeds further leaving a gap behind the trailing edge. This is due to the fact that the airfoil reaches its minimum pitch angle there, staying in this position. The vortices that are generated coincidently behind the trailing edge are captured in the time series, but are then filtered out by the phase-averaging. Those findings can be seen also in Figs. 5.50(g) and 5.50(h), where the airfoil is at its maximum pitch angle with the curved shear layer and the gap after proceeding due to instantaneous vortex shedding. Comparing this to case III in Fig. 5.51, the curvature of the shear layer is sporadically visible for example in Fig. 5.51(e). Though, in the other images, the shear layer is irregularly distributed in the wake.

The normal Reynolds stress component $\overline{w'w'}/U_\infty^2$ describes the averaged quadratic fluctuations related to the vertical velocity component w normalized by the free-stream velocity U_∞^2. Case I is depicted in Fig. 5.52 showing results of small turbulence regions, which can be seen exemplarily in Fig. 5.52(a) at $x/c = -0.2$, $z/c = -0.1$ and by Fig. 5.52(b) at $x/c = -0.1$, $z/c = -0.1$ with $\overline{w'w'}/U_\infty^2 \approx 0.021$. Those are representative for a flow separation at the trailing edge of the airfoil. Comparing this to case III, Fig. 5.53 shows larger regions of high turbulence intensity, i.e., in Figs. 5.53(d) at $x/c = 0.2$, $z/c = 0.2$ and 5.53(h) at $x/c = 0.8$, $z/c = -0.2$ with $\overline{w'w'}/U_\infty^2 \approx 0.019$. These turbulence regions can be attributed to large vortices that persist strongly within the wake.

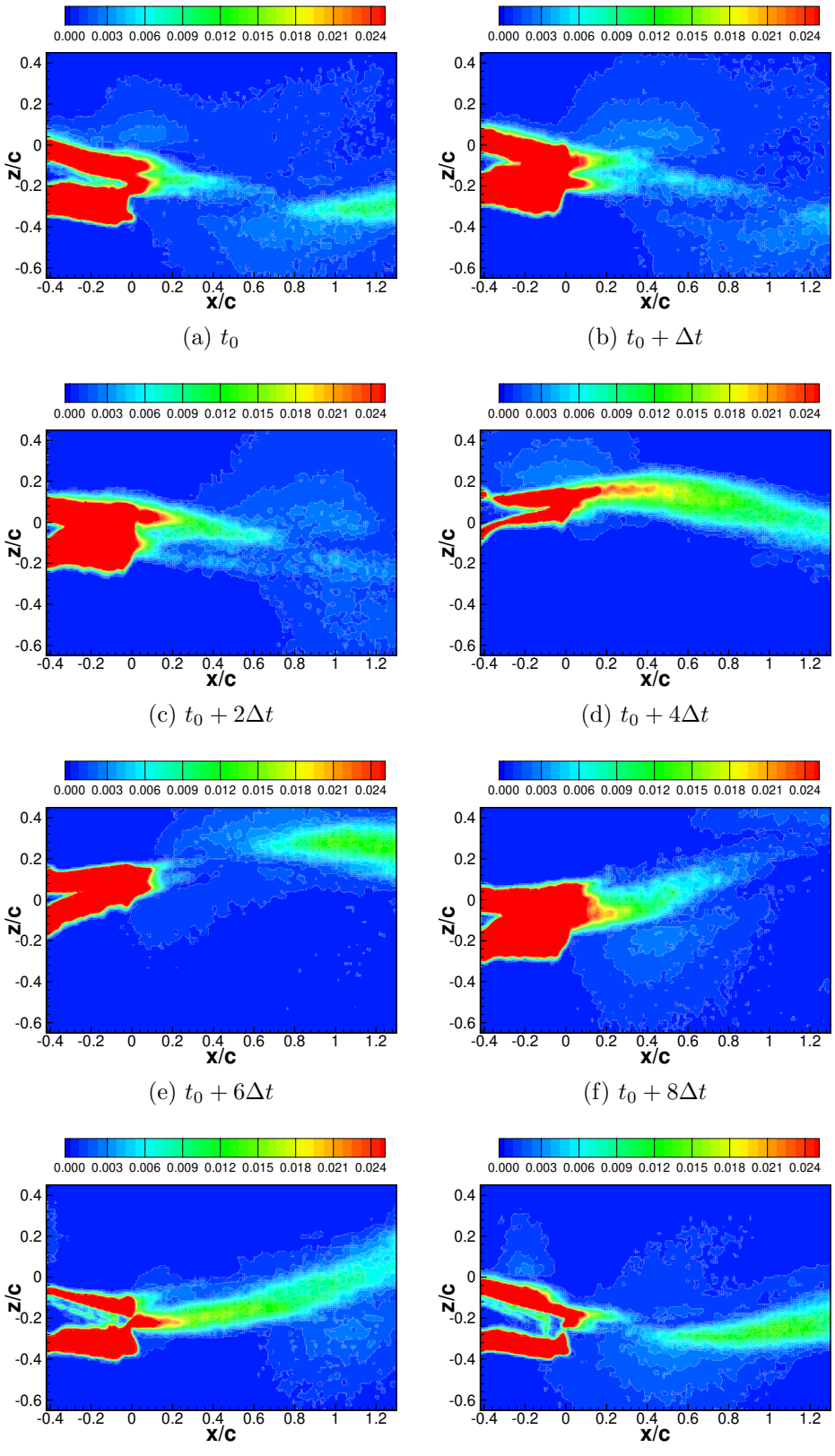

(a) t_0 (b) $t_0 + \Delta t$

(c) $t_0 + 2\Delta t$ (d) $t_0 + 4\Delta t$

(e) $t_0 + 6\Delta t$ (f) $t_0 + 8\Delta t$

(g) $t_0 + 10\Delta t$ (h) $t_0 + 12\Delta t$

Figure 5.50: Case I: Influence of the structural flutter phenomenon on the wake flow. Normal Reynolds stress component in main flow direction $\overline{u'u'}/U_\infty^2$ normalized by the quadratic free-stream velocity.

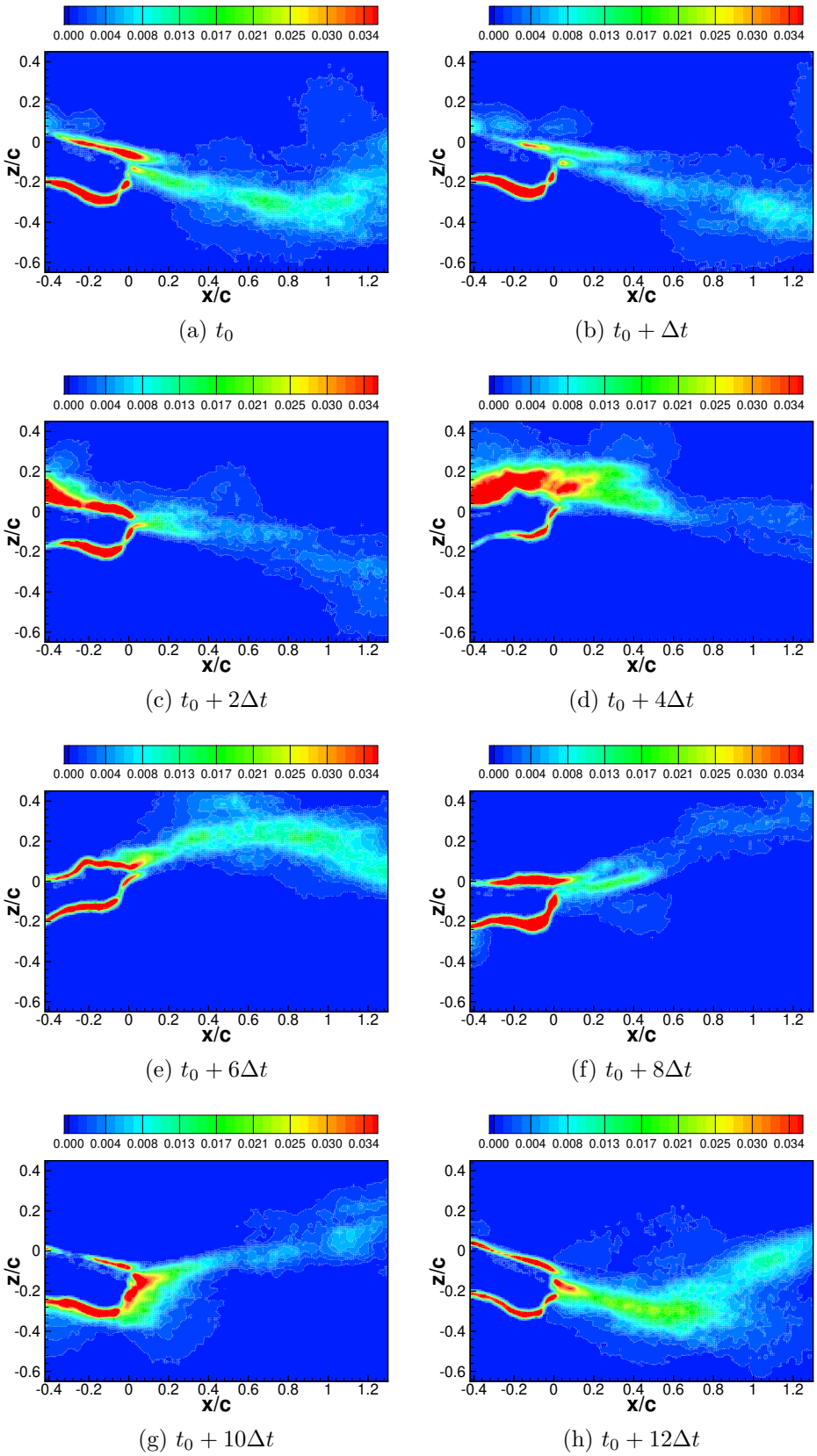

(a) t_0 (b) $t_0 + \Delta t$

(c) $t_0 + 2\Delta t$ (d) $t_0 + 4\Delta t$

(e) $t_0 + 6\Delta t$ (f) $t_0 + 8\Delta t$

(g) $t_0 + 10\Delta t$ (h) $t_0 + 12\Delta t$

Figure 5.51: Case III: Influence of the structural flutter phenomenon on the wake flow. Normal Reynolds stress component in main flow direction $\overline{u'u'}/U_\infty^2$ normalized by the quadratic free-stream velocity.

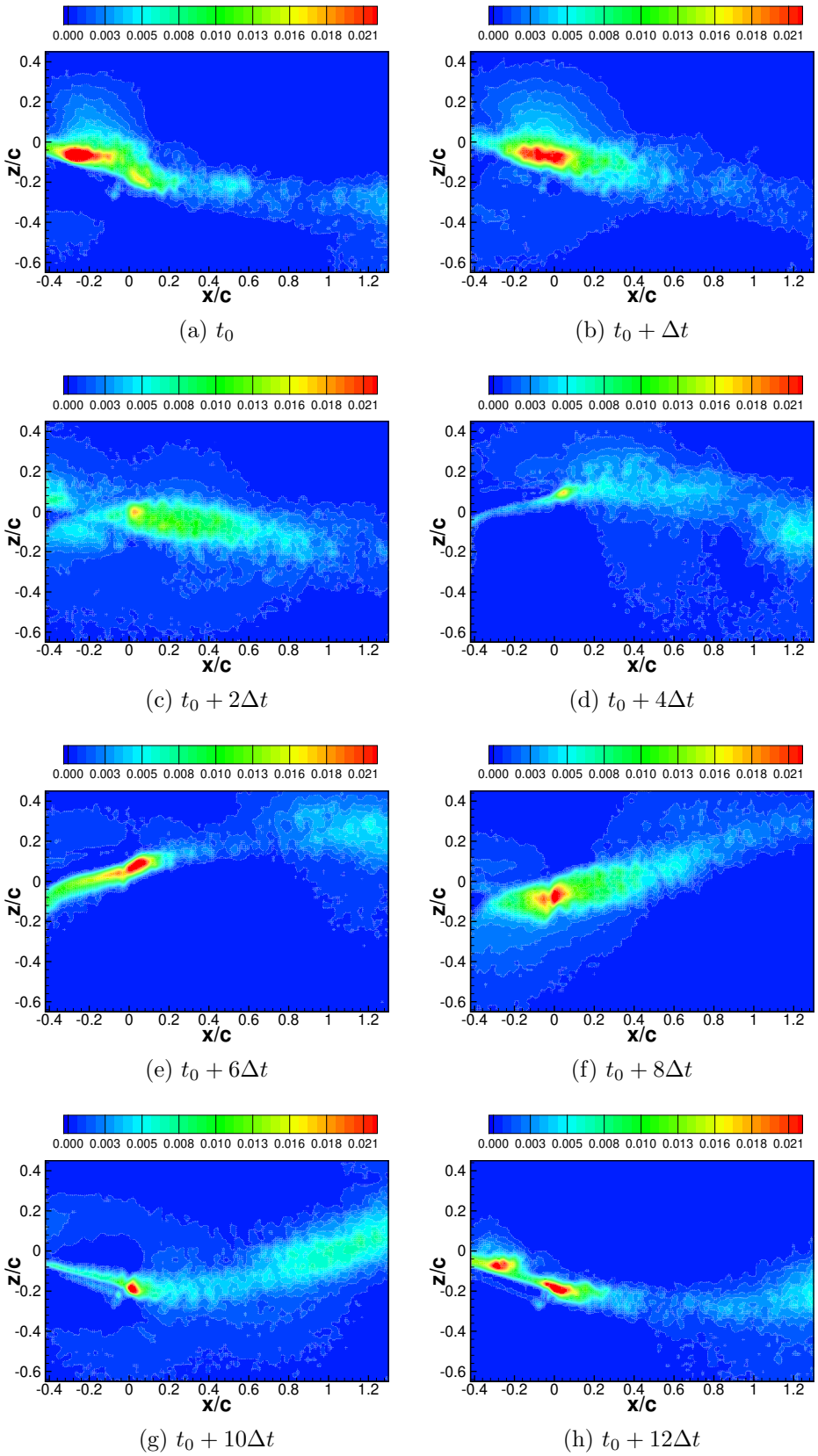

(a) t_0 (b) $t_0 + \Delta t$

(c) $t_0 + 2\Delta t$ (d) $t_0 + 4\Delta t$

(e) $t_0 + 6\Delta t$ (f) $t_0 + 8\Delta t$

(g) $t_0 + 10\Delta t$ (h) $t_0 + 12\Delta t$

Figure 5.52: Case I: Influence of the structural flutter phenomenon on the wake flow. Normal Reynolds stress component perpendicular to main flow direction $\overline{w'w'}/U_\infty^2$ normalized by the quadratic free-stream velocity.

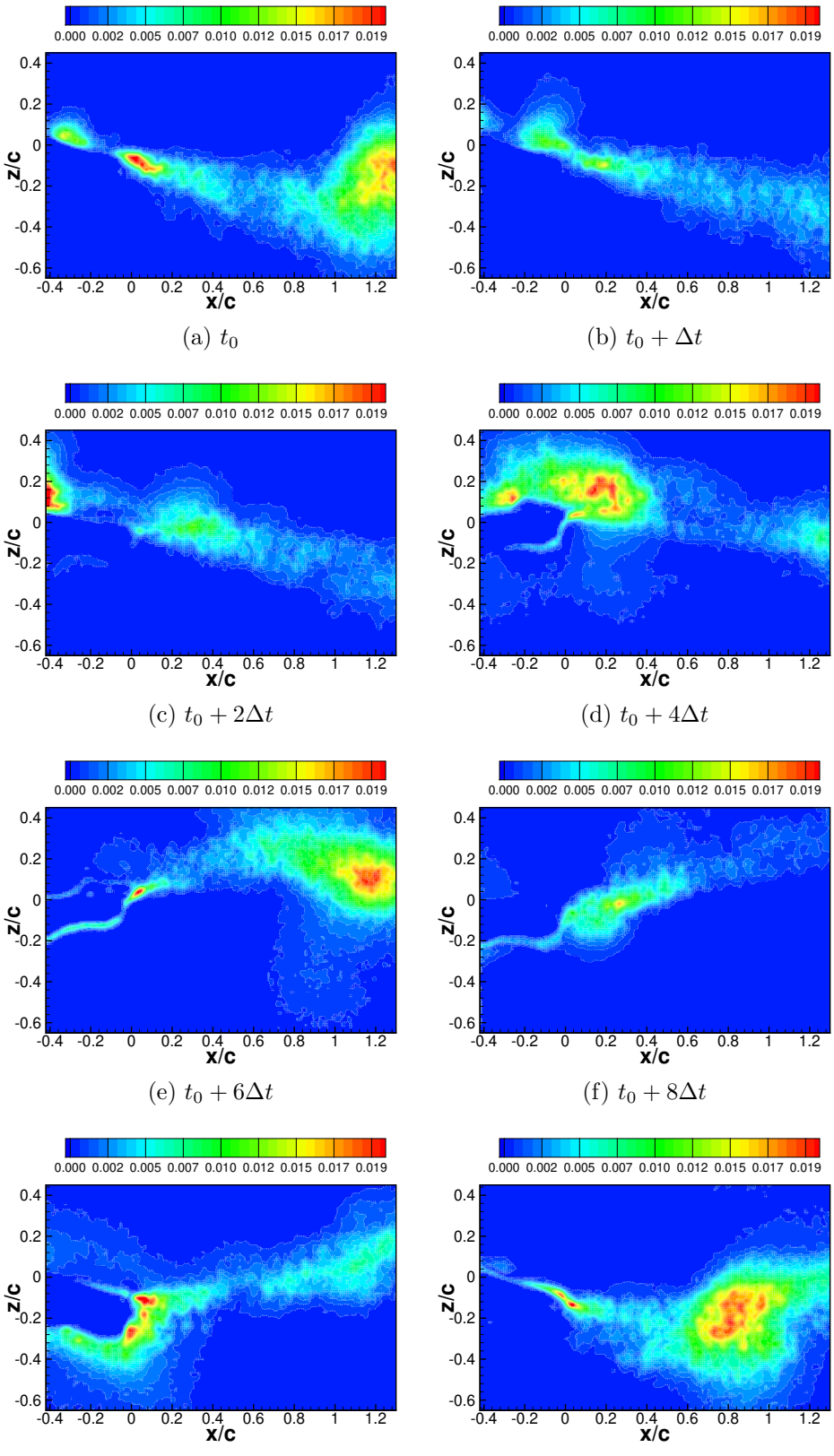

(a) t_0 (b) $t_0 + \Delta t$

(c) $t_0 + 2\Delta t$ (d) $t_0 + 4\Delta t$

(e) $t_0 + 6\Delta t$ (f) $t_0 + 8\Delta t$

(g) $t_0 + 10\Delta t$ (h) $t_0 + 12\Delta t$

Figure 5.53: Case III: Influence of the structural flutter phenomenon on the wake flow. Normal Reynolds stress component perpendicular to main flow direction $\overline{w'w'}/U_\infty^2$ normalized by the quadratic free-stream velocity.

The Reynolds shear stress component $-\overline{u'w'}/U_\infty^2$ gives information about the correlation of the horizontal and vertical fluctuations in the velocity field. The distribution for case I is shown in Fig. 5.54. The development of the shear layer can be seen in the image series. In Fig. 5.54(c) and other figures of this series, the blue and red marked areas at $x/c < 0$ occur due to systematic errors in the image aquisition by PIV or the phase-averaging difficulties. It is caused by the flow fluctuations rather in horizontal direction u' than in vertical direction w', since Fig. 5.50 reveals the error more clearly than Fig. 5.52. However, by the red marked regions at $x/c = [0; 0.6]$, $z/c = [-0.1; 0.1]$ with $-\overline{u'w'}/U_\infty^2 = 0.007$, the first flow separation at the trailing edge is visible. In the following Fig. 5.54(d), the shear layer develops in the wake in the typical form of the curvature due to the motion of the airfoil and then proceeds further. The shear layer gap in Fig. 5.54(e) at $x/c = [0.2; 0.8]$ can be explained by the minimum pitch angle position, where the airfoil is shortly quasi at rest and small-scale vortices are captured in the time series, but filtered out by the phase-averaging. The similar, inversed phenomenon can be seen in the image series of Figs. 5.54(f) to 5.54(h), with the flow separation with $-\overline{u'w'}/U_\infty^2 = -0.007$ at $x/c = [0; 0.4]$, $z/c = [-0.2; 0]$, the curved shear layer, and the gap in the area of $x/c = [0.2; 0.7]$ at the maximum pitch angle position of the airfoil. Comparing those findings with the image series of case III in Fig. 5.55, first of all, it is remarkable that the artefacts according to the systematic measurement errors are smaller here than for case I. This is due to the fact, that the structural flutter oscillation is limited in the region of the trailing edge by the backwards shifted center of gravity. Therefore, the image acquisition by PIV reveal less perspective errors, which can be seen in the horizontal fluctuations of $\overline{u'u'}/U_\infty^2$ in Fig. 5.51, since u' is the dominating parameter for the calculation of $\overline{u'w'}/U_\infty^2$. However, focussing on the wake characteristics, the shear layer is less clearly visible in Fig. 5.55(e) at $x/c = [0.8; 1.2]$, $z/c = [0; 0.3]$ with $-\overline{u'w'}/U_\infty^2 = 0.009$ and in Fig. 5.55(h) at $x/c = [0.6; 1.1]$, $z/c = [-0.3; 0]$ with $-\overline{u'w'}/U_\infty^2 = -0.010$. The gap in both images can be explained again by the observation that at the position where the airfoil is quasi at rest all small-scale vortices are filtered out by the phase-averaging. Additionally, Fig. 5.55(d) shows a turbulent region with high fluctuations at $x/c = [0; 0.4]$, $z/c = [0; 0.2]$ with $-\overline{u'w'}/U_\infty^2 = 0.009$, where a flow separation takes place at the trailing edge. In the other figures, there are regions of increased turbulence intensity sporadically visible which are difficult to assign to the shear layer. It can be assumed that this irregularity in the wake flow originates from the merging of the detached flow from the trailing edge and the midst of the airfoil at higher pitch angles of case III. Thus, the flow velocities around the airfoil are increased and the flow detachment begins already on the upper or bottom line, generating vortices that proceed arbitrarily in the wake. Those unsteady phenomena are filtered out by the phase-averaging.

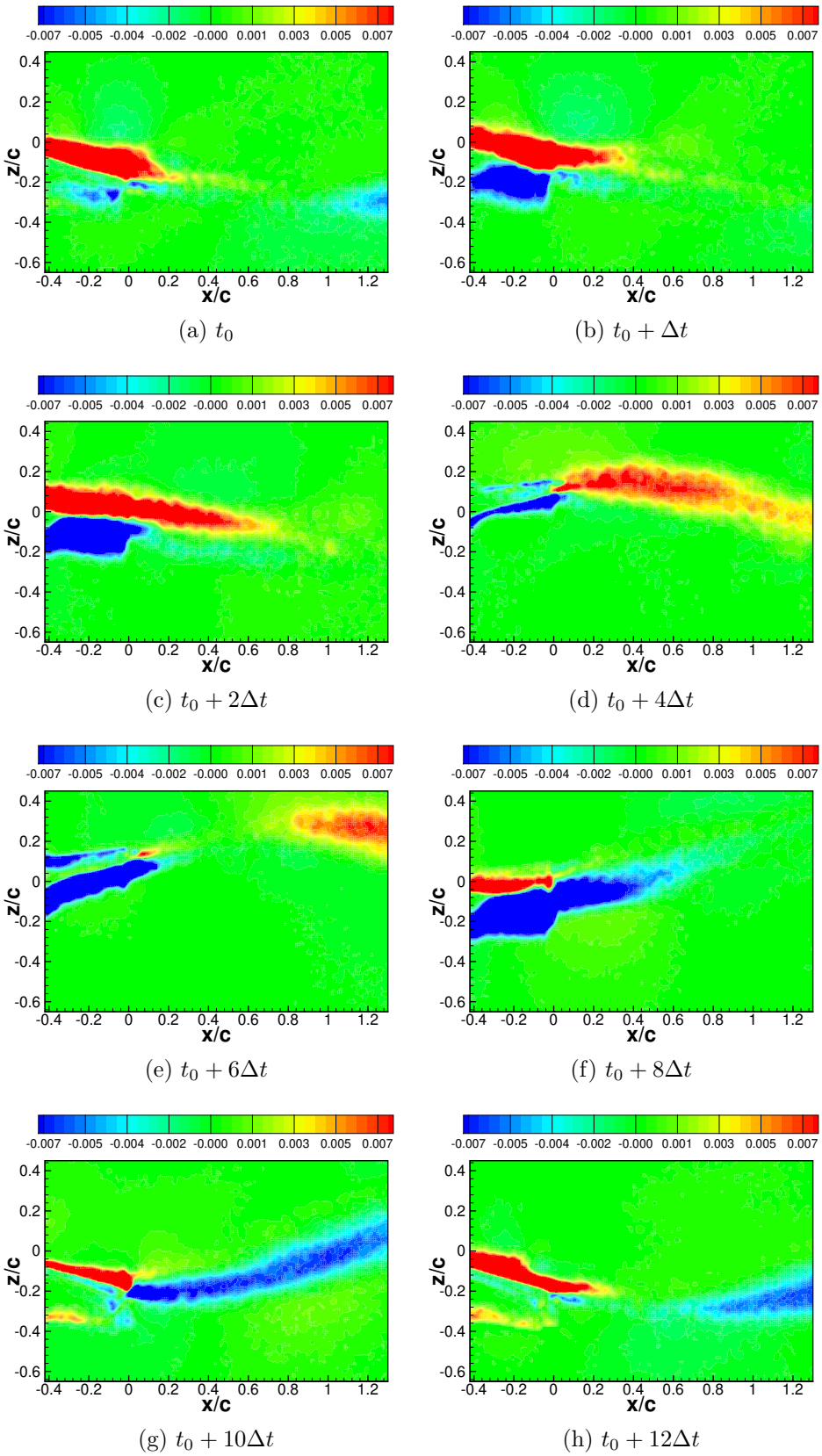

(a) t_0 (b) $t_0 + \Delta t$

(c) $t_0 + 2\Delta t$ (d) $t_0 + 4\Delta t$

(e) $t_0 + 6\Delta t$ (f) $t_0 + 8\Delta t$

(g) $t_0 + 10\Delta t$ (h) $t_0 + 12\Delta t$

Figure 5.54: Case I: Influence of the structural flutter phenomenon on the wake flow. Normal Reynolds stress component perpendicular to main flow direction $\overline{u'w'}/U_\infty^2$ normalized by the quadratic free-stream velocity.

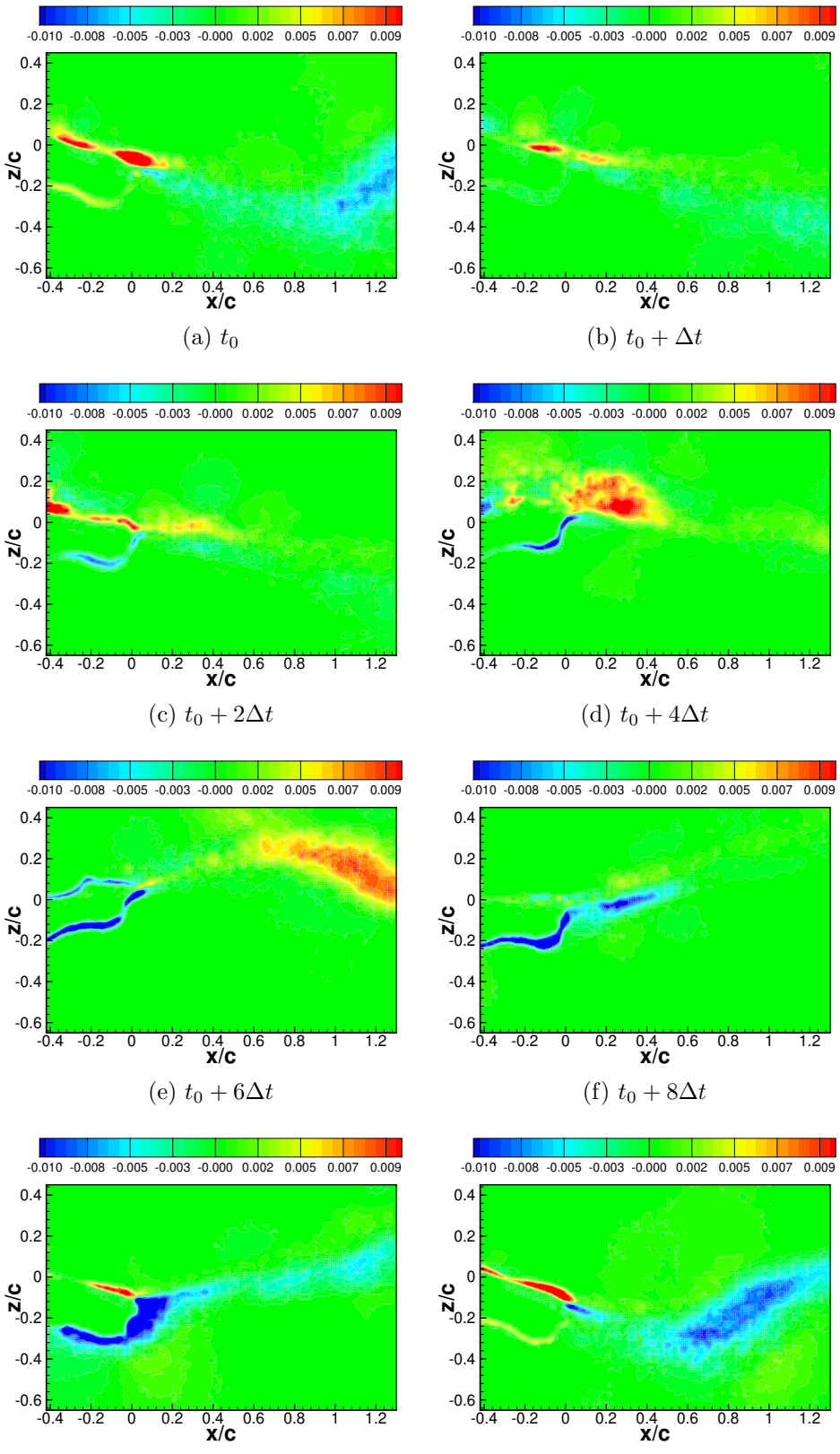

(a) t_0 (b) $t_0 + \Delta t$

(c) $t_0 + 2\Delta t$ (d) $t_0 + 4\Delta t$

(e) $t_0 + 6\Delta t$ (f) $t_0 + 8\Delta t$

(g) $t_0 + 10\Delta t$ (h) $t_0 + 12\Delta t$

Figure 5.55: Case III: Influence of the structural flutter phenomenon on the wake flow. Normal Reynolds stress component perpendicular to main flow direction $\overline{u'w'}/U_\infty^2$ normalized by the quadratic free-stream velocity.

To conclude with the phase-averaged data, the acceleration areas around the airfoil are higher for case III than case I, which can be seen in the mean values of the velocity components. This is due to the fact, that the pitch angle range is increased for case III. Concerning the Reynolds stresses, case I shows a more structured wake flow than case III. Thus, the shear layer is rather continuous in its thickness and shaped as a curvature, which originates from the regular flow detachment at the trailing edge with a level of turbulence at Tu $\approx$ 0.1 (calculated from the shear layer in Figs. 5.50(g) and 5.52(g)). Case III shows an irregularly formed shear layer with Tu $\approx$ 0.14 in the wake (related to Figs. 5.51(e) and 5.53(e)), which originates from the merged flow detachment from the upper/bottom line and from the trailing edge of the airfoil. Therefore, increased local turbulence regions can be observed in the trailing edge area, which can be assigned to the generation of large vortices.

Chapter 6

Conclusions

6.1 Summary

The present thesis is concerned with the experimental investigations in fluid and structural dynamics. High-speed imaging methods are applied, giving an impression of the fluid and structure behavior within a framed test section. The two *non-invasive* measuring techniques are the particle-image velocimetry (PIV) for fluid flow field measurements and the digital-image correlation (DIC) for structural deformation measurements. The test object is an elastically mounted wing system, which is positioned in a subsonic wind tunnel. Within the transitional Re number range, the unsteady fluid flow around the wing system is investigated as well as the structural oscillations of the wing. First of all, the PIV and DIC measurements are carried out separately from each other. Second, an idea is developed to combine these techniques by the synchronization of the measuring processes. The results are compared with the previously published experimental results of Wood et al. [23] and the numerical FSI simulations of De Nayer et al. [15].
Summarizing the measurement methods, the PIV technique considers fluid flow measurements by the illumination of a 2D-plane with a pulsed laser sheet. The flow is seeded by tracer particles, reflecting the received light. A sequence of images of the moving tracer particles within the test section is captured by a high-speed camera. The movement of the particles is analyzed and associated with the fluid flow. The captured 2D-image planes are subdivided into a grid of interrogation windows (IW), from which a correlation algorithm reconstructs the velocity fields. The PIV setup consists of the high-speed laser of the type Litron LD-527 PIV, the high-speed camera Phantom VEO 640S and the control software TSI Insight 4G is used. The tracer particles are provided by a soap bubble generator TSI BG-1000 and the DEHS generator TSI Six-Jet Atomizer 9306. Special properties of the setup or adjustment data are explained in Sections 3.1 and 4.

The DIC technique for structural deformation measurements considers the illumination (standard light) of a 3D object. The object surface is covered by a speckle pattern, from which a sequence of images is captured during the measurements. By the stereoscopic setup of two 2D DIC-cameras and a spatial calibration, 3D movements and deformations of the observed surface can be reconstructed. Thus, the captured images are subdivided into facets including a certain amount of grid cells, for which a correlation function is solved by an iterative process. The DIC setup consists of two high-speed cameras of the type HSVision Speedcam MarcoVis Eo Sens, which are triggered by a manual trigger button connected via BNC- and T-Link adaption. The control softwares for the image saving and post-processing are given by HSVision Visart and Dantec Dynamics Istra 4D. Special properties of the setup or adjustment data are explained in Sections 3.2 and 4.

Considering the test stand, the wing system is a lightweight design with the total mass of $m_w = 0.339\,\text{kg}$ and the airfoil of NACA 0012 type with a chord length of $c = 0.1\,\text{m}$ and a wing span of $l = 0.6\,\text{m}$. The elastic mounting at both ends, consisting of a package of leaf springs and torsional springs, restricts the movement to two degrees of freedom, the heave and the pitch motion of the airfoil, respectively. By fixing extra masses at both ends of the wing at varying locations, different cases are generated, due to the fact that the center of gravity (c.o.g. or G) is shifted along the chord line. In case I, G and the elastic axis (E) are superimposed, while in case III G is shifted behind E near the trailing edge of the airfoil. Compared to the setup of Wood et al. [23], the current wing surface has been varnished in black, which raised the total mass by 0.004 kg. In addition, the torsional springs have been replaced by new ones of the identical type and torsional stiffness of $k_\alpha = 0.3832\,\text{Nm/rad}$. Details of the wing system and its structural mechanics parameters are presented in Sections 2.1.3 and 5.1.1. A subsonic wind tunnel provides the airflow for the measurements. It is designed in the geometric "loop form" known as Göttingen type. The rotation speed of the air blower stands in linear relation to the generated flow velocity, which is adjusted in the transitional Re number range of $9.66 \times 10^3 \leq \text{Re} \leq 3.60 \times 10^4$ for the current measurements. Details of the wind tunnel properties are mentioned in Section 2.2.

Considering the synchronization of the DIC and the PIV measurement techniques, the main ideas are presented here. First, the same illumination source for the 3D object surface (DIC) and the 2D test section (PIV) is provided by the PIV laser. Second, for the image acquisition, the PIV and DIC cameras are synchronized. This is realized by an "I/O-link" cable connection between both cameras, which furthermore replaces the manual trigger button for the DIC setup. The PIV software controls the timing of the laser-pulsed illumination as well as the image acquisition of the PIV camera, which automatically triggers

the image acquisition of both DIC cameras. The laser pulse rate is set to 500 pps, while the PIV and DIC cameras have the sample rate of 500 fps, guaranteeing identical conditions of image illumination and the comparability of structural deformations and fluid flow velocity fields within a certain image sequence. Details of the synchronization idea are presented in Section 3.3, while further timing parameters of the laser and cameras can be found in Section 4.

Focusing on the measurement results, there are DIC measurements carried out for the still air case. By the investigation of the 1-DOF airfoil motion, in which the heave or the pitch DOF are considered separately, the main frequencies of either heave or pitch are gained and specific structural mechanics parameters are calculated such as the heave spring stiffness or torsional damping ratios. These results are compared to the previously published data by Wood et al. [23] and a good agreement has been found. Hence, the structural mechanics properties of the elastically mounted wing system are not significantly changed by the replacement of the torsional springs and the slight increase of the wing mass. Based on the investigation of the 2-DOF airfoil motion, in which the heave and pitch DOF are measured simultaneously, the decaying vibrational behavior is analyzed. The generated FFT plots reveal the characteristic heave and pitch frequency peaks, which correspond well to the results of Wood et al. [23] considering the beat frequencies and the heave-to-pitch frequency ratios.
Furthermore, the unsynchronized and synchronized DIC results are compared for the still air case and for several fluid velocities in the transitional Re range of $9.66 \times 10^3 \leq \mathrm{Re} \leq 3.60 \times 10^4$. First, it has to be mentioned that the recording times are different, since the unsynchronized measurements are carried out with a camera frame rate of 250 fps and the synchronized ones with 500 fps. Second, the time histories at lower flow velocities are usually similar showing mostly *in-phase*, damped oscillations, although the amplitudes slightly differ due to the individual manual excitation of the wing. At higher flow velocities, the manual excitation is not necessary, since the wing system is self exciting. The increasing amplitudes show slight differences between the synchronized and unsynchronized results, which may originate from statistical variations of the single (non-repeated) measurements. Third, the FFT plots show similar frequency distributions despite different lengths of the recording time for the unsynchronized and synchronized method. By increasing the flow velocity, the heave and pitch frequency peaks are drawing near to each other, until one single frequency is visible for the flutter motion.
Based on the PIV results, the unsteady wake flow phenomena are investigated. For the fluid velocity set at $\mathrm{Re} = 2.39 \times 10^4$, the convection of vortices is captured in a sequence of images, from which a linear relation between the proceeding time and the

vortex convection position is found with the vortex convection velocity of $U_{cv} = 3.18\,\mathrm{m/s}$ and a calculated Strouhal number of $\mathrm{Sr} = 0.42$. For other flow velocities, the Sr numbers are determined, too. Furthermore, the fluid velocities u and w at certain points in the flow field are extracted from the PIV measurements by setting a monitoring point in the wake. Time histories are recorded and FFTs are carried out. Especially in the FFT plots, the lower frequency region shows that the airfoil motion with its specific heave and pitch frequencies are represented also in the wake flow with corresponding frequencies of the flow fluctuations. In the higher frequency regions the vortex shedding frequencies are revealed. Unfortunately, those are disappearing for the higher Re numbers due to blurring effects of the flutter motion, which is found in agreement with the CTA measurements of Wood et al. [23].
Finally, the synchronized PIV-DIC measurements and phase-averaged velocity fields are presented. For one single period of flutter oscillation, a sequence of images presents the velocity fields u/U_∞ and w/U_∞ for case I and III at $\mathrm{Re} = 3.60 \times 10^4$, while the corresponding airfoil positions are superimposed on each image. Describing the properties of the airfoil motion in pictures, the dynamic behavior of case I can be denoted the *swimming fish*, while the dynamic behavior of case III represents the *flapping motion* according to De Nayer et al. [15]. This is due to the fact that the phase shift angle between the heave and pitch oscillations is rather high for case I ($\varphi = 125°$), whereas for case III heave and pitch are nearly in phase ($\varphi = 23°$). Concerning the flow characteristics, the effect of lift at extreme heave and pitch positions is investigated. It is found that the lift forces have a stabilizing, repressing influence on case I and an emphasizing influence on case III. This is supported by the results of the phase-averaged velocity fields with increased acceleration areas around the trailing edge of the airfoil for case III compared to case I. Furthermore, the Reynolds stresses reveal a rather continuous formation of the shear layer in the wake flow for case I compared to case III, which shows a nearly chaotic, irregular behavior.

Discussing and evaluating the synchronized PIV-DIC measurement technique, there are several advantages that can be mentioned. First, the "I/O-link"-connection between the PIV and the DIC cameras is a positive achievement, since the cameras can be triggered at the same time by the PIV software, which also controls the pulsing of the PIV laser as illumination source for the synchronized measurements. Second, the internal parameter of the cameras (PIV, DIC) and the PIV laser are aligned with the frame and pulse rates of 500 fps and 500 pps, respectively. Third, considering the illumination of DIC by the PIV laser, a comparison to the standard light illumination of DIC is presented. For case I at still air, the measurement uncertainties of the displacements in z-direction are sufficiently low with a relative mean error of 0.046 % for the synchronized method and 0.07 % for

the unsynchronized method. For case I at flutter, the measurement uncertainties of the displacements in z-direction are also comparable with a relative mean error of 0.103 % for the synchronized method and 0.064 % for the unsynchronized method. Surely there are also difficulties that have to be mentioned and may be improved in future works. The illumination of the DIC-speckle pattern by the PIV-laser has some restrictions. Due to the high intensity of the laser light sheet, there is an overexposed area on the speckle pattern that can not be used for DIC. Only the neighboring areas with decreased light intensity are usable, which in this case is half of the whole speckle pattern area. Furthermore, the laser light can cause a damage on the test object, such as blisters, which happens during a longer measurement time and is rather unfavorable. Hence, a solution for these problems of illumination may be found in future works.

6.2 Outlook

Beyond the investigations of this thesis, several experimental topics can be focused on. First, the illumination area of the synchronized DIC measurements can be expanded by the usage of a beam splitter which is interposed between the laser head and the light sheet optics (LSO). The idea is schematically depicted in Fig. 6.1.

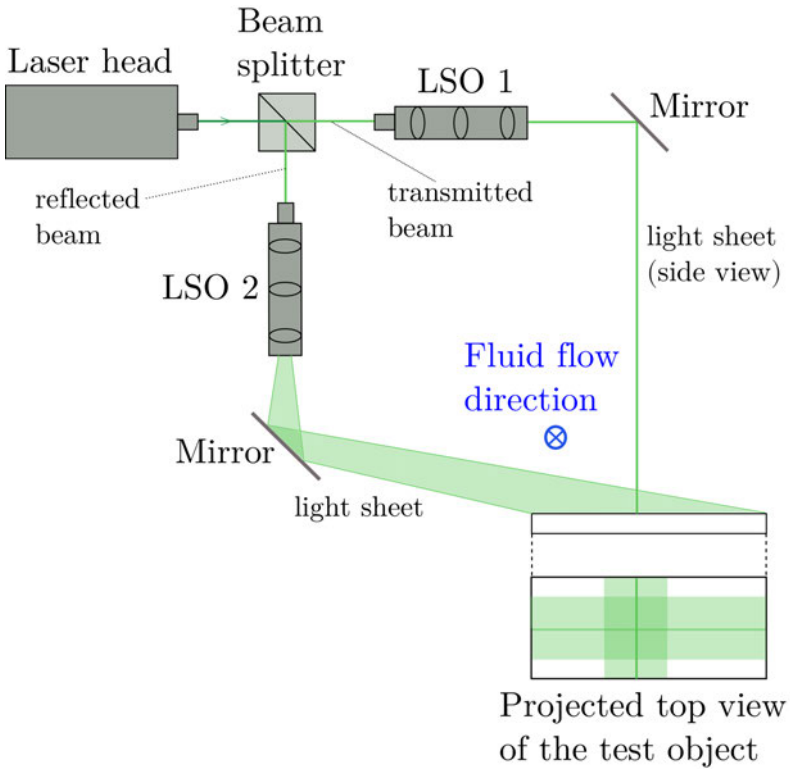

Figure 6.1: Idea of expanding the illumination area of a test object for the synchronized DIC-PIV measurements by the usage of a laser beam splitter.

The laser beam is subdivided into a transmitted and a reflected beam. The splitting ratio can be chosen, i.e., with 70/30 (transmitted/reflected), since the transmitted beam needs a higher intensity for the illumination of the 2D-PIV-plane. However, the transmitted and reflected beams are conducted through the LSO 1 and 2, respectively, which generate the light sheets. By two mirrors, they are redirected to the test object. For the purpose of expanding the illumination area for DIC, the light sheets are positioned vertically towards each other, forming a "cross" on the surface of the test object. Additionally, the problem of the overexposed illumination area, caused by one light sheet with high intensity, can be reduced by splitting the laser beam.
Second, the PIV measurements can be extended by adding a second HS-PIV-camera. This can be either used to capture a larger part of the flow field. The second option is to upgrade the former mono PIV-measurements for 2D velocity fields to a stereoscopic setup, comparable to the DIC-setup. This method can provide 3D velocity fields out of a planar region illuminated by the laser light sheet, while the images are captured by the two PIV-cameras from different perspectives. At PfS, a second HS-PIV-camera has been acquired recently.
Finally, considering further studies at PfS, an actual topic is the simulation of wind gusts, appearing in the nature and having a strong effect on, i.e., wind energy plants and the dynamic properties of their tower or rotor blades. For the experimental investigations, the wind gusts may be generated by a defined construction in the laboratory scale connected to the wind tunnel. Thus, unsteady turbulent FSI phenomena related to flexible structures may be analyzed in the future.

Appendix A

Calculations related to measurement conditions

A.1 Bubble Generator: Calculation of the Stokes number and settling velocity

The Stokes number Sk is the quotient of the particle response time τ_p, caused by the inertia effect, and of the fluid's characteristic time scale τ_f, based on the friction velocity u_τ. It follows, that

$$\mathrm{Sk} = \frac{\tau_p}{\tau_f} = \frac{\rho_p\, d_p^2/(18\,\mu_f)}{\mu_f/(\rho_f\, u_\tau^2)} = \frac{\rho_p\, d_p^2\, \rho_f\, u_\tau^2}{18\,\mu_f^2} \quad , \tag{A.1}$$

where d_p and ρ_p are the tracer particle's diameter (Most Penetrating Particle Size, MPPS) and the density of its chemical composition. The fluid flow properties are given by the density ρ_f and the dynamic viscosity μ_f. The friction velocity u_τ of the fluid flow can be calculated approximately, as presented in [19, 25]:

$$u_\tau = \sqrt{\frac{c_f}{2}} \cdot U_\infty \quad , \tag{A.2}$$

with the skin friction coefficient c_f taken from the investigations by H. Blasius (1908)[1] considering the *Plate Boundary Layer* at laminar fluid flow, which can be approximately transfered to this transitional case [19]:

$$c_f = 0.664 \cdot \mathrm{Re}_x^{-1/2} \quad . \tag{A.3}$$

[1] Paul Richard Heinrich Blasius (1883–1970). German fluid dynamics physicist

For ideal tracers, the Stokes number should tend towards zero (Sk $\ll 1$).
Secondly, the settling velocity u_{ts} follows with the gravitational constant g, the tracer particle's diameter d_p (MPPS) and density ρ_p, as well as the fluid density ρ_f and the dynamic viscosity μ_f:

$$u_{ts} = g \cdot d_p^2 \cdot \frac{(\rho_p - \rho_f)}{18\,\mu_f} \quad . \tag{A.4}$$

For ideal tracers, the settling velocity should be much smaller than the airstream velocity ($u_{ts} \ll U_\infty$).
Thus, calculating the Stokes number and the settling velocity, the following fluid and tracer particle properties are considered:

- the density of air $\rho_f = \rho_{air} = 1.225\,\mathrm{kg/m^3}$,
- the dynamic viscosity of air $\mu_f = \mu_{air} = 18.72 \cdot 10^{-6}\,\mathrm{Pa\,s}$,
- the density of the soap bubble tracer $\rho_p = \rho_{\mathrm{soap}} = 998\,\mathrm{kg/m^3}$,
- the diameter of the soap bubble tracer (MPPS) $d_p = d_{\mathrm{soap}} = 10\,\mu\mathrm{m}$,
- the gravitational constant $g = 9.81\,\mathrm{m/s^2}$,
- the airstream velocity range of $(U_{\infty,a} = 1.44\,\mathrm{m/s}) \leq U_\infty \leq (U_{\infty,b} = 5.37\,\mathrm{m/s})$,
- the Reynolds number range of $(\mathrm{Re}_{x,a} = 9.66 \cdot 10^3) \leq \mathrm{Re}_x \leq (\mathrm{Re}_{x,b} = 3.60 \cdot 10^4)$.

The skin friction coefficient from Eq. (A.3) according to the mentioned velocity range for U_∞ yield:

$$c_{f,a}(\mathrm{Re}_{x,a}) = 0.664 \cdot \mathrm{Re}_{x,a}^{-1/2} = 6.7560 \times 10^{-3} \quad , \tag{A.5a}$$

$$c_{f,b}(\mathrm{Re}_{x,b}) = 0.664 \cdot \mathrm{Re}_{x,b}^{-1/2} = 3.4996 \times 10^{-3} \quad . \tag{A.5b}$$

The friction velocity according to Eq. (A.2) follows for both skin friction coefficients :

$$u_{\tau,a} = \sqrt{\frac{c_{f,a}}{2}} \cdot U_{\infty,a} = 0.08369\,\frac{\mathrm{m}}{\mathrm{s}} \quad , \tag{A.6a}$$

$$u_{\tau,b} = \sqrt{\frac{c_{f,b}}{2}} \cdot U_{\infty,b} = 0.22463\,\frac{\mathrm{m}}{\mathrm{s}} \quad . \tag{A.6b}$$

Finally, the Stokes numbers according to Eq. (A.1) result for the friction velocity range in $\mathrm{Sk}_a \leq \mathrm{Sk} \leq \mathrm{Sk}_b$ with:

$$\mathrm{Sk}_a = \frac{\rho_p \, d_p^2 \, \rho_f \, u_{\tau,a}^2}{18 \, \mu_f^2} = 0.1358 \quad , \tag{A.7a}$$

$$\mathrm{Sk}_b = \frac{\rho_p \, d_p^2 \, \rho_f \, u_{\tau,b}^2}{18 \, \mu_f^2} = 0.9780 \quad . \tag{A.7b}$$

The settling velocity of the tracer particle from Eq. (A.4) results in:

$$u_{ts} = g \cdot d_p^2 \cdot \frac{(\rho_p - \rho_f)}{18 \, \mu_f} = 2.9019 \cdot 10^{-3} \, \frac{\mathrm{m}}{\mathrm{s}} \; . \tag{A.8}$$

Thus, the Stokes number and the settling velocity fulfill the required conditions.

Appendix B

Calculations related to measurement results

B.1 Parameters of the airfoil system

B.1.1 Case I

These calculations refer to the characteristics of the 1-DOF-free-oscillation for case I in Fig. 5.1. In the following, the parameters in Tab. 5.1 are calculated. One important parameter is the total damping ratio, which is computed by the logarithmic decrement of two neighbouring amplitude peaks within the period time T_d of a decaying sine-wave function which is depicted in Fig. B.1. The calculation formula is presented according to Gross et al. [10]:

$$\Lambda = \ln\left(\frac{\Delta z(t) = \Delta z(t)_i}{\Delta z(t+T_d) = \Delta z(t)_{i+1}}\right) = \delta\, T_d = \frac{2\pi\delta}{\omega_d} = 2\pi\,\frac{D}{\sqrt{1-D^2}} \quad . \tag{B.1}$$

To minimize the local measurement error, the logarithmic decrement is executed for amplitudes that are located afar from each other, i.e. a multiple of the period time $n \cdot T_d$. Then the logarithmic decrement yields:

$$\Lambda = \frac{1}{n}\ln\left(\frac{\Delta z(t)_i}{\Delta z(t)_{i+n}}\right) = 2\pi\,\frac{D}{\sqrt{1-D^2}} \quad . \tag{B.2}$$

The equation can be converted by the total damping ratio:

$$D = \frac{\Lambda}{\sqrt{(2\pi)^2+\Lambda^2}} \quad . \tag{B.3}$$

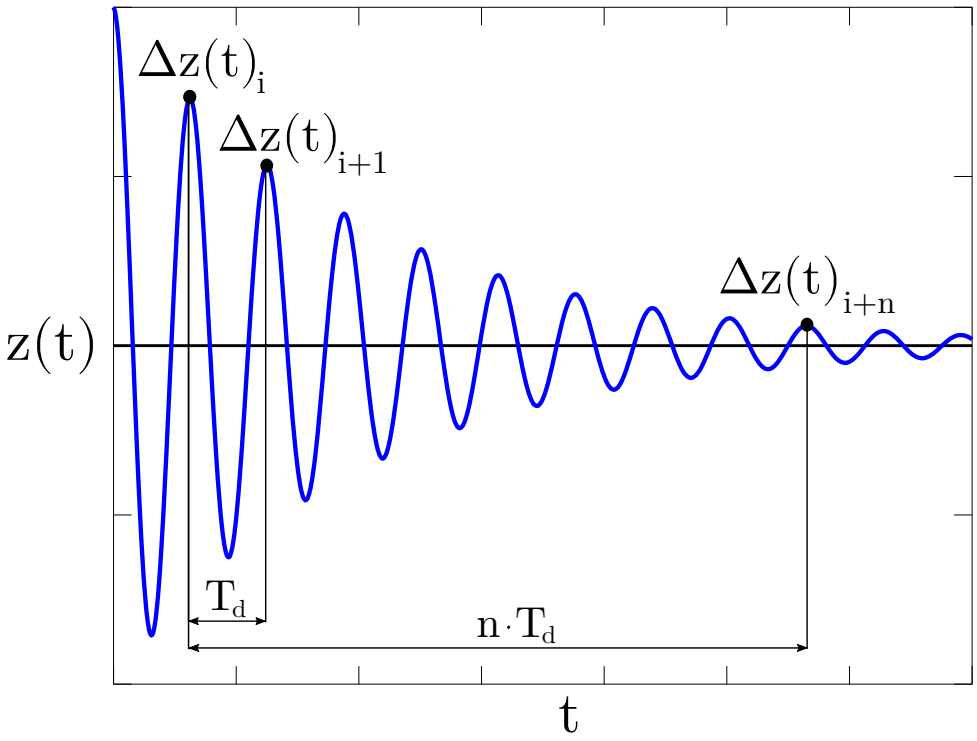

Figure B.1: Principle of the logarithmic decrement.

Now, regarding the time histories of the 1-DOF-free-oscillations for heave and pitch in Figs. 5.1a and 5.1c, the logarithmic decrement can be calculated. Within the time range of $4\,\mathrm{s} \leq t \leq 6.8\,\mathrm{s}$, two amplitudes with the amount of $n = 20$ periods in between are considered and it follows:

$$\Lambda_h = \frac{1}{20} \ln\left(\frac{3.08499\,\mathrm{mm}}{2.05801\,\mathrm{mm}}\right) = 0.02024 \quad , \tag{B.4a}$$

$$\Lambda_\alpha = \frac{1}{20} \ln\left(\frac{2.6803\,\mathrm{mm}}{1.8034\,\mathrm{mm}}\right) = 0.01981 \quad . \tag{B.4b}$$

The total translational and rotational damping ratios result in

$$D_h^{1-\mathrm{DOF},tot} = \frac{\Lambda_h}{\sqrt{(2\pi)^2 + \Lambda_h^2}} = 3.2214 \times 10^{-3} \quad , \tag{B.5}$$

$$D_\alpha^{1-\mathrm{DOF},tot} = \frac{\Lambda_\alpha}{\sqrt{(2\pi)^2 + \Lambda_\alpha^2}} = 3.1533 \times 10^{-3} \quad . \tag{B.6}$$

The bending stiffness is calculated by:

$$k_h = (2\pi\, f_\mathrm{h}^{1-DOF})^2\, m_\mathrm{w} = 732.92\,\mathrm{N/m} \quad , \tag{B.7}$$

while the total mass of the wing system including the extra mass yields $m_\mathrm{w} = 0.33921\,\mathrm{kg}$. It is around 4 g higher than the total mass m_w in [23], due to the fact that the varnishing of the wing caused this slight weight increase. The frequency $f_\mathrm{h}^{1-DOF} = 7.398\,\mathrm{Hz}$ of the 1-DOF free-osillation of the heave motion of case I represents the characteristics of the analogous model of the translational spring-mass-system. The torsional stiffness of the rotational spring is taken from the data sheet of the manufacturer with $k_\alpha = 0.3832\,\mathrm{Nm/rad}$. Moving to the mass moment of inertia, it is computed corresponding to [23] with the frequency $f_\alpha^{1-DOF} = 8.378\,\mathrm{Hz}$ of the 1-DOF free-osillation of the pitch motion of case I, representing the characteristics analogous model of the rotational spring-mass-moment-of-inertia-system as follows:

$$I_\alpha^E = \frac{k_\alpha}{(2\pi\, f_\alpha^{1-DOF})^2} = 1.383 \times 10^{-4}\,\mathrm{kg\,m^2} \quad . \tag{B.8}$$

Finally, the total translational and rotational damping is calculated by:

$$b_h^\mathrm{tot} = 2\, D_\mathrm{h}^{1-\mathrm{DOF,tot}} \sqrt{k_\mathrm{h}\, m_\mathrm{w}} = 10.16 \times 10^{-2}\,\mathrm{Ns/m} \quad , \tag{B.9a}$$

$$b_\alpha^\mathrm{tot} = 2\, D_\alpha^{1-\mathrm{DOF,tot}} \sqrt{k_\alpha\, I_\alpha^E} = 4.59 \times 10^{-5}\,\mathrm{Nm/s} \quad . \tag{B.9b}$$

B.1.2 Case III

These calculations refer to the characteristics of the 1-DOF-free-oscillation for Case III in Fig. 5.2. In the following, the parameter results of Tab. 5.2 are calculated. Regarding the time histories of the 1-DOF-free-oscillations for heave and pitch in Figs. 5.2a and 5.2c, the logarithmic decrement can be calculated. Within the time range of $4\,\mathrm{s} \leq t \leq 6.8\,\mathrm{s}$, two amplitudes with the amount of $n = 20$ periods in between are considered and it follows:

$$\Lambda_h = \frac{1}{20} \ln\left(\frac{2.8712\,\mathrm{mm}}{1.8611\,\mathrm{mm}}\right) = 0.02168 \quad , \tag{B.10a}$$

$$\Lambda_\alpha = \frac{1}{20} \ln\left(\frac{1.5572\,\mathrm{mm}}{1.1213\,\mathrm{mm}}\right) = 0.01642 \quad . \tag{B.10b}$$

The total translational and rotational damping ratios result in

$$D_h^{1-\mathrm{DOF},tot} = \frac{\Lambda_h}{\sqrt{(2\pi)^2 + \Lambda_h^2}} = 3.4502 \times 10^{-3} \quad , \tag{B.11}$$

$$D_\alpha^{1-\mathrm{DOF},tot} = \frac{\Lambda_\alpha}{\sqrt{(2\pi)^2 + \Lambda_\alpha^2}} = 2.6133 \times 10^{-3} \quad . \tag{B.12}$$

The bending stiffness is the same as for case I with $k_h = 732.92\,\mathrm{N/m}$ due to identical heave frequencies and the total mass of the wing system including the extra mass and the

varnishing influence, which yields $m_{\mathrm{w}} = 0.33921\,\mathrm{kg}$. The torsional stiffness of the rotational spring is taken from the data sheet of the manufacturer with $k_\alpha = 0.3832\,\mathrm{Nm/rad}$. The mass moment of inertia with the pitch frequency of $f_\alpha^{1-DOF} = 7.576\,\mathrm{Hz}$ of the 1-DOF free-oscillation analysis results in:

$$I_\alpha^E = \frac{k_\alpha}{(2\pi\, f_\alpha^{1-DOF})^2} = 1.69 \times 10^{-4}\,\mathrm{kg\,m^2} \quad . \tag{B.13}$$

Finally, the total translational/rotational damping is calculated by:

$$b_h^{\mathrm{tot}} = 2\, D_{\mathrm{h}}^{1-\mathrm{DOF,tot}} \sqrt{k_{\mathrm{h}}\, \mathrm{m_w}} = 10.88 \times 10^{-2}\,\mathrm{Ns/m} \quad , \tag{B.14a}$$

$$b_\alpha^{\mathrm{tot}} = 2\, D_\alpha^{1-\mathrm{DOF,tot}} \sqrt{k_\alpha\, I_\alpha^E} = 4.21 \times 10^{-5}\,\mathrm{Nm/s} \quad . \tag{B.14b}$$

Bibliography

[1] Kapitel 74 Methode der kleinsten Quadrate. https://www.mia.uni-saarland.de/Teaching/MFI0708/kap74.pdf. Accessed: 2020-10-7. 48, 49

[2] Anderson, J. D. *Fundamentals of Aerodynamics*, second ed. McGraw-Hill Education New York, 2016. VI, 15, 16

[3] Bing, P., Hui-min, X., Bo-qin, X., and Fu-long, D. Performance of sub-pixel registration algorithms in digital image correlation. *Measurement Science and Technology 17* (2006), 1615–1621. 55, 56

[4] Bruck, H. A., McNeill, S. R., Sutton, M. A., and Peters, W. H. Digital image correlation using Newton-Raphson method of partial differential correction. *Experimental Mechanics 29*, 3 (1989), 261–267. 58

[5] Brunn, W. N. A. *Strömungsmesstechnik*, second ed. Springer-Verlag Berlin Heidelberg, 2006. 31, 36

[6] Cardona, J. L., Miller, M. J., Derecktor, T., Winckler, S., Volkmann, K., Medina, A., Cowles, S., Lorick, R., Breuer, K. S., and Mandre, S. Field-testing of a 1 kW oscillating hydrofoil energy harvesting system. *Brown University School of Engineering, Providence, RI, USA; BluSource Energy, Inc, Portsmouth, RI, USA* (2016). V, 1, 2

[7] De Nayer, G., and Breuer, M. Numerical FSI investigation based on LES: Flow past a cylinder with a flexible splitter plate involving large deformations (FSI-PfS-2a). *Int. Journal of Heat and Fluid Flow 50* (2014), 300–315. V, 1, 3

[8] Ferziger, J. H., and Peric, M. *Numerische Strömungsmechanik*. Springer Berlin Heidelberg, 2008. IX, 64

[9] Giovannetti, L. M., Banks, J., Turnock, S., and Boyd, S. Uncertainty assessment of coupled digital-image correlation and particle-image velocimetry for

fluid-structure-interaction wind tunnel experiments. *Journal of Fluids and Structures 68* (2017), 125–140. VI, 8, 9

[10] Gross, D., Hauger, W., Schröder, J., and Wall, W. A. *Technische Mechanik 3*. Springer Berlin Heidelberg, 2019. 155

[11] Horn, B. K. P. Tsai's camera calibration method revisited. *Massachusetts Institute of Technology, Department of Electrical Engineering and Computer Science* (2000), 1–13. 42, 49

[12] Ihlenburg, F. Mathematische Grundlagen der Numerischen mechanik. Master's course Lecture, 2018. 49

[13] Kalmbach, A., and Breuer, M. Experimental PIV/V3V measurements of vortex–induced fluid–structure interaction in turbulent flow — A new benchmark FSI–PfS–2a. *Journal of Fluids and Structures 42* (2013), 369–387. V, 2, 3

[14] Métivier, V., Dumas, G., and Poirel, D. Aeroelastic Dynamics of a NACA 0012 Airfoil at Transitional Reynolds Numbers. *39th AIAA Fluid Dynamics Conference 4034* (2009), 1–18. VI, 9

[15] Nayer, G. D., Breuer, M., and Wood, J. Numerical investigations on the dynamic behavior of a 2-DOF airfoil in the transitional Re number regime based on fully coupled simulations relying on an eddy-resolving technique. *Int. Journal of Heat and Fluid Flow 85* (2020), 108631. XII, XVI, 10, 11, 12, 75, 117, 120, 123, 125, 128, 145, 148

[16] Nocedal, J., and Wright, S. J. *Numerical Optimization*, second ed. Springer New York, 2006. 51

[17] Papula, L. *Mathematik für Ingenieure und Naturwissenschaftler Band 3*. Springer Fachmedien Wiesbaden, 2016. 61, 62

[18] Poirel, D., and Mendes, F. Experimental small-amplitude self-sustained pitch–heave oscillations at transitional Reynolds numbers. *AIAA Journal 52*, 8 (2014), 1581–1590. 10

[19] Schlichting, H., and Gersten, K. *Boundary-Layer Theory*. Springer Berlin Heidelberg, 2017. 151

[20] Sutton, M. A. Digital-Image Correlation for Shape and Deformation Measurements. In *Springer Handbook of Experimental Solid Mechanics*. Springer US, 2008, pp. 565–600. VIII, 54, 55

[21] Tsai, R. A versatile camera calibration technique for high-accuracy 3D machine vision metrology using off-the-shelf TV cameras and lenses. *IEEE Journal of Robotics and Automation RA-3, No. 4* (1987), 125–140. 42

[22] Winslow, J., Otsuka, H., Govindarajan, B., and Chopra, I. Basic understanding of airfoil characteristics at low Reynolds numbers ($10^4 - 10^5$). *Journal of Aircraft 55*, 3 (2018), 1050–1061. VI, 15, 16, 17

[23] Wood, J., Breuer, M., and Nayer, G. D. Experimental investigations on the dynamic behavior of a 2-DOF airfoil in the transitional Re number regime based on digital-image correlation measurements. *Journal of Fluids and Structures 96* (2020), 103052. VI, VII, IX, XI, XII, XV, XVI, 3, 10, 11, 12, 17, 18, 20, 21, 22, 40, 73, 74, 75, 76, 77, 78, 79, 80, 81, 82, 96, 97, 100, 102, 103, 104, 106, 107, 108, 112, 113, 114, 117, 123, 145, 146, 147, 148, 157

[24] Wood, J. N. Windkanal-Dokumentation. Tech. rep., Helmut-Schmidt University, Hamburg, Germany, Professur für Strömungsmechanik, 2015. VI, 23, 24

[25] Wood, J. N. *Experimentelle Untersuchungen zur Fluid-Struktur-Interaktion einer deformierbaren Membran-Halbkugel in turbulenter Strömung.* PhD thesis, Helmut-Schmidt-Universität / Universität der Bundeswehr Hamburg, 2019. VI, VII, IX, 22, 23, 28, 33, 36, 38, 39, 41, 57, 64, 151

[26] Wood, J. N. 3D Digital-Image-Correlation: Digitale Bildkorrelation für Strukturmessungen. Tech. rep., Helmut-Schmidt University, Hamburg, Germany, Professur für Strömungsmechanik, 2020. VII, VIII, XV, 42, 43, 45, 48, 51, 56

[27] Wood, J. N. Bubble Generator/ Blasengenerator. Tech. rep., Helmut-Schmidt University, Hamburg, Germany, Professur für Strömungsmechanik, 2020. VII, 33

[28] Wood, J. N. Constant-Temperature-Anemometry (CTA) - TSI CTA 1750. Tech. rep., Helmut-Schmidt University, Hamburg, Germany, Professur für Strömungsmechanik, 2020. VII, 25

[29] Wood, J. N. High-Speed Particle-Image Velocimetry (HS-PIV-System). Tech. rep., Helmut-Schmidt University, Hamburg, Germany, Professur für Strömungsmechanik, 2020. VII, 31, 35

[30] Zhang, P., Carretto, A., and Porfiri, M. Simultaneous digital image correlation/particle image velocimetry to unfold fluid–structure interaction during air-backed impact. *Journal of Fluids and Structures 95* (2020), 102980. V, 4, 5, 9

[31] Zhang, P., Peterson, S. D., and Porfiri, M. Combined particle image velocimetry/digital image correlation for load estimation. *Experimental Thermal and Fluid Science 100* (2019), 207 – 221. V, 6, 7, 9

[32] Zhang, P., and Porfiri, M. A combined digital image correlation/particle image velocimetry study of water-backed impact. *Composite Structures 224* (2019), 111010. V, 5, 6, 9

Hochschule für Angewandte Wissenschaften Hamburg
Hamburg University of Applied Sciences

Erklärung zur selbstständigen Bearbeitung einer Abschlussarbeit

Gemäß der Allgemeinen Prüfungs- und Studienordnung ist zusammen mit der Abschlussarbeit eine schriftliche Erklärung abzugeben, in der der Studierende bestätigt, dass die Abschlussarbeit „– bei einer Gruppenarbeit die entsprechend gekennzeichneten Teile der Arbeit [(§ 18 Abs. 1 APSO-TI-BM bzw. § 21 Abs. 1 APSO-INGI)] – ohne fremde Hilfe selbständig verfasst und nur die angegebenen Quellen und Hilfsmittel benutzt wurden. Wörtlich oder dem Sinn nach aus anderen Werken entnommene Stellen sind unter Angabe der Quellen kenntlich zu machen."

Quelle: § 16 Abs. 5 APSO-TI-BM bzw. § 15 Abs. 6 APSO-INGI

Dieses Blatt, mit der folgenden Erklärung, ist nach Fertigstellung der Abschlussarbeit durch den Studierenden auszufüllen und jeweils mit Originalunterschrift als letztes Blatt in das Prüfungsexemplar der Abschlussarbeit einzubinden.
Eine unrichtig abgegebene Erklärung kann -auch nachträglich- zur Ungültigkeit des Studienabschlusses führen.

Erklärung zur selbstständigen Bearbeitung der Arbeit

Hiermit versichere ich,

Name: Clasen

Vorname: Michael

dass ich die vorliegende Masterarbeit bzw. bei einer Gruppenarbeit die entsprechend gekennzeichneten Teile der Arbeit – mit dem Thema:

High-Speed Messverfahren für die instationäre Umströmung und die Strukturoszillationen eines beweglich aufgehängten Tragflügels im Windkanal

ohne fremde Hilfe selbständig verfasst und nur die angegebenen Quellen und Hilfsmittel benutzt habe. Wörtlich oder dem Sinn nach aus anderen Werken entnommene Stellen sind unter Angabe der Quellen kenntlich gemacht.

- die folgende Aussage ist bei Gruppenarbeiten auszufüllen und entfällt bei Einzelarbeiten -

Die Kennzeichnung der von mir erstellten und verantworteten Teile der -bitte auswählen- ist erfolgt durch:

Hamburg	09.11.2020	[redacted]
Ort	Datum	Unterschrift im Original